Master thesis
Delft University
of Technology

Xiao Sen Zheng

An investigation of hydrogen-ammonia combustion inside internal combustion engines

An investigation of hydrogen-ammonia combustion inside internal combustion engines

by

Xiao Sen Zheng

to obtain the degree of Master of Science
at the Delft University of Technology,
to be defended publicly on Monday November 30, 2020 at 9:30 AM.

Student number:	4377370	
Project duration:	January 2020 – November 2020	
Thesis committee:	Ir. K. Visser, Rear-Admiral (ME) ret.,	Chairman graduation committee
	Dr. Ir. P. de Vos,	Supervisor
	Ir. H. Sapra,	Supervisor
	Dr. Ir. X. L. J. Seykens,	External committee member

TU Delft

Abstract

Ammonia can become an attractive alternative fuel source on-board of ships, since it does not produce SOx and carbon related emissions (including CO_2, CO and soot) [1]. However, pure ammonia combustion is too slow to drive an internal combustion engine (ICE), a promoter fuel such as hydrogen is needed to speed up the combustion process. Since the SOFC can be used as a power generator and ammonia cracker, an interesting proposal is to have a hybrid ICE-SOFC power generation system on-board ships. A vast amount of papers concerning directly fueled ammonia SOFCs have been published throughout the years. This concept has already been extensively modeled and successfully tested on large-scale. On the other hand, not much is known about hydrogen-ammonia combustion inside an ICE. Although the flammability behaviour and chemical kinetics during combustion have been widely investigated. Publications concerning the in-cylinder combustion characteristics are scarce. Since there are already a number of working ammonia fueled SOFC models in the literature, the thesis will be mostly emphasised on the investigation of hydrogen-ammonia fueled internal combustion engines.

Conducted experiments on automotive sized engines have shown that hydrogen-ammonia combustion during SI mode is possible, but not optimal because of the high auto-ignition resistance and low flame propagation speed of ammonia. Hence, poor engine efficiencies, low power densities and large amounts of unburned fuel are more likely to occur during spark ignition. Compression ignition on the other hand is largely affected by great amounts of NOx production inside the flame zone. The NOx is primarily produced from fuel-bound nitrogen, which can unlike the nitrogen (N_2) in air easily re-bond with free oxygen during the combustion process. HCCI combustion is a promising candidate to overcome these disadvantages ($i.e.$ low power density and high NOx emissions).

In this thesis, four models have been developed for the in-cylinder analysis of hydrogen-ammonia combustion inside internal combustion engines. Firstly, the in-cylinder combustion characteristics for a range of fuel blends (31 to 47 vol. percent hydrogen) have been simulated in the in-cylinder model. The modelling results showed that lower hydrogen concentrations will lead to a more spread out combustion event, while the power output remained almost similar between these fuel blends. However, it has been observed by Pochet et al. [2] that the reduction in hydrogen content will lead to lower maximum temperatures, which will affect the combustion efficiency in case the maximum temperature is below the minimum threshold of 1400 $[K]$. This maximum temperature threshold is an important requirement because of the high auto-ignition resistance of ammonia fuel. Hence, the ammonia fraction should be as high as possible while its maximum temperature during combustion has to stay above the temperature threshold to ensure high combustion efficiencies.

Secondly, because of the absence of hydrogen-ammonia experiments on marine sized engines, theoretical engine scaling laws are the sole methods to obtain insight in the power output of larger sized engines. The engine scaling model is based on relatively simple criteria, however, these scaling laws have been observed to be the most effective when two conditions are met. First, the geometric similarity have to be maximised, so that both engines have similar boundary conditions. Secondly, matching com-

bustion characteristics are needed to achieve similarity in engine performances and emissions. Three scaling laws have been proposed in the literature, the speed law (S Law) by Chikashisa et al. [3], lift-off law (L Law) by Stager et al. [4] and the Pressure law (P Law) proposed by Bergin et al. [5]. However, in case of HCCI combustion, most of the scaling parameters such as the spray penetration length, mixing spray, fuel spray distribution, injection timing and many more become irrelevant and have to be neglected in the modelling process. However, these scaling parameters are crucial for conventional diesel engines, because of the limited mixing time (diffusion combustion) which is not the case for premixed combustion strategies. From these scaling laws, the S Law has shown the closest resemblance in combustion characteristics with the baseline engine, because of the identical timescale for the chemical reactions between both engines.

However, matching the heat transfer losses between both engines is also a crucial requirement when making the assumption of similar combustion characteristics. This assumption is necessary, since there is no experimental data (*i.e.* pressure trace) available for the scaled engine. However, smaller engines have in contrast to larger engines relatively greater surface to volume ratios. As a result, smaller engines are subjected to proportionally larger convective heat transfer losses, which translates to a lower pressure rise rate and peak cylinder pressure. In this respect, the scaling laws are more accurate for small differences in bore ratios between the baseline and scaled engine. Hence, it is not recommended to scale an automotive sized engine to a marine or truck sized variant, since this will affect the accuracy of the scaled model as a result of the noticeable difference in combustion characteristics between both engines. However, with the absence of hydrogen-ammonia experiments on marine sized engines, scaling laws are the sole methods to obtain insight in the power output and fuel demand of larger sized engines. According to the single value principle, the amount of heat release should be proportional to the in-cylinder volume (L^3 [1]). The S Law, P Law and L Law have shown heat loss scaling factors of $L^{2.47}$, $L^{2.57}$ and $L^{2.81}$, respectively, for a 47 vol. % hydrogen fuel blend. Hence, in order to use the S Law scaling method, heat loss calibration is necessary to obtain identical heat losses per mg injected fuel between the baseline and scaled engine. Decreasing the wall temperature has shown respectable results, however, this method requires a thermal system management strategy, when applied on a real case scenario. In this respect, the temperature of the cylinder wall that can be controlled by the cooling water has to be scaled accordingly to ensure the same cumulative convective heat transfer loss per mg injected fuel for both engines. However, lowering the temperature for the heat loss calibration will result in less optimistic power output than in reality for the scaled engine.

From the literature study, it became evident that HCCI engines have issues with auto-ignition control. Here, the inlet conditions are the decisive parameters in the location of the start of combustion crank angle. Hence, a parametric study on the initial conditions is necessary to get a better understanding which intake parameters have the greatest impact on the auto-ignition and how changes in the initial conditions will affect the combustion characteristics. For the analysis, the modified knock integral model (MKIM) and the Single-Wiebe function have been developed. Here, the MKIM function is necessary to determine the shift in the start of combustion crank angle when adjusting the initial conditions. Then, the Single-Wiebe model is used to determine the new mass fraction burn distribution for the simulation of the in-cylinder combustion characteristics in the anti-causal version of the in-cylinder model from **Chapter 5**.

Changes in the initial conditions have shown big impacts on the auto-ignition of HCCI engines and could result in undesired early knock or misfire. Small fluctuations in the engine's intake conditions will be inevitable when the HCCI engine is integrated in an SOFC-ICE system design. Hence, with the

---

[1] L is the scaling factor based on the size of the engine bore ($L = \frac{D_{B,1}}{D_{B,2}}$).

current knowledge on HCCI engines, it can be concluded that hydrogen-ammonia HCCI combustion is not optimal for an SOFC-ICE design. However, HCCI mode can become a reliable option in case its whole operational area can be mapped and implemented into an automated ignition control system. Changes in the initial conditions (*i.e.* inlet pressure, engine speed, equivalence ratio, fuel composition and inlet temperature) will result in a shift in the auto-ignition crank angle. In this respect, the HCCI engine should be able to anticipate whether the shift in the location of the start of combustion is within its operational area. Otherwise, adjustments in the inlet temperature, injected fuel mass and fuel composition are necessary to stay outside the early knock and misfire region. Because of the relatively small load-range of HCCI mode when fueled with hydrogen-ammonia, the engine should be able to switch to SI mode, when the load condition cannot be satisfied. This so called ’Hybrid mode’ is an optimal way to increase the load range of the engine. Here, the engine is operating in HCCI mode during low to medium load and low engine speed conditions, while SI mode is activated during the cold start, idling and at high engine speeds. However, the technical feasibility for this so called hybrid system has to be further investigated.

All in all, hydrogen-ammonia combustion inside HCCI engines is a novel concept that requires lots of large-scale experiments and simulation studies to find the most optimal engine geometry, operating range and hydrogen concentration.

Preface

The report in front of you is written to conclude my study at the Delft University of Technology for the degree of Master of Science in Marine Engineering. This thesis could not have been completed without the support of several people, who I would like to thank beforehand.

Firstly, I want to express my gratitude to Peter de Vos for this fascinating thesis topic and for his critical aiding mindset during the meetings that were shown to be crucial in the development of the overall quality and depth of this project. Next, a very special thanks to Harsh Sapra for his patience and kindness in helping me with the modelling and for providing me with well structured feedback. Even during his own tight deadlines, I was always able to count on him. In addition, I would like to thank Klaas Visser for being the Chairman of this project and for his valuable feedback during the kick-off and mid-term meetings. I also want to show my gratitude to the external committee member Xander Seykens for having found time to be part of the thesis committee.

In addition, I want to thank my friends for the great student time. A special thanks to Ting-Kai and my girlfriend who both supported me during my master and lighted up my life whenever I felt demotivated. Lastly, I wish to thank my parents and my two sisters for their steadfast support since the beginning of this wonderful journey.

Xiao Sen Zheng
Delft, November 2020

Nomenclature

List of Abbreviations

CO_2	Carbon dioxide
H_2	Hydrogen
N_2	Nitrogen gas
N_2O	Nitrous oxide
NO_x	Nitrogen oxides
O_2	Oxygen gas
SO_X	Sulfur oxides
$vol.\%$	Percentage of total volume
$wt.\%$	Percentage of total weight
0D	Zero dimensional
31H	31 vol.% hydrogen and 69 vol.% ammonia fuel blend
38H	38 vol.% hydrogen and 62 vol.% ammonia fuel blend
44H	44 vol.% hydrogen and 56 vol.% ammonia fuel blend
47H	47 vol.% hydrogen and 53 vol.% ammonia fuel blend
AFR	Air to fuel ratio
aTDC	After top dead center
BDC	Bottom dead center
BD	Burn duration
BOP	Balance of plant
CAD	Crank angle degree
CDC	Conventional diesel combustion
CHP	Combined heat and power
CI	Compression ignition
CN	Cetane number
CRR	Combustion reaction rate
DC	Direct current
DIR	Direct internal reformer
DME	Dimethyl ether
EC	Exhaust valve closed
EGR	Exhaust gas recirculation
EM	Electric motor
EOC	End of combustion
EO	Exhaust valve open
GAHRR	Gross apparent heat release rate
GB	Gear box
GHG	Greenhouse gas emissions
HCCI	Homogeneous compression charge ignition
HEX	Heat exchanger
HFO	Heavy fuel oil
HHV	Higher heat value
HRR	Heat release rate
ICE	Internal combustion engine
IC	Inlet valve closed
IC	Intercooler
IIR	Indirect internal reformer
IMEP	Indicated mean effective pressure
IMO	International Maritime Organization
IO	Inlet valve open
KIM	Knock integral model
LHV	Lower heat value

LNG	Liquid natural gas
Max	Maximum
MBT	Maximum brake torque
MCR	Maximum continuous rating
MEP	Mean effective pressure
mfb	Mass fraction burn
MKIM	Modified knock integral model
MVFP	Mean value first principle
NAHRR	Net apparent heat release rate
OCV	Open circuit voltage
PEMFC	Proton exchange membrane fuel cell
ppm	Parts per million
RCCI	Reactivity controlled compression ignition
RCO	Reaction coordinate
rpm	Revolutions per minute
SCC	Stress corrosion cracking
SCR	Selective catalytic reduction
Sf	Scaling factor
SI	Spark ignition
SOC	Start of combustion
SOFC-H	Proton conducting solid oxide fuel cell
SOFC-O	Oxygen ion conducting solid oxide fuel cell
SOFC	Solid oxide fuel cell
SOI	Start of injection
SSAS	Solid state ammonia synthesis
TDC	Top dead center
TPB	Triple phase boundary

List of symbols

α	Heat transfer coefficient $[W/m^2K]$
$\dot{E}_f$	Energy of fuel flow $[kJ/s]$
$\dot{Q}_{comb}$	Combustion heat flow $[kJ/s]$
$\dot{Q}_{loss}$	Heat loss flow $[kJ/s]$
$\dot{W}$	Indicated work $[kJ/s]$
η_{carnot}	Carnot efficiency $[-]$
η_{comb}	Combustion efficiency $[-]$
η_e	Effective efficiency $[-]$
η_i	Indicated efficiency $[-]$
η_m	Mechanical efficiency $[-]$
η_{td}	Thermodynamic efficiency $[-]$
λ	air excess ratio $[-]$
ϕ	Equivalence ratio $[-]$
σ	Air/fuel ratio $[-]$
τ	Ignition delay $[CAD]$
θ_d	Burn duration $[CAD]$
θ_{SOC}	Start of combustion $[CAD]$
A	MKIM empirical parameter $[-]$
a	Iso-volumetric pressure ratio Seiliger $[-]$
a	Wiebe constant efficiency factor $[-]$
b	Iso-baric volume ratio in Seiliger $[-]$
b	MKIM empirical parameter $[-]$
C	Burn duration model empirical parameter $[-]$
c	Iso-thermal volume ratio in Seiliger $[-]$
c	MKIM empirical parameter $[-]$
c_m	Mean piston speed $[m/s]$
c_p	Specific at constant pressure $[kJ/kgK]$
c_v	Specific heat at constant volume $[kJ/kgK]$

D	Burn duration model empirical parameter $[-]$
D_b	Bore diameter $[m]$
E	Burn duration model empirical parameter $[-]$
E_A	Activation energy $[kJ]$
E_f	Heat of vaporization $[J]$
F	Faraday's constant $[C/mol]$
G	Gibbs free energy $[J/mol]$
h^L	Lower heat value $[kJ/kg]$
h^{ref}	Heat of formation at ref. temp. $[kJ/kg]$
I	Current $[A]$
i	Number of cylinders $[-]$
$IMEP$	Indicated mean effective pressure $[bar]$
L	Scaling factor $[-]$
L_s	Stroke length $[m]$
M	Molar mass $[-]$
m	Exponent in Woschni heat transfer $[-]$
m	Wiebe constant form factor $[-]$
m_f	Fuel mass $[kg]$
m_r	Residual mass $[kg]$
m_t	Trapped mass $[kg]$
m_{air}	Air mass $[kg]$
m_{bf}	Fuel burnt $[mg]$
$m_{f,inj.}$	Injected fuel mass $[mg]$
N	Engine speed $[rpm]$
n	MKIM empirical parameter $[-]$
n	Polytropic exponent $[-]$
n_c	Polytropic compression coefficient $[-]$
n_e	Polytropic expansion coefficient $[-]$

P	Pressure $[bar]$
P_i	Indicated power $[kW]$
P_{stack}	Power output stack $[kW]$
q	Specific heat quantity $[kJ/kg]$
R	Gas constant $[kJ/kgK]$
r_c	Effective compression ratio $[-]$
r_e	Effective expansion ratio $[-]$
R_M	Universal gas constant $[kJ/kmolK]$
T	Temperature $[K]$
u	Internal energy $[kJ]$
u^L	Lower combustion value $[kJ/kg]$
u^{ref}	Heat of formation at ref. temp. $[kJ/kg]$
U_f	Fuel utilization $[-]$
V	Electic potential $[V]$
V	Volume $[m^3]$
v_c	Ratio between the volume at IVC and volume at a specific crank angle $[-]$
V_s	Stroke volume $[m^3]$
x_b	Mass fraction burn $[-]$
X_d	Mixture dilution fraction $[-]$
X_r	Internal residual gas mass fraction $[-]$
x_{H_2}	Hydrogen molar fraction $[-]$
x_{sg}	Mass fraction stoichiometric gas mixture $[-]$

Subscripts

a	air
c	compression
comb	combustion
cyl	cylinder
d	duration
dis	displacement

e	effective
e	expansion
f	fuel
g	gas
i	indicated
in	into the system
inj	injected
m	mechanical
max	maximum
min	minimum
r	residual gas
S	stroke
sg	stoichiometric combustion gas
t	trapped gas
td	thermodynamic
vol	volumetric
w	wall

Contents

List of Figures

List of Tables

Chapter 1

Background

1.1 Introduction

1.1.1 Forecasted carbon footprint reduction in the shipping industry

During the meeting in May 2018, the IMO has adopted a new strategy aiming for a reduction in total marine greenhouse gas emissions (GHG) of at least 50% by 2050 compared to 2008 [36]. The maritime industry has to face a major transition towards carbon neutral fuels in the upcoming decades. Liquid natural gas (LNG) has been highly emphasized as one of the best alternatives to oil fuels, mainly because of its lower emissions of sulphur (SOx), nitrogen (NOx) and carbon dioxide (CO_2) [6]. Nonetheless, LNG is a carbon based fuel, which can make it only a transitional fuel towards a fully carbon-free based future.

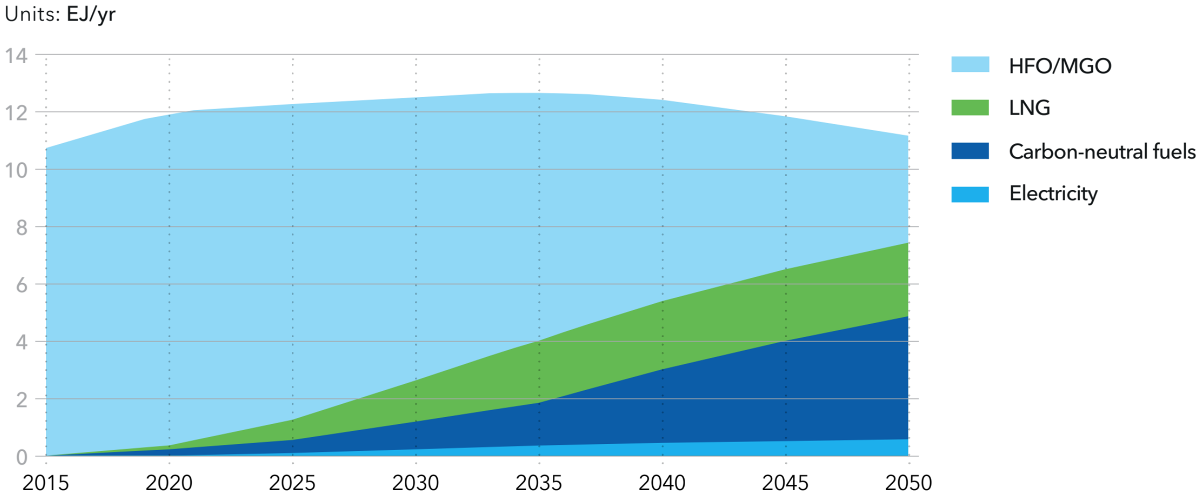

Figure 1.1: Forecasted shipping energy mix (1 [EJ] equals 278 [TWh]) [6]

According to the latest model forecast by DNV-GL [6], the shipping energy will gradually shift to carbon-neutral fuels, which is estimated to overtake the 34% share of liquid fossil fuel by 2050 as shown in Figure 1.1. The term carbon-neutral refers to fuels with no carbon footprint or net GHG, such as biofuels, hydrogen and ammonia, provided that the energy needed to create the fuel also does not emit greenhouse gasses. Batteries have shown to be effective for small yachts and short-distance ferries. However, for medium- and long-distance vessels a different type of energy carrier is needed that is in line with the reduced carbon strategy adopted by IMO. Ammonia has shown to be a great candidate for medium-distance, because of its high energy density in comparison to other carbon free alternatives, such as liquid hydrogen and batteries as can be seen in Figure 1.2. However, the volumetric energy density of ammonia is lower than that of carbon based fuels. As a matter of fact, ammonia requires approximately 3.3 times the volume compared to the same amount of energy stored in HFO [7]. This may be problematic for ammonia fueled long-distance container vessels, which as a consequence have to refuel more frequently than they do today, which may lead to more downtime and congested harbours.

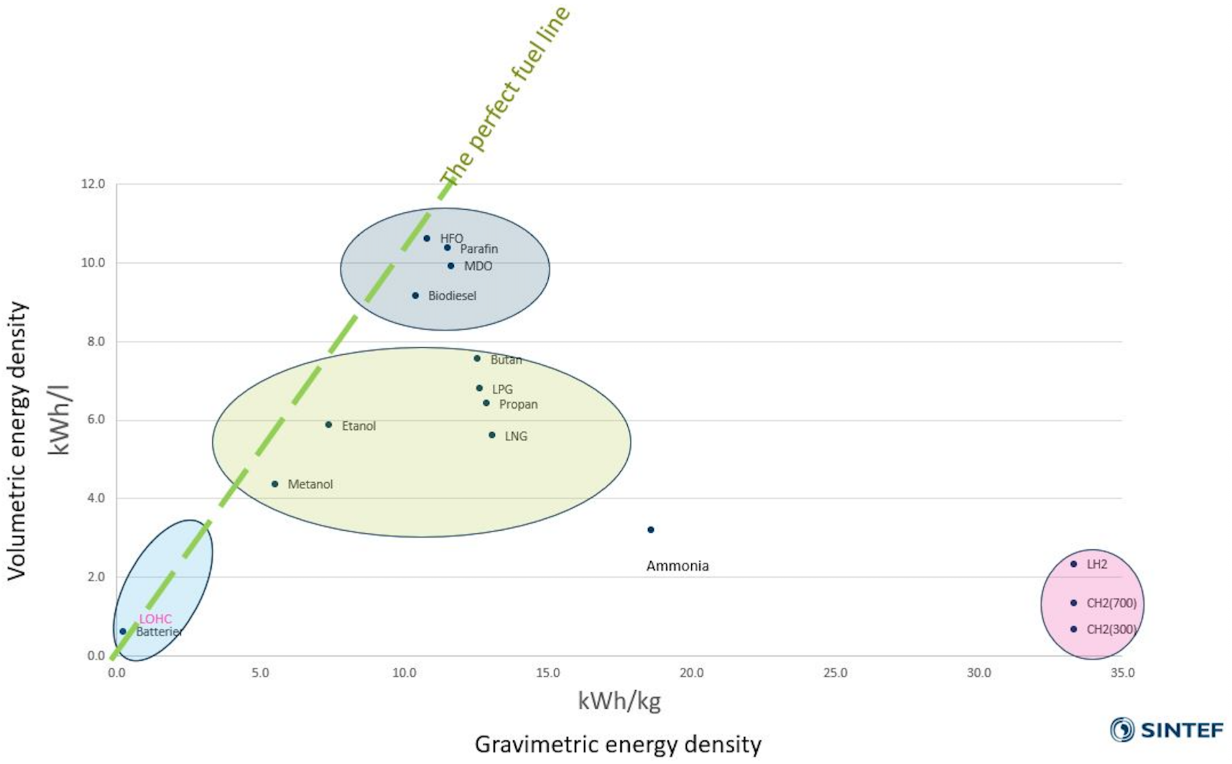

Figure 1.2: Gravimetric and volumetric energy densities of various fuel types [7].

1.1.2 Ammonia as marine fuel

The good side of ammonia

The interest in ammonia as a potential fuel alternative has been increasing throughout the years. Ammonia can be an attractive alternative fuel on-board of ships, since it does not produce SOx and carbon related emissions (including CO_2, CO and soot) [1]. Liquid ammonia can be easily stored under room temperature at 10 $[bar]$, which makes it excellent for storage and transportation. Unlike hydrogen, liquid ammonia is non-explosive and has a low risk of fire [37]. Because of the odorless scent of hydrogen and its high explosiveness when mixed with air, storage and transportation regulations are strict. This increases the difficulty of building a fully operational hydrogen infrastructure across all harbors. In addition, ammonia is also excessively used in the commercial agricultural fertilizer industry, therefore the infrastructure for ammonia manufacturing and distribution have already been fully established. As shown in Figure 1.3, the global annual production rate of ammonia has been steadily increasing throughout the years. It has been projected that the ammonia market will grow approximately 3% in the upcoming 10 years, making it one of the conventional fuel sources in the future [38].

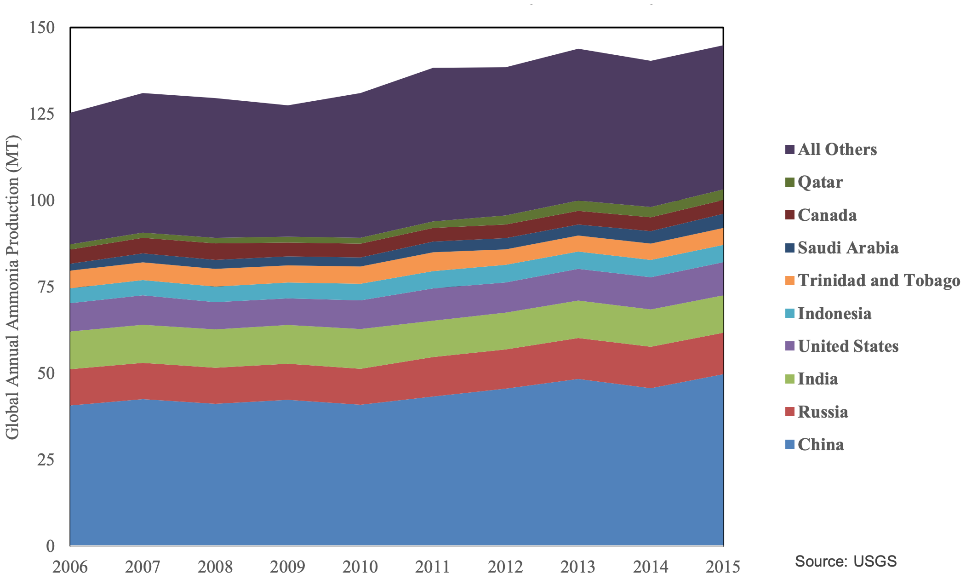

Source: USGS

Figure 1.3: Global annual ammonia production per country [8]

Nowadays, the hydrogen that is necessary for the ammonia synthesis is mostly produced from natural gas and other types of carbon based fuels, such as petroleum, coke or biomass. Nonetheless, a more eco-friendly approach is to produce ammonia from clean or renewable electrical energy sources. This reduces the total carbon footprint of ammonia to 0% at the cost of an increase in ammonia price [6]. Presently, the Haber-Bosch system is responsible for over 90% of the world ammonia production [39]. The Haber-Bosch synthesis loop as shown in Equation 1.1 combines the hydrogen and nitrogen into ammonia.

$$N_2 + 3H_2 \rightarrow 2NH_3 \tag{1.1}$$

Recent developments have led to a more advanced and efficient method to produce ammonia from renewable energy sources. In this case the ammonia is directly produced from air and water, which eliminates the Haber-Bosch synthesis loop and the need for an electrolyzer for the hydrogen production, thus decreasing the power input necessary to operate the system [39]. This method is known as solid state ammonia synthesis (SSAS), which uses a membrane to directly convert the nitrogen and water into ammonia and oxygen as shown in Equation 1.2. Industrial sized application of SSAS presents a promising and less expensive alternative for the ammonia production from renewable sources.

$$2N_2 + 6H_2O \rightarrow 4NH_3 + 3O_2 \tag{1.2}$$

The application of ammonia as fuel source may also decrease the on-board fuel processing necessities, which reduces installation costs and space requirements. In addition, since storing and transporting large amounts of ammonia over long distances can easily be achieved, ammonia production facilities near large remote solar- or wind farms can be an interesting option. In this respect, the produced energy from the renewable sources can be used for the electrolysis of water into oxygen and hydrogen. The hydrogen can then be used inside the Haber-Bosch Synloop for the production of ammonia as can be seen in Figure 1.4.

The ugly side of ammonia

On the other side, ammonia has handling issues because of its corrosive nature, low pH value and high acidity constant, which makes it toxic to the environment. Concentrations at 300 $[ppm]$ can already have

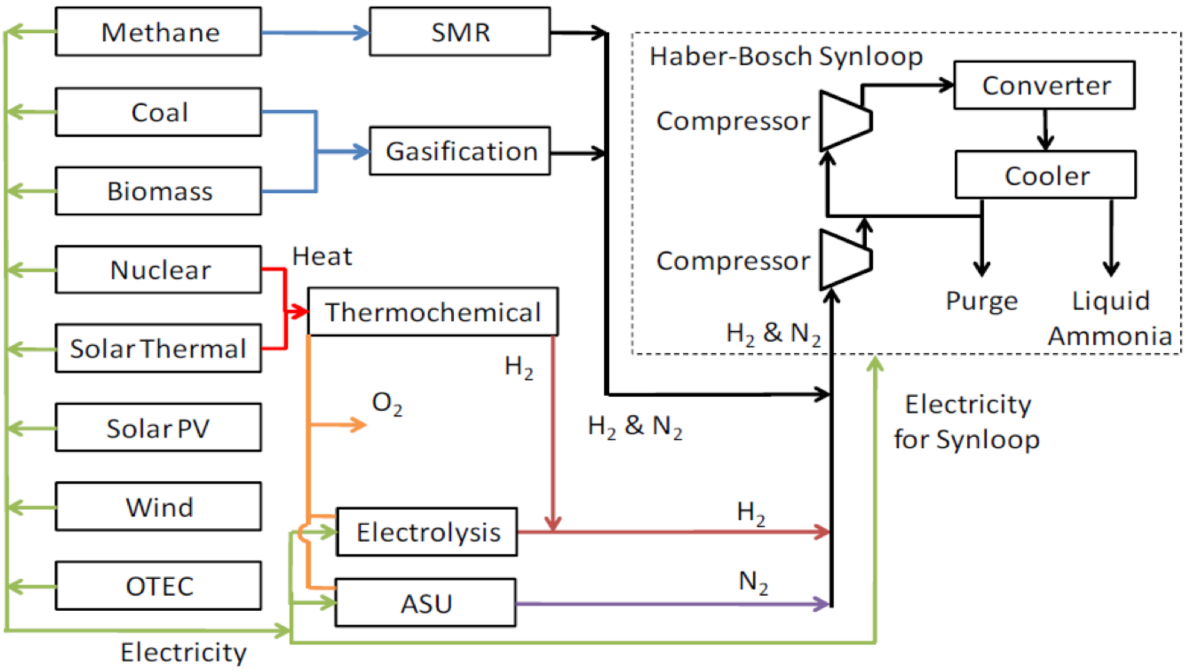

Figure 1.4: Different energy sources for the production of ammonia using the Haber-Bosch Synloop [9].

negative effects on the human's respiration system and concentrations above 5000 [ppm] have shown to be lethal for humans [40]. Hence, the areas near the ammonia storage tanks should be well-ventilated and great care has to be taken to minimise leakage. In addition, ammonia cannot come in direct contact with plastics and metals such as brass, copper and zinc alloys, therefore, suitable materials such as stainless steel and Teflon have to be used for the storage compartment [19]. Presently, ammonia is commonly stored in metal ammines or diluted in water [41]. However, stress corrosion cracking (SCC) inside metal ammines can occasionally occur, therefore, periodic examinations of these tanks are a necessity in order to minimise the probability of system failures [42].

1.1.3 Solid oxide fuel cell and internal combustion engine system layout

As mentioned in the introduction, the application of ammonia as a marine fuel is a novel concept, which is still under research. Since pure ammonia combustion is too slow to drive an internal combustion engine (ICE), a promoter fuel is needed to speed up the combustion process [14]. Alternatively, ammonia powered solid oxide fuel cells (SOFC) are a great way to generate on-board power [43]. However, similar to the pure ammonia combustion in an ICE, both of the concepts cannot cope with typical transient power requirements on board of ships. Thus, an ICE with a promoter fuel seems to be the best approach for the on-board propulsion system [14].

An interesting proposal by the the Delft University of Technology is to have a hybrid ammonia fueled SOFC-ICE power generation system on-board ships as shown in Figure 1.5. This combination of a hybrid power generation system has already been on the market for gas drive, which can raise the total power efficiency by approximately 10%, when compared with an SOFC only setup [10]. In case of the ammonia fueled SOFC-ICE layout, the SOFC can be used for the auxiliary power demand and for the cracking of ammonia, while the ICE is used to satisfy the on-board propulsion demand. On-board cracking of ammonia requires heat and as a result reduces the overall power generation efficiency. However, the overall losses can be minimized when the heat necessary for the ammonia cracking is utilized from the waste heat produced by the SOFC. In this way, the leftover hydrogen[1]from the SOFC can be used as the promoter fuel for the ICE, which can theoretically increase the overall efficiency of the system design in comparison to an ICE or SOFC only design.

The addition of small quantities of hydrogen to the ammonia fueled ICE has shown stability and performance improvements, especially during the early combustion stages [19]. Ammonia also has a high hydrogen content of 17.7 wt.% [44]. All in all, the ammonia fueled SOFC-ICE combination as shown in Figure 1.5 makes it for the shipowner possible to only refuel the ammonia, since the hydrogen can be obtained from the SOFC's anode-off gas.

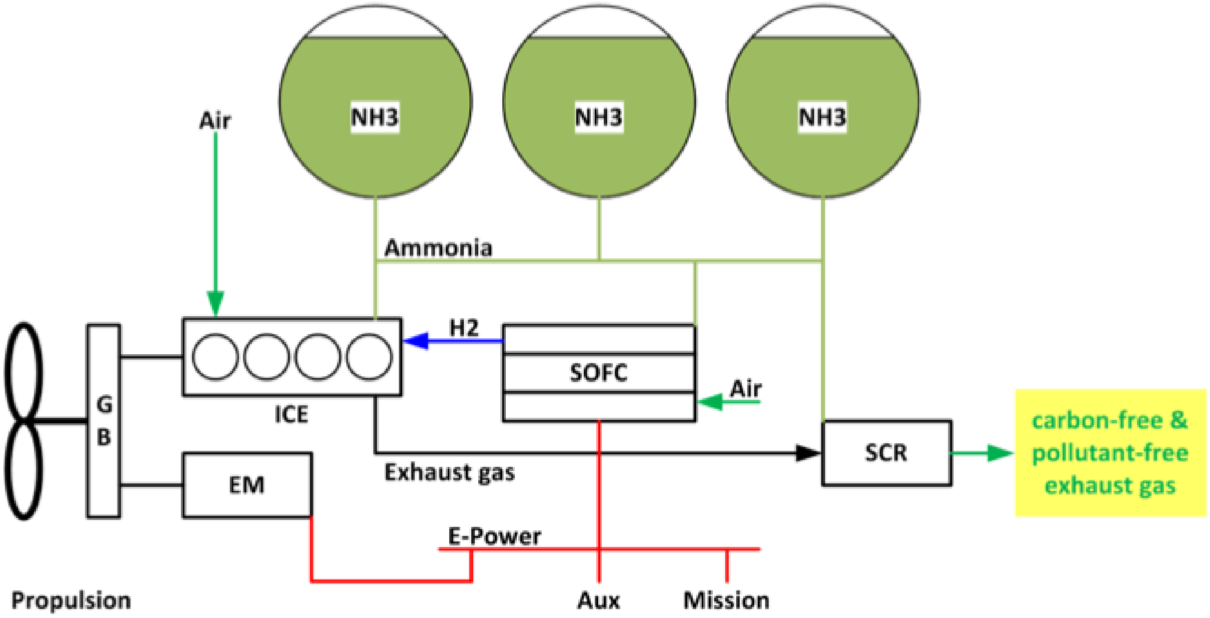

Figure 1.5: Preliminary system design proposed by Dr.ir. Peter de Vos of an ammonia fueled SOFC-ICE combination.

1.2 Introduction literature study

To get a quick impression whether the proposed ammonia fueled SOFC-ICE combination could be practical, both the SOFC and ICE components have been separately reviewed. The primary purpose of the literature study is to acquire comprehensive knowledge concerning the ICE and SOFC characteristics, when fueled with ammonia. In addition, the literature review will also give a concise overview of the recent technological innovations, which may improve the preliminary system design described in **Section 1.1.4**. These interesting technological developments including proton conducting SOFCs and RCCI engines are still novel concepts, but can be interesting alternatives to the conventional oxygen ion conducting SOFCs and engines in the near future. All in all, the literature review of the hydrogen-ammonia fueled ICE and ammonia fueled SOFC is the first step in the exploration of the practicality of the ammonia fueled SOFC-ICE concept design.

---

[1] The concentration leftover hydrogen fuel leaving the anode of the SOFC is usually between 10-20% depending on the fuel utilization factor (U_f) [10].

1.3 Research objectives

The literature study gave us an indication what we can expect when we run the ammonia fueled SOFC and hydrogen-ammonia fueled ICE independently as single systems. A vast amount of papers concerning directly fueled ammonia SOFCs have been published throughout the years. This concept has already been extensively modeled and successfully tested on large-scale. On the other hand, not much is known about hydrogen-ammonia combustion inside an ICE. Although the flammability behaviour and chemical kinetics during combustion have been widely investigated. Publications concerning the in-cylinder combustion characteristics are scarce. To make it worse, the conducted experiments are all based on automotive engines. The novelty of the hydrogen-ammonia fueled ICE concept has led to the following main question:

What is the impact of hydrogen-ammonia combustion on the performance of a marine-sized engine in relation to ammonia fueled SOFC-ICE system design, and how to quantify the operation of the hydrogen-ammonia engine to investigate energy efficiency, engine scaling, and engine performance?

The main question is then split in several sub questions that are formulated as follows:

Sub question 1: Which ignition method is preferred for hydrogen-ammonia combustion?

Several ignition methods are on the market, for which each of them have their own advantages and disadvantages.

Sub question 2: How will engine scaling impact the combustion characteristics and which scaling law is the most suitable when considering the hydrogen-ammonia fueled HCCI test engine?

This question becomes relevant since there are only hydrogen-ammonia based experiments on automotive sized engines in the literature. This thesis uses the engine experiments conducted by Pochet et al. [23].

Sub question 3: How will changes in the engine's intake conditions affect the start of combustion and the performance when considering hydrogen-ammonia fueled HCCI engines?

Changes in the initial conditions heavily influence the location of the start of combustion crank angle during HCCI mode and might lead to undesired early knock or misfire. For this question, the magnitude of the change in combustion characteristics are being investigated when altering the intake conditions.

Sub question 4: What should be the preferred hydrogen-ammonia fuel blend ratio for HCCI combustion?

The effects of the hydrogen concentration on the combustion characteristics are being investigated.

Sub question 5: What should be the expected indicated power output and the fuel flow for a hydrogen-ammonia fueled marine sized HCCI engine?

Because of the absence of hydrogen-ammonia experiments on marine sized engines, theoretical engine scaling methods are used to investigate what engine performances can be expected for larger sized engines.

Sub question 6: What are the major technical limitations in the SOFC-ICE system when the engine is running in HCCI mode and how can these problems be mitigated?

Since auto-ignition for HCCI engines is largely dictated by the initial conditions, some system design considerations are being suggested to enhance the workability and flexibility in the SOFC-ICE design.

1.4 Research scope

The application of hydrogen as an ammonia fuel promoter is still in its early development phase. Other investigated fuel promoters applicable for internal combustion engines, such as dimethyl ether (by Gross et al. [45]), gasoline (by Grannell et al. [46]) and diesel (by Reiter et al. [47]) all showed promising combustion characteristics when mixed with ammonia. However, in this thesis only the promoter hydrogen will be investigated. There are a few reasons for this. Firstly, hydrogen is readily available when cracking ammonia on-board of the vessel. Other mentioned promoters on the other hand need their own storage, which increases the complexity of the system layout in contrast to having only one fuel type on-board. In addition, the generated heat from the SOFC can be conveniently used for the ammonia cracking process. Hence, when using a different fuel promoter, the usefulness of the proposed combination falls apart. At last, the fuel promoters except hydrogen are all carbon based, meaning that CO_2 will be produced during combustion. What makes the novel ammonia fueled SOFC-ICE system design proposal unique is the possibility to become completely carbon free.

At last, the thesis will be emphasised on the in-cylinder modeling of hydrogen-ammonia combustion. Publications concerning this topic are scarce and the conducted experiments and modeling are all based on automotive sized engines. Because of the large scope of the project and the limited amount of time, dynamic engine simulations and the modeling of the complete SOFC-ICE design will not be part of the scope. In addition, research on the NOx concentrations will also not be part of the scope, since this study requires a detailed analysis of the oxidation pathways and chemical kinetics modeling, which is not related to in-cylinder modelling.

1.5 Thesis layout

The first part of the report contains the literature review. A concise overview of the performed study on ammonia fueled SOFCs and hydrogen-ammonia fueled ICEs can be found in **Chapters 2 and 3**, respectively. **Chapter 4** gives a summary of the conclusions from the literature study and also contains the project definition. The second part of the thesis starts with **Chapter 5**, which contains the development of the hydrogen-ammonia fueled in-cylinder model. Next, engine scaling modeling that is necessary since the available data for hydrogen-ammonia HCCI engines are based on automotive sized engines and not marine sized engines is described in **Chapter 6**. **Chapter 7** describes the MKIM and Wiebe models that were necessary for the parametric study on the initial conditions. From the parametric study it became evident that the performance of the HCCI engine is highly influenced by the intake conditions and will therefore show performance issues when it is integrated in an SOFC-ICE system. In **Chapter 8**, additional system design considerations are discussed that are able to mitigate these large fluctuations in the HCCI engine's intake conditions. At last, the final conclusions and recommendations are discussed in **Chapter 9**. An overview of the outline of the thesis and the connections of the chapters to the research objectives can be found in Figure 1.6.

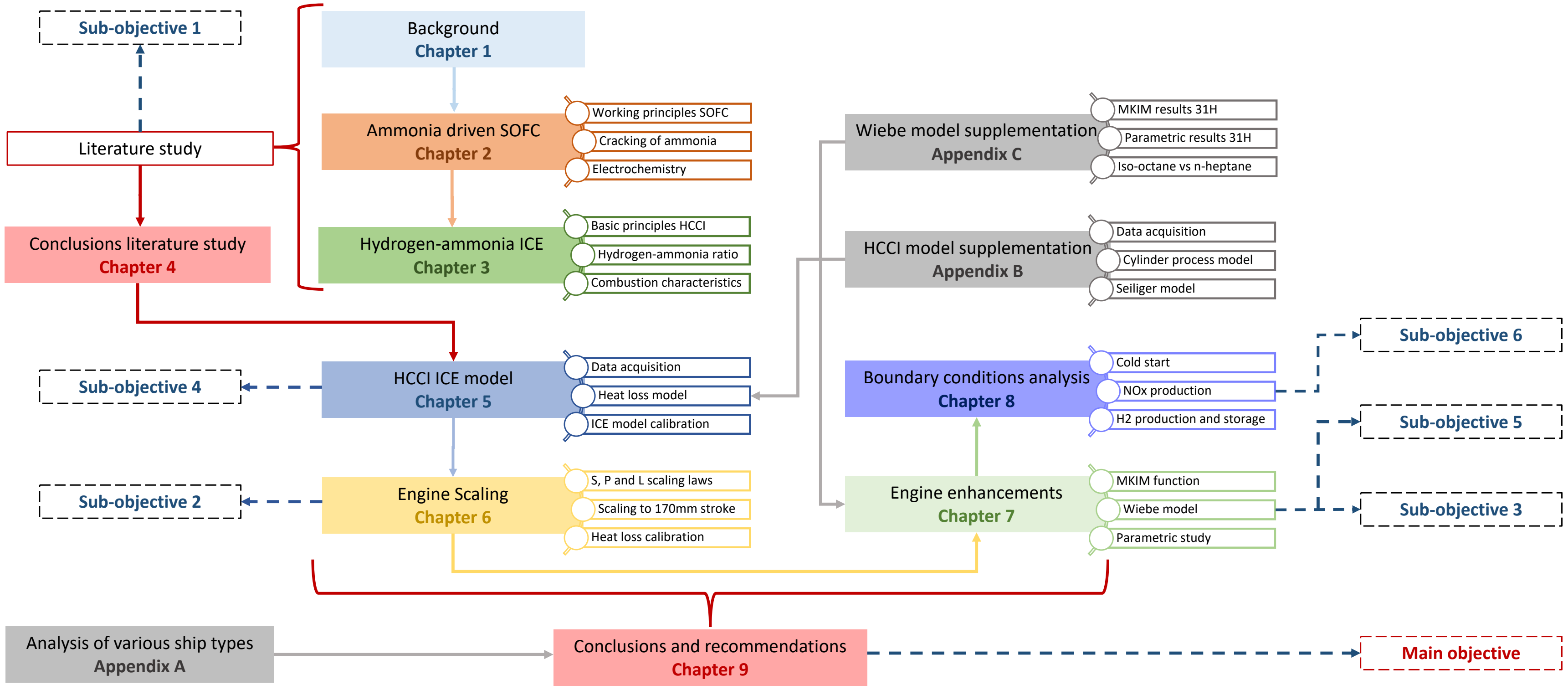

Figure 1.6: The outline of the thesis and the connections of the chapters to the research objectives. the flow blocks are colour coded according to the colour of the chapter.

Chapter 2

Ammonia driven SOFC

2.1 Chapter overview

Solid oxide fuel cells have been an interesting alternative to nowadays main prime movers in an effort to reduce the GHG emissions on-board of ships. Developments in proton conducting SOFCs are increasing at a faster pace, due to its higher theoretical efficiency in contrast to traditional oxygen conducting SOFCs. This together with the basic working principles of SOFCs will be shortly introduced in **Section 2.2**.

As mentioned in **Chapter 1**, ammonia can be directly fueled into the SOFC. In **Section 2.3**, the endothermic cracking reaction including several commonly used catalysts for the ammonia conversion will be briefly discussed. The electrochemistry of an SOFC-O and SOFC-H design will be briefly discussed in **Section 2.4**. Since the endothermic cracking reaction at the anode will affect the performance of the SOFC, a comparison will be made in **Section 2.5** in terms of system losses when using pure ammonia and pure hydrogen as fuel.

2.2 Working principles of an SOFC

A solid oxide fuel cell converts chemical energy into electrical energy by oxidizing the hydrogen molecules into water as illustrated in Figure 2.1. Fuel and air are supplied to the anode and cathode, respectively. An SOFC consists of five layers: the cathode, anode, two interconnecting plates on the outside and a solid electrolyte in the middle.

The oxidation of ammonia fuel in an oxide-ion-conducting solid oxide fuel cell (SOFC-O) can be regarded as a two-stage process in which the cracking of ammonia happens initially, followed by the electro-chemical oxidation of the produced hydrogen to water at the anode [48]. The overall chemical reactions for ammonia fueled SOFCs can be written as [49]:

$$NH_3 + 0.75\lambda(O_2 + 3.67N_2) \rightarrow (1-U)\cdot NH_3 + 1.5U\cdot H_2O + 0.75(\lambda - U)\cdot O_2 + (2.82\lambda + 0.5U)\cdot N_2 \quad (2.1)$$

Where λ is the air excess ratio and U the fuel utilization factor, which can be regarded as:

$$U = \frac{Mass\ of\ NH_3\ reacted\ in\ cell}{Mass\ of\ NH_3\ input\ to\ cell} \quad (2.2)$$

The conducted experiments by Stoeckl et al. [50] showed no voltage degradation during a 100 hour operating time of the ammonia fueled SOFC at a fuel utilization factor of 80%. The author also observed greater internal resistances and a reduction in the performance of the ammonia fueled SOFC stack, when

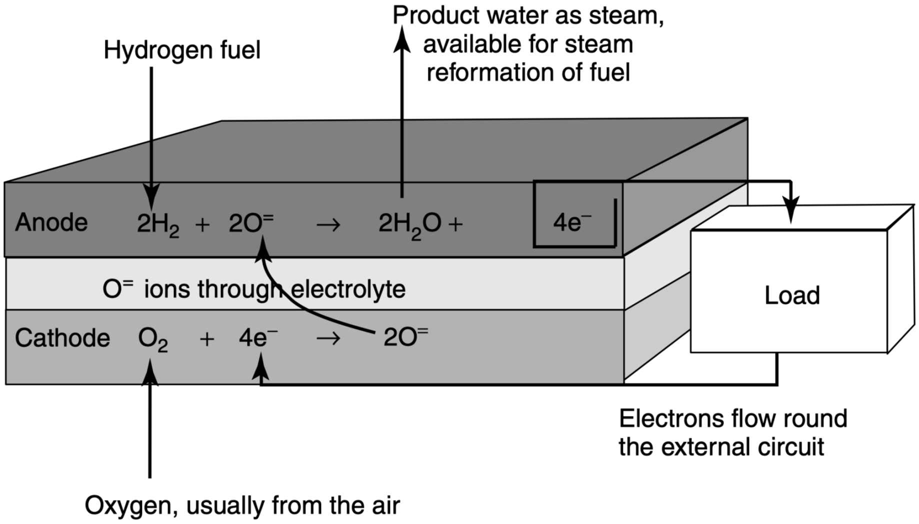

Figure 2.1: The anode and cathode reactions with hydrogen as fuel [10].

further lowering the fuel utilization factor. Hence, the fuel utilization factor should preferably be around 80% for optimal performances.

A simplified version of the exergy flow diagram for both an SOFC and PEMFC are shown in Figure 2.2. It can be seen that the thermo-mechanical exergy outflow of an SOFC is far greater than that of a low temperature PEMFC. The exhaust gases of the SOFC can be directed to a turbine to generate more electric energy or it could be used for the on-board central heating. This makes high temperature fuel cells very suitable for the application of a combined heat and power (CHP) configuration. SOFCs with an afterburner can achieve efficiencies up to 80% when heat recovery is applied [10].

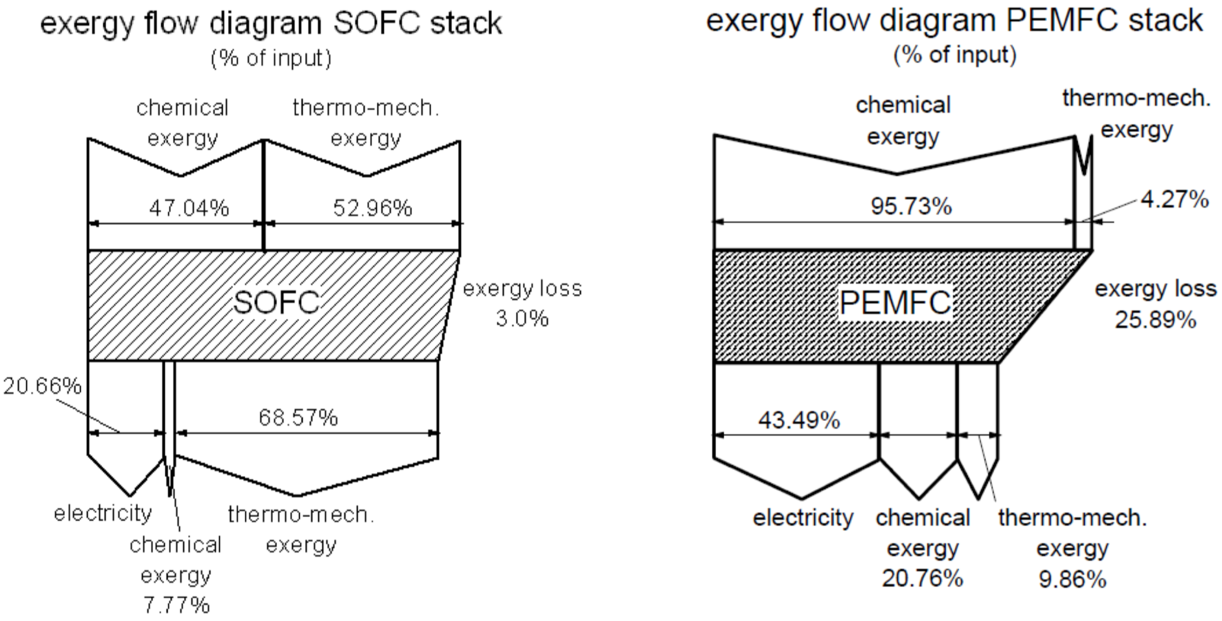

Figure 2.2: Simplified Grassman diagrams of an SOFC and PEM type fuel cell [10].

2.2.1 Direct- (DIR) or indirect (IIR) internal reforming of ammonia

Internal reforming of ammonia in an SOFC can be performed in two different ways, direct- (DIR) or indirect (IIR) internal reforming. For IIR, the reformer is in thermal contact with the anode channel, but it is separated from the fuel cell [10]. IIR has the advantage that the reformer does not influence the reaction process inside the anode, which could be beneficial when the catalyst inside the reformer is poison to the oxidation reaction happening inside the fuel cell. However, this is less the case for high temperature fuel cells including the SOFC [10].

When fuel reforming takes place inside the anode of an SOFC-O, we are talking about a DIR configuration. SOFC stacks are commonly cooled by high air flow rates through the cathode. However, in case of DIR, a smaller airflow is needed because of the endothermic cracking reaction of ammonia. This decreases the energy consumption necessary for maintaining the air stream, resulting in a higher system efficiency [48]. When operating in counter-flow, lower ohmic and diffusion resistances were measured in comparison to co-flow [48]. Nonetheless, the benefits of operating in co-flow is the absence of dangerous hot spots and the easy monitoring of temperature gradients. Co-flow is currently receiving a lot of attention, mainly since the benefits are more favorable than the slight decrease in resistance of counter-flow.

2.2.2 Differences between an SOFC-O and SOFC-H

The SOFC-H is characterized by its proton conducting electrolyte-based configuration, while the SOFC-O uses oxygen ion as conductor. Another noticeable difference between those two designs is the absence of water in the output of the SOFC-H anode, since those molecules are formed inside the cathode. This is beneficial, since the fuel inside the anode cannot be diluted by the water vapor generated by the electrochemical reaction [11].

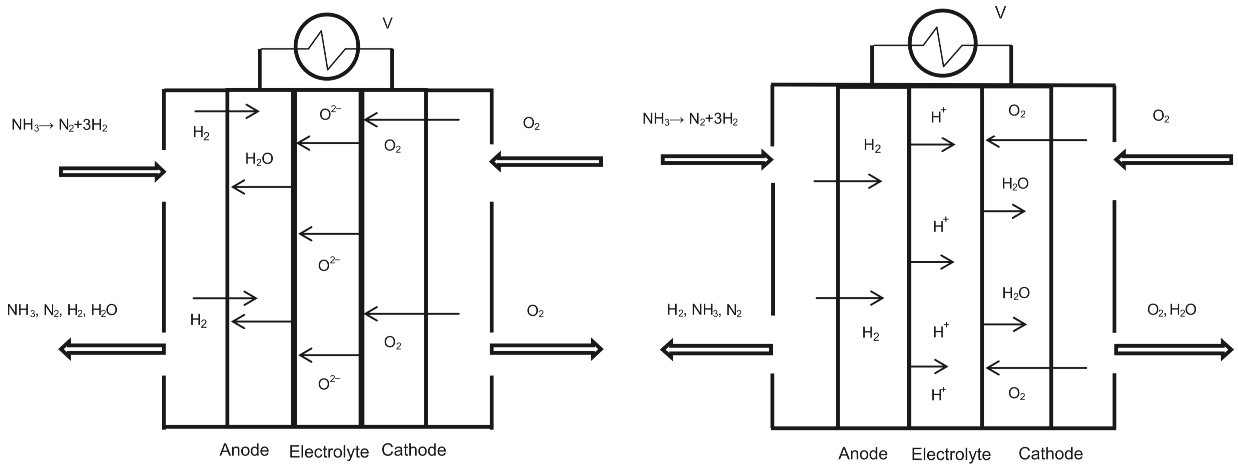

(a) (b)

Figure 2.3: Schematic representation of direct ammonia-fed (a) SOFC-O and (b) SOFC-H [11].

Experimental studies have shown lower cell performance for SOFC-H fuel cells in comparison to SOFC-O. Nonetheless, in terms of theoretical modeling, higher peak power densities and open circuit voltages were predicted for SOFC-H, which contradicts the experimental results [11]. The lower SOFC-H performance could be explained by the dilution of hydrogen in nitrogen at the anode, which is usually neglected in the theoretical analysis [51]. At medium operating temperature of 600 [°C] and fuel utilization (U) of 0.85, a 6% higher theoretical overall energy efficiencies were observed for proton conducting solid oxide fuel cells (SOFC-H) [49]. The higher CHP efficiency (82% in comparison to 76% for SOFC-O) can be explained by the difference in ion transport direction, which resulted in a lower anode concentration overpotential in contrast to the SOFC-O. For both configurations it has been observed that the theoretical efficiency increases when decreasing the operating temperature. This supports the endeavor for intermediate temperature ammonia fueled SOFC rather than high operating temperatures as stated by the author in [49].

Oxygen conducting SOFCs have been the main focus point in the last couple of decades. According to the recent published paper (2019) by Mojaver et al. [52], an SOFC-O configuration is still highly favored over SOFC-H. He concluded that the SOFC-O configuration in his experiment has shown better performances in terms of overall voltage losses and exergy losses for his set of experiments. A reason for this is the high ohmic overpotential caused by the low proton conductivity of existing proton conducting membranes. A suitable membrane that has a high conductivity and long-term stability has still yet to be discovered [53]. All in all, the above mentioned issues together with the slightly higher overall cost have made proton conducting SOFCs not very popular.

The scarcity of available research papers on SOFC-H stacks does not necessarily mean that the concept is completely irrelevant. Oxygen conducting SOFCs typically require high operating temperatures to improve the ion conductance of the electrolyte. This affects the durability of the materials inside the stack. Therefore, low to medium temperature SOFCs can still play a part in the near future. However, more research is needed to improve the system efficiency and effectiveness on proton conducting SOFCs. The ohmic overpotential can be improved by the use of thinner and higher conductive proton electrolyte materials [54].

2.2.3 Tubular and planar fuel cell configurations

From the two configurations, the planar design is the most popular one. In contrary to a tubular design, it enables a far more superior power density and stack performance, mainly due to the lower ohmic losses. A downside, however, is the extra care that has to be taken in keeping the stacks gas tight. This is less the case for a tubular design, since the fuel flows along the outside of the tube and air is fed through the inside. In addition, the sealing of a planar arrangement that is usually made of brittle glass has to withstand thermal stresses. Hence, faster degradation of the stack can be expected when increasing the temperature inside the fuel cell, [10].

2.3 Cracking of ammonia

The dissociation reaction (cracking) of ammonia in an SOFC happens in the presence of usually an inexpensive metal-based catalyst, such as iron (Fe_2O_3), copper, cobalt or a nickel-based compound. For the reaction to work at a satisfactory rate, ammonia has to be heated to high temperatures, typically between 600 and 800 [$°C$]. This commonly depends on the type of catalyst, a nickel-based compound. for instance, requires a higher operating temperature compared to a stainless steel alloy [42]. Higher operating temperatures often require good insulation of the fuel cell, which increases the weight of the SOFC and it will also make it more difficult to crack ammonia during a cold start [42].

2.3.1 Ammonia conversion catalysts

Nickel is a widely used catalyst inside SOFCs, because of its high electronic conductivity and stability under chemically reducing conditions [10]. In addition, nickel also works as a catalyst for the ammonia conversion to hydrogen and can be used as the internal reforming catalyst for ammonia fueled SOFCs.

According to Molouk et al. [55], the cracking of ammonia in the presence of a nickel-based catalyst occurs in three steps. The absorption of ammonia on the catalyst, followed by the cleavage of the NH bond of the absorbed ammonia and finally the desorbing of N_2 molecules from the catalyst. Metal cermet anodes based on nickel/zirconia can beneficially increase the surface area of the catalyst [56], resulting in a higher cracking rate.

By incorporating an additional sub-catalyst to nickel, the performance at lower temperatures can be even further enhanced. Various promising metals have already been studied as a sub-catalyst to nickel. As can be seen in Figure 2.4, a ruthenium-nickel based catalyst shows the best performance for various reactor temperatures. Nonetheless, if we take the scarcity of noble metals into consideration, platinum, ruthenium and palladium may not be the best option. Cheaper metals, for instance nickel only or nickel aluminium-oxide based catalyst can also achieve high activity at the cost of a high working temperature.

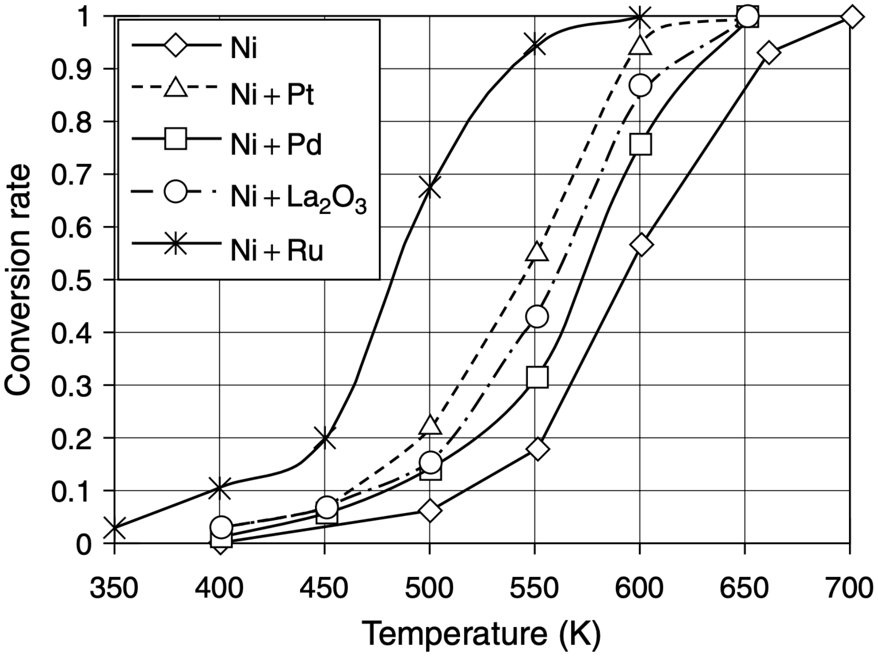

Figure 2.4: Conversion rate of ammonia as a function of reactor temperature for different catalysts [12].

A temperature range between 800 and 1100 [°C] is needed inside an SOFC-O stack for zirconia (cermet), the oxygen ion conductor (inside the electrolyte) to work properly [10]. At these temperatures, a nickel catalyst would give an ammonia conversion rate close to 100% as shown in Figure 2.4. It has already been experimentally demonstrated that such temperatures allow for almost complete decomposition of ammonia, resulting in more or less approachable performances to that of hydrogen-fed SOFCs [11]. Nonetheless, the efficiency is always lower, since the created nitrogen gas at the anode can dilute the hydrogen concentration. which will result in a reduction of the reversible cell potential [11].

However, since this thesis is considering the ICE for propulsion and the SOFC mainly to power the auxiliary systems (as mentioned in **Section 1.1.3**), the power output requirement will most likely be higher for the ICE. For this configuration, an additional indirect pre-reformer to the ICE may be necessary, if the hydrogen supply from the anode-off gas is not sufficient enough. In this case a low working temperature catalyst inside the extra indirect pre-reformer can result in higher efficiencies, if the heat can be acquired from the SOFC's waste heat with the help of heat exchangers. New developments in economical low-temperature based catalysts are still going on. In 2018, Gencell a company specialised in fuel cells published a paper about the use of a new nano material-based catalyst, which allows the endothermic cracking process to happen satisfactorily at temperatures below 500 [°C] [57]. This will make the cracking reaction more cost efficient for intermediate temperature SOFCs, without the use of expensive metal alloys.

2.3.2 Endothermic reaction

The decomposition of ammonia into hydrogen and nitrogen molecules is an endothermic reaction, meaning that energy is needed to start the process.

$$NH_3 \rightarrow \frac{1}{2}N_2 + \frac{3}{2}H_2 \tag{2.3}$$

Besides the dissociation reaction ($\triangle H = +46.4\ KJ\ mol^{-1}$), heating of ammonia to the working temperature of the catalyst ($\triangle H = +29.1\ KJ\ mol^{-1}$) for an 800 [°$C$] rise and the phase change of liquid to gas ($\triangle H = +23.3\ KJ\ mol^{-1}$) are also absorbing energy from the fuel cell **??**.

$$NH_3(l) \rightarrow NH_3(g) \tag{2.4}$$

The cracking of ammonia results in the production of 1.5 moles of hydrogen, for which we consider the molar enthalpy of formation to be the higher heat value (HHV of $-285.84\ KJ\ \ mol^{-1}$). This will result in an upper limit efficiency of 0.77, when taking the endothermic losses into consideration [10]. This upper limit means that the maximum overall efficiency of the system is limited to 0.77 because of the endothermic losses from the ammonia cracking.

$$\eta_{upper\ limit} = \frac{(285.84 \cdot 1.5) - (46.4 + 29.1 + 23.3)}{285.84 \cdot 1.5} = 0.77 \tag{2.5}$$

The upper limit efficiency does not take the heat losses to the surroundings into consideration.

2.3.3 Conversion rate ammonia cracking

In reality, some ammonia decomposes spontaneously at temperatures over 573 [K], even without the presence of a catalyst [58]. Besides the characteristics of the catalyst, the conversion rate also depends on the temperature and the pressure inside the anode part of the fuel cell. An increase in temperature or a decrease in pressure both contribute to a higher equilibrium conversion of ammonia. The ammonia cracking rate is also slower at lower temperatures, because of the rise in electrode polarization resistance of the fuel cell [13].

In addition, according to Stoeckl et al. [48], increasing the ammonia flow rate also negatively impacts the ammonia conversion rate. As can be seen in Figure 2.5, a higher temperature is necessary when increasing the ammonia flow. The author's experiments have been conducted on a large planar SOFC-MEA with Ni/YSZ anodes for various types of flow rates and furnace temperatures. A temporarily increase in the ammonia flow rate will reduce the temperature inside the anode, since more energy is needed to fuel the endothermic cracking reaction, which causes a decrease in the conversion rate of ammonia. This additional decrease in operating temperature has been found to significantly increase the ohmic resistance of the cell. From the conducted experiments, it has been observed that the decrease in temperature was the most pronounced at the anode inlet region. This may indicate that the majority of the ammonia decomposition happens at the fuel inlet of the fuel cell [48].

Undecomposed ammonia molecules can be adsorbed on the anode surface, which severely block the mass transfer process. This causes abnormal behaviour, just like the mass transfer polarization that occurs at high current densities [59]. It is therefore highly recommended to adjust the ammonia flow rate to fit the cell situation instead of (dynamically) optimising the flow rate to match the (transient) hydrogen requirement for the ICE [54].

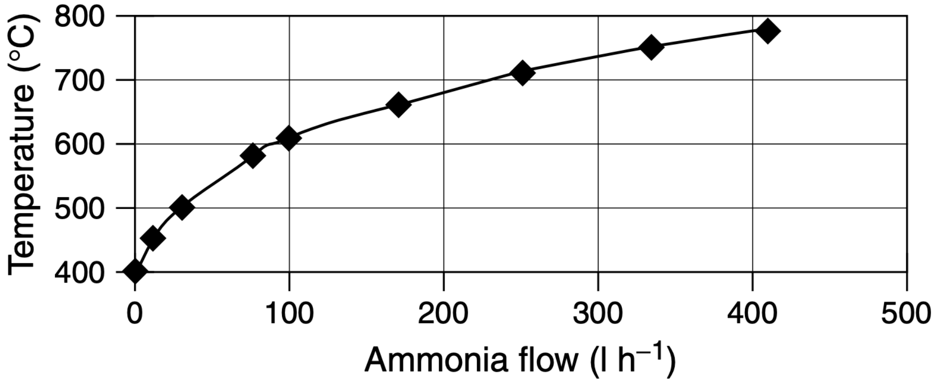

Figure 2.5: Reactor temperature as function of the ammonia flow rate for a conversion rate of 99.99% (Ni/Ru based catalyst) [12].

2.4 Electrochemistry

The theoretical value of the open circuit voltage (OCV) can be written as:

$$E_{OCV} = -\frac{\triangle G}{nF} \tag{2.6}$$

Where n is the number of electrons involved per electrochemical reaction and is equal to 2 for an SOFC-O fuel cell. F is the Faraday constant and $\triangle G$ is the change in Gibbs free energy, which can be calculated as:

$$\triangle G = \triangle H - T_0 \cdot \triangle S \tag{2.7}$$

The equilibrium potential is also affected by the partial pressure of the species involved in the electrochemical reaction [11]. This can be expressed as the Nernst voltage, which is the reversible cell voltage that would exist at a given pressure and temperature.

$$E_{Nernst,SOFC-O} = -\frac{\triangle G}{nF} + \frac{RT}{nF} ln(\frac{[P_{H_2}][P_{O_2}]^{0.5}}{[P_{H_2O}]}) \tag{2.8}$$

$$E_{Nernst,SOFC-H} = -\frac{\triangle G}{nF} + \frac{RT}{nF} ln(\frac{[P_{H_2O}]}{[P_{H_2}][P_{O_2}]^{0.5}}) \tag{2.9}$$

The Nernst equation can also be written in mole fractions at the anode and cathode side, resulting in:

$$E_{Nernst,SOFC-O} = -\frac{\triangle G}{nF} + \frac{RT}{nF} ln(\frac{[y_{H_2}][y_{O_2}]^{0.5}}{[y_{H_2O}]}(\frac{p}{p_0})^{0.5}), \tag{2.10}$$

or

$$E_{Nernst,SOFC-H} = -\frac{\triangle G}{nF} + \frac{RT}{nF} ln(\frac{[y_{H_2O}]}{[y_{H_2}][y_{O_2}]^{0.5}}(\frac{p}{p_0})^{0.5}). \tag{2.11}$$

The voltage as function of the current density of a high temperature fuel cell as shown in Figure 2.6 has its own characteristic shape from four major irreversibilities [10]:

1. **Activation losses**, a highly non-linear voltage drop caused by the slowness of the reactions taking place on the surface of the electrodes. A proportion of the voltage generated is lost in driving the chemical reaction that transfers the electrons to or from the electrode. The voltage drop can be determined by the equation $\triangle V_{act.} = A \cdot ln(\frac{i}{b})$, where the parameters A and b are constants depending on the cell and electrode condition.

2. **Fuel crossover and internal currents**. This type of energy loss results from the waste of fuel passing through the electrolyte and from electron conduction through the electrolyte. The electrolyte should only transport ions through the cell. However, a certain amount of fuel diffusion and electron flow will always be possible.

3. **Ohmic losses**, which are linearly proportional to the current density. This voltage drop is the straightforward resistance to the flow of electrons through the material of the electrodes and the various interconnections, as well as the resistance to the flow of ions through the electrolyte. The voltage drop becomes $\triangle V_{ohm.} = i \cdot r$, where i is the current density and r the area specific resistance.

4. **Mass transport or concentration losses**. These result from the change in concentration of the reactants at the surface of the electrodes as the fuel is used. In an ammonia fed SOFC, the concentration overpotentials can be expressed in terms of the gas concentration difference between the electrode surface and the electrode-electrolyte interface [11]. This results in the equation $\triangle V_{conc.} = -\frac{RT}{nF} ln(1 - \frac{i}{i_1})$ for the concentration or mass transport voltage drop. i_1 is the limiting current density at which the fuel is used up at a rate equal to its maximum supply speed [10]. This means that i cannot be greater than i_1 because the fuel gas cannot be supplied at a greater rate.

When including the irreversibilities, the equation for the operating voltage of an SOFC can be written as:

$$V_{cell} = E_{Nernst} - \triangle V_{conc.} - \triangle V_{act.} - \triangle V_{ohm.} \tag{2.12}$$

For practical reasons the equation is often simplified to [10]:

$$V_{cell} = E_{Nernst} + m \cdot e^{ni} - A \cdot ln(\frac{i}{b}) - ir \tag{2.13}$$

Where E_{Nernst} is the open circuit voltage. The parameters m and n are the constants in the mass-transfer overvoltage depending on the characteristics of fuel cell. Parameter A is also a constant, which value depends on the cell and electrode conditions. However, this simplification is an empirical equation, but it has been proven to give comparable results when compared to the data from real solid oxide fuel cells [10].

The voltage output of one cell is usually below the value required by machines. Higher system voltages (V) and amperes (I) can be generated, by interconnecting the cells in series or in parallel respectively. This principle, known as stacking is used to raise the output power of the fuel cell. The calculation for the amperes of a cell can be found in Equation 2.15

$$I_{cell} = \dot{n}_{H_{2,reacted}} \cdot 2 \cdot F, \tag{2.14}$$

The total SOFC power output is determined by multiplying the power of a single cell with the total number of cells in the stack:

$$P_{stack} = n_{cells} \cdot V_{cell} \cdot I_{cell} \tag{2.15}$$

2.5 Comparison between pure ammonia and hydrogen as fuel

A few studies have been performed on the cell performance of an SOFC using ammonia as direct fuel instead of pure hydrogen. From Ma et al. [13] it should be noted that in the case of ammonia or pure hydrogen fueled SOFCs, similar internal resistances of the cell in particular at temperatures above 800 [°C] were observed [10]. However, when operating the fuel cell at lower temperatures (below 700 [°C]), a slight

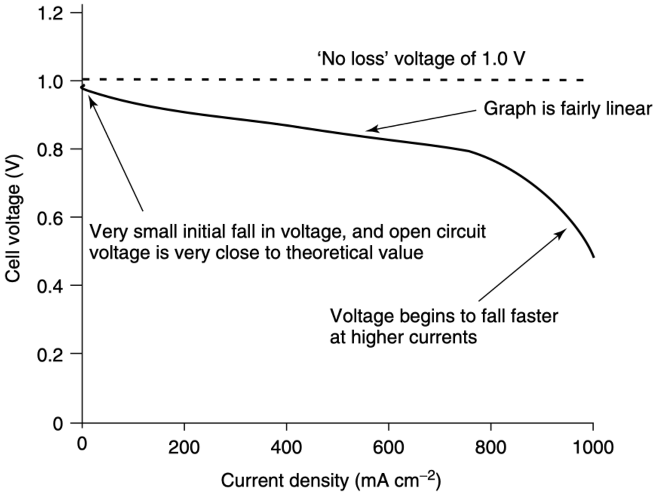

Figure 2.6: Voltage as a function of the current density of a typical air pressure fuel cell operating at 800 [°C] [10].

difference in interfacial polarization occurred as shown in Figure 2.7a. This can be largely explained by the slower hydrogen formation at that temperature, resulting in an increase in activation polarization resistance [13]. Ma also investigated the performance of directly fueled ammonia and hydrogen SOFCs at medium temperatures (550 - 600 [°C]). Lower efficiencies were observed for ammonia fueled SOFCs due to the incomplete cracking reaction. From another experimental study conducted by Fuerte et al [60], the power density of ammonia also showed slightly lower values in comparison to pure hydrogen. According to the author, the lower power output can be attributed to the lower partial pressure of hydrogen when the cell is operated with ammonia.

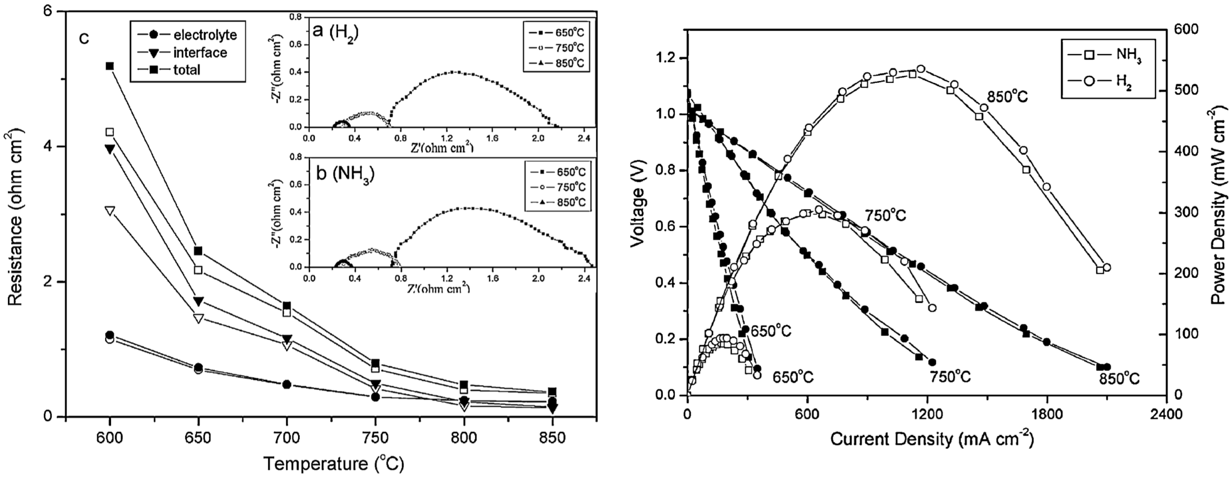

(a)

(b)

Figure 2.7: (a) Comparisons of total resistance between the cell fueled by hydrogen (hollow symbols) or ammonia (solid symbols) under open-current conditions at different temperatures. (b) Comparison of power density (hollow symbols) and cell voltage (solid symbols) as a function of current density between ammonia and hydrogen [13].

Chapter 3

Hydrogen-ammonia driven ICE

3.1 Chapter overview

Internal combustion engines have been the prime movers on-board of ships in the last couple of decades. With the upcoming decarbonisation in the shipping industry, the search for new power sources have become more important than ever. At the current stage of technological development, the ICE concept is still highly favored because of its high power density and transient-load capability. However, there can still be a future for internal combustion engines in case the present fossil fuels can be replaced by carbon neutral fuels such as hydrogen-ammonia.

Chapter 2 gives a concise introduction to the characteristics of hydrogen-ammonia combustion inside an ICE. First, the basic principles of hydrogen-ammonia combustion are described in **Section 3.2**. There are many different ways to ignite the fuel during combustion. **Section 3.3** summarizes the two most prominent ignition methods, compression and spark ignition. RCCI and HCCI are novel compression ignition methods, which will be discussed for hydrogen-ammonia combustion. In **Section 3.4** two different injection methods (direct and port injection) will be briefly discussed. At last, the influences of the hydrogen-ammonia ratio, equivalence ratio, compression ratio and the spark timing on the engine performance will be further elaborated in the **Sections 3.5 to 3.8**, respectively.

3.2 Basic principles of IC engines

By burning the hydrogen-ammonia mixture inside the internal combustion engine, chemical energy will be transformed into mechanical energy. In order to do this, compressed air is blown into the engine cylinder before combustion. In case of marine sized diesel engines, liquid fuel is injected into the cylinder which vaporizes, forming a combustible mixture that ignites after a small delay [61]. The created heat is then transferred by convection and radiation to the surroundings. This results in an expansion of the mixture inside the combustion chamber which creates a direct force moving the piston up and down. Because of the low flame speed during combustion, hydrogen-ammonia as a fuel is more suitable for low speed two-stroke engines [62]. Furthermore, ammonia combustion is suitable in supercharged conditions, meaning that a turbocharger can be used to compress the inlet air for both the SI and CI configurations [19]. In addition, the high specific heat capacity of ammonia could beneficially reduce the combustion temperature inside the combustion chamber, resulting in lower power required to cool the system. Zamfirescu and Dincer et al. [58] proposed to use the ammonia fuel simultaneously as refrigerant for cooling effect. Their results showed that the cooling system can be downsized with up to 20% when using ammonia.

However, the use of pure ammonia has some major drawbacks, because of its low flame speed, flammability and high auto-ignition temperature (650 [°C]). The heat of combustion and the laminar burning velocity are also much lower in comparison to methane and propane fuels as can be seen in Figure 3.1. Because of the low propagation speed of ammonia, poor combustion rates can be expected. This most likely results in inconsistent combustion under high engine speeds and low engine loads [14]. Moreover, because of its narrow flammability limit and low flame speed, high concentrations of ammonia can be found in the exhaust gas due to incomplete combustion. As a result, ammonia fueled ICEs must, therefore, feature compression ratios in the range of 40:1 to 100:1, which is more than four times higher than in conventional ICEs [63]. This makes pure ammonia combustion not economically suitable as the primary source of fuel and has subsequently not been pursued as a fuel for combustion systems [14].

A promoter fuel is therefore necessary to overcome the poor combustion characteristics of ammonia [1]. It has been observed that conventional ICEs can be fueled with ammonia, when a reasonable amount of hydrogen is added to the system [64]. Hydrogen displays a high combustion velocity, low ignition energy and a wide flammability range that allows the engine to operate at high air fuel ratios [16]. However, the drawback of using a dual fuel configuration is the increase in the complexity of the engine's layout, since the system generally requires a dual storage, delivery and injection system.

Fuel	NH_3	H_2	CH_4	C_3H_8
Boiling temperatureat 1 atm (°C)	−33.4	−253	−161	−42.1
Condensation pressure at 25 °C (atm)	9.90	N/A	N/A	9.40
Lower heating value, LHV (MJ/kg)	18.6	120	50.0	46.4
Flammability limit (Equivalence ratio)	0.63∼1.40	0.10∼7.1	0.50∼1.7	0.51∼2.5
Adiabatic flame temperature (°C)	1800	2110	1950	2000
Maximum laminar burning velocity (m/s)	0.07	2.91	0.37	0.43
Minimum auto ignition temperature (°C)	650	520	630	450

Figure 3.1: Fundamental combustion characteristics and thermal properties of ammonia and hydrocarbon fuels [14].

3.3 SI and CI engine characteristics

3.3.1 Conventional ignition concepts

The two common ways to ignite the fuel in an ICE is by compression ignition or spark-ignition that are commonly used for diesel engines and petrol engines, respectively. SI engines are typically characterized by its low *NOx* emissions and rapid response rate at the cost of a relatively lower efficiency in contrast to CI engines [17]. The literature on hydrogen-ammonia SI engines is vast in comparison to other ignition methods and has already shown promising experimental results. The startup time is also considerably lower in contrast to CI engines, since no additional heating of the fuel air mixture is needed during engine startup. Spark-ignition is also a great method to initiate the combustion of ammonia in an ICE, since the octane rating (≈ 110) is relatively higher than that of petrol, which is generally used in SI engines [19]. A higher octane rating results in a greater resistance in knocking or pinging during combustion. As a matter of fact, the high octane rating also allows for higher compression ratios, which can lead to higher engine efficiencies [20]. Knocking is a term used for the spontaneous ignition of the fuel and as a result, the combustion process no longer takes place at the optimum crank angle. This undesired earlier start of combustion is a significant boundary condition for engine control systems to avoid and is often induced by over advancing the start of ignition timing [61].

CI engines on the other hand, offer a relatively greater efficiency and lifespan, which translates back to a lower fuel consumption and less required maintenance [65]. However, for smooth operations, CI engines highly rely on the air-fuel mixture and the cetane number (CN) of the promoter fuel [66]. The cetane rating is an indicator for the combustion speed and compression required for fuel ignition. This rating plays a comparable role for CI engines as octane rating does for SI engines. CI engines are typically characterised by its high emission and slow response rate [17]. Hydrogen-ammonia combustion inside CI engines is commonly affected by great amounts of NOx production inside the flame zone [67]. The NOx is primarily produced from fuel-bound nitrogen, which can unlike the nitrogen (N_2) in air easily re-bond with free oxygen during the combustion process. All in all, both SI and CI engines have their own advantages and disadvantages.

3.3.2 HCCI concept

In 1983 a new ignition concept was introduced that is known as homogeneous compression charge ignition (HCCI). This ignition methodology has been frequently associated with SOFC-ICE combination systems. It is regarded as a combustion strategy in which the gaseous fuel and air are already mixed before it is provided into the combustion chamber [68]. Depending on the compression ratio, the temperature at maximum compression should always be above the auto-ignition point of the hydrogen-ammonia mixture in order to ensure auto-ignition. The HCCI engine has been considered as a promising technological concept, but it has not been commercially applied yet due to some major technical challenges.

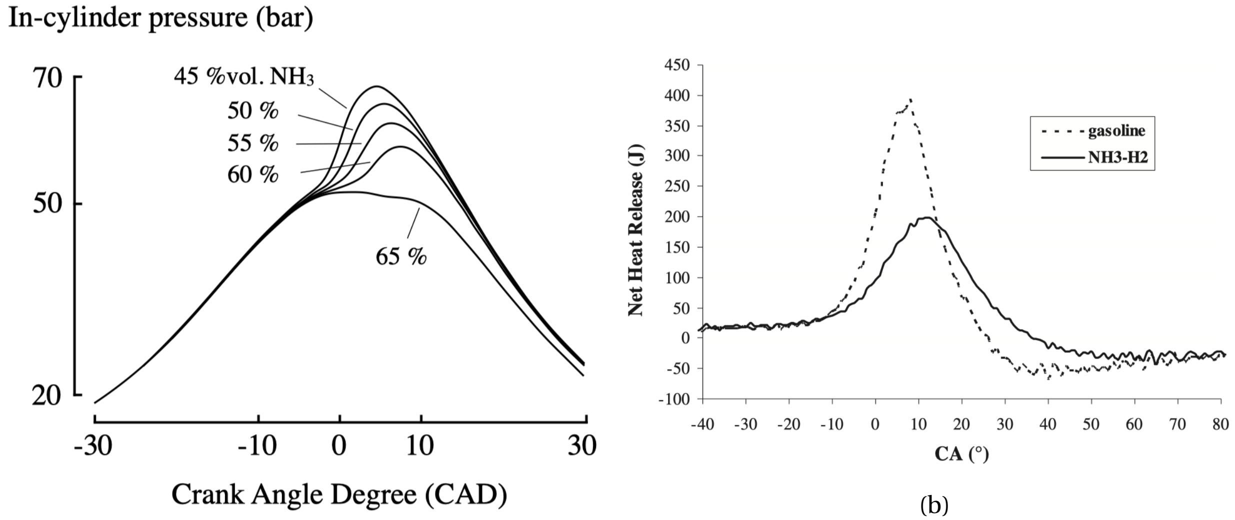

(b)

(a)

Figure 3.2: (a) Experimental results in-cylinder pressure curve for various hydrogen-ammonia blends for an HCCI engine operating at 1.5 [bar] intake pressure and 473 [K] intake temperature [15] and (b) Spark ignition engine net heat release vs crank angle of a 7% volumetric hydrogen-ammonia mixture in comparison to gasoline at full load [16].

The main advantage of this ignition concept is the high achievable performance and efficiency while keeping the emissions low because of the relatively low in-cylinder temperatures [15]. It can be considered as the ignition method which combines the best features of diesel and gasoline to produce diesel like power while maintaining gasoline-like emissions [17]. However, controlling the combustion in HCCI engines is presently still an issue due to its rapid heat release rate and very high maximum pressures [17]. In particularly its narrow operating range of the engine at high loads makes HCCI currently inaccessible for marine engines. In addition, the ignition delay and behaviour is still fairly unpredictable. Therefore a detailed controlling ignition timing over a range of different loads and engine speeds (to stay between knock and misfire) is required and is yet still under development [68].

An experimental study performed by Pochet et al. [23] has shown stable performance for hydrogen-ammonia combustion inside an HCCI engine at a compression ratio of 16:1. However, the volumetric ammonia content has been limited to 57% in order to achieve high operating efficiencies. Higher concentrations resulted in incomplete combustion and the increased probability of misfire due to the high auto-ignition resistance of ammonia [15]. The experiments conducted by Reiter et al. [69] showed comparable results, when increasing the ammonia ratio. Higher ignition delays were detected causing deterioration in the peak pressure during combustion. Higher ammonia concentrations inside an HCCI engine is feasible by increasing the compression ratio and intake pressure [15]. However, the probability of ringing also increases when increasing the compression ratio, leading to a reduction in power density [15]. Therefore a trade-off between low compression ratios to prevent hydrogen from ringing and high compression ratios to promote ammonia combustion is necessary [23]. Figure 3.3 shows the in-cylinder cross sections of the engine's in-cylinder when using the ignition methods, CI, SI and HCCI.

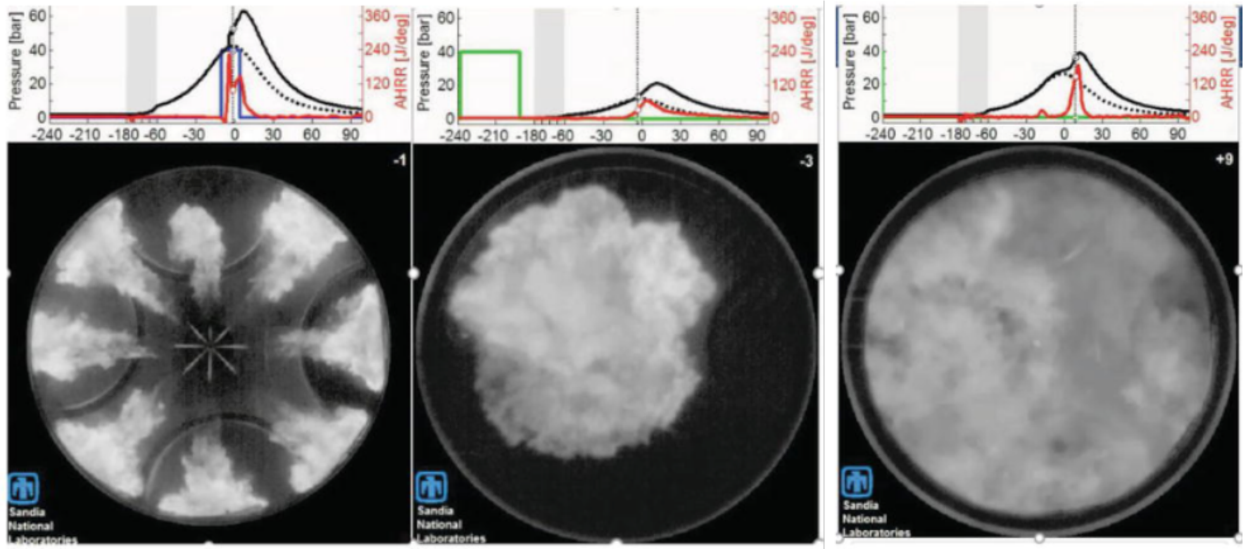

(a) (b) (c)

Figure 3.3: Combustion control strategies **(a)** CI, **(b)** SI and **(c)** HCCI. The green, red and blue coloured lines depict the injection event, HRR and pressure, respectively [17].

3.3.3 RCCI concept

Controlling the combustion rate in HCCI engines is still a known issue as of today. Many developments in improving and especially in slowing down the heat release rate have lead in 2012 to a new compression ignition concept. This ignition strategy is also known as reactivity controlled compression ignition (RCCI) and has risen as a suitable strategy for controlling the HCCI combustion. RCCI engines are typically characterised by its use of two types of fuel. Both fuels have different auto-ignition properties to control the phasing and duration of the combustion process [32].

During the compression stroke, low-reactivity fuel (high octane number) is premixed with air and injected into the cylinder far before reaching TDC. It is important to note that the temperature inside the cylinder during the first injection should be low enough for the fuel not to auto-ignite. During the compression cycle, high-reactivity fuel (high cetane rating) is injected into the cylinder to form a local mixture of both fuel and air blends. At the end of the compression stroke, a second injection of high-reactivity fuel at high pressure starts the ignition and combustion of the fuel and air blend [17]. By following this methodology, the combustion can gradually spread from the high reactivity zones to the rest of the combustion chamber resulting in a more controlled heat release process [70]. The conducted experiments by Kokjohn et al. [71] have shown high thermal efficiencies and low NOx emissions. An improvement of at least 4% in fuel consumption has been observed in comparison to conventional diesel combustion (CDC). This can be explained by the avoidance of high temperature regions which consequently lead to a reduction in heat transfer losses.

Ammonia could be used as the low-reactivity fuel due to its high octane rating. High cetane ratings and auto-ignition characteristics are needed for the high-reactivity fuel, making diesel one of the ideal choices. Hydrogen might also be a candidate due to its high combustion rate. It has in comparison to diesel fuel a significantly higher auto-ignition temperature (809 $[K]$ versus 483 $[K]$), however, hydrogen needs considerably less activation energy to ignite. This indicates that hydrogen burns significantly faster in contrast to diesel fuel when it enters the hot combustion cylinder. As a result, the controllability of the combustion process can be greatly affected by the presence of hydrogen. Ahmadi et al. [70] investigated the influences of hydrogen addition on the performance of an RCCI engine. According to his observations, adding hydrogen to the system increased the in chamber reaction, which as a result accelerated the ignition timing. This, however, lead to an increased probability in knocking. The feasibility and efficiency of hydrogen-ammonia combustion inside RCCI engines cannot be answered yet, since this configuration has not been experimentally tested.

In the next sections, the influences of ammonia on the engine's performance will be further discussed.

3.4 Direct injection and port injection

A high injection pressure in the order of 600 to 700 $[bar]$ enables a nearly complete distribution of the fuel mixture inside the combustion cylinder [37]. Direct liquid injection is commonly used in compression ignition engines such as diesel engines. However, ammonia has a significantly higher latent heat of vaporization (1369 $[kJ/kg]$) in comparison to diesel oil (232.4 $[kJ/kg]$) and gasoline (348.7 $[kJ/kg]$). The latent heat of vaporization represents the total amount of energy per kg required to complete the transition from liquid to gaseous. This phase transition causes a massive cooling effect in the cylinder, resulting in a limitation in operating and performance range, poor efficiency and a greater probability of misfire [67]. However, for a hydrogen-ammonia mixture, the hydrogen can counteract the ammonia's cooling effect, because of its lower auto-ignition temperature requirement. In this respect, the earlier combustion of the hydrogen is able to minimize the cooling effect caused by the liquid to gas transition of ammonia.

Port injection can both be used for spark- and compression ignition engines. The fuel mixture is often delivered in a gaseous state along with the air into the intake port [39]. The main advantage of this type of injection is the elimination of heat loss due to the vaporization of the fuel mixture inside the cylinder. However, when port injected, the gaseous mixture displaces the inlet air delivered to the combustion cylinder resulting in a reduction in the volumetric efficiency of the engine. A combined version of the two injection methods could potentially maximize the volumetric efficiency while minimizing the heat loss due to ammonia vaporization [39]. Such a system could be a highly advanced liquid or gaseous direct injection strategy, which may also increase the maximum allowable concentration of ammonia in case of a dual fuel mixture [39]. Having multiple injection strategies have also shown promising reductions of NOx and unburned ammonia emissions [66].

3.5 Hydrogen-ammonia ratio

From experiments it has been shown that at low hydrogen ratios, the chemical effect becomes the most significant in the enhancement of the heat release. At higher hydrogen ratios, the transport effect becomes evidently dominant, because of the high mobility of the hydrogen [72]. The laminar burning velocities of different ammonia-hydrogen ratios have been conducted by lee et al. [73], Li et al. [74] and Kumar et al. [75]. However, the experiments were all conducted under atmospheric pressure conditions. According to their observations, the laminar burning velocity of premixed ammonia-hydrogen increases exponentially when increasing the hydrogen ratio. In addition, increasing the initial mixture pressure while keeping the hydrogen ratio the same does negatively influence the laminar burning velocity [76, 77]. An experimental study performed by He et al. [78] reported promising results on the auto-ignition properties when the fuel contained 20 vol. % hydrogen at high pressures varying from 20 to 60 $[bar]$ and intermediate temperatures (between 950 and 1150 $[K]$).

The minimum hydrogen concentration depends on factors such as the operating conditions, engine specifications, the temperature of the engine cylinder jacket and the spark properties [79]. Ammonia-hydrogen mixtures containing between 10-20 volume percent hydrogen showed favourable combustion characteristics for SI engines at full load [80]. According to the experiments conducted by Frigo et al. [16] on a four-stroke SI engine, a minimum volumetric hydrogen-ammonia ratio of 7% at full load and 11% at half load was required to get reasonable engine response.

For CI engines, a minimum volumetric hydrogen concentration of 30% is required to obtain decent efficiencies at low compression ratios (12.3:1) and intake pressures [23]. Thus, when increasing the compression ratio, a lower volume concentration of hydrogen is needed at the cost of an increased probability of ringing. The experiments conducted by Duynslaegher et al. [20] has also shown comparable results for the minimum required hydrogen concentration. At intermediate engine speed (1800 $[rpm]$), a minimum hydrogen ratio between 4-5% by weight (which translates to 26-31 vol.% hydrogen) was required. Further decreasing the hydrogen concentration resulted into a rapid fall in engine performance. Adding hydrogen as a combustion promoter does not significantly influence the ammonia reaction pathways. According to the experimental observations by He et al. [78], the hydrogen-ammonia mixture showed the same pathway as for pure ammonia combustion. However, the additive hydrogen does help in increasing the oxidation reaction rate by accelerating the consumption of ammonia and NH_2 through the same pathway as for pure ammonia combustion [78].

3.6 Equivalence ratio

The equivalence ratio, which is the ratio of the actual air–fuel ratio to the stoichiometric air–fuel ratio plays a significant role in the overall performance of the engine and on the composition of the exhaust gas. Changing the equivalence ratio influences the auto-ignition (delay) characteristics and is generally used for air-deficient situations [81]. In case the equivalence ratio exceeds 0.8, stable operation of SI engines cannot be fully guaranteed [1]. The overall chemical combustion equation for an ammonia hydrogen mixture is shown in Equation 3.1. Nitrogen has to be included in the equation, since air is used as the oxidizer instead of pure oxygen [82]. One mole of O_2 equals 3.76 moles of N_2, when the air consists of 79% N_2 and 21% O_2 [23].

$$NH_3 + \frac{3}{4}(O_2 + 3.76N_2) \rightarrow \frac{3}{2}H_2O + \frac{6.64}{2}N_2 \tag{3.1}$$

$$H_2 + \frac{1}{2}(O_2 + 3.76N_2) \rightarrow H_2O + \frac{3.76}{2}N_2 \tag{3.2}$$

The Equations 3.1 and 3.2 can be combined, resulting in Equation 3.3:

$$(1-x_{H_2})NH_3 + x_{H_2}H_2 + \frac{3-x_{H_2}}{4}(O_2+3.76N_2) \rightarrow \frac{3-x_{H_2}}{2}H_2O + (\frac{1-x_{H_2}}{2} + 3.76\cdot\frac{3-x_{H_2}}{4})N_2 \quad (3.3)$$

In which x_{H_2} is the hydrogen molar fraction in the fuel mixture:

$$x_{H_2} = \frac{[H_2]}{[H_2]+[NH_3]} \quad (3.4)$$

The chemical kinetics for the combustion process is extremely complex and difficult to simulate. As a matter of fact, traces of N_2O, NOx and NH_3 are always found in the exhaust gas [81]. In order to get a brief indication of the air fuel ratio, several assumptions have been made. We assume an oxygen air content of 21% and a complete combustion, meaning that the only products after combustion are H_2O and N_2.

$$AFR = \frac{m_a}{m_f} = \frac{\frac{3-x_{H_2}}{4}\cdot(O_2+3.76N_2)}{(1-x_{H_2})NH_3 + x_{H_2}H_2} \quad (3.5)$$

The stoichiometric air-fuel ratio is a function of the air-fuel ratio and the air excess ratio (λ):

$$\sigma = \frac{AFR}{\lambda} \quad (3.6) \qquad \lambda = \frac{m_{a,min}}{m_a} \quad (3.7)$$

For complete combustion, the ideal (theoretical) AFR is also known as the stoichiometric air-fuel ratio. Those ratios are fixed and fuel dependent. Pure hydrogen and ammonia have a stoichiometric AFR of 34.32:1 and 6.06:1 respectively. This means that for 1 $[kg]$ of hydrogen, 34.3 $[kg]$ of air is needed in order to achieve complete combustion, meaning that no excess oxygen and unburnt fuel can be found in the exhaust. The air-fuel mixture is called lean or rich in case the AFR is higher or lower than the stoichiometric ratio [18]. Performing under rich or lean conditions both have their advantages and disadvantages. As can be seen in Figure 3.4a, the maximum power is obtained with rich air-fuel mixtures, while the lowest fuel consumption can be achieved under lean conditions. The AFR ratio for SI engines usually varies (between lean and rich conditions) for different operating points in terms of engines speeds, loads and temperatures as shown in Figure 3.4b. Modern SI engines are, however, operating as much as possible around stoichiometric air-fuel ratios, mainly because of the exhaust gas after treatment reasons [18].

CI engines on the other hand always operate at lean air-fuel conditions. Another major difference between SI and CI engines is that CI engines typically run on stratified (non homogeneous) air-fuel mixtures, while SI engines are operating with homogeneous mixtures (in case of port-injection engines) [18]. Because of the lower stoichiometric value of ammonia in contrast to diesel, more ammonia fuel can be supplied to the combustion chamber with the same amount of air intake. This makes the energy content of the stoichiometric air-ammonia mixture comparable to that of diesel and gasoline fuels [18].

The conducted hydrogen-ammonia experiments on SI engines by Lhuillier et al. [19] have shown minimal values in *NOx* emissions for fuel rich mixtures. He also observed an increase in *NOx* emissions when increasing the hydrogen ratio. A reason for this could be due to the increase in thermal temperature that promotes the *NOx* formation. Increasing the equivalence ratio will also result in an increase of unburned ammonia in the exhaust gas as can be seen in Figure 3.5. In addition, when the equivalence ratio is heading towards very lean mixtures, the concentration of unburned ammonia also increases, because of the poor combustion efficiency [19]. Exhaust gas after treatment concepts such as the SCR could beneficially use the available unburned ammonia to decompose the *NOx* particles. Therefore in order to achieve the best equivalence ratio in terms of minimal unburned ammonia and *NOx* production, a balance has to be found between the amount of available unburned ammonia and the created *NOx* concentration in the exhaust gas.

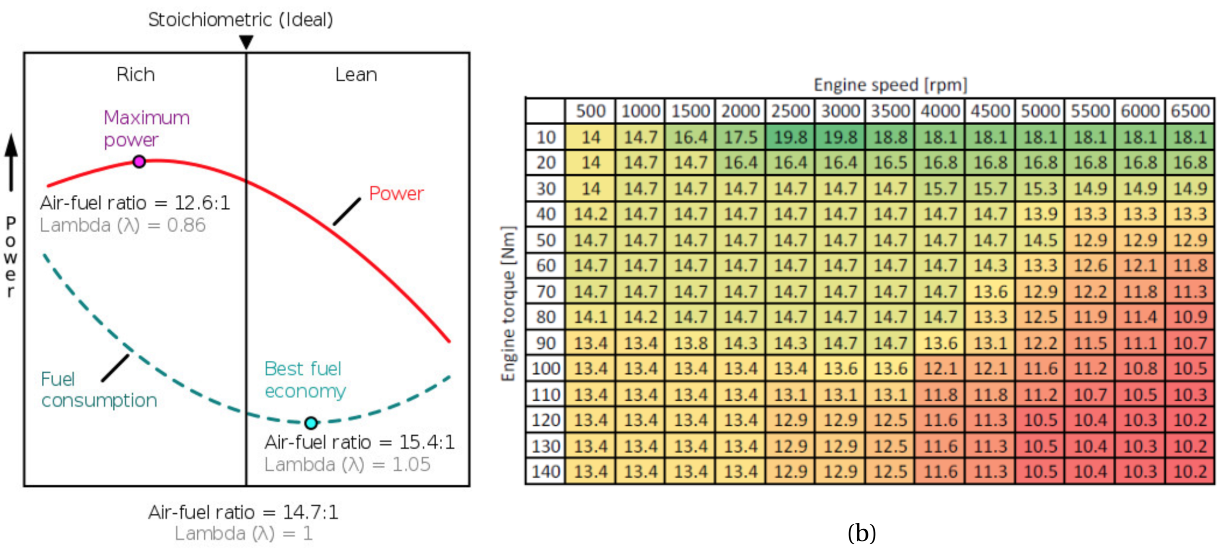

	500	1000	1500	2000	2500	3000	3500	4000	4500	5000	5500	6000	6500
10	14	14.7	16.4	17.5	19.8	19.8	18.8	18.1	18.1	18.1	18.1	18.1	18.1
20	14	14.7	14.7	16.4	16.4	16.4	16.5	16.8	16.8	16.8	16.8	16.8	16.8
30	14	14.7	14.7	14.7	14.7	14.7	14.7	15.7	15.7	15.3	14.9	14.9	14.9
40	14.2	14.7	14.7	14.7	14.7	14.7	14.7	14.7	14.7	13.9	13.3	13.3	13.3
50	14.7	14.7	14.7	14.7	14.7	14.7	14.7	14.7	14.7	14.5	12.9	12.9	12.9
60	14.7	14.7	14.7	14.7	14.7	14.7	14.7	14.7	14.3	13.3	12.6	12.1	11.8
70	14.7	14.7	14.7	14.7	14.7	14.7	14.7	14.7	13.6	12.9	12.2	11.8	11.3
80	14.1	14.2	14.7	14.7	14.7	14.7	14.7	14.7	13.3	12.5	11.9	11.4	10.9
90	13.4	13.4	13.8	14.3	14.3	14.7	14.7	13.6	13.1	12.2	11.5	11.1	10.7
100	13.4	13.4	13.4	13.4	13.4	13.6	13.6	12.1	12.1	11.6	11.2	10.8	10.5
110	13.4	13.4	13.4	13.4	13.1	13.1	13.1	11.8	11.8	11.2	10.7	10.5	10.3
120	13.4	13.4	13.4	13.4	12.9	12.9	12.5	11.6	11.3	10.5	10.4	10.3	10.2
130	13.4	13.4	13.4	13.4	12.9	12.9	12.5	11.6	11.3	10.5	10.4	10.3	10.2
140	13.4	13.4	13.4	13.4	12.9	12.9	12.5	11.6	11.3	10.5	10.4	10.3	10.2

(b)

(a)

Figure 3.4: (a) Fuel consumption and engine power as function of λ and (b) is an example of an SI engine AFR as function of torque and engine speed [18].

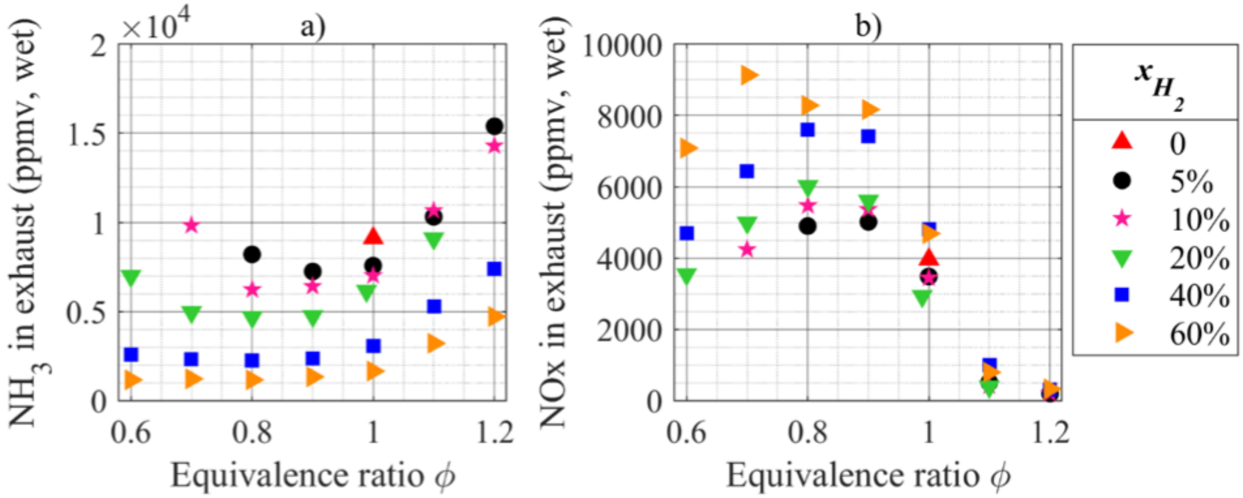

Figure 3.5: Pollutant emissions of unburned ammonia (left) and *NOx* (right) in the exhaust [19].

3.7 Compression ratio

It has been observed from the conducted studies by Duynslaegher et al. [20] that an increase in compression ratio goes together with a slight increase in efficiency and a higher quantity of oxygen and ammonia in the exhaust gas. The unburned ammonia concentration of 8% to 10%, which is significantly higher than the quantities found in conventional fuels (≈ 3%) could not be fully explained. According to the author, the unburned fraction could be the result of poor combustion going together with an increase of the quenching effect at the walls. The term quenching refers to flame extinguish as a result of the heat loss to the cylinder walls.

During the expansion phase, the cylinder piston moves faster than the flame propagation speed due to the low flame speed of ammonia. The energy contained in the flame front is subsequently deluded and does, therefore, not fully preheat the trapped mixture enough to allow for a complete flame propagation [20]. When flame quenches, it leaves a layer or volume of unburned mixture ahead of the flame [83]. Quenching is mostly influenced by the compression ratio and can be mitigated by controlling the turbulence in the cylinder with the use of an appropriate engine geometry or admission phase [20]. In addition, increasing the compression ratio for CI engines will most likely lead to an increased maximum combustion temperature and elevated *NOx* emissions. One way to counter the *NOx* production is the use of alternative combustion techniques, such as lean operation [66].

3.8 Effect of the spark timing

The spark timing at the start of combustion can significantly influence the overall performance of the engine. One of the reasons for this is the low flame speed of ammonia resulting in a higher required spark advance in comparison to gasoline. Proper spark advance timing, which is also influenced by the fuel flow rate is needed to have enough time for the ammonia mixture to burn [19]. In addition, from a theoretical point of view, an increase in spark advance will also result in an increase in the efficiency of the engine.

However, the advance timing cannot be too high and is often limited by the increased probability in knock, which has been experimentally observed starting from 40°before reaching the top dead center (TDC) [20]. Because of the high auto-ignition resistance of ammonia, the maximum efficiency due to the spark advance is well reached before the appearance of knock becomes significant. As a matter of fact, the benefit of having a high knock resistance makes the engine operable at much higher indicated mean pressures in contrast to gasoline fueled engines. As a result greater efficiencies at higher loads can be expected for ammonia fueled engines [20]. This enables the engine at full load to use its maximum brake torque (MBT) spark timing, which is also known as the minimum spark timing for the best torque [84].

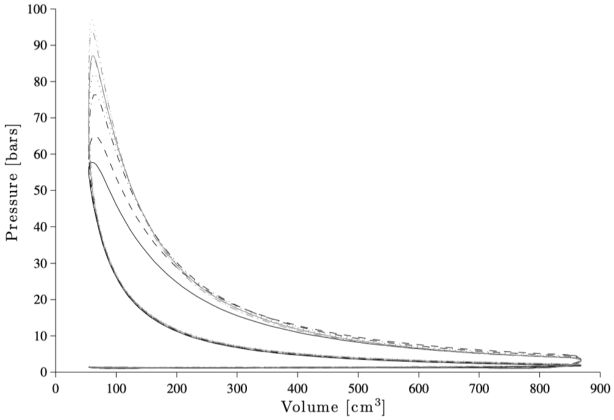

(a)

Spark advance [°]	16	18	20	22	24	26	28	30
T°$_e$ [°C]	543	577	557	545	535	525	515	503
Torque [Nm]	40	52	54	54	54	54	54	54
RPM	1456	1510	1508	1513	1517	1512	1508	1500
bmep [kPa]	618	800	826	826	826	829	834	834
P$_e$ [kW]	6.10	8.20	8.45	8.48	8.50	8.50	8.53	8.48
η_e	0.26	0.34	0.36	0.36	0.36	0.36	0.36	0.36
r$_{air}$	0.63	0.63	0.63	0.63	0.63	0.63	0.63	0.63
Friction torque [Nm]	14.71	15.12	15.10	15.14	15.16	15.13	15.10	15.04
fmep [kPa]	227	233	233	234	234	234	233	232
imep [kPa]	845	1033	1059	1060	1060	1062	1067	1066
η_{mec}	0.73	0.77	0.78	0.78	0.78	0.78	0.78	0.78
η_i	0.35	0.44	0.46	0.46	0.46	0.46	0.46	0.46
Unburned NH$_3$ (%)	16.88	7.93	8.00	8.59	8.89	9.40	10.00	10.54

(b)

Figure 3.6: (a) Pressure-volume diagrams for several spark advances from the ammonia experiments by Duynslaegher et al. [20]: black line = 16°; grey line = 24°; grey dotted line = 30°and (b) the engine performances monitored for several spark advances.

As can be seen in Figure 3.6a from the experimental results by Duynslaegher et al. [20], the maximum efficiency has well been reached at a spark advance of 20°. There is no beneficial effect in increasing the spark advance even further since the engine performance will remain the same, it may even result in a higher unburned ammonia concentrations. In addition, as depicted in Figure 3.6b, the increase in spark advance is also correlated to an increase in maximum pressure. Thus, further increasing the spark advance after reaching the maximum engine efficiency will result in higher maximum pressures inside the cylinder, which is not beneficial for the mechanical durability.

Chapter 4

Conclusions literature study

4.1 Chapter overview

The basic principles of ammonia fueled solid oxide fuel cells (SOFC) and hydrogen-ammonia fueled internal combustion engines (ICE) have been investigated in the literature study. The conclusions for the SOFC (**Section 4.2**) and the ICE (**Section 4.3**) are covered in this chapter. The final conclusions concerning the literature study are drawn in **Section 4.4**, together with the preferred ignition method for the in-cylinder modelling. The literature study gave us an outline of the modelling that has to be done in order to answer the main research question that is stated in **Section 1.3**. **Section 4.5** shows a concise overview of the project definition phase of the thesis.

4.2 Ammonia fueled SOFC conclusions

- The conducted experiments and theoretical based models for directly ammonia fueled solid oxide fuel cells have both shown promising results. System efficiencies above 50% can be expected, however, there are still practical challenges that require further development. The power density and load response capability of solid oxide fuel cells are not at an acceptable level yet, making it in comparison to conventional fossil fueled engines less interesting for ship owners.

- From the conducted experiments by Stoeckl et al. [48], the author observed that the decrease in temperature in the SOFC stack was the most pronounced at the anode inlet region, which may indicate that the majority of the ammonia decomposition happens at the fuel inlet of the anode. The conducted experiments by Stoeckl et al. [50] also showed no voltage degradation during a 100 hour operating time of the ammonia fueled SOFC stack at a fuel utilization factor of 80%. The author observed greater internal resistances and a reduction in the performance of the ammonia fueled SOFC stack, when further lowering the fuel utilization factor. Hence, the fuel utilization factor should preferably be around 80% for optimal performances.

- Nickel is a widely used catalyst inside SOFCs, because of its high electronic conductivity and stability under chemically reducing conditions. In addition, nickel also works as a catalyst for the ammonia decomposition and can be used as the internal reforming catalyst for ammonia fueled SOFCs. A temperature range between 800 and 1100 [$°C$] is needed inside an SOFC-O stack for zirconia (cermet), the oxygen ion conductor (inside the electrolyte) to work properly. At these temperatures, a nickel catalyst would give an ammonia conversion rate close to 100% (as shown in Figure 2.4) in case of direct cracking.

- For ammonia and hydrogen fueled SOFCs, similar internal resistance losses at temperatures above 800 [°C] were observed. However, when operating the fuel cell at lower temperatures (below 700 [°C]), a slight increase in interfacial polarization occurred when fueled with ammonia, which can be explained by the slower hydrogen formation at that temperature.
- The scarcity of available research papers on SOFC-H stacks does not necessarily imply that the concept is completely irrelevant. Oxygen conducting SOFCs typically require high operating temperatures to improve the ion conductance of the electrolyte. This affects the durability of the materials inside the stack. Proton conducting SOFCs on the other hand can operate at lower temperatures, which enhances the durability of the stack. In addition, the absence of water in the output of the anode removes the vapor condenser subsystem requirement that would otherwise be placed between the anode-off gas from the SOFC and the hydrogen storage tank.
- Solid oxide fuel cells are not found on its own, but are integrated with extra components for the fuel cell to work properly such as air compressors, heat exchangers, air blowers, etc. These extras are commonly called the balance of plant (BOP), which has influences on the reaction time of the fuel cell system. Azzopardi et al. [85] has measured the response time of an SOFC when adjusting the load condition to be in the order of 1-2 minutes. The reasons for the slow response lies in the constraint to limit and control the fuel consumption and temperature gradient in the system. This makes SOFCs highly inefficient in coping with transient loading.
- Very little is known about what occurs within the SOFC stack during transient loading. The reason for this is the difficulty of experimentally accessing the internal features of the SOFC stack without modifying the temperature and flow rate which are critical parameters in determining the cell performance [86]. In a paper published by Komatsu et al. [87] indicated that reducing the fuel flow rate by setting a higher U_f may decrease the OCV, increase concentration polarization and also increase the degradation rate of the fuel stack. He also emphasised the importance of operating temperature management which can significantly reduce the effects of polarization during transient loading.
- Cost may also be a deciding factor in the popularity of the SOFC on-board of vessels. At the moment solid oxide fuel cells are costly in terms of high operation and investment expenditures. To make it slightly worse, the fuel stacks have a relatively short life span as they have to be replaced every 2-3 years [43]. SOFC cost per [kWh] has mostly remained the same in the last couple of years. The investment costs are still expected to remain relatively expensive in the near future [11]. However, some novel concepts and manufacturing techniques have shown opportunities in reducing the capital cost. It can be expected that these high investment and operational costs of solid oxide fuel cells can be justified when a reduction in emissions, noise and vibrations play an important role [43].
- At last, steady developments in medium temperature proton conducting SOFCs may enhance the overall performance and durability of ammonia fueled SOFCs in the near future. However, at medium temperatures, more expensive catalysts are required for the cracking of ammonia. Low temperature nano based catalysts may provide a solution to this problem.

4.3 Hydrogen-ammonia fueled ICE conclusions

- Respectable technical performances in terms of load response, power density, system efficiency, part-load performance and coping with marine environment have been observed when comparing ammonia-hydrogen driven ICE with a conventional fossil fueled configuration [88]. Internal combustion engines are in contrast to SOFCs less expensive and do generally also have an acceptable power density and load response capability. This makes ammonia-hydrogen driven engines exceptionally suitable for mechanically driven propulsion on-board of ships in contrast to other carbon free alternatives. Nonetheless, the ammonia-hydrogen driven ICE concept is still in its novel stage.

- The minimum hydrogen concentration depends on factors such as the operating conditions, engine specifications, initial conditions, the temperature of the engine cylinder jacket and the spark properties (in case of SI). Part-load conditions generally require a higher hydrogen concentration. From engine experiments, CI engines require a minimum volumetric hydrogen concentration of 30%, while SI engines have shown respectable combustion characteristics at volumetric hydrogen concentrations between 10-20%.

- Spark ignition has shown promising results for hydrogen-ammonia fueled engines. However, this usually comes at a cost of a relatively lower combustion efficiency in contrast to compression ignition engines. Several advanced compression ignition concepts are under development, such as HCCI and RCCI in which both methods combines the best features of SI and CI engines. Experimental studies by Ahmadi et al. [70] on hydrogen addition during RCCI combustion have shown an increased likelihood in knocking. However, the author used diesel as the prime fuel which has a considerably lower octane rating in comparison to ammonia fuel. Hence, it cannot be said whether the increased likelihood in knocking is also the case for the hydrogen and ammonia fuel combination since it has not yet been experimentally tested in RCCI engines. A concise overview of the combustion strategies can be found in Table 4.1.

- Unlike spark ignition, HCCI does not have a direct control on when combustion takes place. In this regard, the mixture composition, intake temperature and the intake pressure have to be tuned in such that the combustion occurs when desired [15]. In addition, for HCCI engines, both the air and the fuel have to be mixed at the inlet port ($i.e.$ fumigation) or at the beginning of the compression cycle by direct injection [89].

- For typical SI or CI engines, at any point in time, only a fraction of the total fuel is burning. This results in notably lower peak pressures and energy release rates peak values in contrast to HCCI in which the ignition simultaneously occurs on multiple sites inside the cylinder [17]. Hence a much smaller combustion duration and therefore higher peak pressures can be expected for HCCI operation.

- The available experimental results for hydrogen-ammonia combustion are nowadays all based on automotive sized engines. These engines do not show similar combustion characteristics in comparison to large marine engines. A reasonable argument is the time available for the combustion process, which is usually longer for marine engines because of the lower engines speeds. In addition, marine engines typically have a larger combustion chamber volume to surface ratio. This typically results in relatively less heat losses in comparison to automotive engines. This also influences the overall performance output in terms of in-cylinder pressure, combustion heat and temperature per crank angle [32].

- MAN engines has recently published their newly designed two-stroke engine concept, which is able to operate on ammonia and an additional promoter fuel. As of 2020, it has been expected that the development time of ammonia engines will take two to four more years [37]. It is possible for most types of IC engines to operate on ammonia by modifying the compression ratio and changing the fuel line materials to avoid corrosion [66]. However, in order to obtain greater indicated efficiencies, the engine's in-cylinder geometry should be completely optimised for HCCI mode.

With virtually zero carbon, sulphur, unburned hydrocarbons and particular matter emissions and the already existing ammonia production facilities and infrastructures, ammonia will most likely become an abundant marine fuel source in the future. An overview of the ignition methods can be found in Table 4.1.

Table 4.1: Traditional and controlled auto-ignition based combustion methods. The contents in the table are from the paper by Aziz et al. [17].

Combustion mode	SI	CI	HCCI	RCCI
Fuel	Gasoline-like	Diesel-like	Flexible fuels	Multifuels
Lambda	1	1.2 to 2.2	>1	>1
Ignition	Spark ignition	Auto-ignition	Auto-ignition	Auto-ignition
Combustion form	Premixed	Diffusion	Premixed [1]	Premixed + stratified
Comb. rate limitation	Flame propagation	Mixing rate	Spontaneous	Fuel reactivity
Comb. temperature	High	Partially high	Relatively low	Relatively high

4.4 Final conclusions

The literature study gave us an indication what we can expect when we run the ammonia fueled SOFC and hydrogen-ammonia fueled ICE independently as single systems. A vast amount of papers concerning directly fueled ammonia SOFCs have been published throughout the years. This concept has already been extensively modeled and successfully tested on large-scale. On the other hand, not much is known about hydrogen-ammonia combustion inside an ICE. Although the flammability behaviour and chemical kinetics during combustion have been widely investigated. Publications concerning the in-cylinder combustion characteristics are scarce. To make it worse, the conducted experiments are all based on automotive engines, which outcomes cannot be entirely translated or extrapolated to large marine sized engines. This makes the latter also difficult to conclude whether hydrogen-ammonia fueled SI or CI engines are the most suitable for marine applications.

For automotive sized engines, hydrogen-ammonia combustion during SI mode is possible, but not optimal because of the high auto-ignition resistance and low flame propagation speed of ammonia. Hence, poor engine efficiencies, low power densities and large amounts of unburned fuel are more likely to occur during spark ignition. Compression ignition on the other hand is largely affected by great amounts of NOx production inside the flame zone. The NOx is primarily produced from fuel-bound nitrogen, which can unlike the nitrogen (N_2) in air easily re-bond with free oxygen during the combustion process. The latter may explain why there are more papers published for SI engines instead of CI. HCCI combustion on the other hand is a promising candidate to overcome these disadvantages ($i.e.$ low power density and high NOx emissions). Hydrogen-ammonia fueled HCCI combustion for a range of fuel blends have been documented by Pochet et al. [15, 23, 2]. The conducted experiments on his automotive sized engine have shown promising results. However, hydrogen-ammonia combustion inside HCCI engines is still a novel concept that requires lots of large-scale experiments and simulation studies to find the most optimal engine geometry, operating range and hydrogen concentration.

---

[1] But dominated by chemical kinetics

4.5 Project definition

The performance of the SOFC is not affected by the operational condition of the HCCI engine, while the ICE is dependent on the hydrogen concentration in the SOFC's anode-off gas. Since there are a number of working ammonia fueled SOFC models in the literature, the thesis will be mostly emphasised on the investigation of hydrogen-ammonia fueled HCCI combustion. Here, we will make the assumption that the SOFC is able to provide sufficient hydrogen and heat to the ICE.

4.5.1 Project approach

To answer whether HCCI mode is a suitable candidate for engine combustion on-board of ships for an ammonia fueled SOFC-ICE design, we firstly have to develop a working hydrogen-ammonia fueled in-cylinder model that is able to simulate HCCI combustion. The input parameters for the model are from the experimental results by Pochet et al. [23]. Because of the incompleteness of the input data, several unknown parameters have been calibrated by fitting the output results (*i.e.* indicated efficiency, injected fuel mass, Maximum temperature and combustion efficiency) from the in-cylinder model with the results from the paper.

Since the available experimental data for hydrogen-ammonia combustion are all based on automotive sized engines, several scaling laws have been investigated to search for the most optimal way to enlarge the size of the automotive engine to a truck sized variant. The scaling results may give a first impression what we can expect the engine power output, fuel mass flow and engine performances to be for a truck sized hydrogen-ammonia fueled HCCI engine. Further enlarging the truck sized engine to a marine sized variant has been considered, but this has shown inaccurate output results because of the growing differences in the relative heat loss between both engines.

From the literature study, it became evident that HCCI engines have issues with auto-ignition control. The inlet conditions have shown to be the decisive parameters in the location of the start of combustion crank angle. Hence, a parametric study on the initial conditions is necessary to get a better understanding which intake parameters have the greatest impact on the auto-ignition and how changes in the initial conditions will affect the combustion characteristics. For this parametric study, the modified knock integral model (MKIM) and the Single-Wiebe function have been developed. Here, the MKIM function is necessary to determine the shift in the start of combustion crank angle when adjusting the initial conditions. Then, the Single-Wiebe model is used to determine the new mass fraction burn distribution for the anti-causal in-cylinder model to simulation the in-cylinder combustion characteristics.

The scaled engine model for hydrogen-ammonia combustion has shown poor performances in comparison to a similar sized engine that is running on carbon fuel. In order to enhance the power output of the scaled engine, several modifications in the initial conditions (*i.e.* intake temperature, engine speed, equivalence ratio and intake pressure) have been proposed and further investigated. At last, since the location of the start of combustion for HCCI engines is almost fully controlled by the initial conditions, an analysis has been performed to find ways to enhance the flexibility of the proposed SOFC-ICE design layout. These system design considerations are mitigation measurements to decrease the fluctuations in the engine's intake conditions.

A concise overview of the main purpose and output results for each of the developed models can be found in Figure 4.1.

In-cylinder model

Input

- Incomplete experimental data set (discussed in **Section 5.3.2**)
- Engine specifications
- Fuel and air composition and characteristics
- The model has been calibrated using the output results from the paper in order to determine the unknown parameters

Purpose

- The in-cylinder model is necessary to simulate the in-cylinder HCCI combustion process for a range of hydrogen-ammonia fuel blends
- The model also provides insight how the combustion characteristics are influenced by the change in hydrogen concentration

Output

- Indicated power output
- IMEP
- Burn duration
- Hydrogen and ammonia mass flow
- The start of combustion (CA1)

Engine scaling

Input

- Scaling laws
- In-cylinder model
- Thermodynamic results from the in-cylinder model, which are necessary for the heat loss calibration

Purpose

- Engine scaling is necessary to obtain the performance output of a larger sized engine
- Here, the stroke of the engine has been enlarged from 88 to 170 [mm]
- The scaling models provide insight how effective engine scaling is and whether we can use the scaling laws to enlarge an automotive sized engine to a truck sized variant
- The model provides insight which scaling law fits the best for HCCI combustion

Output

- Indicated efficiency
- Heat loss
- Indicated power output
- Hydrogen and ammonia mass flow
- The start of combustion (CA1)

MKIM

Input

- The initial conditions (i.e. equivalence ratio, engine speed, intake temperature and intake pressure) from the in-cylinder model
- The start of combustion crank angle (CA1) and the polytropic exponent of compression (nc) from the in-cylinder model
- Initial values for the empirical MKIM function

Purpose

- For HCCI combustion, the location of the start of combustion shifts when adjusting the intake conditions
- In this respect, the MKIM function is necessary to determine the new location of the start of combustion when modifications in the intake conditions

Output

- Start of combustion (CA1) crank angles for a range of different intake conditions

Single-Wiebe model

Input

- Start of combustion from MKIM
- Burn duration and combustion efficiency
- Experimental data from the in-cylinder model for the determination of the form factor

Purpose

- Parametric study: the mass fraction burn for a range of different initial conditions

Output

- Mass fraction burn

Anti-causal in-cylinder model

Input

- Mass fraction burn from the Single-Wiebe model

Purpose

- In-cylinder combustion characteristics for a range of different intake conditions

Output

- Indicated power output
- Hydrogen and ammonia mass flow
- Indicated efficiency
- Heat loss

Figure 4.1: Concise overview of the 4 developed models

Chapter 5

In-cylinder combustion model

5.1 Chapter overview

As mentioned in **Chapter 4**, not much is known about hydrogen-ammonia combustion inside internal combustion engines, while directly fueled ammonia SOFCs have already been extensively modeled and tested on large-scale. In-cylinder modeling for hydrogen-ammonia HCCI combustion is a useful way to obtain insight in the combustion characteristics of the fuel blends. In this chapter, the in-cylinder model for HCCI combustion will be further elaborated. **Section 5.3** will discuss the engine specifications and the methodology in the creation of the HCCI engine model. This section also provides a concise explanation for the heat release and heat loss models. The results from the in-cylinder model are discussed in **Section 5.4**. At last, the reflection on the results and the conclusions drawn from the results can be found in **Section 5.5** and **Section 5.6**, respectively.

5.2 Introduction

The main objective for the in-cylinder model is to simulate the in-cylinder hydrogen-ammonia combustion characteristics from the conducted HCCI experiments by Pochet et al. [23] as accurately as possible. Here, the main output parameters from the in-cylinder model are the brake power, fuel mass flow, most optimal hydrogen ratio and the minimum required inlet temperature. The model also provides insight what we can expect the in-cylinder temperature and the heat release distribution to be during the combustion process. However, these distributions may no be completely accurate because of the incomplete data that has been used for the calibration of the model. The developed in-cylinder model has shown similar overall output results including the injected fuel mass, indicated efficiency, combustion efficiency and the heat loss with the results from the paper by Pochet. However, it cannot be verified whether the heat release rate and temperature distribution during the combustion process from the developed in-cylinder model are similar with the conducted experiments by Pochet.

Sapra et al. [32] modeled and conducted experiments on hydrogen natural gas combustion inside a spark ignited ICE. Sapra kindly provided his findings and his verified and validated hydrogen-NG in-cylinder model as a baseline for the hydrogen-ammonia HCCI in-cylinder model. The framework components of the in-cylinder model (*i.e.* heat release, heat loss, combustion characterization and the in-cylinder process) components have been modified for hydrogen-ammonia fuel. Due to the incomplete set of experimental data from Pochet, the unknown input parameters for the in-cylinder model have been determined based on reasonable assumptions and on engine calibration that will be discussed in Section **5.3.2**. The absence of a complete data set will affect the reliability of the in-cylinder modeling results.

5.3 Methodology

5.3.1 Modelling approach

The main components of the in-cylinder model are the heat release model (**Section 5.3.3**), the heat loss model (**Section 5.3.4**), fuel and air property block components and the mass balance and composition models (**Appendix B3**). Here, the components of the model have been modified for hydrogen-ammonia combustion. The in-cylinder model simulates the in-cylinder process from the crank angle inlet valve close (IC) to exhaust valve open (EO). The ideal gas behaviour is assumed for the air, stoichiometric gas and the exhaust gas, which means that the thermodynamic properties only depend on the change in temperature. In addition, no leakage from the fuel and air through the cylinder has been assumed for the in-cylinder modeling.

The parameters in the model are categorised in four divisions as a result of the incompleteness of the data set. In this respect, the model contains fixed parameters, iterative parameters, calibration parameters and the parameters that are based on reasonable assumptions. The next subsections contain an in-detail explanation of these input parameters and the main model components that have been used to model the combustion characteristics of hydrogen-ammonia fuel. The flowchart in Figure 5.2 gives a concise overview of the most important steps that have been taken during the development of the in-cylinder model. An in-detail explanation of the in-cylinder model can be found in [21].

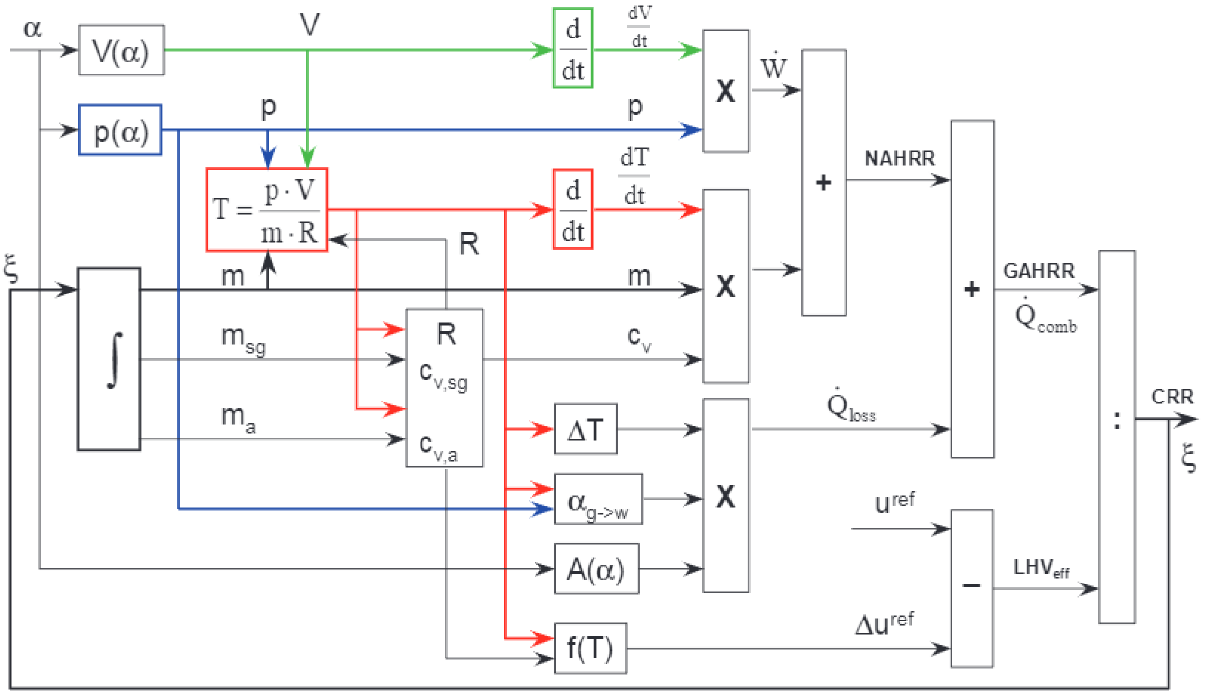

Figure 5.1: Block diagram overview for the simulation of the heat release rate. The figure has been taken from Stapersma [21].

5.3.2 Input parameters

As mentioned earlier, the amount of available experimental data concerning hydrogen-ammonia fueled HCCI engines is limited. Due to this scarcity and the absence of a complete data set, the in-cylinder

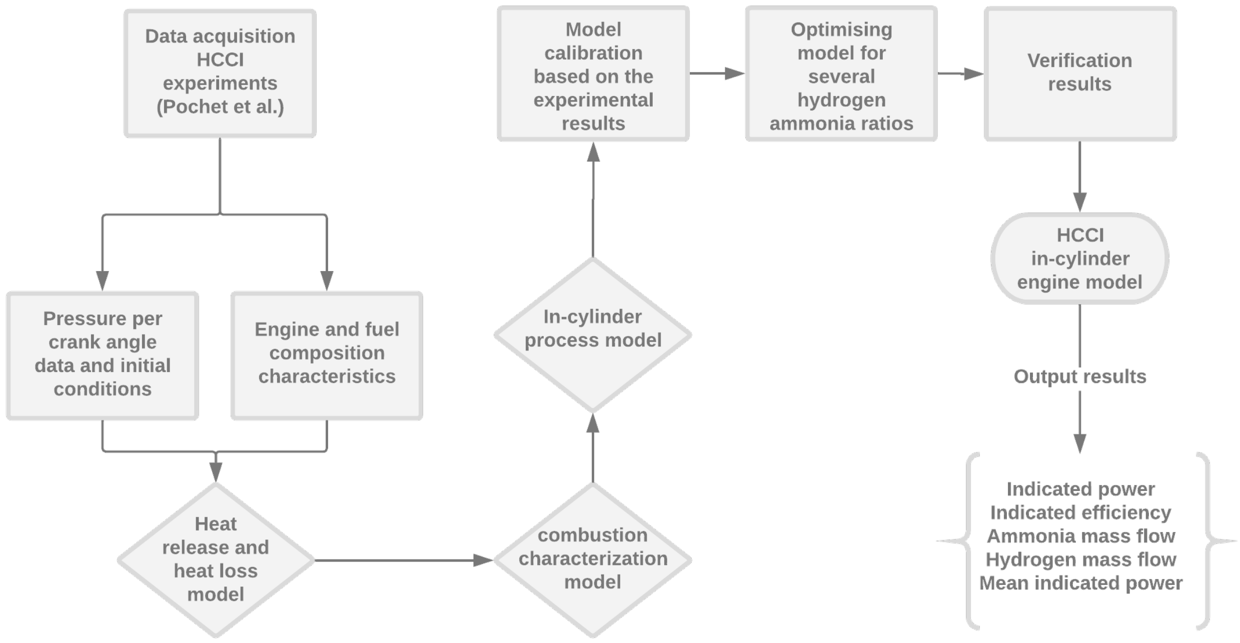

Figure 5.2: Flowchart overview of the steps taken in the creation of the HCCI engine model.

model has been developed using incomplete experimental engine data from Pochet et al. [15, 23]. The parameters in the model are categorised in four divisions: fixed parameters, iterative parameters, calibration parameters and the parameters that are based on reasonable assumptions.

Fixed parameters

The fixed parameters are the fuel and air properties (see **Appendix B3**) for a range of hydrogen-ammonia fuel blends and the input parameters provided by the paper [15, 23]. These input parameters include the engine specifications, equivalence ratio, inlet temperature, injected fuel mass, inlet pressure and the pressure crank angle distributions for various hydrogen-ammonia ratios. However, the data for the pressure distribution for the hydrogen-ammonia fuel blends are only available from -30 [$CADaTDC$] to 30 [$CADaTDC$] as can be seen in Figure 5.3. In short, the remaining parts of the pressure trace are unknown and had to be manually extended. An in-detail explanation and methodology for the pressure trace extension can be found in **Appendix B2**.

Next, the stoichiometric ratio of the fuel mixture has been determined using the Equations 3.3 to 3.7 (in **Chapter 3**). In addition, the valve timings at IC and EO are available, while the valve timings for IO and EC are unknown. However, zero valve overlap can be assumed, since the fuel is premixed with air before entering the cylinder. Thus, having a valve overlap is expected to drastically increase the undesired ammonia slip. However, the absence of a valve overlap will result in a larger concentration of trapped residual gas inside the cylinder. The quantity of this concentration (x_{sg}) is also unknown, but it has to be taken into account, since this parameter has a major influence on the heat release value, in-cylinder temperature and the trapped mass [32].

The HCCI experiments by Pochet have been conducted with the use of a modified version of the PSA DW10 engine. The engine specifications are shown in Table 5.1 together with the specifications used by Sapra et al. [32].

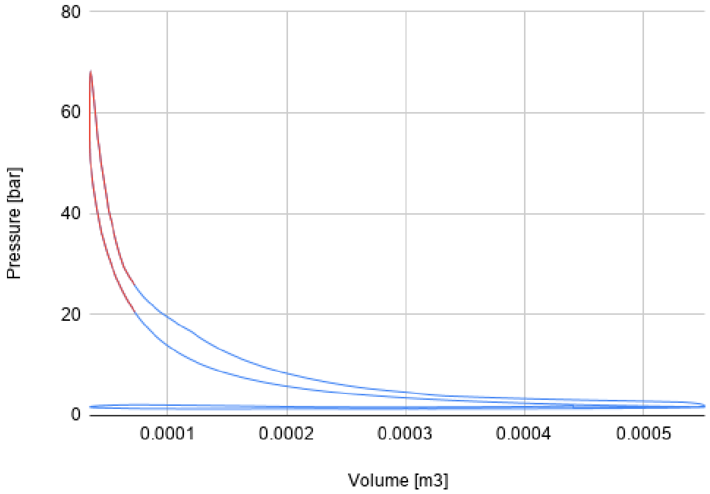

Figure 5.3: P-V diagram ammonia hydrogen (47 vol. percent hydrogen) HCCI combustion, in which the available data is shown in red and the manually extended data in blue.

Table 5.1: Natural gas SI and ammonia HCCI engine specifications.

	Unit	SI engine	HCCI engine
Bore	$[mm]$	170	85
Stroke	$[mm]$	190	88
Conrod length	$[mm]$	816	145
Geometric compression ratio	$[-]$	12:1	16:1
Rated power	$[kW]$	500	-
Rated speed	$[rpm]$	1500	1500
compression ratio	$[-]$	12:1	15.3:1
Displacement volume	$[cm^3]$	4312.6	499
Number of cylinders	$[-]$	8	1

Iterative parameters

The values for the iterative parameters are influenced by the results of the model. These parameters, including n_c, n_e, R_6 and m_6 have to be corrected for each new iteration. In addition, since the data set didn't provide the start of combustion, this crank angle has been defined from the heat release rate. In this respect, the start of combustion occurs when 1% of total cumulative heat release has been released.

Calibration parameters

The model has to comply with the results mentioned in the HCCI paper by Pochet (see Table 5.2). This includes a matching indicated efficiency, maximum temperature and RCO. The initial equivalence ratio has also been given, however, this value can not be entirely trusted as stated by the paper. Mostly since this value has not taken into account the exhaust gas re-circulation (EGR). Because of this, the author introduced a new parameter; the energy contained in the cylinder per unit volume ($FuelMEP$), which is not influenced by the EGR. The latter can be calculated from Equation 5.1 in which both the in-cylinder volume (V_c) and the LHV_{fuel} are already known values.

$$FuelMEP = \frac{m_{fuel} \cdot LHV_{fuel}}{V_c} \tag{5.1}$$

The complexity of the model and the wide range of parameters that are influencing each other makes it difficult to get identical results with the HCCI paper. Therefore the $FuelMEP$ parameter will be mainly prioritised during the model calibration. A reason to choose this value over the others, is that the exact values for the indicated efficiency, maximum temperature and RCO are not explicitly mentioned for the given pressure crank angle diagram experiment. It has to be noted that both papers have performed multiple sets of experiments (ranging from experiment 1 to 6) with the same engine, however, with a slightly different range of initial conditions. From each of these experiments, only a small portion of the results were published. In this respect, the indicated efficiency values do correspond with the given hydrogen-ammonia ratio, but are not from the same experiment as the one with the pressure crank angle data (experiment 3 from the paper), since these values have not been published. This means that the actual indicated efficiency from experiment 3 could be slightly higher or lower.

Table 5.2: The calibrated results in comparison to the results from the HCCI paper by Pochet et al. [23] for various hydrogen concentrations.

		47H		44H		38H		31H	
	Unit	Model	Pochet	Model	Pochet	Model	Pochet	Model	Pochet
FuelMEP	$[bar]$	8.490	8.5	8.582	8.6	8.794	8.8	8.810	8.8
η_i	$[-]$	0.3146	0.315	0.3064	0.307	0.2948	0.295	0.2897	0.29
T_{max}	$[K]$	1480	1450	1464	1430	1412	1400	1389	1380
RCO	$[-]$	0.7293	0.73	0.7243	0.725	0.7219	0.722	0.7187	0.72

The calibration parameters include the crevice volume, x_{sg}, p_7, TDC synchronisation correction, T_{wall}, air excess ratio and the heat loss coefficient (C_2 mentioned in Equation 5.6) to match the results. The latter is based on the heat loss model developed by Hohenberg to determine the heat transfer coefficient, which can be found in Equation 5.7. The temperature and pressure sensitive coefficient depends on the engine in-cylinder dimensions and empirical data from heat loss experiments. Table 5.3 shows the noticeable effect of the calibration parameters (on the left hand side) on the $FuelMEP$, η_i, T_{max} and the RCO.

Table 5.3: The influences of the calibration parameters on the results.

	$FuelMEP$	η_i	T_{max}	RCO
↑ x_{sg}	↓			↑
↑ C_2 (Heat loss)	↑	↓		↑
↑ TDC correction		↓		↓
↑ T_{wall}				↓
↑ Air excess ratio (λ)	↑			↑
↑ $V_{Crevices}$	↑	↑	↑	

Parameters based on reasonable assumptions

However, there are still many missing parameters left that have to be estimated based on assumptions. The exact temperature for the cylinder wall, piston crown and cylinder head are not known and have been assumed to be 352, 470 and 475 $[K]$, respectively. For simplicity reasons, these temperatures have been kept constant during the combustion cycle, which is in reality not true. In order to obtain more accurate results, precise in-cylinder temperature measurements have to be conducted on the hydrogen-ammonia fueled engine.

5.3.3 Heat release model

An HRR analysis for the in-cylinder combustion provides valuable information about the rate of the the chemical energy that is being released. The combustion process inside the cylinder can be modeled as a single-zone or multi-zone. The benefit of using a single-zone model lies in its simplicity, however, it only provides information about the mean temperature per crank angle inside the combustion chamber. Without proper modeling of the local in-cylinder hot spot temperatures, an accurate estimation of the NOx formation rate cannot be fully determined. These temperature hot spots are regarded as the main stimulus of excessive NOx formation.

For single-zone models, the injection, evaporation, mixing and combustion rates inside the control volume are assumed to be equally the same [21]. However, this may give inaccurate results for ammonia combustion, since we already know that the combustion rate of ammonia (because of its low propagation speed) is significantly lower than that of diesel fuel. Hence, if we want to consider the differences in injection, evaporation, mixing, rate of combustion and include the crevice and quench layer zones, the layout has to be extended to a multi-zone model. Zhong et al. [90] investigated the differences between a single- and multi-zone model for HCCI combustion. According to his observations, the developed 9-zone model has shown better performances in simulating the heat release processes and in predicting the auto-ignition timing in contrast to a single-zone simulation.

In short, a multi-zone model is required to obtain heat release results that are close to the experiments. However, because of the short duration of the thesis, a single-zone model has been adopted, since it provides sufficient estimation of the thermodynamic process during combustion and the accuracy of the model is already affected by the incomplete data set and the list of assumptions. In this respect, having a more complex and fine tuned HRR model will not make any differences, if some of these input parameters for the HRR model such as the crevice volume and the quenching zone still have to be assumed because of the absence in experimental data.

Single zone heat release calculation

The heat release calculations are based on energy conservation by the first law of thermodynamic, which means that the total energy in the system remains constant. Here, the heat release rate is reconstructed with the help of the pressure trace and the physical principles ($i.e.$ first law of thermodynamics and the gas law) [91]. The total energy in the system consists of three components: the heat release from combustion, the heat losses ($\dot{Q}_{loss}$) and the indicated work ($\dot{W}$). Combining these components will lead to the gross apparent heat release rate (GAHRR) as shown in Equation 5.3. The net apparent heat release rate (NAHRR) can be directly calculated in from the temperature and pressure in the cylinder and ignores the heat losses in the cylinder as shown in Equation 5.2. On the other hand, the accuracy of the GAHRR heavily relies on the estimation model of the heat loss.

$$NAHRR = \dot{Q}_{comb} - \dot{Q}_{loss} + \dot{E}_f = m \cdot c_v \cdot \frac{dT}{dt} + p \cdot \frac{dV}{dt} \tag{5.2}$$

and

$$GAHRR = \dot{Q}_{comb} + \dot{E}_f = m \cdot c_v \cdot \frac{dT}{dt} + p \cdot \frac{dV}{dt} + \dot{Q}_{loss} \tag{5.3}$$

where, $\dot{E}_f$ is the energy of the fuel, m is the in-cylinder mass $[kg]$ and c_v is the specific heat $[kJ/kgK]$. $\dot{Q}_{comb}$ is the combustion heat rate, which is described as the time and temperature dependent heat input by the fuel:

$$\dot{Q}_{comb} = (u^{ref}_{comb} - \triangle u^{ref}_{comb}) \cdot \xi \tag{5.4}$$

Where, u^{ref}_{comb} is the reference value for the internal energy, $\triangle u^{ref}_{comb}$ is the temperature correction parameter and ξ is the fuel combustion rate.

Dividing the GAHRR by the energy contained in the hydrogen-ammonia mixture will lead to the combustion reaction rate (CRR):

$$CRR = \xi = \frac{m \cdot c_v \cdot \frac{dT}{dt} + p \cdot \frac{dV}{dt} + \dot{Q}_{loss}}{u_{comb} + e_f} \tag{5.5}$$

The integration of Equation 5.5 results in the reaction coordinate (RCO), which is one of the key parameters for the engine calibration. A concise overview of the mass balance, in-cylinder gas and the fuel properties can be found in **Appendix B3**. The papers from Ding et al.[91] and Sapra et al. [32] can be consulted for a more in-detailed explanation of the used HRR model.

5.3.4 Heat loss model

Because of the strong temperature influence on the auto-ignition process in HCCI engines, over- or under-prediction of the heat transfer loss can already have a major impact on the start of combustion and the shape of the pressure trace. Empirical heat loss models including the ones from Annand, Woschni, Hohenberg, Chang, Hensel and Bargende are available for SI and CI engines, however, not much is known about HCCI combustion. Due to the unfamiliar combustion process in HCCI engines, it is expected that the heat transfer models developed for SI and CI engines are not applicable for HCCI combustion. According to the HCCI experiments performed by Broekaert et al. [92], none of these existing heat loss models can provide accurate results without calibrating the scaling coefficient first for which detailed heat flux measurements from experiments are needed. In this respect, the scaling coefficients have to be adjusted to highest measured heat flux value during base operation.

In order to achieve reasonable Woschni heat loss results, the coefficients $C1$ and $C2$ have to be calibrated to match the maximum heat flux during motored operation and fired operation, respectively. Broekaert et al. [92] observed a significant decrease in $C2$ by a factor of 11 when using HCCI instead of SI combustion. In addition, he also emphasised that the standard Woschni model becomes useless in case the model coefficient a and b used for the compression and expansion phase are not modified for HCCI combustion, even when the scaling coefficients are correctly calibrated. However, existing heat loss models covering HCCI combustion are still overestimating the total heat loss by 14 to 68% for the best and worst model, respectively [92]. The engine's heat loss model has not been fully optimised for hydrogen-ammonia HCCI combustion, because of the missing calibration coefficients. In future works, implementing an accurate heat loss model in the in-cylinder model will contribute to more realistic HCCI combustion results.

Heat loss calculations

The modified Woschni heat transfer coefficient for HCCI combustion can be written as follows:

$$\alpha_{W1}(t) = C_2 \cdot L(t)^{-(1-m)} \cdot P(t)^m \cdot T(t)^{-((1+q)\cdot m-p)} \cdot (C_3 \cdot c_m + \frac{C_4}{6} \cdot \frac{p-p_o}{p_1} \frac{V_s}{V_1} \cdot T_1)^m. \tag{5.6}$$

The Hohenberg heat transfer coefficient can be written as follows [93]:

$$\alpha_H(t) = C_2 \cdot V(t)^{-0.06} \cdot P(t)^{0.8} \cdot T(t)^{-0.4} \cdot (c_m + b)^{0.8}. \tag{5.7}$$

The coefficient C_2 in the heat loss model is adjusted to satisfy the energy balance at each operating point and hydrogen-ammonia ratio. In the case of the Hohenberg model, the C_2 value ranges from 112.5 to 125. This is slightly lower than the mean value of 130 which had been experimentally determined by Hohenberg himself on various engines that are ranging from 128 $[mm]$ to 97 $[mm]$ bore [94]. The b parameter in the Hohenberg equation addresses the combustion turbulence and the radiation losses inside the cylinder. This constant is also derived from measurements for which Hohenberg found a value equal to 1.4. In the case of the Woschni model, the m, q and p parameters have been chosen to be 0.79, 0.62 and 0.75 respectively. It can be noted that the HCCI Woschni model is based on the time dependent stroke (L_s) as the length scale, while the typical Woschni coefficient for conventional diesel engines uses the constant bore diameter. From the experiments by Chang et al. [95], the Hohenberg coefficient showed the closest similarity with the measured heat flux trace in case of HCCI combustion and will therefore also be used in this in-cylinder model. The Woschni heat transfer model (Equation 5.8) for conventional diesel engines has also been investigated to observe to what extend the use of an SI heat loss model will impact the HCCI in-cylinder model.

$$\alpha_{W2}(t) = C_2 \cdot D_b^{-(1-m)} \cdot P(t)^m \cdot T(t)^{-((1+q)\cdot m-p)} \cdot (C_3 \cdot c_m + C_4 \cdot \frac{p-p_o}{p_1}\frac{V_s}{V_1} \cdot T_1)^m \tag{5.8}$$

Table 5.4: The results when applying different heat loss models.

	Unit	Paper	Woschni	Hohenberg	Hohenberg + V_{crev}
$FuelMEP$	$[bar]$	8.5	8.500	8.490	8.484
η_i	$[-]$	0.315	0.3145	0.3146	0.4162
T_{max}	$[K]$	1450	1479	1480	1722
RCO	$[-]$	0.73	0.7294	0.7304	0.7268

As shown in Figure 5.4a, the implementation of the crevice loss in the model resulted in a less downwards RCO curve at the start of combustion. However, after calibration the maximum in-cylinder temperature and η_i still showed noticeably higher values in comparison to the results presented in the paper. The reason could presumably be traced to the huge list of made assumptions that may negatively influence the outcome of the crevice model. However, the crevice volume and quenching do become more pronounced at higher ammonia fractions and are both also greatly influencing the combustion efficiency. From the observations of Pochet et al. [2], the crevice volume and a quenching distance of 0.1 $[mm]$ can already equal 7% and 5% of the total TDC volume, respectively. Hence, the addition of the crevice loss will lead to a more realistic HCCI ammonia combustion model. However, the present heat loss models without the crevice loss implementation have shown a greater fit after the calibration and will therefore be used to answer the thesis objectives.

The value of the cumulative heat loss is constrained by the known calibration results including the injected fuel ($FuelMEP$), indicated efficiency and combustion efficiency. This explains the almost identical RCO, temperature slope and energy losses (as shown in Figure 5.5b), when comparing the results of both heat loss models. While the enclosed area of the heat transfer coefficients are similar, the shape of the SI Woschni correlation shows a higher peak value (Figure 5.5a). As a consequence, the latter has shown a lower maximum temperature and a slightly retarded start of combustion (0.2 $[CAD]$) in contrast to the HCCI Hohenberg correlation.

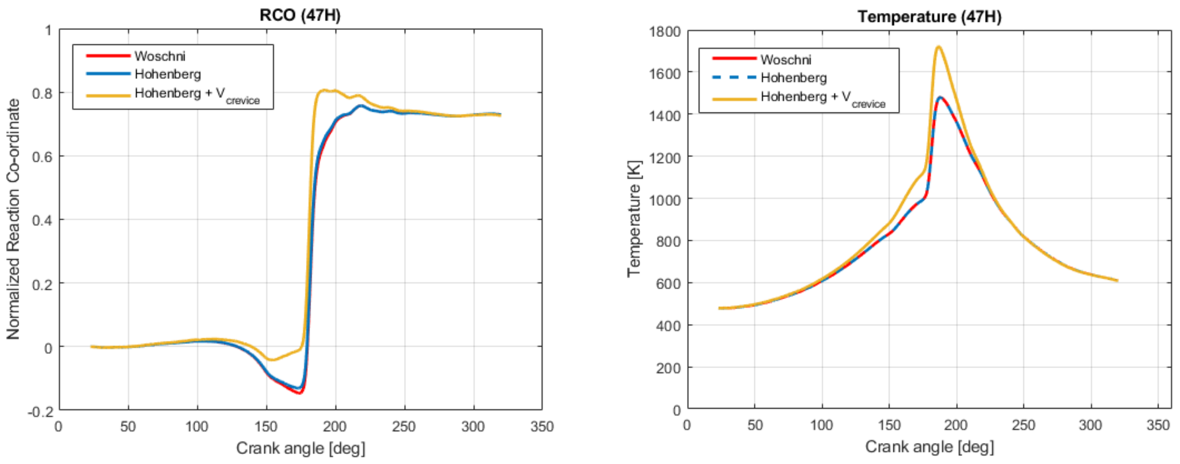

(a) (b)

Figure 5.4: (a) RCO as function of the crank angle for the Woschni and Hohenberg heat loss model. The Woschni model that includes the crevice heat loss has also been included in the Figure and (b) shows the temperature as function of the crank angle.

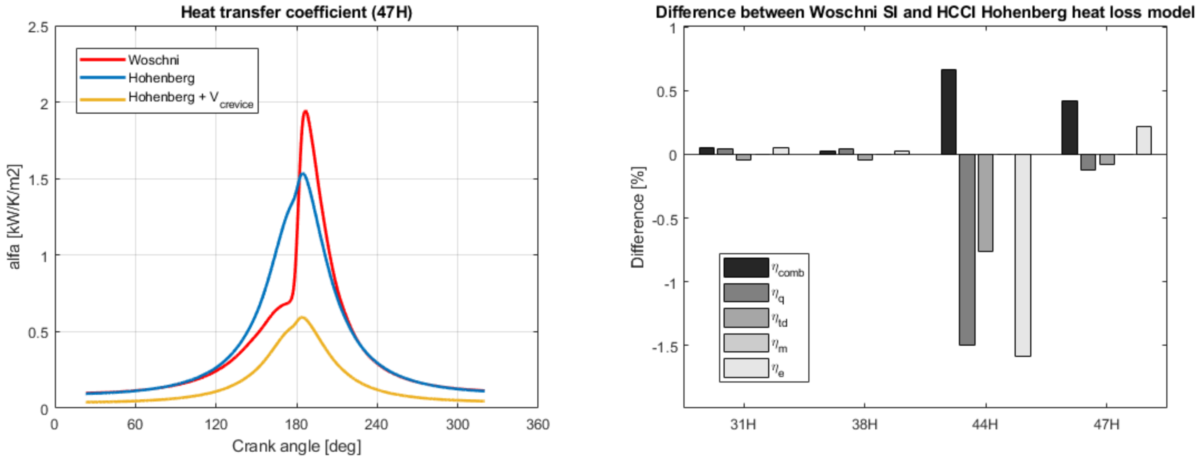

(a) (b)

Figure 5.5: (a) The heat transfer coefficient α as function of the crank angle for various heat loss models. (b) Differences in energy losses between Woschni SI and Hohenberg heat loss results for a variety of volumetric hydrogen concentrations. The difference can be interpreted as the relative change between the x_{ref} reference value (Woschni SI) and the x value (Hohenberg) using Difference = $\frac{x_{ref}-x}{x_{ref}} \cdot 100$.

It can be concluded that the SI Woschni model has shown to be inadequate for HCCI engines. Even when the cumulative heat loss for both models were identical, the difference in shape between the heat transfer coefficient (α) still had a major impact on the ignition timing of the engine. Especially for HCCI combustion, the auto-ignition and combustion rates are closely coupled to the in-cylinder thermal conditions.

Table 5.5: Effects of the heat loss models on the combustion characteristics (47H).

	Unit	Woschni	Hohenberg	Wosch + V_{crev}
CA10	$[CAD]$	180.70	180.40	178.30
CA50	$[CAD]$	183.69	183.29	180.49
CA90	$[CAD]$	194.09	193.99	190.60

5.4 In-cylinder results

As can be seen in the steep *RCO* curve (Figure 5.6a), the combustion event happens at a rapid pace. This often results in pressure rise rates that can exceed 10 bar/ms, which is commonly the material limit of the rings on the piston engine [96]. A blend of two fuels that have different auto-ignition properties is therefore highly recommended for HCCI combustion. In this respect, one fuel would burn earlier than the other which will result in a more spread out combustion duration.

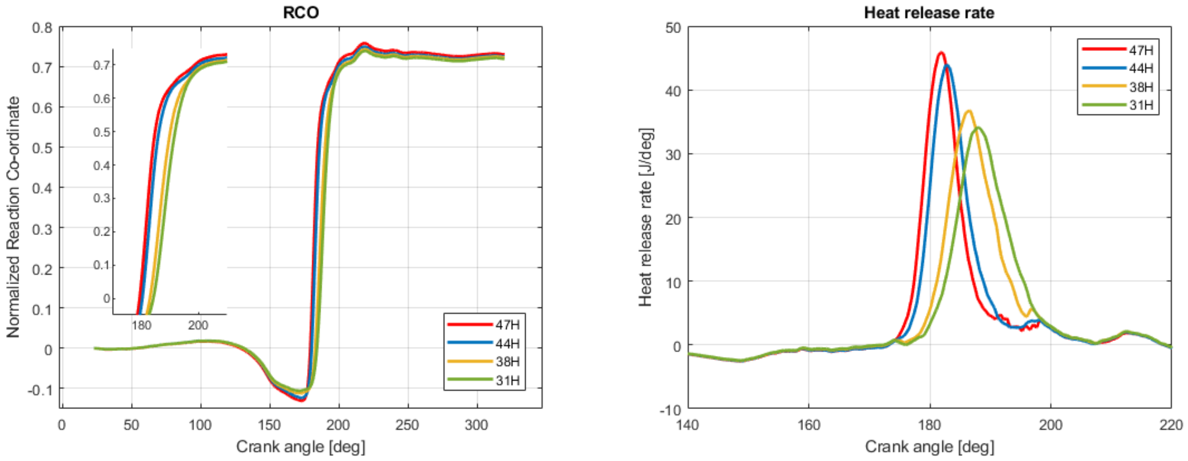

(a)

(b)

Figure 5.6: (a) *RCO* slope and (b) heat release rate curve for a range of hydrogen-ammonia fractions.

According to the model outputs, increasing the ammonia fraction will result in a more spread out combustion event and also a noticeable retardation and decrease of the HRR and temperature peaks. Retardation of the start of combustion (CA10) has also been observed at increased ammonia fractions, in which CA10 starts at 180.69 $[CAD]$ for 47% hydrogen and gradually increases to 186.19 $[CAD]$ at 31% hydrogen.

As mentioned earlier, it cannot be said how accurately the in-cylinder model is able to simulate the combustion characteristics from the HCCI paper. While important parameters such as the η_i, η_{comb}, m_{bf} and T_{max} are closely calibrated, there can still be deviations in the combustion process (*i.e.* shape of the *RCO* and HRR model). This uncertainty can also be explained when comparing the SI Woschni and HCCI Hohenberg heat loss models. Here, both have shown the same cumulative heat loss per mg injected fuel (end result), but the shape of the heat transfer coefficients (Figure 5.5a) are different (**Section 5.3.4**). As previously mentioned in **Section 5.3.2**, the value for η_i has been acquired from the same HCCI paper, but from a different experiment (*i.e.* slight difference in equivalence ratio and a fixed CA50 calibration). It has been observed that a decrease in the indicated efficiency minimises the drop of the *RCO* during the compression phase. The magnitude of the drop in the *RCO* between 140 $[CAD]$ and SOC can be explained by the last discussed aspects and the omission of the crevice losses (**Section 5.3.4**).

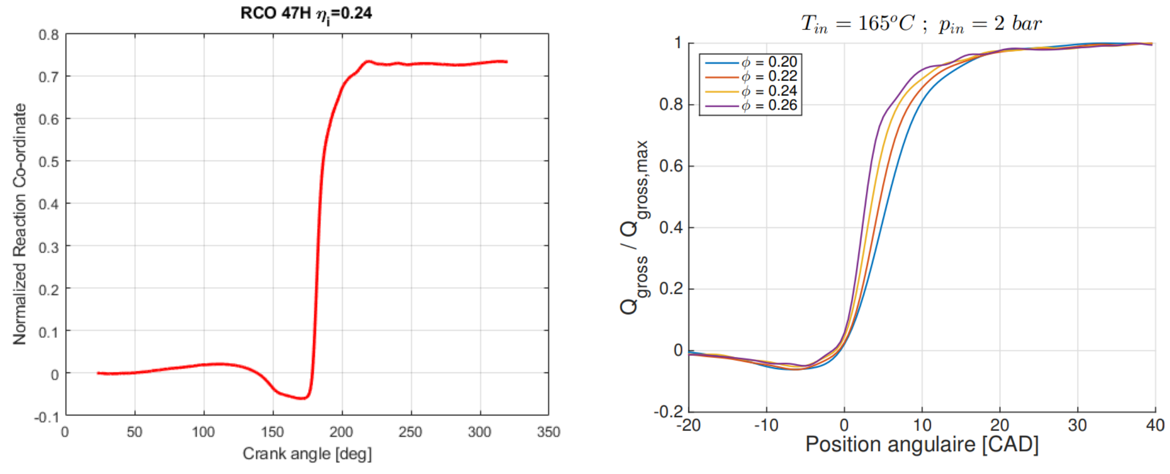

(a) (b)

Figure 5.7: (a) *RCO* slope in case the indicated efficiency has been decreased from 0.314 to 0.240. (b) Normalised cumulative heat release graph for NG HCCI combustion [22].

The drop in the RCO curve during the compression stroke may be caused by the high inlet temperature. As can be seen in Figure B.7a, the temperatures during the compression stroke are exceeding the fixed wall temperature of 352 [K] from the heat loss model. As a result, we see a dip in the RCO curve, which may be the result from the heat loss to the cooling water. The master thesis concerning NG HCCI combustion by Boveroux et al. [22] (under guidance of Pochet, the author of the ammonia HCCI paper) also observed a large negative value before reaching SOC (as depicted in Figure 5.7b).

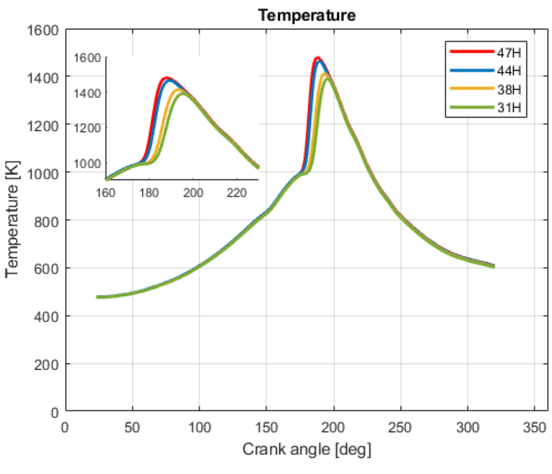

(a)

Figure 5.8: (a) Temperature slope for a range of hydrogen-ammonia fuel blends.

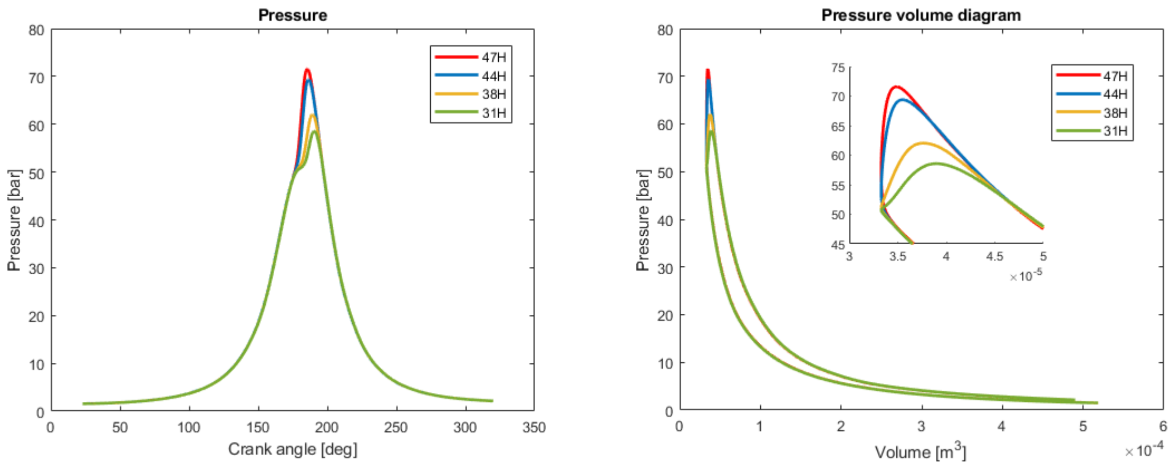

(a) (b)

Figure 5.9: (a) Pressure crank angle and (b) pressure volume diagram for different hydrogen-ammonia blends.

5.5 Reflection

As mentioned in **Section 5.3.2**, the paper by Pochet et al. [23] performed multiple sets of experiments (ranging from experiment 1 to 6) with the same engine, but with different operational conditions. From these experiments, only a small portion of the results were published. In this respect, the indicated efficiency values do correspond with the given hydrogen-ammonia ratio, but are not from the same experiment as were we used the pressure crank angle data from (experiment 3 from the paper), since these values have not been published. This means that the actual indicated efficiency from experiment 3 could be slightly higher or lower.

To get a better understanding how accurately the in-cylinder model is able to predict the combustion characteristics and to put the results in perspective, the in-cylinder results are compared with the 39H fuel blend result from experiment 2 by Pochet [23]. Experiment 2 (39H data) has a slightly higher intake temperature of 479 $[K]$ in comparison to the temperature of 474 $[K]$ used in the in-cylinder model, which explains the earlier start and finish of the combustion as can be seen in Figure 5.10. From the graph, it can be observed that the RCO slope CA10 to CA50 are almost identical, which may give an indication that the results from the in-cylinder model are not that far off.

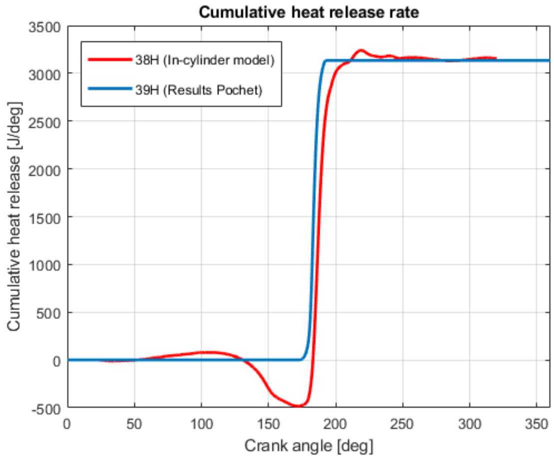

Figure 5.10: Comparison between the cumulative heat release rate from the in-cylinder model (38H) and the results (39H) from Pochet et al. [23]. Note: the heat release rate between the crank angles IVC and 174 $[CAD]$ have been set to zero, since we do not know the exact values. In Figure 5.7b from **Section 5.3.4**, Boveraux et al. [22] (under guidance of Pochet) observed a negative cumulative heat release rate for NG HCCI combustion between IVC and SOC. Hence, for the 39H data, we may also expect a slight negative heat release during the compression stroke.

5.6 Conclusions

The in-cylinder model has been developed with the notion to provide an in-detail simulation of the in-cylinder HCCI combustion of hydrogen-ammonia fuel. The input parameters and pressure traces from Pochet et al. [23] have been used to calibrate the model to obtain equivalent output results. In this respect, the model has shown the same indicated efficiency, injected fuel mass, combustion efficiency and in-cylinder temperatures that are reasonably close to the measured ones. However, as mentioned earlier, many assumptions have been made during the development phase, which will affect the accuracy and the trustworthiness of the model. With the current input data, it is difficult to say how accurately the model is able to predict the hydrogen-ammonia combustion characteristic. Therefore, the main focus of the model has been shifted more towards identifying different trends when adjusting the hydrogen-ammonia ratio. In this respect, the combustion characteristics from four hydrogen fractions have been modelled to investigate the optimal hydrogen-ammonia ratio during HCCI combustion.

The experiments conducted by Pochet et al [2] show that higher ammonia fractions do result in higher concentrations of ammonia in the exhaust. It also shows that the combustion efficiency of ammonia is primarily a function of the maximum in-cylinder temperature, rather than the hydrogen-ammonia ratio as can be seen in Figure 5.11. However, higher ammonia fractions are indirectly responsible for the combustion efficiency, since high maximum temperatures are more difficult to be achieved at higher ammonia ratios as can be seen in Figure B.7a. High ammonia fractions on the other hand will broaden the controllability and also enable the engine to run on higher loads. Therefore the optimal ammonia-hydrogen ratio has to be preferably as high as possible, keeping the combustion event spread out, while maintaining a maximum temperature above 1400 $[K]$ to keep the unburned ammonia ratio to a minimal. In addition, a lean inlet mixture is preferred to maximise the fuel consumption efficiency and also to mitigate the fuel losses in terms of leakage at the cost of a relatively lower maximum power output [97].

The low fuel burnt fraction as shown in Figure 5.6a is still a major issue that has to be solved, since

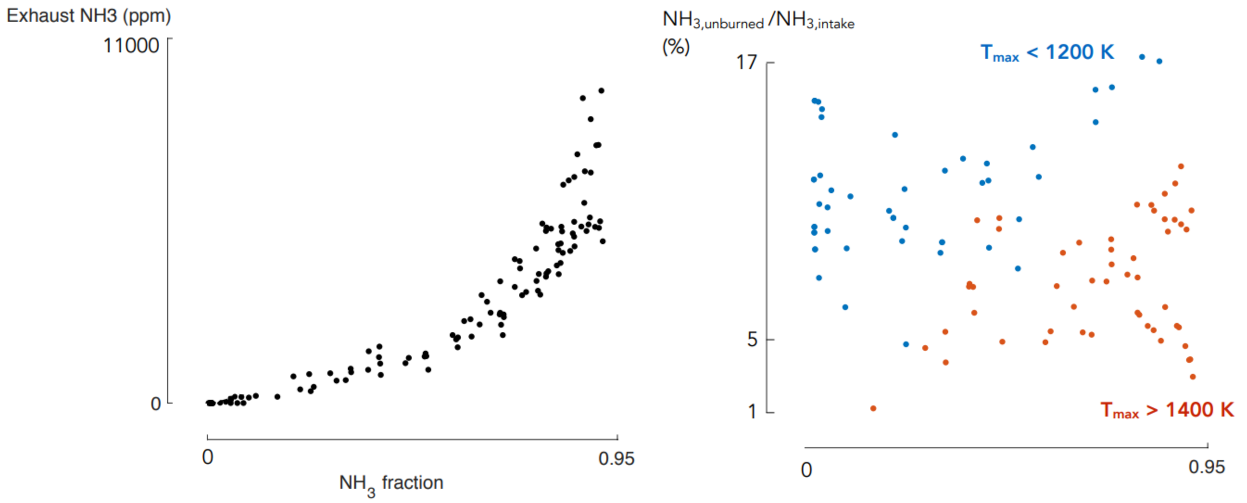

Figure 5.11: (Left) exhaust ammonia and (right) unburned ammonia ratio as functions of the ammonia fraction from ammonia hydrogen HCCI experiment conducted by Pochet et al. [2].

ammonia is harmful to the environment. Ideally, we want the same amount of unburned ammonia and produced *NOx* particles in the exhaust that will neutralise each other inside the SCR. This is further elaborated in **Section 8.3**. Another proposal is to use EGR, in which a portion of the exhaust gas has to go through an ammonia cracking catalyst (mentioned in **Section 2.3**) to increase the hydrogen content before recirculating back to the inlet. In this respect, less hydrogen is needed from the SOFC's anode-off gas. In addition, exhaust gas re-circulation (discussed in **Section 7.3.4**) could play a role in satisfying the inlet temperature requirement of 473 $[K]$. The relatively cold air from the turbocharger could then be mixed with a portion of the exhaust gas that has a temperature expected to be slightly above 600 $[K]$.

At last, the author of the HCCI paper [23] emphasised that the test engine was not optimised for HCCI combustion, which may explains the poor combustion efficiencies. Pochet et al [2] is recently conducting ammonia experiments on a new test engine that has a significantly higher compression ratio (22:1 vs 16:1). His results are not published yet, but we can expect better engine performances and significantly lower fractions of unburned ammonia.

The conclusions drawn from the in-cylinder model design are as follows:

- The cumulative heat loss is constrained by the $FuelMEP$, η_i and the combustion efficiency. Because of this, both the SI Woschni and HCCI Hohenberg heat loss models have shown almost similar engine performances after the calibration.
- However, since both heat loss models do have a different heat transfer coefficient shape, the HCCI Hohenberg coefficient shows an earlier CA10 (180.69 vs 180.99 $[CAD]$) and a slight higher T_{max} (1480 vs 1479 K). Thus, the application of an SI heat loss model to simulate HCCI combustion will lead to a noticeable difference in combustion characteristics.
- Crevice heat losses have been neglected in the model design, since the addition of the latter made the model unable to obtain the identical results as presented in the paper. For future models, both the crevice and quenching losses have to be considered to obtain a more realistic ammonia HCCI combustion representation.

In addition, several hydrogen-ammonia fractions have been modeled and observed. The trends in combustion characteristics when lowering the hydrogen content are listed below:

- Decreasing the hydrogen content from 47H to 31H showed a noticeable retardation in the CA10 (180.69 versus 186.19 [CAD]). In addition, the indicated power output also drops with 4.5% (from 1.66 to 1.58 [kW]). The only slight decrease in power can be owed to the increase in injected fuel at higher ammonia ratios, since the AFR of ammonia is much smaller than for pure hydrogen (34.32:1 vs 6.06:1 mentioned in **Section 3.6**).
- Furthermore, the combustion efficiency reduced slightly, when decreasing the hydrogen content. At 31H, the maximum in-cylinder temperature falls below 1400 [K], which indicates that further decreasing the hydrogen content will negatively impact the combustion efficiency.
- The hydrogen fraction highly influences the maximum peak of the heat release rate. In this respect, decreasing the hydrogen ratio will result in a lower and more evenly spread out HRR curve. This is beneficial for HCCI engines, since large peaks in the HRR induce large stress on the engine materials.

In conclusion, hydrogen-ammonia combustion inside HCCI engines is a novel concept that still requires lots of real scale experiments to find the optimal engine geometry and hydrogen concentration. More recently, Lhuillier et al. (March 2020) [98] published a paper concerning hydrogen-ammonia combustion inside an SI engine. While his experiments have shown high indicated efficiencies that are exceeding 0.35 for 40% vol hydrogen at stoichiometric mixture, the power density has been observed to be considerably lower than that of the HCCI engine. In this respect, the $IMEP$ and $FuelMEP$ of the 38H HCCI engine are, respectively, a factor 2.9 (0.85 [bar] vs 2.573 [bar]) and 3.7 (2.4 [bar] vs 8.8 [bar]) greater than the values from the SI paper [98]. However, the hydrogen-ammonia HCCI test engine is still lacking in power density, when compared to fossil fueled diesel engines. Conventional natural aspiring diesel engines are typically operating at MEP values ranging from 5 [bar] to 6.2 [bar], which is more than doubled in contrast to the HCCI engine. An overview of the results for various hydrogen-ammonia ratios can be found in Table 5.6.

Table 5.6: Overview of the in-cylinder modelling results for a range of hydrogen-ammonia blends.

	Unit	47H	44H	38H	31H
CA10	[CAD]	180.40	181.49	184.39	185.79
CA50	[CAD]	183.29	184.49	188.20	189.80
CA90	[CAD]	193.99	195.80	197.50	197.90
IMEP	[bar]	2.651	2.610	2.573	2.532
Indicated power output	[kW]	1.655	1.610	1.606	1.581
LHV fuel	[MJ/kg]	27.125	26.144	24.422	22.737
fuel burnt mass	[mg]	11.400	11.871	12.980	13.907
Injected fuel mass	[mg]	15.631	16.390	17.980	19.350
RCO	[$-$]	0.7293	0.7243	0.7219	0.7187
Maximum temperature	[K]	1480	1464	1412	1387
Indicated efficiency	[$-$]	0.3146	0.3064	0.2948	0.2897

Chapter 6

Engine scaling

6.1 Chapter overview

Experimental research concerning in-cylinder hydrogen-ammonia HCCI combustion characteristics are scarce. The latter is especially true for marine sized engines since there are no large scale experiments available in the literature. As a result, the in-cylinder model in **Chapter 5** has been developed using the data from an automotive sized engine. From the model, we see that the indicated power output is limited to 1.655 $[kW]$ for a 47H fuel blend. However, the power output for marine sized engines are multiple times higher. In this chapter the geometry of the engine used in the in-cylinder model will be scaled to a truck sized engine with the help of the scaling laws that are available in the literature.

In **Section 6.2**, the methodology of the engine scaling will be briefly discussed. After that, the Speed Law, Pressure Law and the Lift-off Law will be further elaborated in **Section 6.3**. The assumptions and simplifications will be discussed in **Section 6.4**. Since the surface area to the displacement volume ratio is higher for smaller engines, relatively lower heat losses can be expected for the scaled engine. The differences in relative heat losses become more pronounced when we have to scale the automotive engine to a truck sized engine. Hence, a heat loss calibration mentioned in **Section 6.5** to **6.7** is necessary to obtain matching cumulative heat losses per mg inject fuel between both engines. The calibration is crucial since we made the assumption of similar combustion characteristics.

6.2 Introduction

TNO is developing a modular 1-cylinder setup for truck and inland shipping applications that enables the test engine to have a wide range of customization options. The baseline geometric (*i.e.* stroke, bore and cylinder head) is largely based on the DAF MX 11 engine in which the maximum stroke length is set to 170 $[mm]$. The main research focus of this 1-cylinder setup is to get a better understanding of the combustion concepts when using different fuels and fuel blends. Ammonia is in this respect an interesting carbon free alternative in which the concept has proven to work on small scaled internal combustion engines. Based on the engine dimensions and specifications, the design power output of the 170 $[mm]$ stroke test engine has a target design power output of 50 $[kW]$ when fueled with fossil fuel. This will most likely be lower for hydrogen-ammonia fuel blends because of the low volumetric fuel density of hydrogen, hence less fuel can be injected into the cylinder.

As previously stated in **Chapter 3**, experiments on hydrogen-ammonia fueled HCCI engines are scarce and have mainly been based on automotive sized engines. In this Chapter, the car sized HCCI engine setup (88 $[mm]$ stroke) that has been used in the in-cylinder model (**Chapter 5**) will be enlarged to a truck sized 170 $[mm]$ stroke variant with the use of existing engine scaling laws. The emphasis in this study does not lie in the accuracy of the scaling results, since there is no experimental data to validate the results from the scaling output. Here, the modelling results may give a first impression what we can expect the engine power output, in-cylinder process, fuel mass flow and engine performances to be for a truck sized hydrogen-ammonia fueled HCCI engine. The scaling model uses the in-cylinder model from **Chapter 5** as the baseline for the engine modelling. Here, the engine dimensions (**Section 6.3**) and the heat losses (**Section 6.5**) have been proportionally scaled based on the scaling factor L[1].

Future large-scale experiments by TNO on ammonia fuel will unveil the real combustion characteristics in a 170 $[mm]$ stroke engine. In a later stage, TNO Helmond might also look into the hydrogen-ammonia fueled SOFC-ICE combination as mentioned in **Section 1.1.4**. This concept could potentially enhance the overall efficiency output of the engine system on-board of ammonia fueled ships.

6.2.1 Introduction scaling laws

Based on relatively simple criteria, the scaling laws have been observed to be the most effective when two conditions are met. Firstly, the geometric similarity have to be maximised, so that both engines have similar boundary conditions. In this respect, the bore, stroke, piston bowl shape, squish height and the resulting compression ratio have to be relatively scaled for both engines. Secondly, matching combustion characteristics are needed to achieve similarity in engine performances and emissions. This means, the same initial conditions (*i.e.* inlet pressure and temperature) and initial flow conditions such as the swirl ratio for both engines.

Three scaling laws have been proposed, the speed law (S Law) by Chikashisa et al. [3], lift-off law (L Law) by Stager et al. [4] and the Pressure law (P Law) proposed by Bergin et al. [5]. However, in case of HCCI combustion, most of the scaling parameters such as the spray penetration length, mixing spray, fuel spray distribution, injection timing and many more become irrelevant and have to be neglected in the modelling process. However, these scaling parameters are crucial for conventional diesel engines, because of the limited mixing time (diffusion combustion) which is not the case for premixed combustion strategies. This chapter also includes L^2 engine speed scaling, which uses the same assumptions and simplifications mentioned in **Section 6.4**. Specifically speaking, this engine speed scaling is not a scaling law, since L^2 engine speed scaling will not result in similar combustion phasing with the baseline engine [99]. In this respect, L^2 scaling will only lead to matching heat transfer losses per mg injected fuel between the baseline and the scaled engine. Hence, L^2 engine speed scaling has only been evaluated in the heat loss scaling in **Section 6.5**.

In addition, most of the proposed scaling laws have been experimentally proven to work well for small differences in bore ratios [100], but have not yet been accurately tested for automotive engines that are scaled into marine sized engines. In this respect, the output values of this scaled engine model cannot be verified. The proposed scaling laws have their own advantages and weaknesses and have to be selected according to the preferred requirements. The scaling parameters for the three different methods can be found in Table 6.1.

6.3 Speed, Pressure and Lift-off scaling laws

For all three scaling laws, the scaling factor L is based on the size of the engine bore (L = $\frac{D_{B,1}}{D_{B,2}}$ = 1.93). As a consequence, the same relative dimensions at TDC can be expected. Since λ (3.4 for 47H) has been kept constant for both engines, the same relative scaling of m_f and m_{air} and equivalence ratio can be expected.

---

[1] L is the scaling factor based on the size of the engine bore ($L = \frac{D_{B,1}}{D_{B,2}}$) mentioned in **Section 6.3**.

Table 6.1: Overview of the geometric scaling results for the three scaling laws in which Sf shows the proportion of the scaling factor.

	Unit	Engine	S Law	Sf	L Law	Sf	P Law	Sf
Bore	$[mm]$	85	164.2	L^1	164.2	L^1	164.2	L^1
Stroke	$[mm]$	88	170	L^1	170	L^1	170	L^1
Stroke bore ratio	$[-]$	1.035	1.035	L^0	1.035	L^0	1.035	L^0
Compression ratio	$[-]$	16	16	L^0	16	L^0	16	L^0
Connecting rod	$[mm]$	145	280.1	L^1	280.1	L^1	280.1	L^1
TDC volume	$[cm^3]$	33.29	240.00	L^3	240.00	L^3	240.00	L^3
Displacement	$[cm^3]$	499.36	3600.05	L^3	3600.05	L^3	3600.05	L^3
Surface volume ratio	$[-]$	0.5842	0.3024	L^{-1}	0.3024	L^{-1}	0.3024	L^{-1}
IVC (BTDC)	$[CAD]$	157	157	L^0	157	L^0	157	L^0
EVO (BBDC)	$[CAD]$	20.1	20.1	L^0	20.1	L^0	20.1	L^0
Engine speed	$[rpm]$	1500	1500	L^0	776.47	L^{-1}	1204.4	$L^{-\frac{1}{3}}$

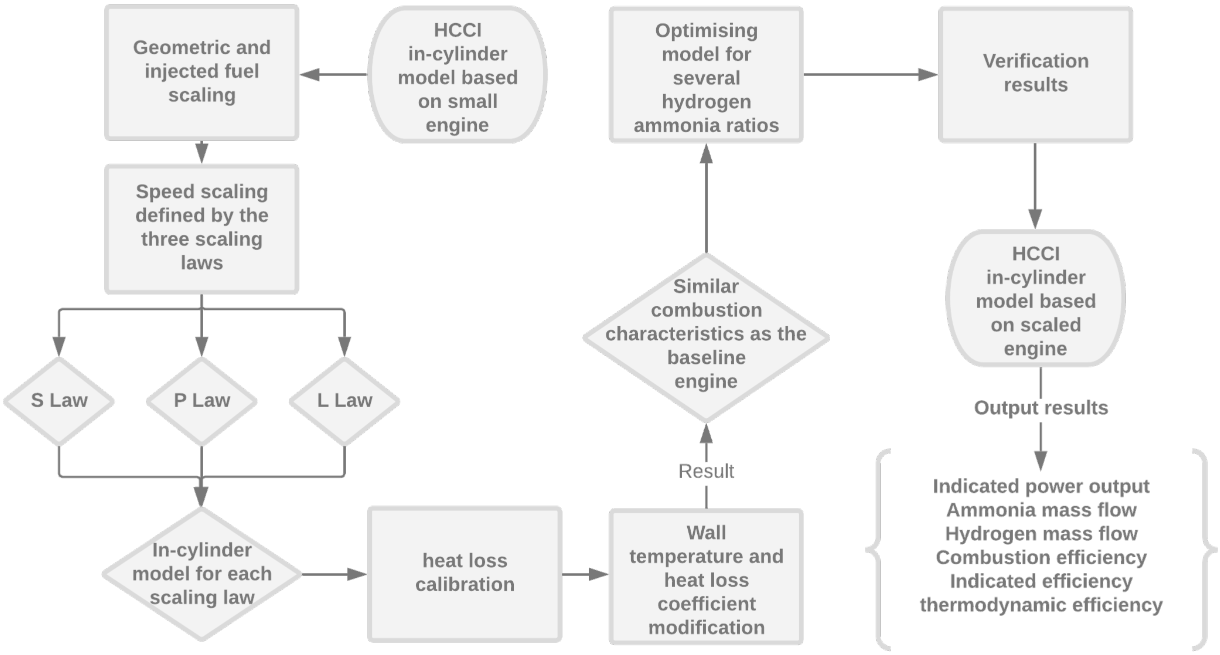

Figure 6.1: Flowchart overview of the steps taken in the creation of the scaled HCCI engine model.

First, the Pressure Law in which the engine speed is scaled to $L^{-\frac{1}{3}}$ has shown matching combustion characteristics and engine performance scaling at the cost of a larger difference in emissions [101]. However, this scaling law may not be useful for HCCI combustion, since the engine speed is scaled in such a way to achieve the same injection duration on a crank angle basis. The latter is beneficial for conventional diesel engines to obtain the same pressure crank angle distribution and specific indicated work $(\frac{W_i}{m_f+m_{air}})$ that are scale independent [25].

Chuahy et al. [99] suggested to modify both engine models accordingly to achieve equivalent brake thermal efficiencies (BTE). In order to do this, both the combustion characteristics and heat transfer

& friction losses have to be equally scaled. However, due to the different characteristics of the latter two losses, both cannot be matched simultaneously with the engine bore [99]. The engine speed for the scaled engine has to be scaled to L^2 to obtain matching heat transfer losses per mg injected fuel between the scaled and baseline engine [99]. The Lift-off scaling (L Law) on the other hand scales the friction mean effective pressure (FMEP) better, since the mean piston speed (c_m) has been kept constant. However, L Law scaling might not be the best method for HCCI combustion, since the latter has been primarily based to keep the flame lift-off length scaled [25].

The S Law (equal time scaling) is often restricted by the design limitation (structural strength) of the engine. This is due to large inertia forces as a result of the increased piston speed (c_m). However, because of the same engine speed, the combustion phasing of both engines can be matched, which enables the combustion process to happen at the same crank angle time basis. The latter is important for HCCI and RCCI engines since both combustion characteristics are dictated by the chemical reaction rates [99]. Small changes can already have large consequences on the start of ignition.

The scaling models are all based on the assumption of the same thermodynamic conditions. However, in reality, the smaller engine will have a slightly higher pressure peak because of the relatively higher heat transfer losses for the same HRR distribution. As can be seen in Table 6.1, the ratio surface area to the displacement volume is greater for the smaller engine, which results in relatively larger convection heat loss through the cylinder walls. Finding two engines that share exactly the same relative geometric dimensions can be difficult. Especially since automotive engines have a different geometry layout in comparison to marine sized engine. Small variations of the piston bowl shape and swirl ratio can easily affect the flow field inside the cylinder, which can already lead to a noticeably different combustion characteristic between both engines.

Shi et al. [25] emphasised the importance of matching the thermodynamic conditions at TDC for both engines that is required to reproduce almost the same combustion characteristics. These initial conditions at the start of combustion cannot be easily matched in case the stroke to bore ratio and connecting rod length are not proportionally scaled. Marine engines typically have larger stroke to bore ratios in contrast to automotive engines, since they are running at lower engine speeds. The baseline engine for the model scaling has a stroke to bore ratio equal to 1.035. This ratio however, has to stay fixed during the engine scaling, otherwise equivalent initial conditions and pressure traces between both engines cannot be maintained. Such design constraints will result in a less optimal brake power configuration for the scaled engine. However, ignoring these constraints will lead to a noticeably less accurate representation of hydrogen-ammonia HCCI combustion. Therefore the geometrical similarities between the baseline and scaled engine have been maximised as much as possible. A list of suggestions to enhance the power output of the scaled engine can be found in **Section 7.3**. All in all, the effectiveness of the scaling laws decreases with the increase in the scaling factor L. This is caused by the cylinder's surface to volume ratio that becomes smaller when enlarging the engine, which will result in a reduction of its relative heat loss. For the scaling factor of 1.93, large differences in heat loss characteristics have been observed, which negatively impacted the accuracy of the scaled engine model. Hence, it is not recommended to further enlarge the scaled model engine's stroke length of 170 $[mm]$ to an even larger marine sized engine, since the combustion characteristics between both engines will otherwise be too far apart.

6.4 Assumptions and simplifications L Law, S Law and P Law

1. The engine has to be scaled accordingly to ensure similar relative geometric dimensions. This also means a scaled version of the piston bowl shape to maintain the same swirl ratio. The scaling factor for each geometric engine component can be found in Table 6.1.
2. Similar inlet valve closing (IVC) and exhaust valve opening (EVO) timings are required to maintain

the same effective compression ratio. Keeping the same CR for the scaled engine is necessary to match the thermal efficiency between both engines. In addition, increasing the CR will also cause higher temperatures and peak pressures for a given initial condition.

3. The scaled engine model uses the same initial conditions at (IVC) and pressure crank angle distribution for all scaling laws. However, for HCCI engines, changes in the engine speed will likely impact the pressure distribution. In this respect, the slower engine speed from the L Law is expected to cause an earlier start of combustion that will lead to a different pressure distribution in comparison to the baseline engine.

6.5 Heat loss scaling

According to the single value principle, the amount of heat released should be proportional to the in-cylinder volume (L^3), while the heat transfer is proportional to the surface area (L^2) [101]. Smaller engines have in contrast to larger engines relatively greater surface to volume ratios as can be seen in Table 6.1. As a result, smaller engines are subjected to proportionally larger convective heat transfer losses, which translates to a lower pressure rise rate and peak cylinder pressure. Because of this, the emissions, in-cylinder temperature and pressure traces between both engines cannot be fully scaled without additional heat loss calibration. The latter is important since we do not have the pressure crank angle distribution for the larger engine and as mentioned before, the pressure traces of the scaled engine are close to the baseline engine when scaled properly. Hence, if the scaling law requirements including similar relative geometric dimensions are met and when the combustion characteristics are almost identical, the same pressure data can be used for both engine. Chikahisa et al. [3] proposed a strategy to obtain the same relative heat transfer loss effect between both engines. Equation 6.1 shows the condition that has to met in which T_{wall} has to be controlled to obtain the same results between both engines [3]:

$$\frac{\alpha}{u_0} \cdot (T - T_{wall}) = constant \tag{6.1}$$

Where α is the heat transfer coefficient and u_0 is the mean piston speed (c_m). Since the Hohenberg heat transfer coefficient is dependent on $V(t)$ while the Woschni coefficient uses D_b, both models have been investigated for the heat loss calibration. As can be seen in the Equations 6.2 and 6.3, $\frac{\alpha}{u_o}$ scales proportionally to $(D \cdot u_0)^{-(1-m)}$ and $V(t)^{-0.06} \cdot u_0^{-(1-m)}$ for the Woschni and Hohenberg coefficients, respectively. The complete formulations for the Woschni and Hohenberg heat loss coefficients can be found in **Section 5.3.4**.

$$\alpha_{Woschni} \propto D^{-(1-m)} \cdot c_m^m \propto D^{-(1-m)} \cdot u_0^m \tag{6.2}$$

and

$$\alpha_{Hohenberg} \propto V(t)^{-0.06} \cdot c_m^m \propto V(t)^{-0.06} \cdot u_0^m. \tag{6.3}$$

For both models the heat transfer coefficient increases when u_0 decreases. Because of this, T_{wall} has to be adjusted accordingly to achieve equivalent heat transfer affects that correspond to the change in size and engine speed. Zhou et al. [101] observed respectable similarities in ignition delay, in-cylinder pressure traces and normalised HRR at light load, after scaling the accumulated heat transfer losses for the S Law. His results are also in alignment with the theoretical analysis of same speed scaling in where premixed combustion dominates the heat release process [102]. The theory shows that the Damköhler number (Da_I) should be kept the same for both engines to enable similarity in premixed combustion. To achieve similar Da_I values, both engines have to run on the same engine speed.

Another suggestion by Shi et al. [25] is to decrease the intake temperature of the larger engine. The latter compensates the relatively lower heat loss by scaling T_{in} to achieve equivalent motoring pressure traces for both engines. The reason for calibrating the motoring pressure instead of the firing pressure lies in obtaining the same thermal conditions at the start of the combustion process. However, the author emphasised that a huge intake temperature difference can affect the initial thermal conditions significantly, which may result in different ignition delays and combustion characteristics. The major change in combustion characteristics when altering the inlet temperature has also been observed during the parametric study in **Section 7.7.4**. As can be seen in Figure C.17b from **Appendix C**[2], the reduction in the intake temperature lead to a lower pressure peak and a retardation of the SOC crank angle. Hence, the alteration in combustion characteristics after the inlet temperature calibration have shown to be too significant too make the assumption of similar combustion characteristics between both engines.

Table 6.2: Hohenberg convective heat transfer loss for 47H and 31H.

	Unit	Baseline	S Law	Sf	P Law	Sf	L Law	Sf	L^2	Sf
Heat loss 47H	[$kJ/cycle$]	0.116	0.588	$L^{2.47}$	0.632	$L^{2.57}$	0.740	$L^{2.81}$	0.994	$L^{3.26}$
Heat loss 31H	[$kJ/cycle$]	0.130	0.662	$L^{2.47}$	0.712	$L^{2.58}$	0.835	$L^{2.82}$	1.118	$L^{3.26}$

It can be observed from Table 6.2 that the heat loss scaling factors from the L Law and S Law have shown, respectively, the closest and worst results ($L^{2.81}$ and $L^{2.47}$ for 47H) when compared to the ideal scaling factor of L^3. This is in agreement with the theoretical correlation as shown in Equation 6.3, in which the scaling model with the largest increase in c_m ($i.e.$ S Law) will lead to the lowest relative heat loss value. In addition, the conducted scaling experiments by Tess et al. [103] which are $L^{2.57}$, $L^{2.64}$, $L^{2.79}$ for the S Law, P Law and L Law, respectively also showed that the differences in the heat loss scaling becomes more pronounced for the S Law in comparison to L Law.

6.6 Scaling results before heat loss calibration

The baseline engine has a mean piston speed (c_m) of 4.4 [m/s] which is on the narrow side, since low-speed engines are typically running at 8 [m/s] and medium to high-speed engines at around 9 to 12 [m/s] [104]. In addition, the mean indicated pressure of 2.651 [bar] is noticeably smaller in contrast to conventional natural aspiring engines that are typically operating at p_{me} values ranging from 5 to 6.2 [bar] [104]. Hence, when assuming a mechanical efficiency equal to 0.9, the p_{me} value of the HCCI engine will become 2.39 [bar]. The mean effective pressure (P_{me} can be determined from Equation 6.4.

$$IMEP = P_{mi} = \frac{W_i}{V_s} = \frac{p_{me}}{\eta_m} \tag{6.4}$$

An overview of the scaling results[3]can be found in Table 6.3 in which the S Law (constant [rpm] scaling) and the L^2 engine speed scaling has set to be the upper and lower engine limit, respectively. In this respect, the application of the S Law is frequently limited by its high mean piston speeds that may exceeds it material limits, while L^2 engine speed scaling leads to a very low engine power output.

The wear index introduced by the authors Klein Woud and Stapersma [104] can give us an indication how the engine wear of the baseline engine is affected by the engine scaling. As shown in Table 6.3, when utilising the L^2 engine speed scaling, the wear index has the same value as the baseline engine. The S Law engine scaling on the other hand lead to the greatest increase in wear index.

$$Wear\ index = i \cdot D_b \cdot p_{me} \cdot c_m \tag{6.5}$$

---

[2] **Appendix C** contains the results from the parametric study performed in **Chapter 7**.

[3] It has been assumed that the pressure trace from the scaling laws are similar to the baseline engine.

Table 6.3: Overview of the results of the scaling laws in which Sf shows the proportion of the scaling factor in comparison to the baseline engine. The values are depicted in orange when identical results have been observed in contrast to the baseline engine. The values coloured in green show the closest resemblance to the ideal scaling results, which are L^3 and L^0 for $m_{bf,cycle}$ and RCO, respectively.

	Unit	Baseline	S Law	Sf	P Law	Sf	L Law	Sf	L^2	Sf
c_m	$[m/s]$	4.4	8.5	L	6.825	$L^{\frac{1}{3}}$	**4.4**	L^0	2.278	L^{-1}
m_{bf}	$[g/s]$	0.143	0.915	$L^{2.82}$	0.751	$L^{2.52}$	0.510	$L^{1.94}$	0.295	$L^{1.10}$
$m_{bf,cycle}$	$[mg]$	11.4	73.22	$L^{2.87}$	74.81	$L^{2.91}$	**78.78**	$L^{2.98}$	87.99	$L^{3.15}$
RCO	$[-]$	0.731	0.650	$L^{-0.17}$	0.664	$L^{-0.14}$	**0.699**	$L^{-0.06}$	0.781	$L^{0.10}$
$m_{f,injected}$	$[mg]$	15.6	**112.68**	$L^{3.00}$	**112.70**	$L^{3.00}$	**112.66**	$L^{3.00}$	**112.66**	$L^{3.00}$
$Wear_{index}$	$[bar]$	0.89	3.33	$L^{2.00}$	2.68	$L^{1.67}$	1.73	L^1	**0.89**	L^0

As can be seen in Table 6.4, the indicated power output is highly influenced by the change in engine speed while the injected fuel mass, indicated efficiency and the $IMEP$ remained almost the same for all scaling methods.

Table 6.4: The results of the three scaling laws in which Sf shows the proportion of the scaling factor.

	Unit	Baseline	S Law	Sf	P Law	Sf	L Law	Sf
P_i	$[kW]$	1.64	11.93	$L^{3.00}$	9.58	$L^{2.67}$	6.18	L^2
η_i	$[-]$	0.3146	0.3147	L^0	0.3147	L^0	0.3147	L^0
$FuelMEP$	$[bar]$	8.49	8.49	L^0	8.49	L^0	8.49	L^0
IMEP	$[bar]$	2.651	2.651	L^0	2.651	L^0	2.651	L^0

The in-cylinder volume and total trapped mass are both scaled by L^3. As can be observed in Equation 8.2, when keeping identical pressure traces for both engines, the temperature per crank angle distribution remained mostly the same as can be seen in Figure 6.2b.

$$T = \frac{P \cdot V}{m \cdot R} \tag{6.6}$$

As shown in Table 6.4, a reduction in the RCO has been observed for the scaled engine. This is caused by the pressure trace that has been kept the same for both engines. In this respect, the noticeable lower in-cylinder surface to volume ratio of the scaled engine (as shown in Table 6.1) resulted in a lower heat loss per mg injected fuel. Since the injected fuel mass is proportionately scaled, less fuel is being burnt in order to satisfy the identical pressure trace constraint between both engines. As can be observed in Figure 6.3b, The L Law has shown the smallest difference in heat release rate per mg injected fuel with the baseline engine out of the three scaling laws.

The overall efficiency of the engine can be seen as the the work output divided by the total heat input [104]:

$$\eta_e = \eta_{comb} \cdot \eta_q \cdot \eta_{td} \cdot \eta_m \tag{6.7}$$

Where, the combustion efficiency (η_{comb}) includes the energy losses due to incomplete combustion. Next, the heat input efficiency (η_q) includes the heat losses to the walls and cooling water. The thermodynamic losses during compression and expansion are defined in the thermodynamic efficiency (η_{td}) [104]. The noticeably higher thermodynamic efficiency of the HCCI engine in contrast to the NG result from Harsh [32], as shown in Table 6.5, can be attributed to the difference in compression ratio and the

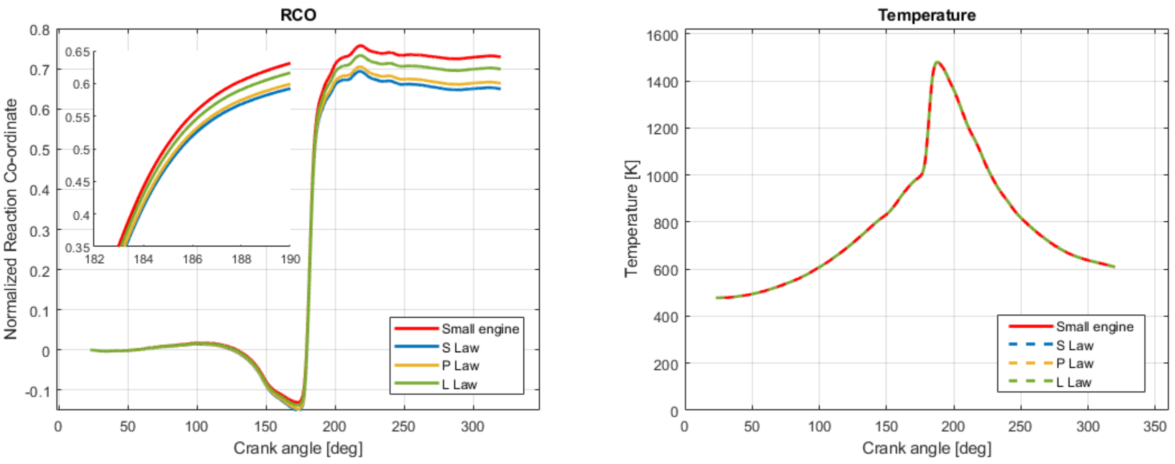

(a)

(b)

Figure 6.2: (a) *RCO* slope and (b) temperature crank angle distribution for the S, P and L scaling laws.

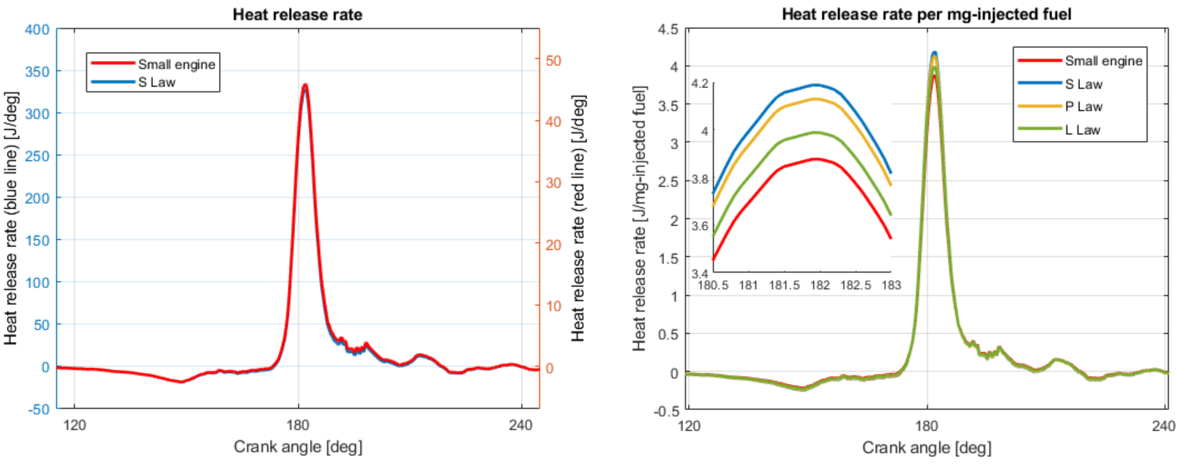

(a)

(b)

Figure 6.3: (a) A comparison of the S Law and the baseline engine HRR curves. (b) The heat release rate distribution for the S, P and L scaling laws.

HCCI combustion properties. Lastly, the mechanical efficiency (η_m) is assumed to be 0.9 for both the large and small engine. This is in reality not true, since η_m generally reduces when operating the engine at lower engine speeds [104].

The Figures 6.4a and 6.4b show the total energy losses for a range of hydrogen concentrations for the baseline engine and the scaled S Law engine, respectively. For the distribution of the energy losses, Q_f is assumed to be equal to the injected fuel mass times the LHV of the fuel. Q_{comb} is the heat release from the combustion. Q_{in} is the heat that is being used for the cycle process and can be obtained by subtracting the heat losses from the cooling water and lubrication oil from Q_{in}. At last, the parameters W_i and W_e are the indicated work and the work output of the engine, respectively [104].

The efficiency losses from the baseline and S Law scaled engine can be found in Table 6.5. Here, the results from the spark ignited hydrogen-NG experiments by Harsh [32] have also been included for comparison. The engine results from Harsh showed a lower thermodynamic efficiency in comparison to

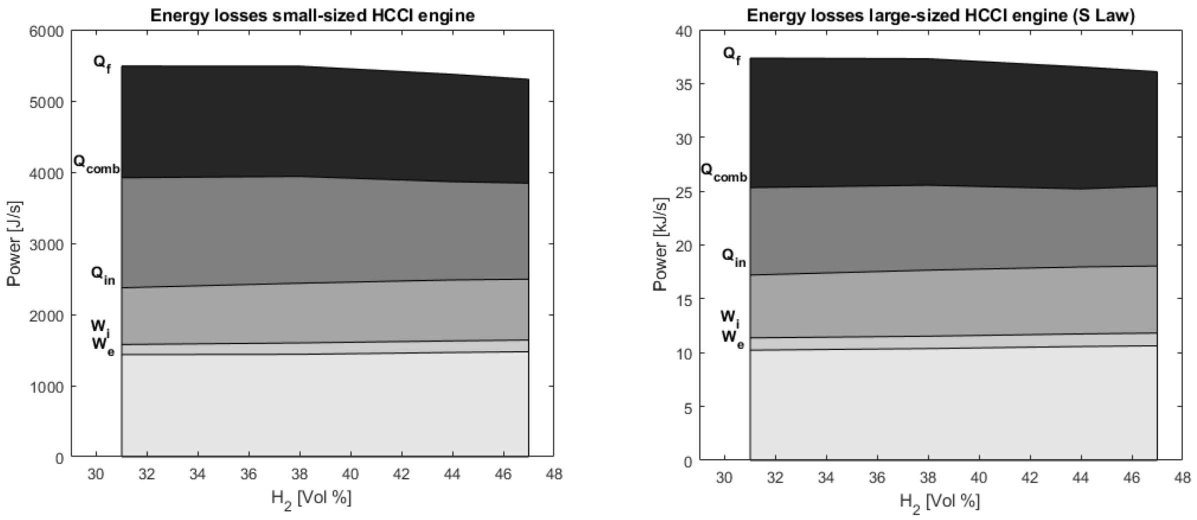

(a)

(b)

Figure 6.4: (a) Energy losses of the small HCCI engine as function of the volumetric hydrogen concentration. (b) Energy losses of the large scaled engine (S Law) as function of the volumetric hydrogen concentration.

the hydrogen-ammonia results from the scaled S Law engine model. On the other hand, the hydrogen-NG engine showed a higher η_{comb} and η_q, which explains the noticeably greater η_e.

Table 6.5: Energy loss distribution in case of hydrogen-ammonia combustion for the small & scaled version of the HCCI engine and the hydrogen NG SI engine used by Harsh as a comparison [32]. Note: the efficiency results from the S Law engines are from before the heat loss calibration (that will be discussed in **Section 6.7.1**).

	η_{comb}	η_q	η_{td}	η_m	η_e
20H NG Harsh	0.996	0.802	0.510	0.9	0.366
31H small-engine	0.713	0.585	0.689	0.9	0.259
47H small-engine	0.724	0.623	0.692	0.9	0.281
31H S Law	0.628	0.667	0.686	0.9	0.259
47H S Law	0.645	0.702	0.690	0.9	0.281

As can be seen in Table 6.5, η_q becomes greater when scaling up the engine size. Arisawa et al. [105] reported similar findings in his numerical study on the S Law. The increase in η_q could be attributed to the decrease in heat transfer loss because of the decrease in surface volume ratio. The model is based on the key assumption that the initial conditions and the pressure distributions between both engines remain the same. For the S Law model, a small retardation of the start of combustion (CA10) and a slight higher normalised HRR curve compared to the baseline engine have been observed. The differences are caused by the mismatch in the relative heat loss between both engines.

6.7 Best Scaling law for HCCI combustion

While the L Law has shown the closest similarity in the heat loss scaling factor, the reduction in engine speed is expected to cause an earlier start of combustion leading to a different pressure distribution and therefore also an alteration in combustion characteristics. The impact of the engine speed has been investigated as part of the parametric study in **Section 7.7.2**. From Figure C.13b in **Appendix C**, it can be observed that the pressure peak has shown a noticeable increase when reducing the engine speed from 1500 $[rpm]$ to 1000 $[rpm]$. Hence, the L Law engine, which operates at 776 $[rpm]$ cannot meet the scaling requirement of identical combustion characteristics with the baseline engine.

The S Law on the other hand showed the least favourable heat loss scaling factor, however, the combustion characteristics are largely unaffected because of the unscaled engine speed. As a result of the large difference in relative heat loss, the S Law showed a retardation of the CA10 from 180.40 $[CAD]$ to 180.70 $[CAD]$. Matching the heat transfer losses between the S Law and the baseline engine is still a major obstacle that has to be solved to achieve equivalent overall engine performances. Decreasing the wall temperature has shown respectable results in the literature, however, this method requires a thermal system management strategy, when applied on a real case scenario [106, 101]. In this respect, T_{wall} that can be controlled by the cooling water has to be scaled accordingly to ensure the same cumulative convective heat transfer loss per mg injected fuel for both engines.

6.7.1 Scaling results of the S Law after heat loss calibration

Because of the large difference in relative heat loss between the S Law and baseline engine as can be observed in Figure 6.5a, additional heat loss calibration is necessary for the scaled engine to obtain almost similar combustion characteristics. In this section the cumulative heat loss will be calibrated by reducing the in-cylinder wall temperature (T_{wall}).

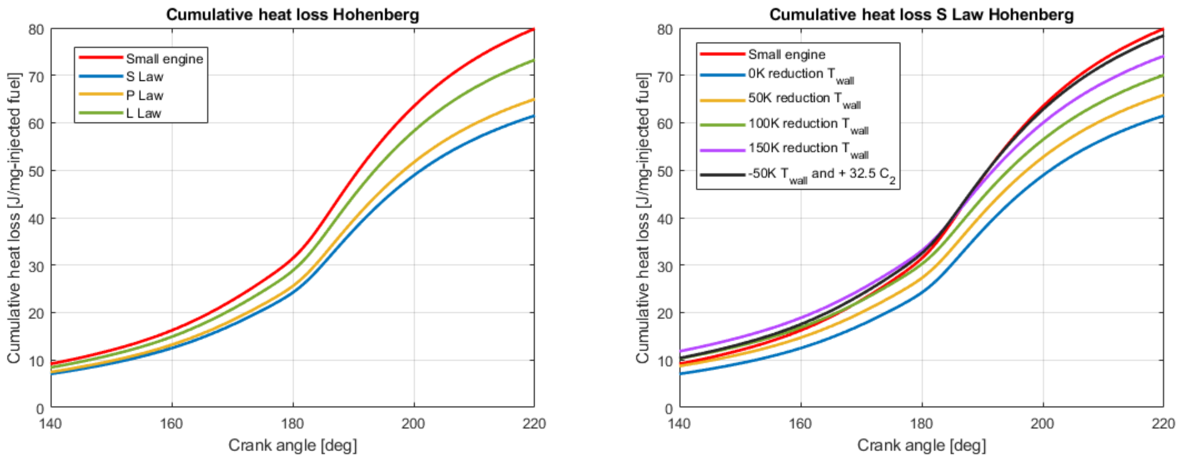

(a)

(b)

Figure 6.5: (a) Cumulative heat transfer loss per mg injected fuel as a function of the crank angle for the three scaling laws; and (b) the S Law cumulative heat transfer loss per mg injected fuel as a function of the crank angle for several T_{wall} temperature reductions.

The heat loss coefficient (C_2) changes during the engine scaling, since the value of this coefficient highly depends on the shape of the combustion chamber ($i.e.$ piston bowl shape) and the magnitude and direction of the intake swirl [94]. However, these values are unknown for the scaled engine. In case the C_2

coefficient has been kept the same during engine scaling, unrealistic wall temperature reductions were necessary for the heat loss calibration as can be seen in Figure 6.5b. The baseline temperatures for the cylinder wall, piston crown and cylinder head are 352, 470 and 475 $[K]$, respectively. As can be observed in Figure 6.6b, the 150 $[K]$ temperature reduction showed an over prediction of the calibrated heat loss model in the cumulative heat loss per mg fuel during the compression stroke, while it under predicted the cumulative heat loss per mg fuel during the combustion phase. This means that the performed heat loss calibration while keeping the same C_2 coefficient is not able to fully simulate the same heat loss characteristics with the baseline engine. The (C_2) coefficient contributes to the shape of the cumulative heat loss curve and since this value is not known the exact shape of the cumulative heat loss per mg fuel as function of the crank angle will also remain unknown. Hence, modifying the wall temperature while keeping the C_2 coefficient similar is only able to correct the cumulative heat loss per mg injected fuel, while the shape of the heat loss per crank angle remains unknown.

However, for the scaling laws to work effectively, the heat loss characteristics between both engines have to be matched in order to use the same pressure traces for both engines. From the large differences in heat loss between both engines, it can be assumed that the scaling factor of 1.93 (mentioned in **Section 6.3**) may be too large to make the assumption of similar combustion characteristics. In the literature, the scaling laws have shown to be the most effective for small differences between the engine's dimensions. in order to use the scaling factor of 1.93, we have to make another assumption that the C_2 coefficient increases from 122.5 to 155 (for 47H). The change in C_2 and a 50 $[K]$ reduction in the wall temperature will lead to an almost identical cumulative heat loss curve with the baseline engine as can be seen in Figure 6.5b. However, engine experiments are necessary to find out whether the assumption of an increase in C_2 when up sizing the engine geometry for HCCI combustion is correct.

All in all, since we do not have experimental data for the scaled engine, we can only speculate that if the temperatures of T_{wall} can be sufficiently cooled down, the same overall relative heat loss can be expected between both engines.

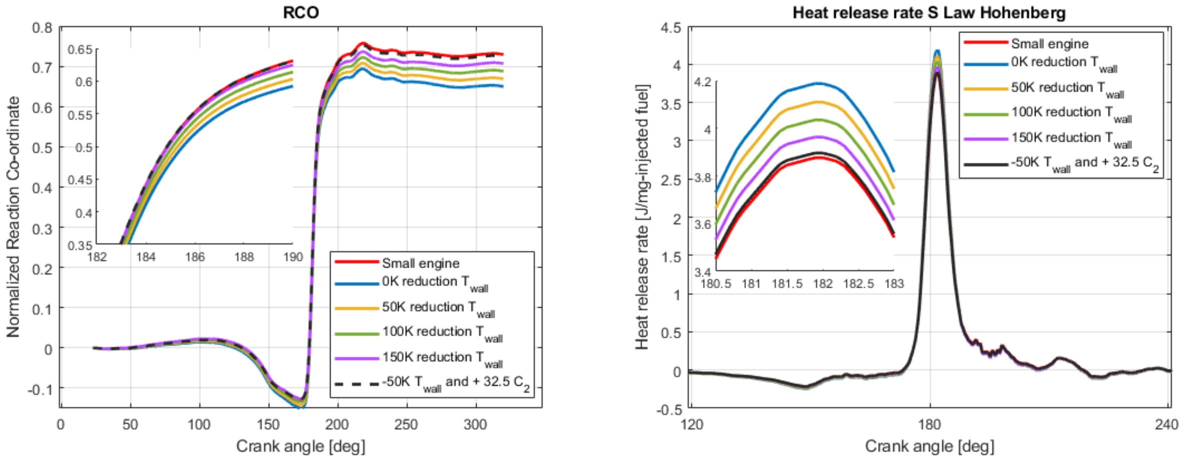

(a)

(b)

Figure 6.6: (a) *RCO* slope and (b) normalised HRR curve for various T_{wall} temperature reductions.

6.8 Conclusions

- Matching the heat transfer losses between the S Law and the baseline engine is still a major obstacle that has to be solved to meet the equivalent overall engine performance constraint. This is necessary, since there is no pressure trace data available for the scaled engine. Hence, the assumptions of an increase in the C_2 coefficient and a reduction in wall temperature are necessary to meet the requirement of similar heat loss characteristics between both engines. Decreasing the wall temperature has shown respectable results, however, this method requires a thermal system management strategy when applied on a real case scenario. In this respect, T_{wall} that can be controlled by the cooling water has to be scaled accordingly to ensure the same overall cumulative convective heat transfer losses per mg injected fuel for both engines.

- The exact shape of the heat loss curve is unknown for the scaled engine, since the C_2 coefficient changes when enlarging the engine. In this respect, the scaling laws are more accurate for small differences in bore ratio between the baseline and scaled engine. Hence, it is not recommended to scale an automotive sized engine to a marine or truck sized variant, since this will affect the accuracy of the scaled model that is the result of the noticeable differences in combustion characteristics between both engines. However, with the absence of hydrogen-ammonia experiments on marine sized engines, scaling laws are one of the sole methods to obtain insight in the performance of larger sized engines.
- While the L Law has shown the closest similarity in the heat loss scaling factor, the reduction in engine speed is expected to cause an earlier start of combustion that will lead to a different pressure distribution. The impact of the engine speed has been investigated as part of the parametric study in **Section 7.7.2**. From Figure C.13b in **Appendix C**[4], it can be observed that the pressure peak increases when reducing the engine speed. Hence, the L Law cannot have the same combustion characteristics compared with the baseline engine.
- The S Law, on the other hand, showed the least favourable heat loss scaling factor, however, from previous papers, the S Law has shown the most optimal result in terms of combustion characteristics when premixed combustion (*i.e.* HCCI) dominates the heat release process. This is because of the timescale for the chemical reactions that can be kept identical for both engines. Without heat loss calibration, the S Law showed a retardation in CA10 from 180.40 [CAD] to 180.70 [CAD]. When including heat loss scaling, the S Law showed similar CA10 values with the baseline engine as can be seen in Table 6.6.
- The application of the S Law is largely limited due to engine's material design limitation. This is caused by unrealistic piston speeds as a result of the constant speed scaling. However, since the mean piston speed (c_m) of the baseline engine has been running on 4.4 [m/s], the scaled c_m value of 8.5 [m/s] as a result of the S Law still fits within the maximum piston speed limitation. In other words, increasing the mean piston speed to 8.5 [m/s] is still within the engine's material capability.
- Large engines have shown relatively lower heat transfer losses in contrast to its down scaled variant. Hence, when both engines are operating at the same initial conditions, a higher pressure trace and overall efficiency can be expected in favour of the larger engine. Thus, the theoretically scaled S Law (including the heat loss calibration) engine will show a less optimistic performance output than in reality since it is assumed that both engines have identical pressure traces.

The heat loss calibrated S law model has shown close similarities in combustion characteristics with the baseline engine. These similarities are mentioned below:

- Both the indicated mean effective pressure (IMEP) and the indicated specific fuel consumption (ISFC) are identical between both engines.

---

[4] **Appendix C** contains the results from the parametric study performed in **Chapter 7**.

- The injected fuel, fuel burnt (m_{bf}) and indicated work output scales with the displacement volume (L^3) after calibration, which is in line with the theory.
- The HRR per mg injected fuel and RCO are in good agreement between the baseline and S law engine after the calibration.
- The temperature crank angle distribution and the initial value at valve inlet closing (T_1) have shown great similarities.
- The CA10 are for both engines exactly the same. The efficiency losses η_{comb}, η_q and η_{td} are also close to the baseline engine.

An overview of the engine scaling results for a 31H and 47 fuel blend with and without heat loss calibration can be found in Table 6.6.

Table 6.6: Overview of the S Law 47H and 31H scaling results, before and after the heat loss calibration (-50 T_{wall} & +32.5 C_2 for 47H and -50 T_{wall} & +47.5 C_2 for 31H).

	Unit	**Small engine**	**S Law**	**Sf**	**S Law + T_{wall}**	**Sf**
47H						
CA10	$[CAD]$	180.40	180.70	-	180.40	-
IMEP	$[bar]$	2.651	2.651	L^0	2.651	L^0
P_i	$[kW]$	1.640	11.93	L^3	11.93	L^3
m_{bf}	$[mg]$	11.400	73.222	$L^{2.82}$	81.622	$L^{2.99}$
$m_{f,injected}$	$[mg]$	15.631	112.684	L^3	112.645	L^3
$FuelMEP$	$[bar]$	8.494	8.49	L^0	8.482	L^0
RCO	$[-]$	0.731	0.650	$L^{-0.17}$	0.714	$L^{-0.01}$
Heat loss	$[kJ/cycle]$	0.116	0.588	$L^{2.47}$	0.818	$L^{2.97}$
η_{comb}	$[-]$	0.724	0.645	$L^{-0.17}$	0.719	$L^{-0.01}$
η_q	$[-]$	0.623	0.702	$L^{0.18}$	0.628	$L^{0.01}$
η_{td}	$[-]$	0.692	0.690	L^0	0.692	L^0
η_i	$[-]$	0.3147	0.3147	L^0	0.3146	L^0
31H						
CA10	$[CAD]$	185.79	186.29	-	185.79	-
IMEP	$[bar]$	2.532	2.532	L^0	2.532	L^0
P_i	$[kW]$	1.58	11.40	L^3	11.40	L^3
m_{bf}	$[mg]$	13.907	88.333	$L^{2.81}$	99.178	$L^{2.98}$
$m_{f,injected}$	$[mg]$	19.350	139.481	L^3	139.471	L^3
$FuelMEP$	$[bar]$	8.81	8.81	L^0	8.81	L^0
RCO	$[-]$	0.719	0.633	$L^{-0.19}$	0.711	$L^{-0.02}$
Heat loss	$[kJ/cycle]$	0.130	0.662	$L^{2.47}$	0.914	$L^{2.96}$
η_{comb}	$[-]$	0.713	0.628	$L^{-0.19}$	0.706	$L^{-0.02}$
η_q	$[-]$	0.585	0.667	$L^{0.19}$	0.592	$L^{0.02}$
η_{td}	$[-]$	0.689	0.686	L^0	0.673	$L^{-0.04}$
η_i	$[-]$	0.2898	0.2898	L^0	0.2810	$L^{-0.05}$

Chapter 7

Engine enhancements

7.1 Chapter overview

The engine in **Chapter 6** has been proportionally scaled to match the same combustion and pressure trace characteristics as the baseline engine. As a result, the maximum indicated work output is limited to 11.82 $[kW]$ (for the S Law), which is far below the 50 $[kW]$ target mentioned in **Section 6.2**. There are many possible ways to enhance the power output of the engine such as increasing the stroke to bore ratio and compression ratio, which will be discussed in **Section 7.3**.

Section 7.4 gives an introduction and methodology for the engine enhancement modelling. The results from the models which consists of the modified knock integral, Single-Wiebe function and the anti-causal in-cylinder model that requires the mass fraction burn as input give us a better understanding how the combustion characteristics of the fuel blend are influenced when making variations in the initial conditions. The modeling approach for the knock integral model and Wiebe function are discussed in the **Section 7.5** and **7.6**, respectively. Next, a parametric study will be performed in **Section 7.7** to get a quick impression of how modifications in the inlet pressure, engine speed, equivalence ratio and inlet temperature will impact the model results. From the parametric study, 2 new operational design conditions have been investigated in **Section 7.8**. The main goal of this study is to find out whether the engine is able to reach higher power outputs when altering the intake conditions.

7.2 Introduction

As already stressed by the author [15] of the ammonia fueled HCCI paper, his test engine has not been optimised for HCCI combustion. The indicated efficiency could be increased by several percentages when optimising the engine dimensions for HCCI combustion. Thus, for future ammonia fueled HCCI engines, great care has to be taken into the dimensioning of the cylinder chamber to get the highest possible combustion efficiency and power density. Quenching has to be minimised as much as possible and combustion temperatures above 1400 $[K]$ are necessary to keep the concentration of unburned ammonia to a minimum [2].

As mentioned in **Chapter 6**, the combustion characteristics of the S Law engine has to be identical to the small engine in order to comply with the scaling requirements. Both engines will therefore have identical indicated efficiencies, which is in reality not the case. Modern automobile sized engines have peak thermal efficiencies[1] at around 35-40% and 40-45% for gasoline and diesel, respectively [107]. Large marine sized engines on the other hand can achieve thermal efficiencies over 60%, making those far more efficient than automotive engines [107]. In the next section, several engine modifications are proposed to enhance the power output of the S Law engine.

7.3 Proposed engine enhancements

7.3.1 Increasing the stroke to bore ratio

Several studies [108, 109] have observed a rise in indicated efficiency when increasing the stroke to bore ratio while keeping the cylinder displacement similar. Both the two- and four-stroke engines have shown a positive effect when increasing the stroke length, in which the increase in engine performances was the most pronounced during part-load conditions [110]. Hence, HCCI engines that are commonly operating at mid-load conditions could benefit the most from the increase in stroke to bore ratio. The increase in efficiency for longer stroke engines can be explained by the relatively lower convective heat wall losses as result of the lower surface to volume ratio, when compared to short stroke engines that have the same cylinder volume.

The stroke to bore ratio of 1.035 that has been used in the in-cylinder model is in the range of generic passenger car engines, as depicted in Figure 7.1. Slow speed marine engines on the other hand commonly have stroke to bore ratios ranging from 2.2 to 2.7. Studies [110, 111] have shown that the increase in stroke to bore ratio goes together with the decrease in mechanical efficiency. Thus, at a certain stroke to bore ratio and load condition, the mechanical losses can negate the increase in indicated efficiency. On the other hand, short stroke engines have shown greater brake efficiencies when operating at low mean effective pressure (MEP) conditions, while long stroke engines performed better at higher MEP ($i.e.$ under turbocharged conditions) [111]. In short, doubling the engine's stroke to bore ratio from 1.035 to 2 could potentially increase the brake efficiency of the engine.

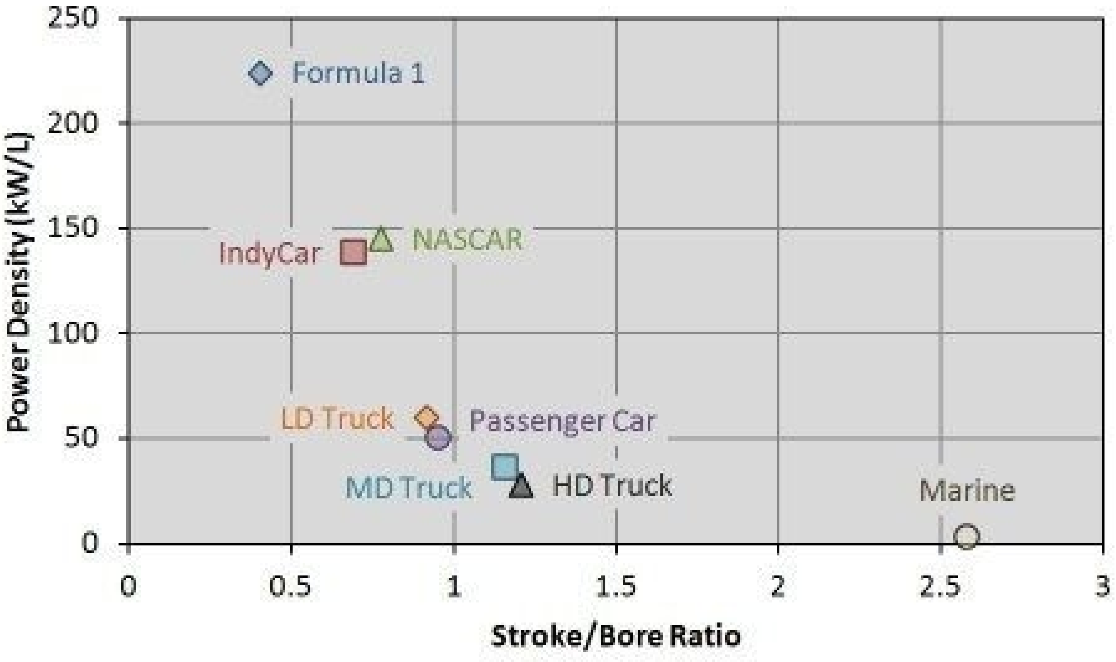

Figure 7.1: Power density as function of the stroke to bore ratio for several engine types [24].

---

[1] The thermal efficiency is the percentage of heat energy that is transformed into work.

7.3.2 Increasing the compression ratio

Another engine modification that could positively impact the indicated efficiency efficiency is the increase in compression ratio. Firstly, a higher CR will result in a decrease in intake temperature requirement. New sets of (unpublished) hydrogen-ammonia HCCI experiments by Pochet et al. [2] includes a test engine with a greater compression ratio of 22:1 in contrast to its previous 16:1 engine. Here, the intake temperature of the 22:1 CR is lowered to 373 $[K]$ (for 40 vol% ammonia), which is a reduction of 100 $[K]$ compared to the 16:1 CR that is being used in the in-cylinder model. Lower intake temperatures will result in higher air densities, meaning that more fuel and air can be injected in the cylinder.

In short, greater thermal efficiencies (η_{td}) and power densities can be expected when increasing the compression ratio. This, however, comes at the cost of an increase in friction and heat losses to the walls (decrease in η_q) and relatively lower combustion efficiencies (η_{comb}) [96]. The mentioned losses do not fully erase the increase in η_{td}, meaning that the η_i will still be slightly higher when increasing the CR.

7.3.3 Implementation of a turbocharger

Turbocharging is commonly used on marine sized diesel engines to increase the power density and in reducing the amount of space needed per $[kW]$ power [34]. The main principle of turbocharging lies in pre-compressing the charged air before it enters the cylinder. This increases the density of the air and therefore also the mass of oxygen into the engine. As a result more fuel can be injected into the cylinder in contrary to a natural aspiring engine. Turbocharging is suitable for HCCI engines, however, the latter is not as effective in comparison to conventional diesel engines because of the low HCCI exhaust temperature. Hence, a passive system in which the compressor is mechanically connected to a turbine that is being driven by the exhaust gas has to be modified to work with lower energy enthalpies. In addition, the exhaust gas has to be processed in the SCR before it can flow into the turbine, which will further lower down the temperature.

In contrast to SI engines, the compressor and turbine for HCCI combustion has to operate at higher compression ratios and a smaller turbocharger because of the lower exhaust energy [112]. Hence, a two-stage turbocharged system is highly recommended in case the HCCI engine has the option to switch to SI combustion during operation. Increasing the in-cylinder model's intake pressure from 1.5 $[bar]$ to 5 $[bar]$ with the implementation of a turbocharger can already drastically increase the power output of the engine.

7.3.4 Exhaust gas re-circulation (EGR) implementation

The ideal situation for HCCI combustion is to have the CA50 at or right after reaching TDC, mainly to avoid having the peak pressure to work against the piston's motion. This maximises the efficiency and reduces the maximum peak pressure rise rate, hence avoiding knock [2]. The crank angle position of CA50, which is commonly seen as the control parameter for HCCI engines greatly depends on the combustion duration and the ignition timing. Both of those are mainly controlled by the intake temperature and the use of exhaust gas re-circulation (EGR). In short:

- EGR is a great method to delay the auto-ignition of the air/fuel mixture, since the water vapour from the exhaust gas re-circulation has a higher heat capacity than the species in the air mixture, hence resulting in a lower bulk temperature rise.
- The benefits of EGR are an increased efficiency and power density, since more fuel or a higher intake pressure can be achieved in comparison to the same engine without EGR. In addition, the reduction in the in-cylinder oxygen availability because of the EGR system has proven to be a reliable way to reduce the NOx production in engines [66].

- Such engine enhancements that benefit and maximize the overall efficiency of the system are important to consider, since the volumetric density of ammonia is significantly lower than that of MFO/HFO. Hence, a small efficiency increase can already have a major impact on the size of the fuel storage.

7.3.5 Flexible operating conditions

Fast pressure rise rates are common for HCCI combustion, because of the instantaneous auto-ignition characteristic. These pressure rise rates are noticeably large during high load conditions and should be negated by lengthening the combustion phasing [113]. The experiments from Pochet et al. [2] have shown that high ammonia fractions (preferable above 40 vol. %) will lead to a mores spread out combustion event. This will broaden the controllability and enables the engine to run on higher loads.

The operating range of HCCI engines are limited by misfire at very low load conditions and high pressure rise rates at high load conditions [113]. The generally small load-range during HCCI combustion is still a major obstacle that has to be solved. A solution to broaden the operating range could be to enable the engine to switch from HCCI mode to SI or diesel mode, when the load cannot be satisfied. In this respect, the engine can run on HCCI mode during medium loads and on SI or CI combustion during very low and high loads. This enables optimum engine performances and flexibility for many different load and speed conditions [114]. HCCI combustion generally has a higher indicated efficiency and lower NOx production in contrast to SI or CI combustion.

7.4 Modelling approach parametric study

From the literature study, it became evident that HCCI engines have issues with auto-ignition control. The inlet conditions have shown to be the decisive parameters in the location of the start of combustion crank angle[2]. Hence, a parametric study on the initial conditions is necessary to get a better understanding which intake parameters have the greatest impact on the auto-ignition and how changes in the initial conditions will affect the combustion characteristics.

The in-cylinder model developed in **Chapter 5** requires for each change in the intake conditions a new pressure trace input for the simulation of the combustion characteristics. In order to obtain accurate results for the in-cylinder model, these pressure distributions have to be obtained from experiments. However, since there is no experimental pressure data available for the parametric study, new sets of models have been developed to study the effects of the initial conditions on the combustion characteristics. First, the modified knock integral model (MKIM) is necessary to determine the shift in the start of combustion crank angle when adjusting the initial conditions. The empirical parameters have been fitted with the modelling results from the scaled S Law engine (mentioned in **Chapter 6**). After calibration, the empirical constants have been kept the same for the parametric study.

In short, from the MKIM function, reasonable predictions of the shift in the start of combustion can be obtained for variations in the initial conditions. The location of the start of combustion can then be used inside the Single-Wiebe model in order to determine the mass fraction burn distribution, which can be used inside a modified version[3]of the in-cylinder model that has discussed in **Chapter 5**. In this way, the combustion characteristics for a range of intake conditions can be modelled without the need of experimental pressure data. The hydrogen-ammonia anti-causal in-cylinder model is based on the hydrogen-NG model from Sapra et al. [32]. The main framework components of the anti-causal model, which includes the heat loss, fuel property library, combustion characterization and the in-cylinder process components have been modified for hydrogen-ammonia fuel. Since the combustion duration of

---

[2] The the start of combustion is located at the crank angle in which 1% of the fuel has been burnt (CA1).

the fuel blend will vary when adjusting the initial conditions, an empirical combustion duration has been used to predict the changes in combustion duration.

However, because of the empirical MKIM and Single-Wiebe parameters that have been set constant for the parametric study, the modelling results may not be as accurate in comparison to the results from the in-cylinder model that uses the pressure trace as input from **Chapter 5**. A flowchart of the modelling approach for the parametric study on the initial conditions can be found in Figure 7.2.

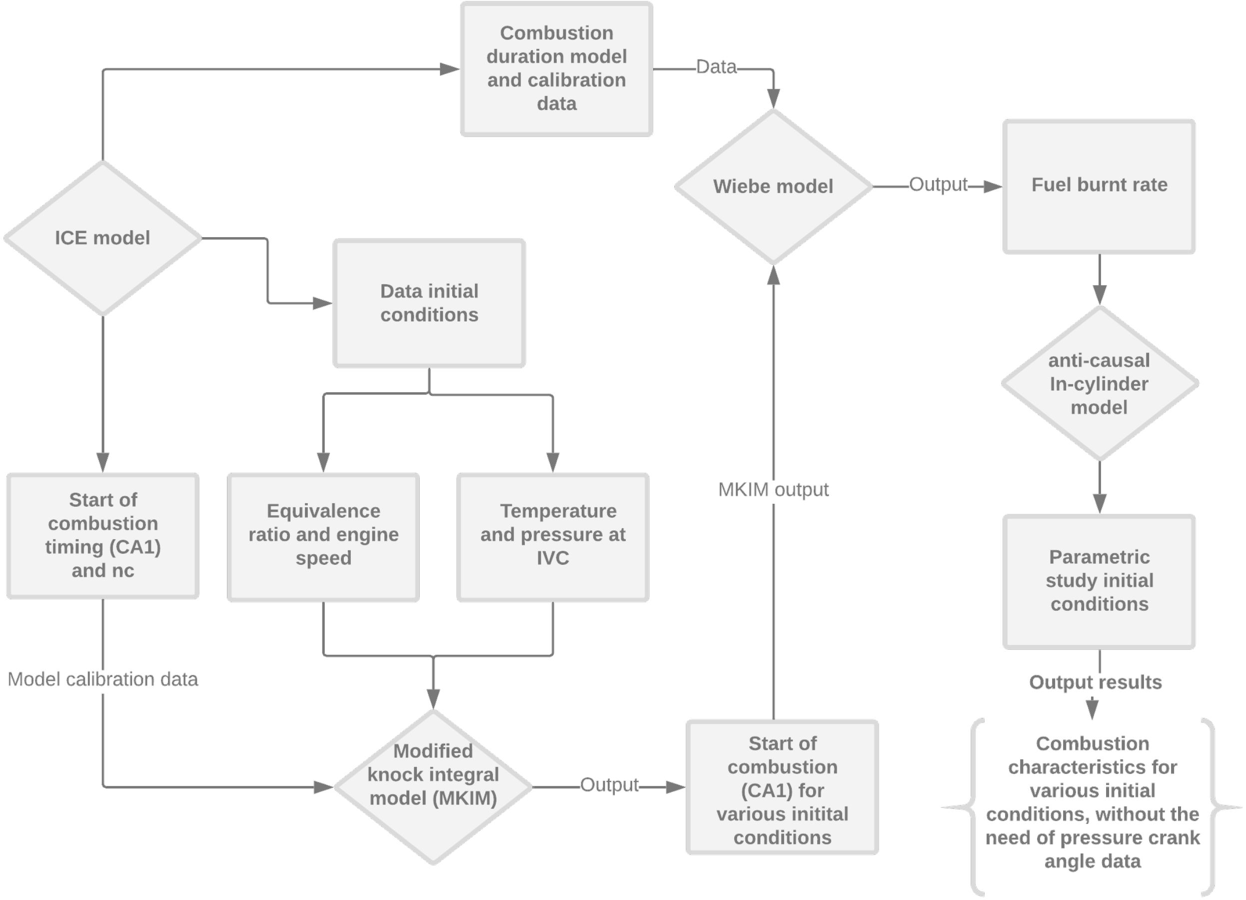

Figure 7.2: Flowchart overview of the steps taken in the creation of the anti-causal in-cylinder model that requires the mass fraction burn as input.

7.5 Modified knock integral model (MKIM)

7.5.1 Approach MKIM function

The application of a simple zero dimensional knock integral model provides relevant results with the benefit of a fast calculation rate [115]. The main component of the knock integral is based on the empirical Arrhenius relationship as shown in the equation below [116]:

$$\tau = A \cdot exp\left(\frac{b}{T} \cdot p^{n}\right) \tag{7.1}$$

---

[3] The term anti-causal in-cylinder model will be used for the modified version of the in-cylinder model.

Where, τ is the ignition delay and p and T are respectively the pressure $[kPa]$ and temperature $[K]$ as function of the time. The empirical parameters A, b and n are constants and can be determined from the model calibrations. The crank angle dependent knock integral is able to predict the start of combustion with the main assumption that the reaction is zero order and the reaction rate will not change during the compression stroke [117]. Here, the auto-ignition of the homogeneous mixture is predicted by an exponential correlation. Auto-ignition occurs when the relationship between the concentration and auto-ignition delay (also known as the concentration ratio) reaches unity, as shown in Equation 7.2 [116].

$$\frac{x}{x_c} = \int_{\theta_0=\theta_{IVC}}^{\theta=\theta_{SOC}} \frac{1}{N\cdot\tau} d\theta = \int_{\theta_0=\theta_{IVC}}^{\theta=\theta_{SOC}} \frac{1}{N\cdot A\cdot exp([\frac{b}{T}]\cdot P^n)} d\theta = 1.0 \tag{7.2}$$

Where, θ_{IVC} and θ_{SOC} are the crank angles at inlet valve closing (IVC) and start of the combustion (SOC), respectively. the parameter N is the engine speed in $[rpm]$ and τ is the ignition delay mentioned in Equation 7.1. Since the input pressure and temperature are as function of the time, experimental data is required to solve the knock integral. A way to bypass this requirement is to assume that the pressure and temperature increase during engine compression occur as a polytropic process. In this respect, the heat release as a result of pre-combustion that occurs before reaching the SOC is neglected in the modelling. This methodology is known as the modified version of the knock integral model (MKIM). Here, the initial temperature and pressure at inlet valve closing and the polytropic parameter (n_c) have to be acquired from experiments. In this way, the temperature and pressure contributions are written as function of the change in in-cylinder volume as can be seen in the Equations 7.3 and 7.4 [118].

$$T = T_{IVC}\cdot v_c(\theta)^{n_c-1} \tag{7.3}$$

$$p = P_{IVC}\cdot v_c(\theta)^{n_c} \tag{7.4}$$

The crank angle dependent variable $v_c(\theta)$ is the ratio between the volume at inlet valve closing and the volume at a specific crank angle.

$$v_c(\theta) = \frac{V_{IVC}}{V(\theta)} \tag{7.5}$$

Substituting Equations 7.3 to 7.5 into the knock integral will lead to the MKIM function as shown in Equation 7.6 [116]. Experiments and modelling performed by Shahbakhti et al. [118] have shown that the KIM predicts the start of combustion more accurately in contrast to the MKIM. This is mainly because the MKIM only uses the pressure and temperature values at IVC, in which the polytropic parameter n_c has been kept constant during the entire compression phase.

$$\int_{\theta_0=\theta_{IVC}}^{\theta=\theta_{SOC}} \frac{1}{N\cdot A\cdot exp\left(\frac{b\cdot[P_{IVC}\cdot v_c^{n_c}]^n}{T_{IVC}\cdot v_c^{n_c-1}}\right)} d\theta = 1.0 \tag{7.6}$$

A way to enhance the accuracy of the predicted SOC for a range of hydrogen-ammonia ratios is to integrate the equivalence ratio into the empirical MKIM function. The latter is important, since it gives a good indication of the amount of initial fuel and air inside the engine. Another way to optimise the model for a range of fuel blends is to include the initial concentrations of the fuel and oxygen as shown in Equation 7.7 [118].

$$\int_{\theta_0=\theta_{IVC}}^{\theta=\theta_{SOC}} \frac{[Fuel]^d\cdot[O_2]^e}{N\cdot A\cdot exp\left(\frac{b\cdot[P_{IVC}\cdot v_c^{n_c}]^n}{T_{IVC}\cdot v_c^{n_c-1}}\right)} d\theta = 1.0 \tag{7.7}$$

Where, $[Fuel]$ and $[O_2]$ are the concentration fuel and oxygen, respectively. The parameters d and e are empirical constants and can be determined from model calibration.

However, Equation 7.7 requires data that has to be acquired from exhaust gas analyzers and oxygen sensors. The in-cylinder fuel and oxygen data has not been provided by the HCCI paper, which makes the integration of the equivalence ratio the only viable option to optimise the model for a range of different hydrogen-ammonia ratios.

The final version of the MKIM model [116] that includes the contribution of the equivalence ratio can be found in Equation 7.8. This equation will be used for the auto-ignition modeling and will be described as the MKIM function in the upcoming sections.

$$\int_{\theta_0=\theta_{IVC}}^{\theta=\theta_{SOC}} \frac{\phi^c}{N\cdot A\cdot exp\left(\frac{b\cdot[P_{IVC}\cdot v_c^{n_c}]^n}{T_{IVC}\cdot v_c^{n_c-1}}\right)} d\theta = 1.0 \tag{7.8}$$

7.5.2 Input parameters

The empirical parameters A, b, n and c have been fitted with the use of the 47 volumetric percent hydrogen (47H) data. The data from the 44H, 38H and 31H fuel blends have not been included in the fitting because of the large deviations in the auto-ignition crank angle between the highest and lowest hydrogen concentration that will inevitably lead to less accurate results. Hence, the empirical parameters have only been fitted using the data of one operating condition for 47H. A higher accuracy can be expected when more operating points of the 47H fuel blend are included in the determination of the empirical MKIM parameters. It is therefore highly recommended to re-calibrate the empirical parameters in case more experimental data is available.

The fminsearch tool in the Matlab software has been used to fit the empirical parameters. These parameters are influenced by the fuel properties, engine geometry and the operational condition. In an ideal scenario we want to experimentally determine the empirical parameters in a rapid compression machine for a 53 volumetric % ammonia and 47 volumetric % hydrogen fuel blend. These values then have to be optimised for the given engine dimensions using experimental data and the fminsearch tool. In this respect, the empirical parameters should be further optimised using data for a range of operational conditions ($i.e.$ change in engine speed, inlet pressure, inlet temperature and equivalence ratio). This is required to determine the effect of these engine parameters on the SOC. Hence, the fminsearch tool should ideally be applied on a range of experimental data to obtain more accurate values for the empirical parameters. However, since we do not have the data for hydrogen-ammonia auto-ignition inside a rapid compression machine, the start values of the empirical parameters that are necessary for the first iteration have been acquired from the paper by Swan et al. [119] for iso-octane. The location of the SOC is influenced by the octane rating of the fuel [119]. Iso-octane has an octane rating of 100, which is higher in comparison to the octane ratings of hydrogen (>130) and ammonia (130) [120]. The start values of the empirical parameters A, b, n and c are $9.291e^{-7}$, 16909, -0.1121 and -0.688, respectively. This resulted in the values $1.047e{-}6$, 21573, -0.007 and -0.735 after fitting the empirical parameters for one engine condition. Ideally, we want to analyze the empirical parameters for a range of engine conditions.

The fitted empirical parameters are not completely accurate since the start values for iso-octane have been used. In this respect, another fuel type has been investigated to get a better understanding how the start value will impact the MKIM results. Here, the start values of n-heptane (octane rating of zero) are $5.336e^{-10}$, 14948, -0.038 and -0.930, respectively. This resulted in the values $7.251e{-}10$, 23927, -0.020 and -0.587 after the fitting. As can be seen in Figure 7.3b, the initial start value from the paper by Swan gave a function value of almost $2.088e^4$ for the first iteration and a value of $1.1838e^{-28}$ after the last iteration. The large function value output from the first iteration gives us an indication that the iso-octane empirical start values do not completely fit to the experimental data from Pochet et al. [23]. When the start start value for n-heptane is being used, the function value becomes $5.956e^7$ after the first iteration. Hence, iso-octane has shown to be a better fit in contrast to n-heptane. However, more accurate results can be expected when the start values for a hydrogen-ammonia blend are used. As depicted in Figure 7.3a, auto-ignition occurs when the area under the MKIM function $1/(N \cdot \tau)$ reaches one. Here the newly fitted empirical parameters give exactly the same start of combustion.

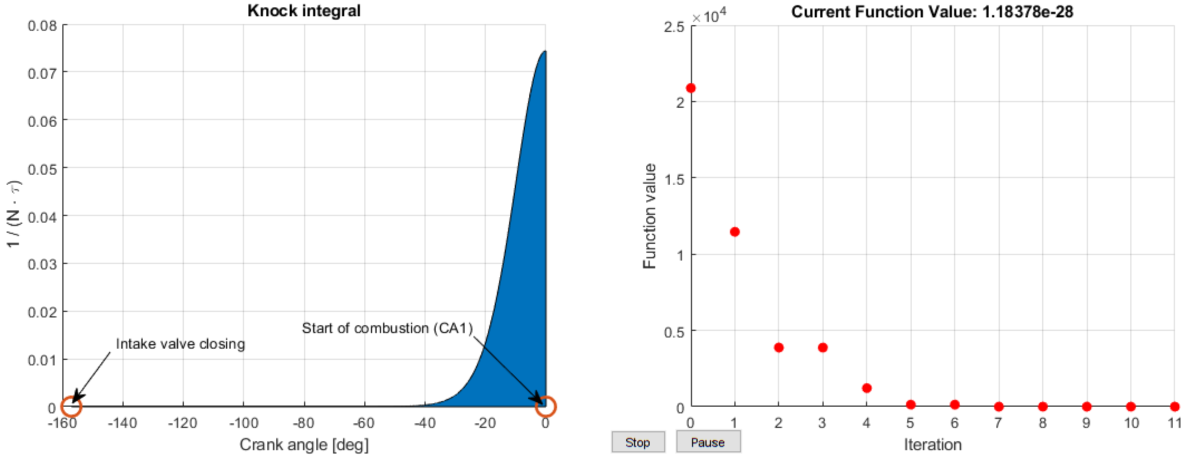

(a)

(b)

Figure 7.3: (a) Graphical representation of the MKIM integration for 47H during the compression stroke. The blue area under the MKIM function corresponds to a value of 1.0. (b) Graphical representation of the function value during each iteration.

7.5.3 Results

The Figures 7.4a to 7.5b show the change in SOC, when altering the engine speed (N), equivalence ratio and initial conditions $(i.e.$ pressure and temperature) at IVC. It can be observed that changes in the pressure or the equivalence ratio have not shown a major impact on the predicted SOC crank angle. On the other hand, a change in initial temperature or engine speed greatly influenced the location of the start of combustion.

As can be seen in Figure 7.4a, the intake temperature plays a crucial factor in the development of the start of combustion crank angle. Decreasing the baseline inlet temperature of 474 $[K]$ to 465 $[K]$ has shown a retardation of the SOC from 0 to 4.89 $[CADaTDC]$ and further lowering the temperature leads to misfire. Increasing the temperature on the other hand resulted in an earlier SOC in which an increase from 474 $[K]$ to 538 $[K]$ leads to an SOC shift from 0 $[CADaTDC]$ to -11.94 $[CADaTDC]$. This is also not favored, since the early heat release before reaching TDC may decrease the indicated power output of the engine. In addition, a greater inlet pressure advances the SOC, as can be seen in Figure 7.4b. Here, a pressure increase from 1.6 $[bar]$ to 5.6 $[bar]$ resulted in a SOC shift from 0 $[CADaTDC]$ to -9.38 $[CADaTDC]$. This earlier start of combustion phenomenon at higher inlet pressure has also been observed by Caton et al. [121]. In his work, he mentioned that the use of EGR could be a great way to suppress the knock integral. In this respect, the earlier SOC caused by the increase in inlet pressure can be counteracted by increasing the EGR.

As can be seen in Figure 7.5a, increasing the engine speed results in a delay in the start of combustion crank angle because of the shortening of the real time combustion period. Here, the SOC for the engine speeds of 500 $[rpm]$ and 2500 $[rpm]$ are -10.56 $[CADaTDC]$ and 10.56 $[CADaTDC]$, respectively. Caton et al. [121] also noticed a retardation of the SOC when increasing the engine speed. The deviations

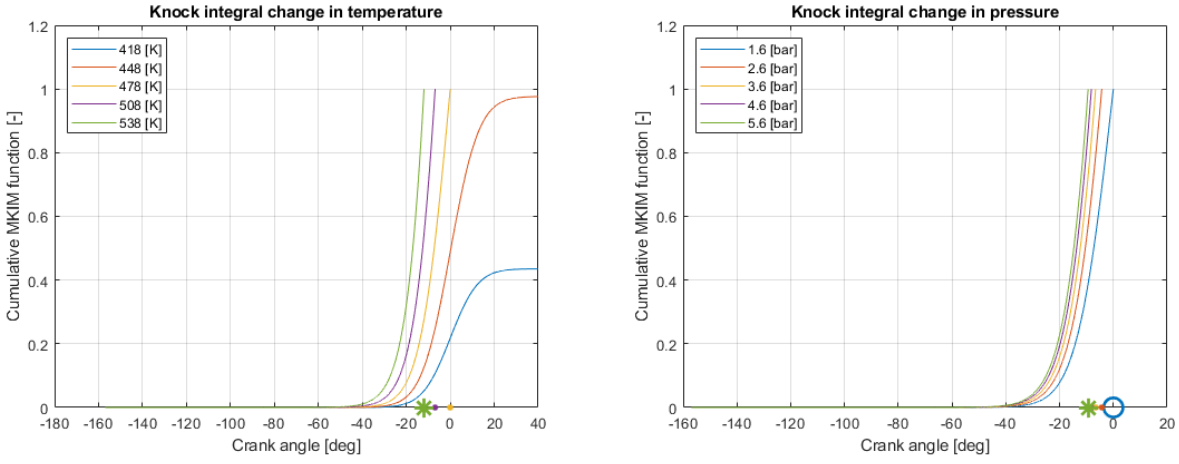

(a) (b)

Figure 7.4: The knock integral function for a range of initial inlet temperatures (a) and pressures (b) at inlet valve closing. The baseline temperature and pressure values that have been used in the in-cylinder model are 478 $[K]$ and 1.6 $[bar]$ (for 47H), respectively.

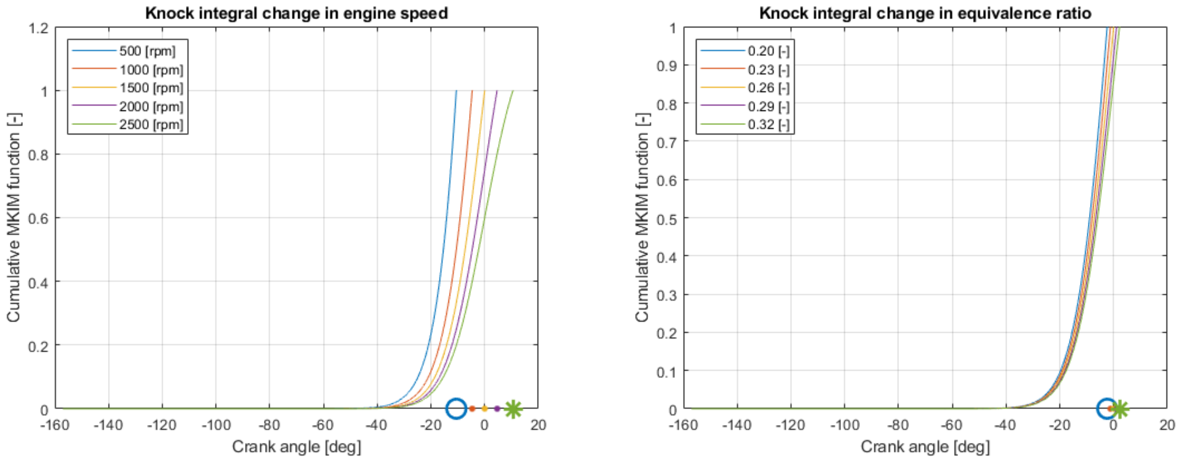

(a) (b)

Figure 7.5: The knock integral function for a range of initial engine speeds (a) and equivalence ratios (b) at inlet valve closing. The baseline engine speed and equivalence ratio that have been used in the in-cylinder model are 1500 $[rpm]$ and 0.26 $[-]$ (for 47H), respectively.

in the SOC when varying the equivalence ratio are on the other hand not that significant. Increasing the equivalence ratio from 0.20 $[-]$ to 0.32 $[-]$ resulted in an SOC shift from -2.38 $[CADaTDC]$ to 2.24 $[CADaTDC]$.

As mentioned earlier, the fitted empirical MKIM parameters are not completely accurate, since values for iso-octane have been used for the first iteration. In Table 7.1, the results from the iso-octane MKIM calibration have been compared with the results from the n-heptane calibration. It can be observed that the deviations in the intake temperature between iso-octane and n-heptane results are above 50%. This indicates that using the start values for iso-octane instead of the hydrogen-ammonia fuel blend may not give very accurate results. Hence, the start values for the empirical MKIM parameters should come from the hydrogen-ammonia rapid compression machine experiment in order to obtain the most accurate results.

Table 7.1: Comparison between n-heptane and iso-octane as the initial values for the first iteration in the MKIM function.

Inlet temperature	Unit	418 $[K]$	448 $[K]$	478 $[K]$	508 $[K]$	538 $[K]$
SOC iso-octane	$[CADaTDC]$	misfire	misfire	0	-6.88	-11.94
SOC n-heptane	$[CADaTDC]$	misfire	misfire	0	-8.49	-14.31
Deviation	[%]	misfire	misfire	0	23.7	19.8
Inlet pressure	Unit	1.6 $[bar]$	2.6 $[bar]$	3.6 $[bar]$	4.6 $[bar]$	5.6 $[bar]$
SOC iso-octane	$[CADaTDC]$	0	-4.30	-6.59	-8.17	-9.38
SOC n-heptane	$[CADaTDC]$	0	-1.85	-2.91	-3.65	-4.22
Deviation	[%]	0	57.0	55.8	55.3	55.0
Engine speed	Unit	500 $[rpm]$	1000 $[rpm]$	1500 $[rpm]$	2000 $[rpm]$	2500 $[rpm]$
SOC iso-octane	$[CADaTDC]$	-10.56	-4.63	0	4.63	10.56
SOC n-heptane	$[CADaTDC]$	-8.69	-3.83	0	3.83	8.69
Deviation	[%]	17.7	17.3	0	17.3	17.7
Equivalence ratio	Unit	0.20 $[-]$	0.23 $[-]$	0.26 $[-]$	0.29 $[-]$	0.32 $[-]$
SOC iso-octane	$[CADaTDC]$	-2.38	-1.16	0	1.13	2.24
SOC n-heptane	$[CADaTDC]$	-1.60	-0.78	0	0.74	1.46
Deviation	[%]	32.8	32.8	0	34.5	34.8

The Figures 7.6a to 7.7a show the results from the predicted MKIM function on the vertical axis and the results from the experiments by Pochet et al. [23] on the horizontal axis.

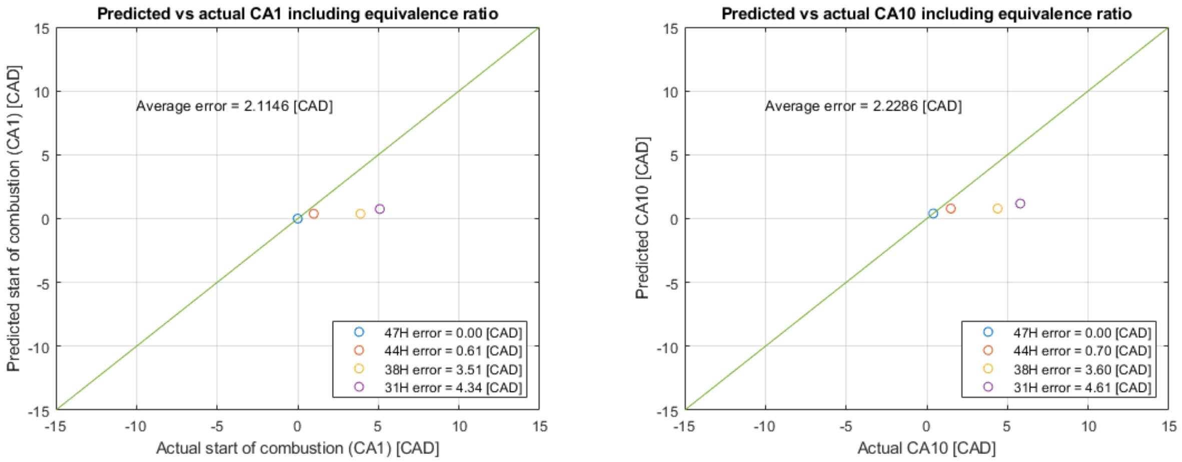

(a) (b)

Figure 7.6: (a) The predicted MKIM SOC vs the SOC from the experiments by Pochet et al. [23] and (b) the predicted CA10 vs the CA10 from the experiments. The error is the absolute difference between the predicted result from the MKIM and the experimental result.

The modified knock integral model in which the empirical parameters have been optimised for 47H has been evaluated for several hydrogen-ammonia blends. As can be seen in Figure 7.6a, the average deviation in the prediction of the SOC and the Auto-ignition crank angle from the experiments by Pochet et al. [122] for 47H, 44H, 38H and 31H are large. The difference of 4.6 $[CAD]$ as shown in Figure 7.6a between the predicted SOC and the SOC from the experiment for the 31H fuel blend is still noticeably high. The average deviation can be minimised by optimising the empirical parameters for all fuel blends. In this respect, the average deviation will decrease at the cost of an increase in the 47H error. Hence, a better suggestion would be to optimise the empirical MKIM parameters for each hydrogen concentration instead of using the same values. From the analysis, it can also be observed that the average deviation of the CA10 is slightly higher to that of the SOC. A possible reason could be that the compression stroke are for each fuel blend more or less the same. From Figures 7.6b and 7.7a, the implementation of the equivalence ratio in the MKIM contributes to a smaller error difference, when using a range of hydrogen-ammonia blends. The accuracy of the MKIM model could potentially be enhanced by switching the equivalence ratio term for the fuel and oxygen concentration [118]. However, this setup requires experimental crank angle measurements from the oxygen and fuel sensors, which we do not have.

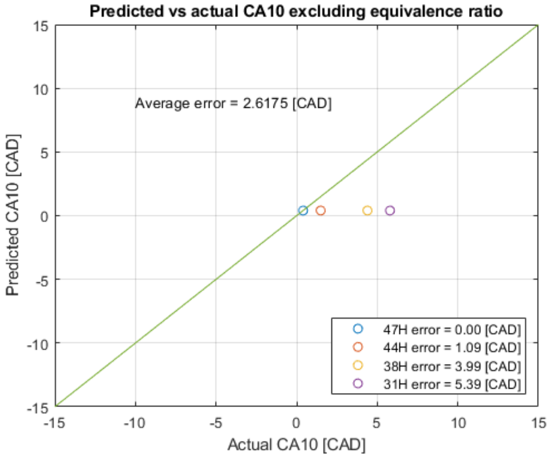

(a)

Figure 7.7: (a) The predicted MKIM CA10 vs the CA10 from the experiments by Pochet et al. [23] excluding the equivalence ratio. The error is the absolute difference between the predicted result from the MKIM and the experimental result.

In reality, it is difficult to maintain the same hydrogen-ammonia ratio of 47H during the whole operation, since the hydrogen production has to be perfectly matched and optimised to the engine's current operational condition. We can therefore expect different hydrogen-ammonia ratios during transient loading for which the engine also has to be optimised for the minimum and maximum acceptable hydrogen concentrations. The latter has not been investigated in this thesis, however, this topic could be an interesting research objective for future work. For the Wiebe model, only the combustion characteristics of the 47H and 31H fuel blends will be investigated. Hence, the empirical parameters have been optimised for both fuel blends to minimize the MKIM error. The next section discusses the develpopment of the Wiebe model.

7.6 Single-Wiebe function model

7.6.1 Approach Wiebe function

In contrast to the in-cylinder model mentioned in **Chapter 5**, the anti-causal in-cylinder model for the Wiebe function requires the burned fuel mass fraction (x_b) instead of the pressure signal as the main time dependent input. The parameter x_b is the output result from the single-Wiebe function which can be determined as follows:

$$x_b(\theta) = 1 - exp\left(-a\left[\frac{\theta - \theta_{SOC}}{\theta_d}\right]^{m+1}\right). \tag{7.9}$$

Where m is the form factor, a is the efficiency factor, θ_{SOC} is the crank angle position at the start of combustion, θ is the current crank angle position and θ_d is the burn duration between crank angle CA1 and CA95.

7.6.2 Input parameters

Since the Wiebe function contains two constants ($i.e.$ m and a), usually an assumption is made with one of the constants. In this respect, the efficiency factor a that is directly related to the combustion duration can be determined using Equation 7.10.

$$a = -ln(1-\eta_{comb}) = -ln(1-0.74) = 1.3471 \tag{7.10}$$

Then, the form factor m, which reflects the distribution of the heat release process can be determined by performing a least square analysis on Equation 7.9 using experimental data and the assumption of a constant efficiency factor (a). This gives an estimated overall form factor m of 0.9214 (slope as shown in Figure 7.8a) -1 = -0.0768 .

The predicted shape of the Wiebe function changes significantly when varying the values of m and a, since these terms are placed within the exponential term of the equation. Yasar et al. [123] found that small changes in the form factor m already has a big impact on the burn fraction (x_b), hence, an accurate value of this constant is necessary. Abbaszadehmosayebi et al. [124] proposed a modified version of the Wiebe function, in which the efficiency factor a is divided out of the equation. For this, he rearranged Equation 7.9 has to Equation 7.11

$$ln(1 - x_b(\theta)) = -a\left[\frac{\theta - \theta_{SOC}}{\theta_d}\right]^{m+1} \tag{7.11}$$

Here, the cumulative mass fraction (x_b) of 0.5 is used as a reference point.

$$ln(0.5) = -a\left[\frac{\theta_{50} - \theta_{SOC}}{\theta_d}\right]^{m+1} \tag{7.12}$$

When dividing Equation 7.11 by Equation 7.12, the Wiebe function can be expressed in terms of $\theta, \theta_{50}, \theta_{SOC}$ and the form factor (m) as shown in Equation 7.13.

$$x_b(\theta) = 1 - exp\left(ln(0.5)\left[\frac{\theta - \theta_{SOC}}{\theta_{50} - \theta_{SOC}}\right]^{m+1}\right) \tag{7.13}$$

Next, the m value can be determined for each time instant by rearranging Equation 7.13 into 7.14. The mass fraction burn for a range of crank angle locations have been obtained from the experiments by

Pochet et al. [23]. A mean value constant of the form factor (m) can be acquired from the slope of the best fit line as shown in Figure 7.8a.

$$ln\left[\frac{ln(1-x_b(\theta))}{ln(0.5)}\right] = (m+1)\cdot ln\left[\frac{\theta-\theta_{SOC}}{\theta_{50}-\theta_{SOC}}\right] \tag{7.14}$$

According to Figure 7.8a, $(m+1)$ is equal to 0.9214, which results in an m value of 0.9214 - 1 = -0.0786.

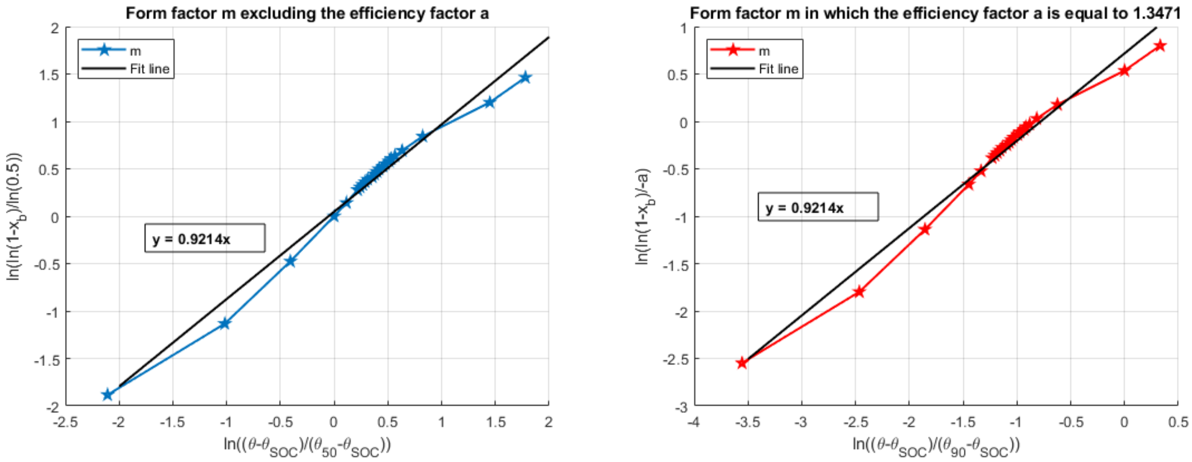

(a) (b)

Figure 7.8: (a) and (b) show the form factor m at each time instant during the combustion process for 47H. Here the Figure on the left excludes the efficiency factor a, while the Figure on the right uses a constant a value that has been derived from Equation 7.10.

As can be seen from the Figures 7.8a and 7.8b, both fit lines have identical slope values of 0.9214 when using the same combustion data set.

7.6.3 Approach in-cylinder model

The anti-causal model is based on the in-cylinder model from **Chapter 5**. Here, the main components and the input parameters for the model are the same from the in-cylinder model in **Chapter 5**. These main components consist of the heat release, heat loss, fuel and air property library and the indicated work blocks. As can be seen in Figure 7.9, the output parameters from the anti-causal in-cylinder model are the temperature and the pressure distributions.

From the literature study, it became evident that HCCI engines have issues with auto-ignition control. The inlet conditions have shown to be the decisive parameters in the location of the start of combustion crank angle. Hence, a parametric study on the initial conditions is necessary to get a better understanding which intake parameters have the greatest impact on the auto-ignition and how changes in the initial conditions will affect the combustion characteristics. For this parametric study, the modified knock integral model (**Section 7.5**) and the Single-Wiebe function (**Section 7.6**) have been developed. Here, the MKIM function is necessary to determine the shift in the start of combustion crank angle when adjusting the initial conditions. Then, the Single-Wiebe model is used to determine the new mass fraction burn distribution for the anti-causal in-cylinder model to simulation the in-cylinder combustion characteristics.

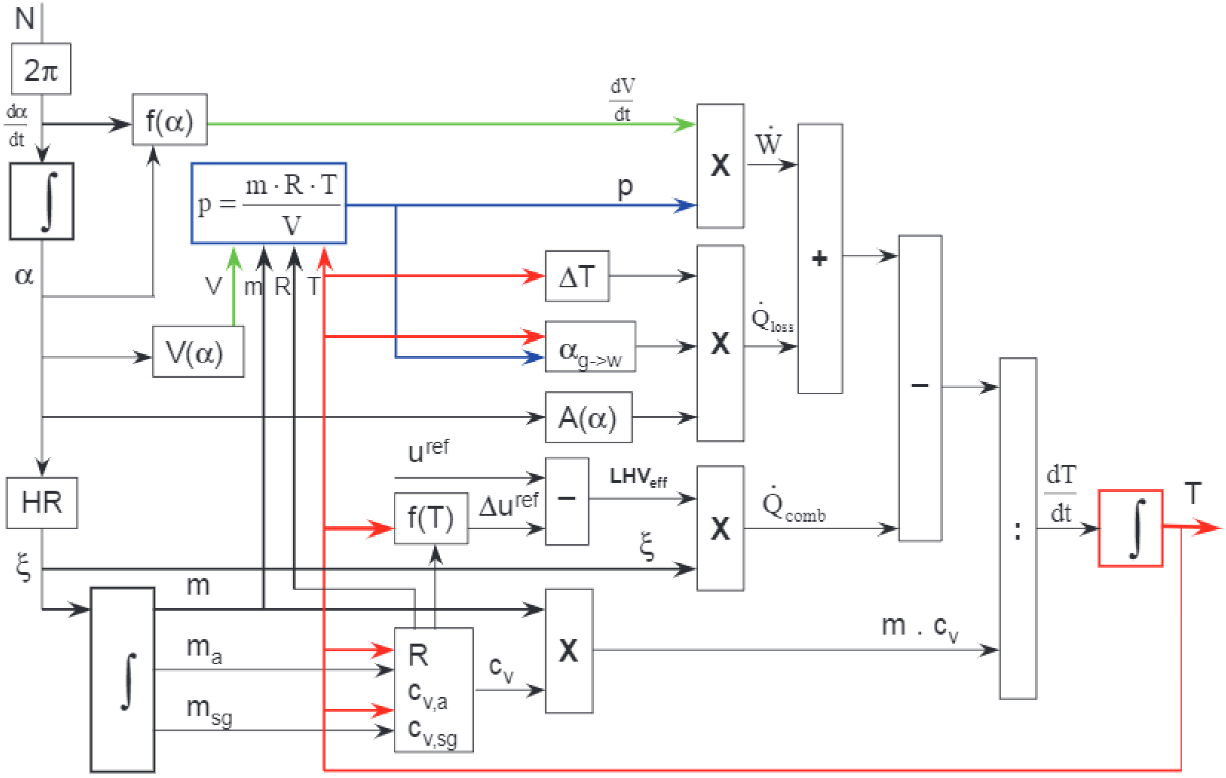

Figure 7.9: Block diagram overview for the simulation of the anti-causal in-cylinder process using the mass fraction burn as input. Figure has been taken from Stapersma [21].

7.6.4 Wiebe model and anti-causal in-cylinder model verification

The output results from the Wiebe model and anti-causal in-cylinder model have been verified with the results from the scaled S Law and heat loss calibrated in-cylinder model mentioned in **Chapter 6**. Here, the 47H and 31H fuel blends have been investigated. In this section, only the results from the 47H fuel blend are shown. The comparison in combustion characteristics between the scaled S Law and heat loss calibrated in-cylinder model and the results from the Wiebe and anti-causal model can be found in **Section C.1.1** in **Appendix C**.

From the pressure curve in Figure 7.10a, it can be observed that the horizontal location and the value of the pressure traces between the scaled S Law in-cylinder model (**Chapter 6**) and the results from the Wiebe model (**Chapter 7**) are almost comparable. However, there is a distinguishable difference in the location of the maximum temperature between the in-cylinder model and Wiebe model as shown in Figure 7.10b. This indicates that the results from the Wiebe model and the anti-causal in-cylinder model are not able to fully simulate the combustion characteristics from the In-cylinder model.

The difference in combustion characteristics can also be observed in Table 7.2. Here, the results in terms of the cumulative heat loss, the pressure trace and the temperature distribution between the in-cylinder model output and the Wiebe function are slightly different since the distributions in the burn fractions are not completely identical. The single-Wiebe function shows larger differences with the experimental results after reaching 190 [*CAD*] as can be seen in the *RCO* curve in Figure 7.11a. This indicates that a single-Wiebe function is not accurate enough to simulate the whole *RCO* curve and that a double- or triple-Wiebe function will most probably lead to more accurate results.

The single-Wiebe function over-predicts the HRR peak value by a factor 1.2, as can be seen in Figure

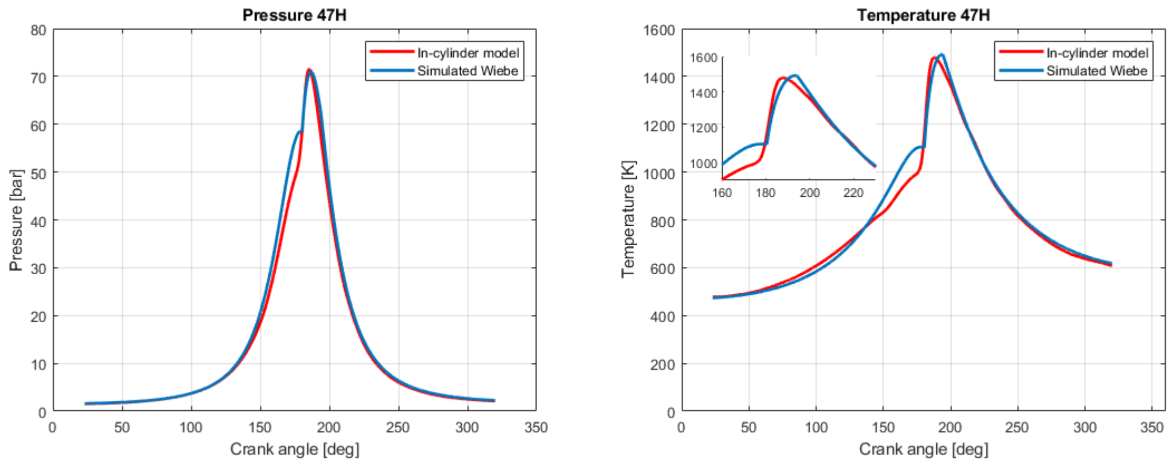

(a) (b)

Figure 7.10: (a) Pressure and (b) temperature distribution for the in-cylinder model from **Chapter 6** (S Law engine) and the simulated single-Wiebe function.

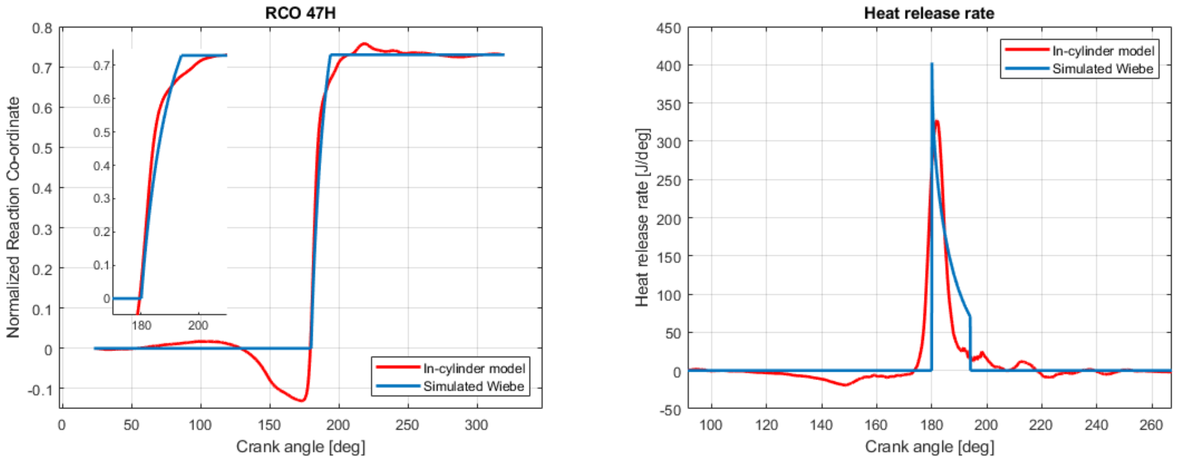

(a) (b)

Figure 7.11: (a) *RCO* and b) heat release rate distribution for the in-cylinder model from **Chapter 6** (S Law engine) and the simulated single-Wiebe function.

7.11b. This large deviation between the single-Wiebe function and experimental results have also been observed by Yasar et al. [123]. According to him, the over-prediction is mainly caused by the slower combustion phase near the cylinder walls that has not been included in a single-zone model. In this respect, a multi-zone approach in which a separate wall-zone is included in the model could offer more accurate results.

7.6.5 Approach combustion duration model

The combustion phasing of HCCI engines is not completely characterised by the start of combustion timing, since different burn durations (θ_d) can occur at the same SOC. Hence, a combustion duration model is necessary to predict the change in combustion duration, when adjusting the initial conditions inside the Wiebe and anti-causal in-cylinder models. Shahbakhti et al. [118] described the relationship

Table 7.2: Comparison in combustion characteristics between the in-cylinder model (heat loss calibrated S Law engine) and the Wiebe function for a 47 vol. percent hydrogen fuel blend (47H).

	Unit	In-cylinder model	Wiebe function	Error [%]
IMEP	$[bar]$	2.651	2.623	1.06
P_i	$[kW]$	11.93	11.80	1.09
m_{bf}	$[mg]$	81.622	85.867	-5.20
$m_{f,injected}$	$[mg]$	112.645	117.738	-4.52
$FuelMEP$	$[bar]$	8.486	8.870	-4.53
RCO	$[-]$	0.731	0.729	0.27
Heat loss	$[kJ/cycle]$	0.818	0.880	-7.58
η_{comb}	$[-]$	0.719	0.724	-0.70
η_q	$[-]$	0.628	0.620	1.27
η_{td}	$[-]$	0.692	0.659	4.77
η_i	$[-]$	0.3146	0.2996	4.77

of the burn duration as a function of the equivalence ratio, the mixture dilution fraction (X_d) and the empirical parameters C, D and E. Here the empirical parameters for the burn duration function have been calibrated using the output data from the in-cylinder model.

$$\theta_d = C(1+X_d)^D \cdot \phi^E \tag{7.15}$$

Where, the mixture dilution fraction (X_d) is a function of the exhaust gas re-circulation (EGR) and the internal residual gas mass fraction (X_r) as shown in Equation 7.16. The internal residual gas mass fraction is the ratio of the in-cylinder residual mass and the trapped mass.

$$X_d = EGR + \left[\frac{X_r}{1-X_r}\right] \tag{7.16}$$

$$X_r = \left[\frac{m_r}{m_t}\right] \tag{7.17}$$

The EGR has not been implemented in this thesis, however, for future performance enhancement studies, the implementation of EGR could play an effective role in increasing the burn duration. This is especially beneficial for high hydrogen fractions to slow down the combustion phasing and less interesting for high ammonia concentrations because of its high octane number that also lead to a longer burn duration.

7.7 Results parametric study

In this study, a list of variations in the initial conditions have been analyzed. The parameters that have been varied are the inlet pressure, engine speed, equivalence ratio and the inlet temperature. Here, the purpose of the analysis is to obtain an understanding how variations in the initial condition will impact the anti-causal in-cylinder model results and which parameter has the highest influence on the indicated power output. During the analysis, only one parameter has been varied at a time in which the results can be found in Table 7.3.

Table 7.3: Overview of the engine modeling results for a range of initial conditions. The values in green represent the baseline results from **Chapter 6** (Engine scaling). The temperature, pressure, RCO and fuel burnt curves can be found in **Section C.2.1** in the Appendix.

Inlet pressure	Unit	$P_{in} = 1.6\ [bar]$	$P_{in} = 2.6\ [bar]$	$P_{in} = 3.6[bar]$	$P_{in} = 4.6\ [bar]$	$P_{in} = 5.6\ [bar]$
SOC	$[CAD]$	**180.00**	175.70	173.41	171.83	170.62
Burn duration	$[CAD]$	**14.00**	14.00	14.00	14.00	14.00
IMEP	$[bar]$	**2.623**	4.319	6.085	7.814	9.546
P_i	$[kW]$	**11.80**	19.43	27.38	35.16	42.95
η_i	$[-]$	**0.3022**	0.3092	0.3126	0.3142	0.3152
P_{max}	$[bar]$	**71.20**	126.3	182.8	239.7	297.1
T_{max}	$[K]$	**1490**	1553	1591	1612	1627
$m_{f,injected}$	$[mg]$	**116.04**	186.76	260.275	332.57	405.14
Engine speed	Unit	$N = 500\ [rpm]$	$N = 1000\ [rpm]$	$N = 1500\ [rpm]$	$N = 2000\ [rpm]$	$N = 2500\ [rpm]$
SOC	$[CAD]$	169.44	175.37	**180.00**	184.63	190.56
Burn duration	$[CAD]$	14.00	14.00	**14.00**	14.00	14.00
IMEP	$[bar]$	2.014	2.470	**2.623**	2.705	2.621
P_i	$[kW]$	3.02	7.410	**11.80**	16.23	19.65
η_i	$[-]$	0.2285	0.2833	**0.3022**	0.3084	0.3009
P_{max}	$[bar]$	82.97	77.71	**71.20**	63.15	59.25
T_{max}	$[K]$	1564	1534	**1490**	1454	1380
$m_{f,injected}$	$[mg]$	117.84	116.62	**116.04**	117.16	116.31
Equivalence ratio	Unit	eq = 0.20 $[-]$	eq = 0.23 $[-]$	eq = 0.26 $[-]$	eq = 0.29 $[-]$	eq = 0.32 $[-]$
SOC	$[CAD]$	177.62	178.84	**180.00**	181.13	182.24
Burn duration	$[CAD]$	16.43	15.09	**14.00**	13.10	12.34
IMEP	$[bar]$	1.898	2.284	**2.623**	2.975	3.311
P_i	$[kW]$	8.54	10.28	**11.80**	13.39	14.90
η_i	$[-]$	0.2768	0.2919	**0.3022**	0.3104	0.3166
P_{max}	$[bar]$	69.84	70.83	**71.20**	71.57	71.66
T_{max}	$[K]$	1400	1447	**1490**	1535	1576
$m_{f,injected}$	$[mg]$	91.62	104.57	**116.04**	128.15	139.86
Inlet temperature	Unit	$T_{in} = 465\ [K]$	$T_{in} = 474\ [K]$	$T_{in} = 493\ [K]$	$T_{in} = 508\ [K]$	$T_{in} = 538\ [K]$
SOC	$[CAD]$	184.89	**180.00**	176.22	173.12	168.06
Burn duration	$[CAD]$	14.00	**14.00**	14.00	14.00	14.00
IMEP	$[bar]$	2.695	**2.623**	2.452	2.272	1.920
P_i	$[kW]$	12.13	**11.80**	11.03	10.23	8.639
η_i	$[-]$	0.3031	**0.3022**	0.2921	0.2800	0.2517
P_{max}	$[bar]$	62.73	**71.20**	75.80	78.40	80.64
T_{max}	$[K]$	1421	**1490**	1569	1626	1718
$m_{f,injected}$	$[mg]$	118.91	**116.04**	112.30	108.51	102.16

7.7.1 Change in initial pressure

Since the efficiency factor (a) and the form factor (m) in the single-Wiebe function remained constant, the combustion efficiency and burn duration are for each engine speed condition the same. In reality, the value for the combustion efficiency that also has an impact on the efficiency factor a is expected to be greater at higher inlet pressures because of the increase in temperature. The parametric results are therefore most likely on the conservative side, hence, higher indicated powers can be expected when including the change in combustion efficiency. The pressure curve increases drastically when using greater inlet pressures. The simulations by Eilts et al. [122] has shown maximum pressures and MEP that are reaching 300 $[bar]$ and 35 $[bar]$, respectively, when using a charged air pressure of 5.6 $[bar]$. The state of art automotive diesel engines are able to reach mean effective pressures of 30 $[bar]$ and maximum pressures of 200 $[bar]$. Higher pressures are achievable, however, material and design solutions are necessary. According to the author, charge air pressures to approximately 10 $[bar]$ are reachable with the use of a two stage turbo charging system.

All in all, the alteration in the inlet pressure has shown the greatest impact on the combustion characteristics. As shown in Table 7.3, increasing the initial inlet pressure from 1.6 $[bar]$ to 5.6 $[bar]$ has shown an almost factor 4 increase in indicated power output (11.80 $[kW]$ vs 44.38 $[bar]$). In addition to the increase in power density at greater inlet pressures, higher η_i have been observed that are in line with the modeling results by Eilts et al. [122]. The author also observed a rise in indicated efficiencies when increasing the charged air pressure.

7.7.2 Change in engine speed

The modeling results on the effects of the engine speed on the combustion characteristics by Uludogan et al. [125] have shown higher power outputs at higher rpms. In addition, his work showed a decrease in the pressure and temperature distribution that has also been observed in the ammonia fueled Wiebe model as shown in Table 7.3. Lower local temperatures and a shorter time of combustion at high engine speeds has a positive impact on the reduction of the NOx emissions. The transition from 1500 $[rpm]$ to 2000 $[rpm]$ has shown an almost 50% increase in the indicated power. Increasing the engine speed retards the start of combustion (SOC) crank angle. This can have a positive impact on the generated work during each cycle, because of the phasing of the heat release distribution in which less fuel is being burnt during the compression stroke.

Since the efficiency factor (a) and the form factor (m) in the single-Wiebe function remained constant, the combustion efficiency and burn duration are for each engine speed condition the same. In reality, the value for the combustion efficiency that has an impact on the efficiency factor a is expected to be slightly higher for higher engine speeds [125]. The results presented in Table 7.3 are most likely on the conservative side, hence, higher indicated powers can be expected when including the change in combustion efficiency. Higher engine speeds have the disadvantage of an increase in durability and noise problems. If this is not an issue, then higher engine speeds are preferred because of the lower emissions and a higher power densities. The optimal engine speed for this modeled engine is expected to be around 2000 $[rpm]$. In the case of a further increase in engine speed (from 2000 $[rpm]$ to 2500 $[rpm]$), a reduction in the indicated efficiency and $IMEP$ have been observed as a result of the noticeable retardation in SOC.

7.7.3 Change in equivalence ratio

An increase in the equivalence ratio from the baseline 0.26 $[-]$ to 0.32 $[-]$ resulted in an indicated power output increase of 27% as can be seen in Table 7.3. The increase in equivalence ratio also shortened the burn duration that has been determined using the empirical Equation 7.15. While the SOC retards when increasing the equivalence ratio, the end of combustion crank angle (CA90) starts earlier. in this respect, 193.7 $[CAD]$ and 194.8 $[CAD]$ for an equivalence ratio of 0.32 $[-]$ and 0.20 $[-]$, respectively.

Besides shortening the burn duration, the increase in equivalence ratio leads to greater maximum temperature and pressure peaks. For HCCI combustion, a longer burn duration is generally more beneficial to spread the heat release distribution and will therefore decrease the peak stresses on the engine's structure. All in all, increasing the equivalence ratio is a suitable option in enlarging the power density of the engine.

7.7.4 Change in inlet temperature

The results in Table 7.3 may not completely represent the real case scenario. Since the efficiency factor a, form factor m and the burn duration remained constant for each change in initial inlet temperature, which explains the not representative combustion efficiencies at intake temperatures below the baseline engine. Here, an inlet temperature of 465 $[K]$ has shown a greater indicated work output in contrast to the baseline inlet condition of 474 $[K]$ that has been used in **Chapter 6** (engine scaling). This is in reality not true as we can expect lower combustion efficiencies for the 465 $[K]$ condition, because of the decrease in maximum temperature.

From the results we can conclude that the engine's inlet temperature has to be adjusted in such a way that the start of combustion timing (SOC) shortly happens after reaching TDC. Further increasing the inlet temperature results in an earlier heat release that is happening before reaching TDC. In this case, the early heat release is working against the piston, which will decrease the indicated work output of the engine.

7.8 Design proposal

In this section, 2 operational design conditions have been evaluated for a 31H and 47H fuel blend. These operational conditions are stated as design 1 and design 2. For design 1, the values for the equivalence ratio and the inlet pressure have been increased from, respectively, 0.26 $[-]$ (S Law engine) to 0.32 $[-]$ and 1.6 $[bar]$ to 5.6 $[bar]$ to maximise the injected fuel mass per cycle. In addition, the engine speed has been increased from 1500 $[rpm]$ to 2500 $[rpm]$ to obtain a higher injected fuel mass per second as can be seen in Table 7.4.

Table 7.4: Overview of the input parameters for the Wiebe and anti-causal in-cylinder model for the baseline engine (**Section 7.6.3**) and the design conditions 1 and 2 mentioned in **Section 7.8** for the 31H and 47H fuel blends.

		31H	47H	31H	47H	31H	47H
	Unit	Baseline	Baseline	Design 1	Design 1	Design 2	Design 2
P_{in}	$[bar]$	1.6	1.6	5.6	5.6	4.6	4.6
T_{in}	$[K]$	474.0	474.0	478.8	482.5	459.4	470.4
Engine speed	$[rpm]$	1500	1500	2500	2500	2000	2000
Equivalence ratio	$[-]$	0.28	0.26	0.32	0.32	0.20	0.20

Design 1 is based on an extreme scenario in which the HRR peak value is a factor 5.9 times (for 47H) larger than the result obtained from the S law engine mentioned in **Chapter 6** (1.941 $[kJ/deg]$ vs 0.327 $[kJ/deg]$). The increase in T_{max} from 1480 $[K]$ to 1655 $[K]$ together with the shortening in burn duration from 14 $[CAD]$ to 12.34 $[CAD]$ will lead to significantly larger forces on the engine's cylinder walls. The engine can potentially achieve an indicated power output of 92.48 $[kW]$ as shown in Table 7.5. The modifications in the engine speed, equivalence ratio and the inlet pressure lead to a noticeable shift in the SOC. For both design conditions, the start of combustion crank angle have been shifted back to TDC by adjusting the inlet temperature. In this way, the amount of heat release that is working against the piston movement has been kept to a minimum.

Table 7.5: Overview of the Wiebe and anti-causal modeling results for the baseline engine (**Section 7.6.3**) and the design conditions 1 and 2 mentioned in **Section 7.8** for the 31H and 47H fuel blends.

		31H	47H	31H	47H	31H	47H
	Unit	Baseline	Baseline	Design 1	Design 1	Design 2	Design 2
SOC	$[CAD]$	185.09	180.00	180.01	180.01	180.03	180.04
Burn duration	$[CAD]$	12.31	14.00	11.44	12.34	14.80	16.43
IMEP	$[bar]$	2.58	2.62	11.55	12.33	5.76	6.12
P_i	$[kW]$	11.61	11.80	86.61	92.48	34.54	36.72
η_i	$[-]$	0.2819	0.3022	0.3291	0.3459	0.2940	0.3114
P_{max}	$[bar]$	60.45	71.20	262.1	267.80	190.0	194.00
T_{max}	$[K]$	1437	1490	1608	1655	1356	1394
$m_{f,injected}$	$[mg]$	144.99	116.04	560.40	477.03	312.33	262.57

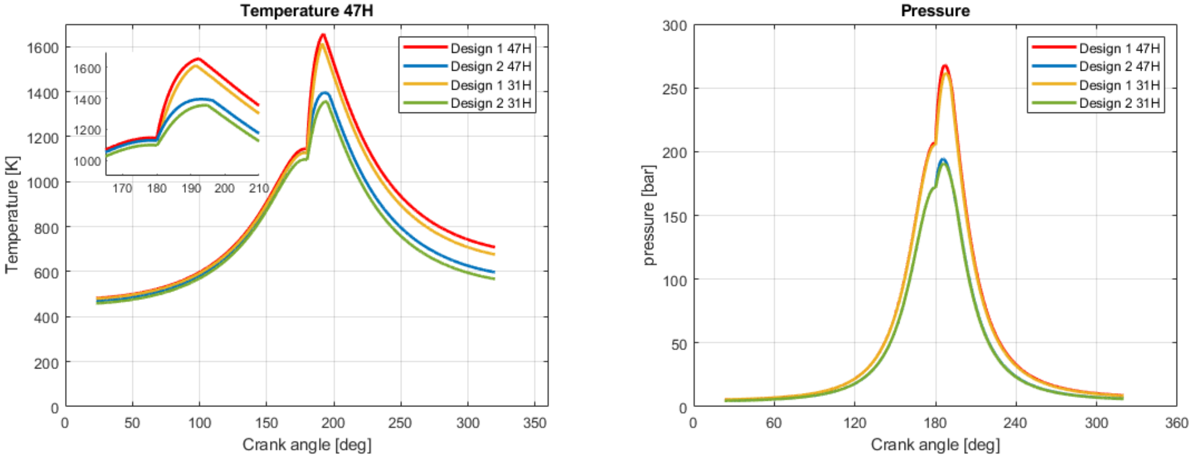

(a) (b)

Figure 7.12: (a) Temperature and (b) pressure distribution for the designs 1 and 2. The input parameters can be found in Table 7.4.

A more plausible and realistic operational design condition would be to extend the burn duration during each combustion cycle by further lowering the equivalence ratio. This massively reduces the HRR peak, which will result in a more spread out heat release. The charged air pressure and engine speed in design 2 are lower in comparison to design 1. The initial conditions for design 1 and 2 for the fuel blends 31H and 47H can be found in Table 7.4. From the Figures 7.12a and 7.12b, it can observed that the initial conditions from design 2 lead to significantly lower temperature and pressure traces. The HRR peak of 0.85 $[kJ/deg]$ is 2.3 times lower in comparison to design 1 and 2.6 times larger than the S Law engine from **Chapter 6** (0.327 $[kJ/deg]$). While the maximum temperature for the 47H fuel blend is close to the minimum requirement of 1400 $[K]$[4], the 31H fuel blend showed a T_{max} which is 44 $[K]$ below the requirement. This means that operational design 2 works great for 47H, but an increase in equivalence ratio or a decrease in engine speed is necessary for 31H to meet the T_{max} requirement.

The almost straight vertical line at 180 $[CAD]$ in the heat release is largely caused by the m value in

---

[4] Hydrogen-ammonia HCCI engine experiments by Pochet et al. [2] have shown that a maximum temperature above 1400 $[K]$ is necessary to keep the unburned ammonia concentration to a minimum. See **Section 5.6** for a more detailed explanation.

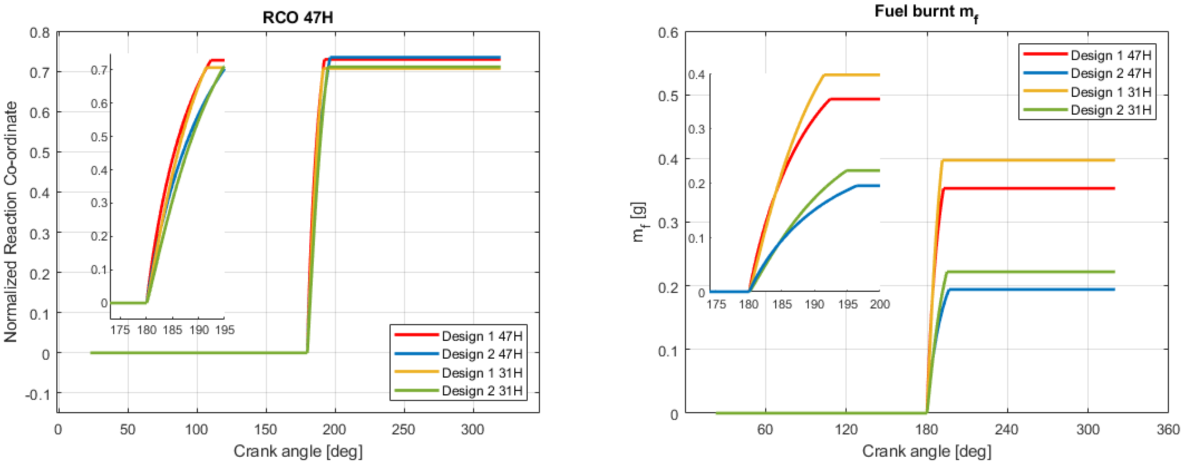

(a)

(b)

Figure 7.13: (a) *RCO* and (b) fuel burnt curve for the designs 1 and 2. The input parameters can be found in Table 7.4.

the Wiebe function. Both 31H and 47H have shown a small m value of 0.1109 and -0.0768, respectively. A smaller m leads to a higher initial heat release rate value, in which a value lower than 0.5 will result in an almost vertical line that occurs slightly after reaching SOC [126].

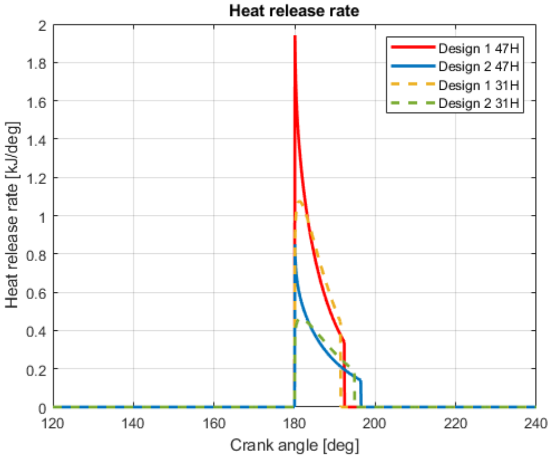

(a)

Figure 7.14: (a) The heat release rate curve.

7.9 Reflection results

7.9.1 Wiebe function m parameter

The m value in the Wiebe function has been set to a fixed constant instead of the function mentioned in 7.14, since we do not have data to determine the actual value after each parametric variation. The conducted research by Johansson et al. [126] has shown that the m value is influenced by the *IMEP* value in which an increase in $IMEP$ was correlated to a greater m value. The author observed that for his engine the m value correlated to the function $0.006 \cdot IMEP$. His HCCI engine experiments were performed with a different fuel blend, however, we can assume that the m value will also increase when increasing the $IMEP$ value.

The exact $IMEP$ value on the other hand, is not known and it greatly depends on the combustion duration which exact value is also not known [118]. To get a better understanding of the influences of the m parameter on the modeling results, we assume the same correlation of $0.006 \cdot IMEP$ that has been observed by Johansson. For a 31H fuel blend, the m parameter went from 0.1109 to 6.0161 and 2.0741 for design 1 and design 2, respectively. As can be seen in Table 7.6, the large increase in m did not impact the indicated efficiency and the power output. The maximum pressure and temperature on the other hand, did show a small deviation. Since a larger m value did not show a big impact on the indicated power output and since we do not have an exact correlation of the m value, the m value will be set as a fixed constant of 0.1109 (for 31H) in the parametric study.

Table 7.6: Overview of the parametric modeling results in which the Wiebe parameter m has been adjusted for the expected IMEP value.

	Unit	Design 1	Design 1 m_{mod}	Design 2	Design 2 m_{mod}
IMEP	$[bar]$	11.55	11.55	5.76	5.77
P_i	$[kW]$	86.61	86.65	34.54	34.61
η_i	$[-]$	0.3291	0.3262	0.2940	0.2918
P_{max}	$[bar]$	262.1	255.6	190.0	171.7
T_{max}	$[K]$	1608	1634	1356	1372
$m_{f,injected}$	$[mg]$	560.40	565.46	312.33	315.29

7.9.2 HRR curve

The HRR curve in Figure 7.11b has shown an almost vertical line upwards that occurs shortly after reaching SOC. While this rapid increase in the heat release rate is a rare phenomenon for SI and CI engines, experiments and modelling in the literature have shown that these mentioned HRR characteristics are common cases for HCCI combustion. This especially happens when the HCCI engine is operating at low to medium-load conditions that have been observed in a number of publications [127, 128, 129, 25]. From the results in the Figures 7.15a and 7.15b by Shi et al. [25], a significantly lower HRR peak value can be observed during full-load in comparison to low-load conditions. Operating at full-load showed a longer combustion duration and a less steep HRR rise at the start of combustion. The engine in **Chapter 6** is most likely operating at low to medium-load condition, since its IMEP value of 2.623 $[bar]$ value (for 47H) is noticeably smaller in contrast to conventional natural aspiring engines that are typically operating at 5 $[bar]$. Hence, at higher load conditions a lower peak pressure increase rate and a longer combustion duration could be expected.

In addition, the rapid increase in HRR can be mitigated by the implementation of exhaust gas recirculation (EGR). An EGR concentration of 10% has shown a major decrease in the steepness and maximum value of the HRR [127]. The HRR increase rate can also be minimized by lowering the equivalence ratio or by extending the combustion duration [129].

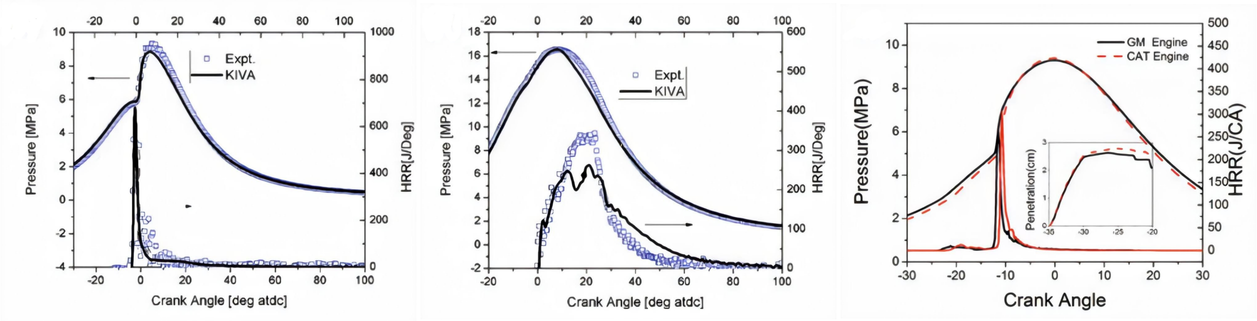

(a)

(b)

(c)

Figure 7.15: (a) Low-load and (b) full-load diesel combustion in which the intake pressure and injected fuel are respectively 2 and 3 times higher for the full-load condition. Here, the KIVA numerical model had been validated using experimental data. (c) Low to medium-load diesel HCCI combustion in which the displacement volume of the CAT engine is 5 times higher in comparison to the GM engine [25].

7.9.3 Wiebe modification for HRR fitting

From Figure 7.11b it can be observed that the Wiebe function is not able to simulate the HRR curve of the in-cylinder model from **Chapter 6** during the compression stroke. The Wiebe parameter m has been determined in **Section 7.6.1** by fitting the burn fraction data from **Chapter 6**. This resulted in a negative m value of -0.0786 for 47H and 0.1109 for 31H when the negative heat release rates during the compression stroke were neglected. This approach allows the RCO slope at TDC of the Wiebe function (blue line) to fit seamlessly with the results from the in-cylinder model (red line) as can be seen in Figure 7.18a. However, the HRR curve as shown in Figure 7.18b shows a greater peak in comparison to the in-cylinder model. The drop in the RCO curve during the compression stroke could be the result from the high intake temperature. As can be seen in Figure 7.17b, the temperatures between 140 $[CAD]$ and SOC are exceeding the fixed wall temperature of 352 $[K]$. Hence, the dip in the RCO curve could be caused by the heat loss to the cooling water. Another reason for the dip in the RCO curve could be traced to the assumptions made for the in-cylinder model (**Chapter 5**) that may impacted the RCO curve.

In case we want the Wiebe model to have a greater HRR fit with the scaled S Law in-cylinder model (**Chapter 6**), we have to include the negative HRR (as shown in Figure 7.16a) when determining the m parameter[5]. This will lead to a start of combustion crank angle that occurs at 176.3 $[CAD]$ instead of 180 $[CAD]$ for the 47H fuel blend. In addition, the burn duration changes from 14 $[CAD]$ to 10.3 $[CAD]$, which will result in an m value of 1.3111 instead of -0.0786 from the RCO fit.

As can be seen in Figure 7.18b, the HRR fit (black dotted line) simulates the slope of the in-cylinder model at the start of combustion well. However, after reaching TDC, the HRR fit method over predicts the heat release rate, which may indicate that a single-Wiebe function is not sufficient to simulate the entire HRR curve. While a greater similarity in the HRR curve has been observed for the HRR fit approach, the RCO fit showed more accurate results in the pressure and temperature distributions. This makes the HRR fit a less accurate method in predicting the combustion characteristics when compared to the RCO fit. A brief summary of the combustion characteristics for both methods can be found in Table 7.7.

---

[5] This method is be called the HRR fit in the following graphs.

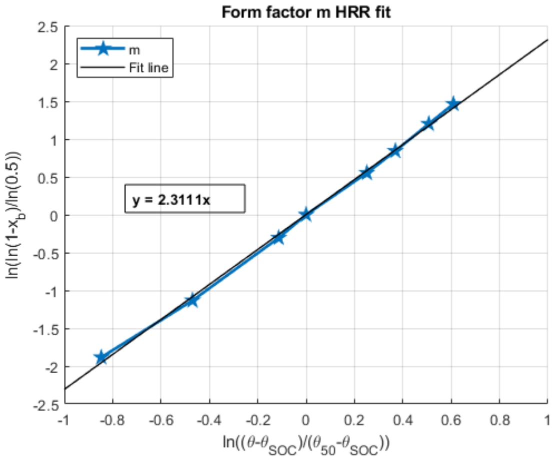

(a)

Figure 7.16: (a) Form factor m at each time instant when including the negative HRR at the beginning of the compression stroke.

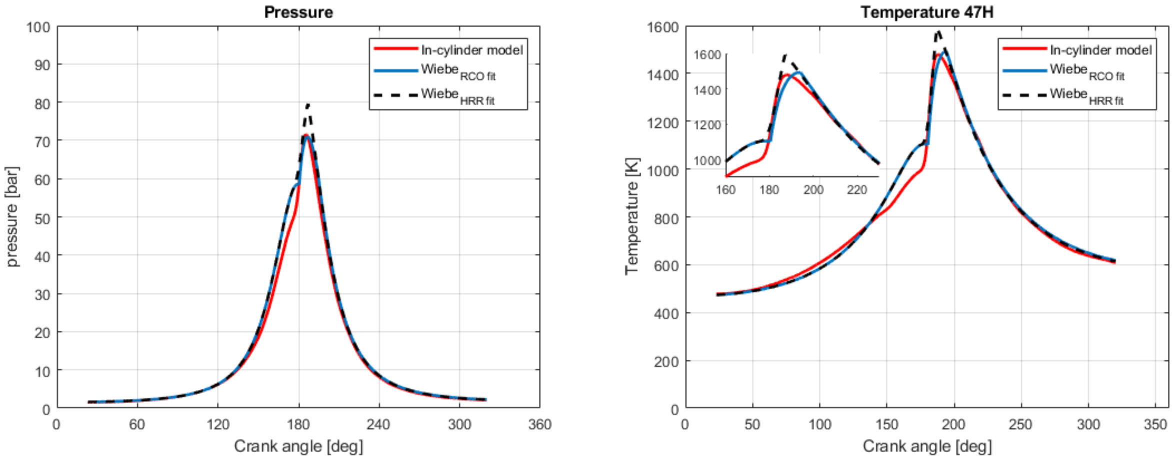

(a) (b)

Figure 7.17: (a) Pressure and (b) temperature distribution for the in-cylinder model from **Chapter 6** (S Law engine) and the simulated single-Wiebe function.

7.10 Conclusions

A reduction can be expected in the accuracy of the combustion characteristics when combining the MKIM, single-Wiebe function and the anti-causal in-cylinder model. The first reduction in the accuracy can be accounted by the polytropic parameter (n_c) and the empirical MKIM parameters that have been set constant during the compression stroke. Shahbakhti et al. [118] observed an average deviation of the predicted SOC of less than 1.0 [CAD] using the MKIM for a range of varying engine conditions.

Furthermore, the fuel type also plays a large role in the average SOC deviation of the MKIM model. He observed a significantly lower average SOC deviation for n-Heptane (0.38 [CAD]) in comparison to iso-octane (0.89 [CAD]) fuel. N-Heptane can be seen as the zero point in the octane rating scale, while iso-octane is in the 100 point range. Hence, a large error in the SOC can also be expected for ammonia

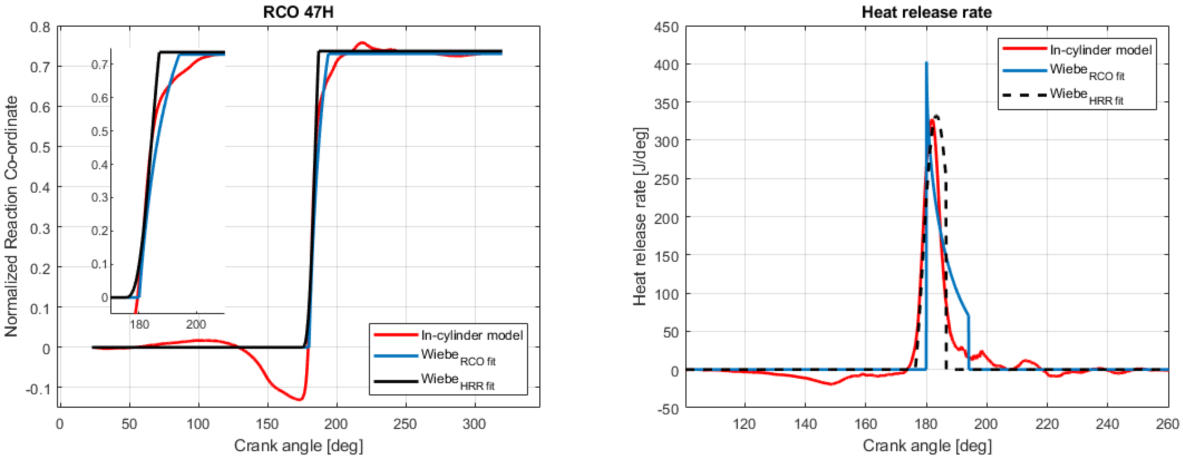

(a) (b)

Figure 7.18: (a) *RCO* and b) heat release rate distribution for the in-cylinder model from **Chapter 6** (S Law engine) and the simulated single-Wiebe function.

Table 7.7: Comparison in combustion characteristics between the in-cylinder model (heat loss calibrated S Law engine) and the Wiebe function for 47 vol percent hydrogen (47H).

	Unit	**In-cylinder model**	**Wiebe(RCO fit)**	**Error [%]**	**Wiebe(HRR fit)**	**Error [%]**
IMEP	$[bar]$	2.651	2.623	1.06	2.657	0.23
P_i	$[kW]$	11.93	11.80	1.09	11.96	0.25
m_{bf}	$[mg]$	81.622	85.867	-5.20	86.650	-6.16
Heat loss	$[kJ/cycle]$	0.818	0.880	-7.58	0.898	-9.78
η_{comb}	$[-]$	0.719	0.724	-0.70	0.731	-1.67
η_q	$[-]$	0.628	0.620	1.27	0.615	2.07
η_{td}	$[-]$	0.692	0.659	4.77	0.667	3.61
η_i	$[-]$	0.3146	0.2996	4.77	0.3011	4.29
T_{max}	$[K]$	1480	1494	4.77	1587	7.23
P_{max}	$[bar]$	71.56	70.96	4.77	79.59	11.22

fuel, because of its high octane value of 130. However, we do not know how accurately the MKIM function is able to predict the auto-ignition crank angle for hydrogen-ammonia fuel and HCCI combustion, since there are no papers published concerning this topic.

7.10.1 MKIM model conclusions

An overview of the expected trend in the start of combustion crank angle when altering the inlet & temperature, engine speed and equivalence ratio can be found in Table 7.8. The conclusions drawn from the MKIM function are as follows:

- The empirical parameters from the MKIM function are influenced by the fuel properties, engine geometry and the operational condition. Since there is no data available for ammonia-hydrogen fuel blends, the model has been optimised using iso-octane for the initial start value and it has then been calibrated using the data from the scaled engine model in **Chapter 6**. The knock crank

Table 7.8: Expected trend in the start of combustion for 47H, when altering the initial conditions. Here, an upward arrow in the SOC column means a retardation of the start of combustion.

	Parameter	SOC
↑	Temperature at IVC	↓
↑	Pressure at IVC	↓
↑	Engine speed	↑
↑	Equivalence ratio	↑

angle is highly influenced by the octane rating of the fuel. Hence, iso-octane has been chosen, because of its octane rating that is reasonably close to that of ammonia and hydrogen.

- In order to get a better understanding in which range the iso-octane initial start values will influence the results, the MKIM function has been evaluated for n-heptane (octane rating of zero vs 100 for iso-octane). From the results in Table 7.1 it can be seen that a change in the inlet pressure and equivalence ratio will result in the greatest deviations in SOC, when comparing iso-octane with n-heptane of 50% and 30%, respectively. Since the differences in octane rating between iso-octane (100) and hydrogen-ammonia (130) is smaller, we can expect a smaller deviation in SOC when using iso-octane.

- The difference between n-heptane and iso-octane becomes more pronounced in the Wiebe function. When using the same initial conditions, n-heptane has shown a retardation in the start of combustion, which resulted in a lower power output. However, n-heptane has shown an almost similar combustion characteristic and power output when shifting the location of the start of combustion to TDC by increasing the inlet temperature as can be seen in the results in Table C.3.

7.10.2 Parametric study conclusions

- The intake conditions considered in the KIM and Wiebe model for the parametric study are the inlet pressure, engine speed, equivalence ratio and inlet temperature. Changing the inlet pressure has shown the greatest impact on the engine performance. When increasing the inlet pressure from 1.6 $[bar]$ to 5.6 $[bar]$, the indicated power output increased from 11.80 $[kW]$ to 44.38 $[bar]$. However, an increase in inlet pressure leads to a higher maximum pressure, higher maximum temperature and an earlier start of combustion, which is unfavourable for the engine's structural rigidity.

- Secondly, a greater engine speed will lead to a retardation in the SOC, because of the shortening of the real time combustion period. The transition from 1500 $[rpm]$ to 2000 $[rpm]$ has shown an almost 50% increase in the indicated power. Disadvantages of increasing the engine speed is a reduction in the maximum temperature, an increase in durability problem and an increase in noise. If this is not an issue, then higher engine speeds are preferred because of the lower NOx emissions and higher power densities.

- Thirdly, deviations in the equivalence ratio have not shown to have a large impact on the SOC. Increasing the equivalence ratio increases the maximum temperature, but leads to larger pressure peaks and a shortening of the burn duration. For HCCI combustion, a higher burn duration is generally more beneficial to spread the heat release distribution and therefore also decreases the peak stresses on the engine's structure. Hence, for the equivalence ratio, a compromise has to be made between a longer combustion duration and maintaining a maximum temperature above 1400 [K] to obtain a high combustion efficiency. The equivalence ratio should preferably be as high as possible and will most likely be limited by the structural capability of the engine.

- Finally, the intake temperature plays a crucial factor in the location of the start of combustion crank angle. A small change in the baseline inlet temperature leads to large changes in the location of the SOC. For example, a decrease of 474 [K] to 465 [K] has shown a retardation of the SOC from 0 to 4.89 [$CADaTDC$] and further lowering the temperature leads to misfire. An increase in inlet temperature results in an earlier heat release that is happening during the compression stroke, leading to a lower indicated power. Therefore, it is important to calibrate the inlet temperature to ensure the combustion timing to take place at TDC.

7.10.3 Design proposal conclusions

- Design condition 1 that is based on an extreme scenario in which the intake pressure, equivalence ratio and engines speed have been drastically increased in order to obtain a higher indicated power output. This engine design condition could potentially achieve an indicated power output of 92.48 [kW] for the 47H fuel blend. The HRR peak value is a factor 5.9 times larger in comparison to the results from the S Law engine mentioned in **Chapter 6**. Design 2 is based on a more realistic operational condition. This design has shown an indicated power output of 36.72 [kW] and an HRR peak that is a factor 2.3 times larger in comparison to the S Law engine.
- The power output for both designs are conservative and can be slightly higher if the m parameter from the Wiebe function has been adjusted with the increase in IMEP discussed in **Section 7.9.1**.
- The combustion efficiency that has been fixed during the parametric study could potentially increase the indicated power output for design 1. A higher maximum temperature will lead to a greater combustion efficiency, which has been observed by Pochet et al. [2] and has been discussed in **Section 5.6**.
- For design condition 2, the equivalence ratio, engine speed and inlet pressure are the same for both the 31H and 47H fuel blend. The results shows that the 31H fuel blend is not able to achieve a T_{max} above 1400 [K]. This means that design condition 2 works great for 47H, but an increase in equivalence ratio or a decrease in engine speed is necessary for 31H to meet the T_{max} requirement.

Table 7.9: Overview of the Wiebe and anti-causal modeling results for the baseline engine (**Section 7.6.3**) and the design conditions 1 and 2 mentioned in **Section 7.8** for the 31H and 47H fuel blends.

		31H	47H	31H	47H	31H	47H
	Unit	Baseline	Baseline	Design 1	Design 1	Design 2	Design 2
SOC	[CAD]	185.09	180.00	180.01	180.01	180.03	180.04
Burn duration	[CAD]	12.31	14.00	11.44	12.34	14.80	16.43
IMEP	[bar]	2.58	2.62	11.55	12.33	5.76	6.12
P_i	[kW]	11.61	11.80	86.61	92.48	34.54	36.72
η_i	[$-$]	0.2819	0.3022	0.3291	0.3459	0.2940	0.3114
P_{max}	[bar]	60.45	71.20	262.1	267.80	190.0	194.00
T_{max}	[K]	1437	1490	1608	1655	1356	1394
$m_{f,injected}$	[mg]	144.99	116.04	560.40	477.03	312.33	262.57

7.10.4 Challenge to face for HCCI engines

Optimizing the inlet temperature to shift the SOC to TDC has shown great effect on the indicated efficiency. However, ensuring the start of combustion to happen at TDC during each combustion cycle is a major challenge that still needs lots of research. Ideally, we want to have the engine to work as efficient as possible during changing load conditions. In this respect, an automatic system is required that is able to modify the inlet temperature to achieve SOC around TDC. This system has to continuously monitor the inlet pressure, inlet temperature, equivalence ratio, engine speed, fuel blend composition and the power demand in order to modify the inlet air temperature for the next combustion round.

From the parametric results in **Section 7.7**, it can be seen that a change in inlet pressure, engine speed, equivalence ratio and inlet temperature can have an enormous impact on the crank angle location of the SOC. Especially during a change in load condition, a spontaneous demand in engine load can lead to an increase in injected fuel, inlet pressure or engine speed, which will result in a shift in the SOC. Since HCCI engines are prone to knock and misfire, the system has to quickly modify the inlet temperature to stay outside the knock and misfire region. The system becomes more complex in case we want to integrate the heat exchange from the SOFC. The SOFC-ICE combination mentioned in **Chapter 1** has to face the challenge that the heat exchange has to be perfectly tuned during transient loading. The addition of a hydrogen storage tank, fuel heater and indirect reformer (mentioned in **Chapter 8**) could play a role in managing the inlet temperature to the internal combustion engine. Another option to control the SOC is to continuously modify the hydrogen concentration during each engine cycle. For example, the in-cylinder modelling results in Table 5.6 (**Chapter 5**) showed that decreasing the hydrogen content could be a great way to retard the SOC.

All in all, HCCI engines can become reliable in case its whole operational area can be mapped and implemented into an automated system. Changes in the initial conditions (*i.e.* inlet pressure, engine speed, equivalence ratio, fuel composition and inlet temperature) will result in a shift in the SOC. In this respect, the HCCI engine should be able to anticipate whether the shift in SOC is within the operational area. Otherwise an adjustment in the inlet temperature or fuel composition is necessary to stay outside the early knock and misfire region.

Chapter 8

System design considerations

8.1 Chapter overview

In case the HCCI engine is integrated in an SOFC-ICE combination depicted in Figure 8.1, the engine's inlet temperature is influenced by the heat exchange from the SOFC. This faces the challenge that the heat exchange has to be perfectly matched during transient loading in which the inlet temperature control system requires a high response rate. From the parametric study performed in **Chapter 7**, it became evident that the HCCI engine performance is highly influenced by the intake conditions. Fluctuations in the inlet temperature and hydrogen concentration, for instance, have shown a great impact on the location of the start of combustion crank angle, which can even lead to undesired early knock or misfire. In the combined system, the HCCI engine's low performance during a cold start, its relatively high *NOx* emissions and the fluctuating hydrogen demand during transient loading should be regarded.

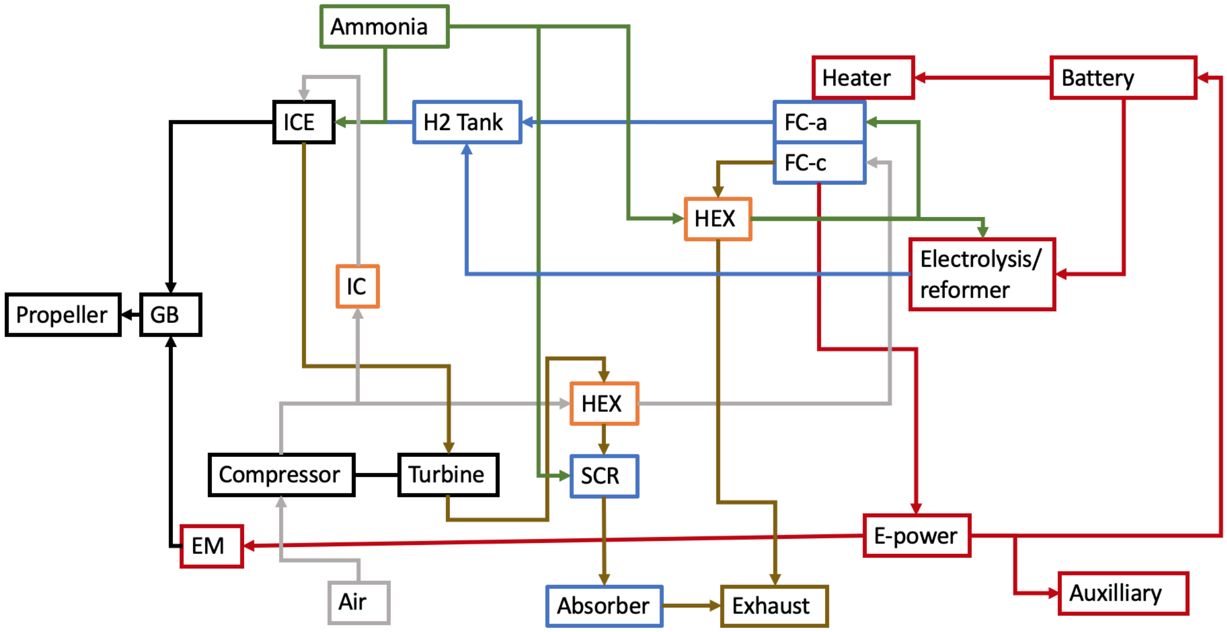

Figure 8.1: SOFC-ICE combination design that includes additional subsystems to enhance the practicality of the system when using HCCI mode.

In this chapter, additional system design considerations are discussed that are able to mitigate the large fluctuations in the HCCI engine's intake conditions. These subsystems will be introduced and elaborated upon the upcoming paragraphs. In **Section 8.6**, two alternative system designs (*i.e.* HCCI ICE only and electric propulsion) will be discussed.

8.2 Cold start

8.2.1 Introduction

Since both the ICE and the SOFC require hydrogen during a cold start, different start-up approaches will be further elaborated upon. The concentration of unburned ammonia in the exhaust is a major concern when starting up the internal combustion engine. Ammonia is toxic to the environment, therefore several mitigation measures have to be introduced.

At low temperatures, the N-H bonds in ammonia are hard to break. Suitable conversion rates of ammonia into hydrogen therefore only start at high temperatures (above 600 [$°C$] for a nickel based catalyst). This indicates that direct reforming of ammonia cannot take place inside an SOFC during a cold start without some system modifications. Moreover, burning pure ammonia in an ICE during a cold start and HCCI mode is not efficient due to incomplete combustion and its high auto-ignition temperature. Combustion instability and low efficiencies, especially at part loads are common phenomenons for ammonia engines that are operating at low hydrogen concentrations. This is due to the narrow flammable limits and low flame speed of ammonia, which indicates that a suitable amount of hydrogen should already be available during a cold start [26]. A possible solution is to have a hydrogen storage tank that is big enough for the cold start and can be recharged when the engines are running at normal conditions.

8.2.2 Ammonia slip and unburned ammonia

In case of direct liquid ammonia injection, the vaporization that shortly happens after injection causes an extreme cooling effect in the cylinder. This cooling effect that can be explained by the large high latent heat of vaporization value of ammonia becomes a critical issue during a cold start. From experiments performed by Koike et al. [26] the unburned ammonia concentration in the exhaust gas for an internal combustion engine during a cold start is about four times higher than that during warmed up operations. Therefore it is necessary to increase the hydrogen ratio during startup. Another alternative that has been proposed by Koike et al. [26] is to place a redox converter and ammonia adsorber at the engine exhaust flow outlet as depicted in Figure 8.2. Emission control during a cold start is still one of the major challenges that have to be solved before ammonia fueled ICEs can be widely used on the market.

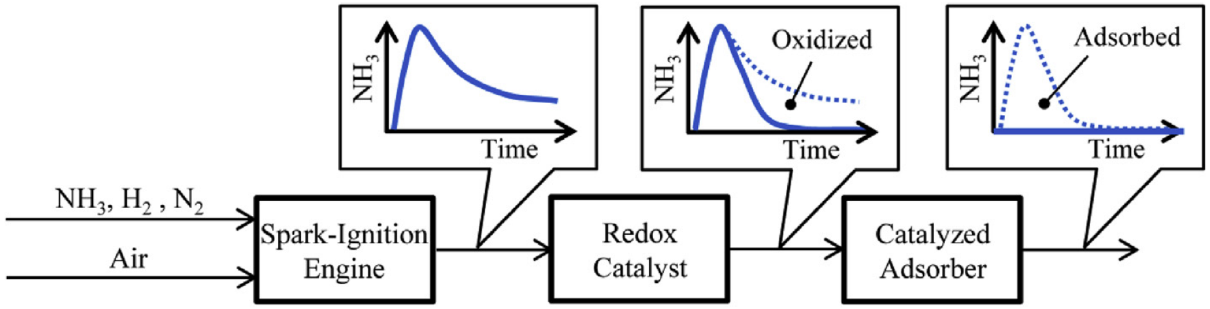

Figure 8.2: Proposed in-line adsorber system by Koike et al. [26] for engines fueled with an ammonia hydrogen mixture

8.2.3 Start-up approach

One way to heat the solid oxide fuel cell to operating temperatures can be achieved by passing high temperature exhaust gases from the ICE through the SOFC stack [49]. However, in case for HCCI mode, large amounts of hydrogen and a high inlet temperature of the air fuel mixture are required to start the engine. In addition, the ICE exhaust gas temperature is according to the in-cylinder model not sufficient enough to fully heat the SOFC to operational temperatures. Hence, a better way to start the SOFC is the use of an electrical heater that heats up one SOFC cell to operational temperatures. The produced heat from the exothermic electro-chemical reaction inside the operating cell can be used to heat adjacent cells in a consecutive manner during the cold start [49]. In addition, to make the cold start more flexible, the ICE should have the option to use SI mode during start up and transition to HCCI combustion after the cold start. This so called 'Hybrid mode' is a way to simplify the start up approach for the SOFC-ICE combination. The inlet temperature for the hydrogen-ammonia fueled SI engine in [98] of 323 $[K]$ is significantly lower in comparison to the 474 $[K]$ requirement for HCCI combustion[1].

8.3 *NOx* emission

8.3.1 Introduction

As mentioned earlier, the high *NOx* concentration in the hydrogen-ammonia HCCI engine's exhaust is a major concern that has to be solved. The *NOx* is primarily produced from fuel-bound nitrogen, which can unlike the nitrogen (N_2) in air easily re-bond with free oxygen during the combustion process. In case of complete ammonia combustion, the end-products of the reaction are nitrogen gas and water vapour as shown in Equation 8.1 [14].

$$4NH_3 + 3O_2 \rightarrow 2N_2 + 6H_2O \tag{8.1}$$

This reaction, however, is only one of the several reactions happening during combustion. To get a more comprehensive understanding of the total emissions being produced by the combustion of ammonia, a detailed analysis of the oxidation pathway is required including a comprehensive understanding of combustion chemistry. Several chemical kinetics models have already been developed and verified including the ones from Kobayashi et al. [14] and Li et al. [72]. *NOx* production is one of the main disadvantages of burning ammonia inside an internal combustion engine (ICE). It has been demonstrated from experiments that increasing the equivalence ratio decreases the production of *NOx* significantly [130]. The NO emission is practically zero at excess air ratios over 3 and a reduction of NO_2 emission below 50 $[ppm]$ at an air excess ratio of 5 [58]. In addition, it has been observed that increasing the hydrogen ratio lead to greater *NOx* emissions [131].

8.3.2 Selective catalytic reduction (SCR)

One way to significantly remove the nitrogen oxides from the exhaust gas (as high as 85 to 90%) is to apply a selective catalytic reduction (SCR) on-board of the ship [21]. The residual ammonia in the exhaust could be used as an additive to the SCR system. The operating temperature of SCRs ranges between 550 to 750 $[K]$ [98], which means that the exhaust gas of the in-cylinder model (550 to 650 $[K]$) does not have to be reheated before entering the SCR. Ammonia has to be supplied to the exhaust gas to initiate the following two reactions:

$$4NO + 4NH_3 + O_2 \rightarrow 4N_2 + 6H_2O \tag{8.2}$$

---

[1] Both engines are running on the same engine speed. The hydrogen content from the SI engine is 40 vol.%, which is slightly higher in comparison to the 38H from the HCCI engine.

and

$$6NO_2 + 8NH_3 \rightarrow 7N_2 + 12H_2O. \tag{8.3}$$

There are, however, some drawbacks, in which cost may play a significant role in the final decision as a ship owner. SCR installations are typically very expensive, take space on-board of a ship and needs additional consumption of ammonia for the reactions to occur. In addition, not all the ammonia reacts with nitrogen oxide, resulting in some some ammonia slip to the environment. The conversion rate usually depends on the quality of mixing and the available reaction time. Another major concern is the formation of N_2O, commonly known as nitrous or laughing gas inside the ICE. This emission substance is one of the significant contributors to the depletion of the ozone layer and because of its high global warming potential, which is around 300 times that of carbon dioxide (CO_2) [80]. Both the spark timing and excess ratio are influencing the formation of N_2O, in which late ignition and high air excess ratios are both contributing to the promotion of N_2O formation [80].

8.4 Hydrogen production

8.4.1 Introduction

It is necessary to investigate whether the hydrogen demand for the ICE can be fully supplied by the anode-off gas of the SOFC. Additional hydrogen production is not only required during a cold start but may also be needed for the ICE to cope with transient loading. In this respect, the response rate, total energy demand and efficiency of both the SOFC and ICE have to be analysed. It is known that solid oxide fuel cells are not great at handling transient loading, therefore a constant ammonia inflow rate is a preferred choice. An external hydrogen production system is necessary when the hydrogen supply from the anode-off gas is insufficient for the ICE.

8.4.2 Electrolyzer

Besides the use of an external indirect internal reformer (discussed in **Section 2.2.1**), the use of an electrolyzer may offer a higher response rate and does not require high temperatures to produce hydrogen. The electrolysis of water is a method to produce oxygen and hydrogen gas, however, a far more efficient method is the electrolysis of ammonia in an ammonia electrolytic cell (AEC) [132]. According to Vitse et al. [133] the theoretical electrolysis of ammonia requires only around 5% of the energy needed for water electrolysis at similar standard conditions. The following reaction occurs on the anode side of the AEC:

$$2NH_3 + 6OH^- \rightarrow N_2 + 6H_2O + 6e^- \tag{8.4}$$

Reaction on the cathode side:

$$6H_2O + 6e^- \rightarrow 3H_2 + 6OH^- \tag{8.5}$$

Here, the hydrogen gas is electro-chemically produced inside the AEC. The overall reaction can be written as:

$$2NH_3 \rightarrow N_2 + 3H_2 \tag{8.6}$$

The theoretical voltage per gram of produced hydrogen at ambient temperature through electrolysis of ammonia is approximately 0.058 $[V]$ with an energy consumption of 1.55 $[Wh]$ [134].

8.5 Hydrogen storage design

8.5.1 Introduction

A hydrogen tank is necessary to temporarily store the anode-off gas hydrogen from the operating SOFC, as a buffer and in case the HCCI engines are turned off. The size and type of the hydrogen storage depends on the response rate of the indirect reformer or electrolyzer and the minimum amount of hydrogen needed for a cold start and during normal operation.

8.5.2 Hydrogen Extraction

Hydrogen and nitrogen gas from the indirect reformer and the anode-off gas from the SOFC can be safely stored together inside a compressed tank. As can be seen in Equation 8.7, 100 [m^3] of ammonia gas fully dissociates into 50 [m^3] of nitrogen gas and 150 [m^3] of hydrogen gas. However, storing both gases together will result in a larger storage unit and more energy is needed to bring down the temperature of the nitrogen and gas mixture for compressed storing.

$$NH_3 \rightarrow \frac{1}{2}N_2 + \frac{3}{2}H_2 \tag{8.7}$$

Moreover, the dilution of hydrogen in nitrogen may lead to a reduction in the burning velocity of the fuel mixture during spark ignition. From experiments, increasing the nitrogen ratio results in a notable reduction of the laminar burning velocity and the diffusivity during injection for SI engines [135]. However, not many experiments have been conducted on the effects of hydrogen-nitrogen based mixtures as a dual fuel promoter for SI engines. Therefore it cannot be safely said whether the nitrogen has to be removed from the mixture. HCCI engines on the other hand, do not face this issue, since the fuel is premixed with air that already consist of 78 vol.% nitrogen before entering the cylinder.

Hence, in case the engine is able to run on SI and HCCI mode, the hydrogen firstly has to be separated from the uncracked ammonia, nitrogen and water vapor in the anode-off gas. A vapor condenser at the end of the anode is necessary to remove water and reduce the temperature of the mass flow. Next, a hydrogen separation membrane should be placed between the vapor condenser and hydrogen storage tank to extract the hydrogen from the nitrogen and leftover ammonia in case pure hydrogen is preferred. Recent developments by CSIRO led to a new membrane design, in which the thin layered metal structure allow hydrogen to pass through the membrane while blocking all other gasses [136]. The high-purity hydrogen gas can than be stored in compressed gas tanks. Another company named Bettergy has made great progress in the development of a high temperature applicable and low cost hydrogen separation membrane that is based on composites [137].

8.5.3 Hydrogen storage

When taking a glance at the refueling aspect of automotive hydrogen vehicles, the hydrogen can either be produced on-site or delivered to the hydrogen refueling stations. On-site hydrogen generation from ammonia is steadily increasing in popularity as ammonia provides in contrast to hydrogen a much better storage and transportation capability. Furthermore, the regulatory and financial barriers are also much lower in comparison to liquid hydrogen transport [138]. Hence, for ships, it is recommended to obtain the stored hydrogen from on-board production rather than from hydrogen delivery stations.

Storing pure gaseous or liquid hydrogen is costly and it must be either compressed to extremely high pressures (in the order of 800 [bar] at room temperature) or cooled down significantly for liquefaction at cryogenic temperatures (ranging from -150 [°C] to -273 [°C]) as can be seen in Figure 8.3b in order to achieve proper storage capabilities [58]. Furthermore, hydrogen can be stored inside a material as depicted in Figure 8.3a. The material-based hydrogen storage method can be divided in three classes: hydride storage systems, liquid (organic) carriers and surface storage systems (sorbents) in which the hydrogen is taken up by adsorption [27].

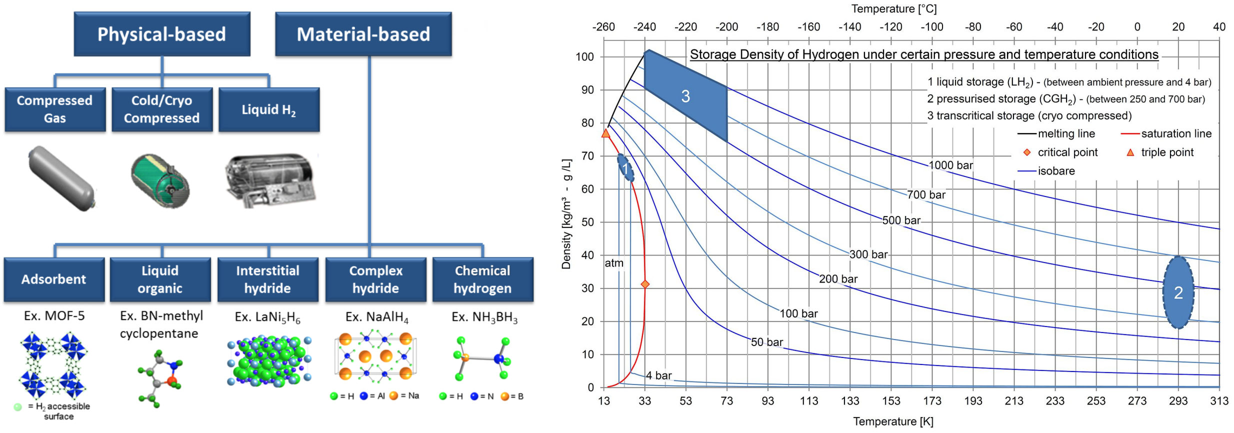

(a)

(b)

Figure 8.3: (a) Possibilities to store hydrogen [27] and (b) net storage density of hydrogen under certain pressure and temperature conditions [28].

Most of the mentioned hydrogen storage methods are, however, still under development and are often inadequate because of the low storage density, the long charge and discharge time and the high cost. Hydrogen storage is mainly needed to provide a sufficient hydrogen flow rate to the ICE during transient loading and a cold start. This means that the response rate of the tank is crucial and should therefore be more important than efficient storing in terms of high gravi- and volumetric energy densities. The compressed pure hydrogen gas storage design might be the best option, however, the temperature of the pressurised hydrogen gas is limited to 40 [°C]. The high temperature hydrogen gas leaving the hydrogen separator membrane has to be drastically cooled that may lead to higher system exergy losses.

8.6 Alternative system designs

8.6.1 Introduction

Most ship types are typically operating at a wide range of operational conditions. Because of this, the hydrogen dependency of the ICE has to be continuously in harmony with the hydrogen output of the SOFC.

In this respect, an electric propulsion system layout could be a more viable solution because of its high flexibility. Hence, in case of electric drive, the internal combustion engines that are connected to a generator can run on its optimal efficiency configuration. This enables the engine operate at its best rotational speed and engine load, commonly at around 75-80% of the maximum continuous ratings (MCR). This eliminates combustion problems which usually occur at part load or an abrupt change in engine load. Since the power demand on-board of ships is not always constant and are highly influenced by its operational profile, batteries are most likely required to temporary store the excessive amount of generated electricity. Nonetheless, electric propulsion is generally more expensive in comparison to direct mechanical drive. Large batteries and generators are necessary, which may negatively impact the overall efficiency of the system. However, in case the propulsion demand is fluctuating a lot, for instance,

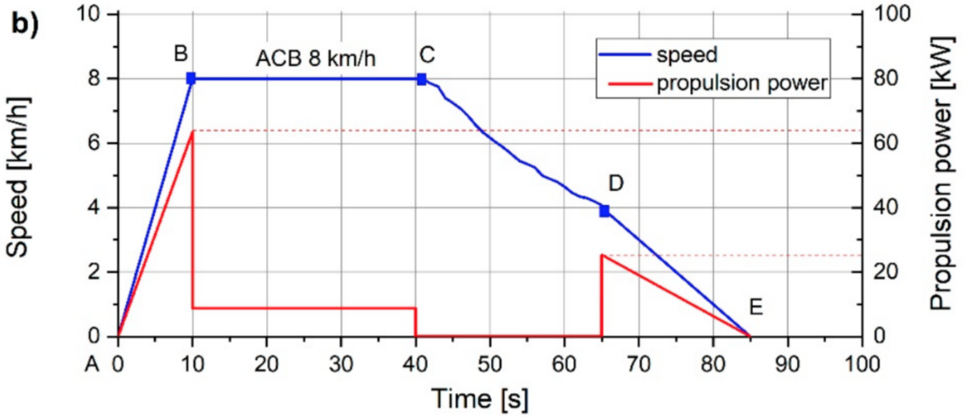

Figure 8.4: Ship speed and power demand of a short-range inland ferry [29].

for short-range inland ferries (Figure 8.5, an electric propulsion system may become a more interesting option.

On the other hand, an ICE only system design depicted in Figure 8.6 may also be an interesting design option that is able to cope with transient loading. In this design, the HCCI engines are not dependent on the heat and hydrogen outflow from the SOFC, but solely on the electrolyzer and electric heater that both have fast response rates. This simplifies the system and enables the HCCI engines to cope with fast changing load conditions. This comes at the cost of a lower overall system efficiency since ammonia fueled SOFCs can reach higher electric efficiencies at around 50%, while hydrogen-ammonia fueled HCCI engines are stuck at around 30 to 35%.

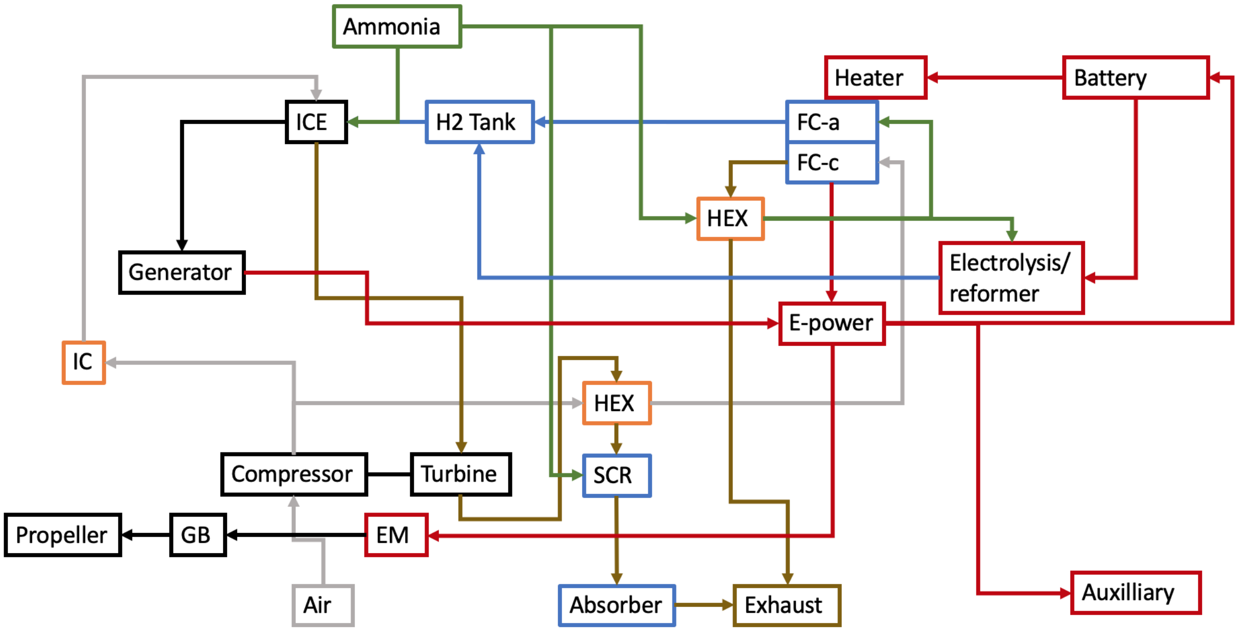

Figure 8.5: System design of the SOFC-ICE combination in case of electric propulsion.

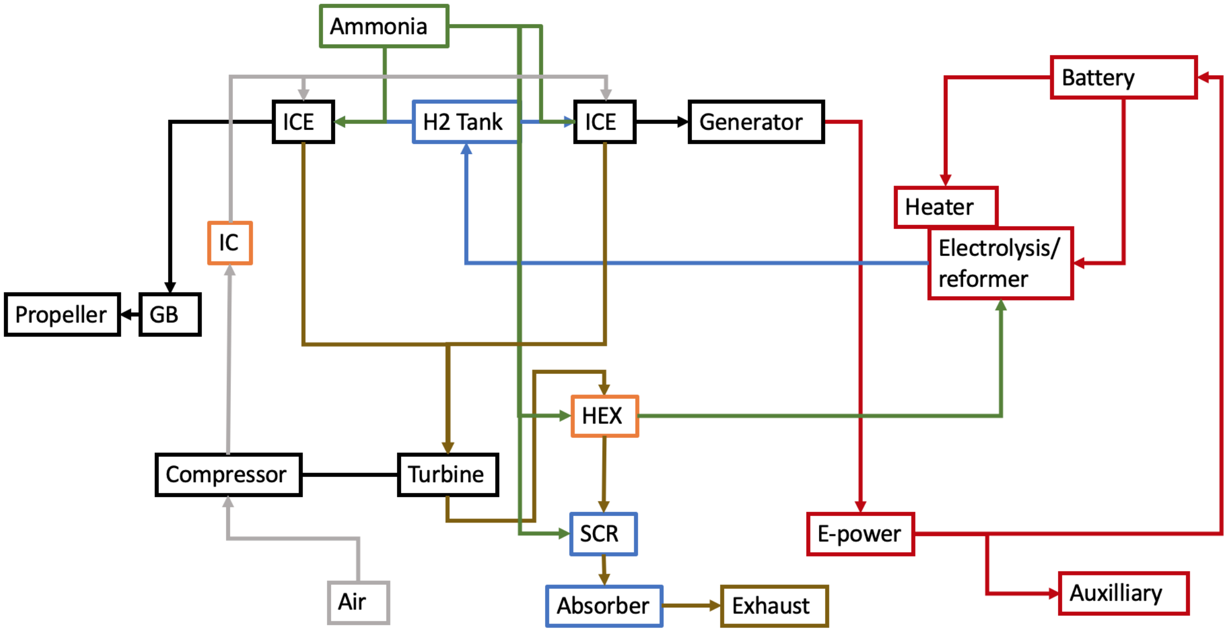

Figure 8.6: System design ICE in combination with an indirect reformer/electrolyzer.

Chapter 9

Conclusions and recommendations

In this chapter the conclusions of this thesis are discussed along with recommendations for further research. First the sub questions are discussed, followed by the main question.

9.1 Conclusions

Sub question 1: Which ignition method is preferred for hydrogen-ammonia combustion?

- HCCI combustion is considered as the preferred ignition method, since it combines the best features of diesel and gasoline to produce diesel like power while maintaining gasoline-like emissions. However, hydrogen-ammonia combustion inside HCCI engines is a novel concept that still requires lots of large-scale experiments to find the optimal engine geometry, operating range and hydrogen concentration.

- Other ignition methods, such as spark ignition and compression ignition methods are less suitable. Ammonia combustion inside an SI engine is not optimal because of the high auto-ignition resistance and low flame propagation speed of ammonia. Hence, poor engine efficiencies and a large amount of unburned fuel are more likely to occur during spark ignition. In addition, the power density of SI engines has been observed to be considerably lower than that of the modeled HCCI engine ($IMEP$ of 0.85 $[bar]$ for the SI engine compared to 2.57 $[bar]$ for the HCCI engine; $FuelMEP$ of 2.4 $[bar]$ and 8.8 $[bar]$, respectively). [1]

- Compression ignition is largely affected by great amounts of NOx production inside the flame zone. The NOx is primarily produced from fuel-bound nitrogen, which can unlike the nitrogen (N_2) in air easily re-bond with free oxygen during the combustion process.

- However, because of the generally small load-range during HCCI combustion, the engine should have the option to switch to SI or diesel mode, when the load cannot be satisfied. This so called 'Hybrid mode' is an optimal way to increase the load range of the engine. Here, the engine is operating in HCCI mode during low to medium load and engine speed conditions, while SI mode is activated during the cold start, idling and at high loads.

Sub question 2: How will engine scaling impact the combustion characteristics and which scaling law is the most suitable when considering the hydrogen-ammonia fueled HCCI test engine?

---

[1] Both the HCCI and SI engine [98] are running on the same engine speed. The hydrogen content from the SI engine is 40 vol.%, which is slightly higher in comparison to the 38H from the HCCI engine.

- The scaling laws[2] are the most effective when two conditions are met. First, the geometric similarity have to be maximised, so that both engines have similar boundary conditions. Secondly, matching combustion characteristics are needed to achieve similarity in engine performances and emissions. However, smaller engines have in contrast to larger engines a relatively greater surface to volume ratio. As a result, smaller engines are subjected to proportionally larger convective heat transfer losses, which translate to a lower pressure rise rate and peak cylinder pressure. Hence, when both engines are operating at the same initial conditions, a higher pressure trace and overall efficiency can be expected in favour of the larger engine. In an ideal situation, the amount of heat release and heat loss are proportional to the in-cylinder volume (L^3) [3]. However, the S Law, P Law and L Law have shown heat loss scaling factors of $L^{2.47}$, $L^{2.57}$ and $L^{2.81}$, respectively, for a 47 vol. hydrogen fuel blend.

- However, apart from the heat release and heat loss, the combustion characteristics are important to consider when using the same pressure trace after scaling. In this respect, the S Law can be considered the best scaling law, since the combustion phasing of both engines can be matched, which enables the combustion process to happen at the same crank angle time basis. This is important for HCCI engines since the combustion characteristics are dictated by the chemical reaction rates.

- Although the S Law has shown the least favourable heat loss scaling factor, additional heat loss calibration can drastically reduce the relative heat loss difference between the scaled and baseline engine. For example, decreasing the wall temperature for the scaled engine lead to a matching cumulative heat loss per mg injected fuel for both engines, but, this method requires a thermal system management strategy, when applied to a real case scenario. However, lowering the wall temperature will result in less optimistic power output than in reality for the scaled engine.

- All in all, engine scaling can be used in obtaining a first impression of the performance output of a marine sized hydrogen-ammonia fueled HCCI engine. However, the results are limited because of the matching combustion characteristics requirement. Marine sized engines typically have greater indicated efficiencies compared to automotive sized engines. Hence, for accurate in-cylinder performance analysis, the scaling laws cannot replace large-scale marine sized engine experiments.

Sub question 3: How will changes in the engine's intake conditions affect the start of combustion and the performance when considering hydrogen-ammonia fueled HCCI engines?

- The intake conditions considered in the Modified Knock Integral Model (MKIM) and Wiebe model for the parametric study are the inlet pressure, engine speed, equivalence ratio and inlet temperature. Changing the inlet pressure has shown the greatest impact on the engine performance. When increasing the inlet pressure from 1.6 $[bar]$ to 5.6 $[bar]$, the indicated power output increased from 11.80 $[kW]$ to 44.38 $[bar]$. However, an increase in inlet pressure leads to a higher maximum pressure, higher maximum temperature and an earlier start of combustion, which is unfavourable for the engine's structural rigidity.

- Secondly, a greater engine speed will lead to a retardation in the SOC, because of the shortening of the real time combustion period. The transition from 1500 $[rpm]$ to 2000 $[rpm]$ has shown an almost 50% increase in the indicated power. Disadvantages of increasing the engine speed are

---

[2] It is necessary to use a scaling law since the available data for hydrogen-ammonia HCCI engines are based on automotive sized engines and not marine sized engines.

[3] L is here the scaling factor based on the size of the engine bore ($L = \frac{D_{B,1}}{D_{B,2}}$).

a reduction in the maximum temperature, an increase in durability problem and an increase in noise. If this is not an issue, then higher engine speeds are preferred because of the lower NOx emissions and higher power densities.

- Thirdly, deviations in the equivalence ratio have not shown to have a large impact on the SOC. Increasing the equivalence ratio increases the maximum temperature, but leads to larger pressure peaks and a shortening of the burn duration. For HCCI combustion, a higher burn duration is generally more beneficial to spread the heat release distribution and, therefore, also decreases the peak stresses on the engine's structure. Hence, for the equivalence ratio, a compromise has to be made between a longer combustion duration and maintaining a maximum temperature above 1400 $[K]$ to obtain a high combustion efficiency. The equivalence ratio should preferably be as high as possible and will most likely be limited by the structural capability of the engine.

- Finally, the intake temperature plays a crucial factor in the location of the start of combustion crank angle. A small change in the baseline inlet temperature leads to large changes in the location of the SOC. For example, a decrease of 474 $[K]$ to 465 $[K]$ has shown a retardation of the SOC from 0 to 4.89 $[CADaTDC]$ and further lowering the temperature leads to misfire. An increase in inlet temperature results in an earlier heat release that is happening during the compression stroke, leading to a lower indicated power. Therefore, it is important to calibrate the inlet temperature to ensure the combustion timing to take place at TDC.

Sub question 4: What should be the preferred hydrogen-ammonia fuel blend ratio for HCCI combustion?

- The hydrogen-ammonia ratio has a direct influence on the maximum in-cylinder temperature. Hydrogen-ammonia HCCI engine experiments by Pochet et al. [2] have shown that a maximum temperature above 1400 $[K]$ is necessary to keep the unburned ammonia concentration to a minimum. Maximum temperatures above 1400 $[K]$ are more difficult to achieve at higher ammonia concentrations. The in-cylinder model has shown a decrease in T_{max} from 1480 $[K]$ to 1389 $[K]$, when lowering the hydrogen ratio from 47H to 31H.

- However, higher ammonia fractions will lead to a more spread out combustion event and a lower HRR peak, which is beneficial since HCCI combustion is commonly afflicted by rapid heat release rates and very high maximum pressures. The 31H fuel blend from the in-cylinder model has shown a factor 1.05 lower IMEP value compared to 47H (2.53 $[bar]$ versus 2.65 $[bar]$), while its maximum HRR and P_{max} are, respectively, 1.34 and 1.22 times lower. Hence, the optimal ammonia fraction should preferably be as high as possible, while maintaining a T_{max} above 1400 $[K]$.

- Finally, in case the HCCI engine is integrated in an SOFC-ICE combination, the engine's inlet temperature is influenced by the heat exchange from the SOFC. This faces the challenge that the heat exchange has to be perfectly tuned during transient loading in which the inlet temperature control system requires a high response rate. Adjustments in the fuel composition could also play a potential role in keeping the engine outside the early undesired knock and misfire region. It has been observed that a 47H fuel blend needs a lower fuel mass flow in contrast to 31H, which means that less heat is necessary to heat the air and fuel mixture. In case the heat exchange from the SOFC unexpectedly drops down, an increase in hydrogen fraction could still keep the engine running at the same load range, while keeping the same hydrogen-ammonia ratio will lead to a retardation of the SOC because of the decrease in inlet temperature. Hence, the hydrogen-ammonia ratio should not be fixed to one value, but should be adjustable according to its operational condition.

Sub question 5: What should be the expected indicated power output and the fuel flow for a hydrogen-ammonia fueled marine sized HCCI engine?

- From the S Law[4] scaled in-cylinder model in **Chapter 6**, a maximum indicated power output per cylinder of 11.93 [kW] and 11.40 [kW] was found for a 47H and 31H fuel blend, respectively. This required a fuel mass flow demand of 1.41 [g/s] and 1.74 [g/s]. The maximum indicated power output are for both fuel blends on the low side, since its mean indicated pressure of 2.65 [bar] is noticeably smaller in contrast to conventional natural aspiring engines that are typically operating at p_{me} values ranging from 5 to 6.2 [bar] [104].
- Hence, some modifications in the initial conditions have been proposed to enhance the power output of the engine. First, the charged air pressure has been increased from 1.6 [bar] to 4.6 [bar] with the addition of a turbocharger. In addition, the engine speed has been increased from 1500 [rpm] to 2000 [rpm], while the equivalence ratio has been decreased from 0.26 [[−]] to 0.20 [[−]] to extend the burn duration. At last the inlet temperature has been optimized to enable the SOC to happen at TDC. The modifications in inlet conditions lead to an indicated power output of 36.72 [kW] and 34.54 [kW] and a fuel mass flow demand of 8.75 [g/s] and 10.41 [g/s] for a 47H and 31H fuel blend, respectively. These values are closer to the target 50 [kW] and 170 [mm] stroke engine that TNO is working on.

Sub question 6: What are the major technical limitations in the SOFC-ICE system when the engine is running in HCCI mode and how can these problems be mitigated?

- **Cold start:** The unburned ammonia concentration in the exhaust gas for an ICE during a cold start is about four times higher than that during warmed up operations [26]. Therefore it is necessary to increase the hydrogen ratio during startup. This means that a suitable amount of hydrogen should already be available during a cold start. A possible solution is to have a hydrogen storage tank which will be recharged when the engines are running at normal conditions. Another option is to place a redox converter and ammonia adsorber at the engine exhaust flow outlet as proposed by Koike et al. [26]. Emission control during a cold start is still one of the major challenges that have to be solved before ammonia fueled ICEs can be widely used on the market. A way to heat the SOFC to operational temperatures is the use of an electrical heater that heats up one SOFC cell to operational temperatures.
- ***NOx* emissions:** *NOx* is primarily produced from fuel-bound nitrogen and is prone to oxidation. One way to significantly remove the nitrogen oxides from the exhaust gas (as high as 85 to 90%) is to apply a selective catalytic reduction (SCR) on-board of the ship [21]. The residual ammonia in the exhaust could be used as an additive to the SCR system. The operating temperature of SCRs ranges between 550 to 750 [K] [98], which means that the exhaust gas of the in-cylinder model (600 [K]) does not have to be reheated before entering the SCR.
- **Hydrogen production:** Combustion instability and low efficiencies, especially at part loads are common for ammonia engines that are operating at low hydrogen concentrations, due to the narrow flammable limits and low flame speed of ammonia [26]. Additional hydrogen production is not only required during a cold start but may also be needed for the ICE to cope with transient loading. During transient loading, the hydrogen supply from the SOFC to the ICE is probably insufficient and therefore an external hydrogen method is necessary. A method to produce hydrogen at ambient temperatures is the use of an ammonia electrolytic cell (AEC) [132]. According to Vitse

---

[4] The engine has been scaled from an 88[mm] stroke to 170 [mm].

et al. [133] the theoretical electrolysis of ammonia requires only around 5% of the energy needed for water electrolysis at similar standard conditions.

- **Fluctuating hydrogen demand:** In the case of excess hydrogen from the SOFC, a hydrogen tank may be necessary to temporarily store the anode-off gas hydrogen. The size and type of the hydrogen storage depend on the response rate of the indirect reformer/ electrolyzer and the minimum amount of hydrogen needed for a cold start. The hydrogen storage is mainly needed to provide a sufficient hydrogen flow rate to the ICE during transient loading and a cold start. This means that the reaction response of the tank is crucial and should therefore be more important than efficient storing in terms of high gravi- and volumetric energy densities. The compressed pure hydrogen gas storage design might be the best option, however, the temperature of the pressurised hydrogen gas is limited to 40 [$°C$]. The high temperature hydrogen gas leaving the hydrogen separator membrane has to be drastically cooled, which requires additional heat exchangers that will lead to higher system exergy losses.

Main question: What is the impact of hydrogen-ammonia combustion on the performance of a marine-sized engine in relation to ammonia fueled SOFC-ICE system design, and how to quantify the operation of the hydrogen-ammonia engine to investigate energy efficiency, engine scaling, and engine performance?

Hydrogen-ammonia combustion inside an internal combustion engine is a novel concept that includes lots of unexplored areas. In this thesis, four models have been developed including the in-cylinder model, scaled engine model, MKIM and the Wiebe function to answer the main research question stated in **Section 1.3**. Firstly, from the in-cylinder model it can be concluded that hydrogen-ammonia HCCI combustion has shown stable engine performances at volumetric hydrogen concentrations between 31% and 47%. Secondly, scaling laws are more accurate for small differences in bore sizes between the baseline and scaled engine. Hence, it is not recommended to scale an automotive sized engine to a marine or truck sized variant, since this will affect the accuracy of the scaled model as a result of the noticeable difference in combustion characteristics between both engines. However, because of the absence of hydrogen-ammonia experiments on marine sized engines, theoretical engine scaling laws are the sole methods to obtain insight in the power output of larger sized engines. The S Law has shown respectable results in terms of combustion characteristics after the heat loss calibration. However, this modelling approach will show less optimistic power outputs in comparison to a real case scenario.

At last, from the MKIM and Wiebe function, a list of variations in the initial conditions have been analyzed in the parametric study to obtain insight into how these variations will impact the HCCI engine's combustion characteristics. The analysis showed that the location of the HCCI engine's start of combustion crank angle is largely controlled by the intake temperature, while the intake pressure has the highest influence on the power output. From the parametric study it became evident that the performance of the HCCI engine is greatly affected by the intake conditions, which makes the integration of HCCI mode inside an SOFC-ICE design combination a risky move because of the slow response rate of the SOFC. In order to use HCCI mode, a dynamic ignition control system is necessary, in which the engine should be able to anticipate whether the shift in SOC is within its operational area. If not, adjustments in the inlet temperature, injected fuel mass, equivalence ratio, effective compression ratio and/or fuel composition are necessary to stay outside the early undesired knock and misfire region.

9.2 Recommendations and future works

- First and foremost, the in-cylinder model discussed in **Chapter 5** should be verified and validated using a complete experimental data set. The model's accuracy is deteriorated since it has been based on large numbers of assumptions and incomplete pressure distributions. In addition, the exact heat transfer coefficients and cylinder wall temperatures for the heat loss model are unknown and for more accurate results, these values have to be determined using detailed heat flux measurements. Thus, new sets of large-scaled hydrogen-ammonia fueled engine experiments are necessary to obtain a more accurate and reliable hydrogen-ammonia HCCI engine model. The experiments should preferably be conducted on marine sized engines, since the implementation of scaling laws will lead to less optimistic and less accurate engine performances because of the additional heat loss calibration.

- Besides a complete set of experimental data, the accuracy of the in-cylinder model could be enhanced by replacing its single-zone heat release model for a multi-zone model that includes crevice and quench layer zones. This is especially important for ammonia fuel because of its low propagation speed and long quenching distance. In addition, the upgrade to a multi-zone model also showed more accurate results in predicting the auto-ignition timing.

- In order to obtain a more accurate MKIM model, the start values discussed in **Section 7.5.1** have to be optimized for hydrogen-ammonia combustion. In an ideal situation, these values are experimentally obtained from a rapid compression machine for each hydrogen-ammonia ratio. In addition, the MKIM empirical parameters should be further optimised using engine data from a range of operational conditions.

- The parametric study in **Section 7.7** may not be accurate since the m value in the Wiebe model does not vary at different initial conditions. Therefore, engine experiments are necessary to validate the results from the parametric study. In addition, the single-Wiebe model becomes inaccurate after reaching 190 $[CAD]$ as can be seen in Figure 7.11a. Hence, a double-Wiebe or triple-Wiebe model may lead to more accurate results. In addition, the over prediction in the Single-Wiebe function is caused by the slower combustion phase near the cylinder walls that is neglected in the single-zone heat release model. In this respect, a multi-zone approach in which a separate wall-zone is included in the model could offer more accurate results.

- The practicality of proton conducting SOFCs (SOFC-H) inside an SOFC-ICE combination has to be investigated. This type of fuel cell can operate at lower temperatures which enhances the durability of the stack. In addition, the absence of water in the output of the anode removes the vapor condenser subsystem requirement that would otherwise be placed between the anode-off gas and the hydrogen storage tank. For the HCCI engine, its intake temperature requirement can be reduced when the engine is running at higher compression ratios. A lower intake temperature could potentially also lead to a higher power output, since more fuel and air can be injected in the cylinder because of the increased inlet air density.

- In case of an HCCI-SI hybrid system, the transition between both ignition methods has to be studied thoroughly for hydrogen-ammonia fuel. There are great differences in the initial conditions between HCCI and SI combustion. For instance, the hydrogen-ammonia fueled SI engine in [98] uses an inlet temperature of 323 $[K]$ and an equivalence ratio of 1, which is different in contrast to the requirements for the HCCI engine (474 $[K]$ and 0.26). The transition from SI to HCCI combustion is therefore a complex process that requires high level of dynamic control. The latter becomes even more challenging when we want to have a stable transition during transient loading.

- Finally, the SOFC-ICE design has to be dynamically modeled to gain insight into the performance of the combination during transient loading. The model should include the response rates of all subsystems ($i.e.$ electrolyzer/indirect reformer and hydrogen tank).

Bibliography

[1] Donggeun Lee and Han Ho Song. Development of combustion strategy for the internal combustion engine fueled by ammonia and its operating characteristics. *Journal of Mechanical Science and Technology*, 32(4):1905–1925, 2018.

[2] Maxime Pochet, Hervé Jeanmart, and Francesco Contino. The use of ammonia in hcci piston engines.

[3] Takemi Chikahisa and Tadashi Murayama. Theory on combustion similarity for different-sized diesel engines. *JSME international journal. Ser. 2, Fluids engineering, heat transfer, power, combustion, thermophysical properties*, 33(2):395–400, 1990.

[4] Laine A Stager and Rolf D Reitz. Assessment of diesel engine size-scaling relationships. Technical report, SAE Technical Paper, 2007.

[5] Mike Bergin, Rolf D Reitz, and Randy P Hessel. Soot and nox emissions reduction in diesel engines via spin-spray combustion. In *ILASS American, 18th Annual Conference on Liquid Atomization and Spray Systems, Irvine, CA*, 2005.

[6] DNV-GL. *Maritime Forecast to 2050.* Energy Transition Outlook 2019, 2019.

[7] Anders Valland. Transitioning from traditional to alternative fuels, https://vpoglobal.com/2019/11/22/transitioning-from-traditional-to-alternative-fuels/, (accessed: 12-12-2019).

[8] John Murphy. *Ammonia Production: Recent Advances in Catalyst and Process Technology and Impacts on the Competitive Landscape.* TCG The Catalyst Group, 2018.

[9] Jeffrey Ralph Bartels. A feasibility study of implementing an ammonia economy. 2008.

[10] James Larminie and Andrew Dicks. *Fuelling Fuel Cells.* John Wiley Sons, Ltd, 2013.

[11] Ahmed Afif, Nikdalila Radenahmad, Quentin Cheok, Shahriar Shams, Jung H Kim, and Abul K Azad. Ammonia-fed fuel cells: a comprehensive review. *Renewable and Sustainable Energy Reviews*, 60:822–835, 2016.

[12] V. Hacker and K. Kordesch. *Ammonia Crackers.* John Wiley Sons, Ltd Chichester, 2003.

[13] Qianli Ma, Jianjun Ma, Sa Zhou, Ruiqiang Yan, Jianfeng Gao, and Guangyao Meng. A high-performance ammonia-fueled sofc based on a ysz thin-film electrolyte. *Journal of Power Sources*, 164(1):86–89, 2007.

[14] Hideaki Kobayashi, Akihiro Hayakawa, KD Kunkuma A Somarathne, and Ekenechukwu C Okafor. Science and technology of ammonia combustion. *Proceedings of the Combustion Institute*, 37(1):109–133, 2019.

[15] Maxime Pochet, Ida Truedsson, Fabrice Foucher, Hervé Jeanmart, and Francesco Contino. " experimental hcci engine using hydrogen and ammonia. In *8th European Combustion Meeting*, 2017.

[16] Stefano Frigo and Roberto Gentili. Analysis of the behaviour of a 4-stroke si engine fuelled with ammonia and hydrogen. *International Journal of Hydrogen Energy*, 38(3):1607–1615, 2013.

[17] Abdul Rashid Abdul Aziz, Morgan Raymond Heikal, Ezrann Zharif Zainal Abidin, Naveenchandran Panchatcharam, et al. Reactivity controlled compression ignition (rcci) of gasoline-cng mixtures. In *Improvement Trends for Internal Combustion Engines*. IntechOpen, 2018.

[18] X-Engineer. Air-fuel ratio, lambda and engine performance, https://x-engineer.org/automotive-engineering/internal-combustion-engines/performance/air-fuel-ratio-lambda-engine-performance/, (accessed: 20-02-2020).

[19] C. Lhuillier, Pierre Brequigny, F Contino, and C Mounaïm-Rousselle. EXPERIMENTAL STUDY ON NH3/H2/AIR COMBUSTION IN SPARK-IGNITION ENGINE CONDITIONS. In *11th Mediterranean Combustion Symposium*, Tenerife, Spain, June 2019.

[20] Catherine Duynslaegher. Experimental and numerical study of ammonia combustion. *University of Leuven*, pages 1–314, 2011.

[21] D Stapersma. *Diesel Engines, Volume 3*. DELFT UT, 2009.

[22] François Boveroux, Amaury Gramme, and Hervé Jeanmart. Développement expérimental d'un moteur hcci au gaz naturel, 2016.

[23] Maxime Pochet, Ida Truedsson, F. Foucher, Hervé Jeanmart, and Francesco Contino. Ammonia-hydrogen blends in homogeneous-charge compression-ignition engine. *SAE Technical Papers*, 2017-24-0087, 09 2017.

[24] Lad Pratik. How does the ratio of stroke and the radius of a cylinder in ice affect the power output?, https://www.quora.com/how-does-the-ratio-of-stroke-and-the-radius-of-a-cylinder-in-ice-affect-the-power-output, (accessed: 06-07-2020).

[25] Yu Shi, Hai-Wen Ge, and Rolf D Reitz. *Computational optimization of internal combustion engines*. Springer Science & Business Media, 2011.

[26] Makoto Koike and Tetsunori Suzuoki. In-line adsorption system for reducing cold-start ammonia emissions from engines fueled with ammonia and hydrogen. *International Journal of Hydrogen Energy*, 44(60):32271–32279, 2019.

[27] Energy.gov. Hydrogen storage,https://www.energy.gov/eere/fuelcells/hydrogen-storage, (accessed: 17-01-2020).

[28] Moritz Kuhn ILK Dresden. Net storage density of hydrogen,http://www.ilkdresden.de/en/service/research-and-development/project/hydrogen-test-area-at-ilk-dresden/, (accessed: 17-01-2020).

[29] Magdalena Kunicka and Wojciech Litwin. Energy demand of short-range inland ferry with series hybrid propulsion depending on the navigation strategy. *Energies*, 12(18):3499, 2019.

[30] Carlo Trozzi. Emission estimate methodology for maritime navigation. *Techne Consulting, Rome*, 2010.

[31] Francesco Baldi, Fredrik Ahlgren, Tuong-Van Nguyen, Marcus Thern, and Karin Andersson. Energy and exergy analysis of a cruise ship. *Energies*, 11(10):2508, 2018.

[32] M Nazemi and M Shahbakhti. Modeling and analysis of fuel injection parameters for combustion and performance of an rcci engine. *Applied Energy*, 165:135–150, 2016.

[33] Joris Rusman. Charge air configurations for propulsion diesel engines aboard fast naval combatants: a simulation study on efficiency and performance. 2018.

[34] D Stapersma. *Diesel Engines, Volume 1*. DELFT UT, 2009.

[35] Bonnie J McBride. *Coefficients for calculating thermodynamic and transport properties of individual species*, volume 4513. National Aeronautics and Space Administration, Office of Management ..., 1993.

[36] IMO. Reducing greenhouse gas emissions from ships, https://www.imo.org/en/mediacentre/hottopics/pages/reducing-greenhouse-gas-emissions-from-ships.aspx, (accessed: 06-07-2020).

[37] MAN Energy Solutions. Engineering the future two-stroke green-ammonia engine. 2020.

[38] Solid ammonia as energy carrier: Current status and future prospects. *Fuel Cells Bulletin*, 2009(10):12 – 15, 2009.

[39] George Zacharakis-Jutz. Performance characteristics of ammonia engines using direct injection strategies. 2013.

[40] Walter S. Kessler. *The Good, the Bad, and The Ugly of using Anhydrous Ammonia Refrigerant in the Process Industries*. PhD thesis.

[41] G Cinti, G Discepoli, E Sisani, and Umberto Desideri. Sofc operating with ammonia: stack test and system analysis. *International Journal of Hydrogen Energy*, 41(31):13583–13590, 2016.

[42] George Thomas and George Parks. *Potential Roles of Ammonia in a Hydrogen Economy*. U.S. Department of Energy, 2006.

[43] L Van Biert, M Godjevac, K Visser, and PV Aravind. A review of fuel cell systems for maritime applications. *Journal of Power Sources*, 327:345–364, 2016.

[44] T Okanishi, K Okura, A Srifa, H Muroyama, T Matsui, M Kishimoto, M Saito, H Iwai, H Yoshida, M Saito, et al. Comparative study of ammonia-fueled solid oxide fuel cell systems. *Fuel Cells*, 17(3):383–390, 2017.

[45] Christopher W Gross and Song-Charng Kong. Performance characteristics of a compression-ignition engine using direct-injection ammonia–dme mixtures. *Fuel*, 103:1069–1079, 2013.

[46] Shawn M Grannell, Dennis N Assanis, Stanislav V Bohac, and Donald E Gillespie. The fuel mix limits and efficiency of a stoichiometric, ammonia, and gasoline dual fueled spark ignition engine. *Journal of engineering for gas turbines and power*, 130(4), 2008.

[47] Aaron J Reiter and Song-Charng Kong. Combustion and emissions characteristics of compression-ignition engine using dual ammonia-diesel fuel. *Fuel*, 90(1):87–97, 2011.

[48] Bernhard Stoeckl, Vanja Subotić, Michael Preininger, Marcel Schwaiger, Nikola Evic, Hartmuth Schroettner, and Christoph Hochenauer. Characterization and performance evaluation of ammonia as fuel for solid oxide fuel cells with ni/ysz anodes. *Electrochimica acta*, 298:874–883, 2019.

[49] KHM Al-Hamed and I Dincer. A new direct ammonia solid oxide fuel cell and gas turbine based integrated system for electric rail transportation. *ETransportation*, 2:100027, 2019.

[50] Bernhard Stoeckl, Michael Preininger, Vanja Subotić, Hartmuth Schroettner, Peter Sommersacher, Michael Seidl, Stefan Megel, and Christoph Hochenauer. Ammonia as promising fuel for solid oxide fuel cells: Experimental analysis and performance evaluation. *ECS Transactions*, 91(1):1601, 2019.

[51] Osamah Siddiqui and Ibrahim Dincer. A review and comparative assessment of direct ammonia fuel cells. *Thermal Science and Engineering Progress*, 5:568–578, 2018.

[52] Parisa Mojaver, Ata Chitsaz, Mohsen Sadeghi, and Shahram Khalilarya. Comprehensive comparison of sofcs with proton-conducting electrolyte and oxygen ion-conducting electrolyte: Thermoeconomic analysis and multi-objective optimization. *Energy Conversion and Management*, 205:112455, 2020.

[53] Miyague Ni, MKH Leung, and DYC Leung. Mathematical modelling of proton-conducting solid oxide fuel cells and comparison with oxygen-ion-conducting counterpart. *Fuel Cells*, 7(4):269–278, 2007.

[54] Yildiz Kalinci and Ibrahim Dincer. Analysis and performance assessment of nh3 and h2 fed sofc with proton-conducting electrolyte. *International Journal of Hydrogen Energy*, 43(11):5795–5807, 2018.

[55] Ahmed Fathi Salem Molouk, Jun Yang, Takeou Okanishi, Hiroki Muroyama, Toshiaki Matsui, and Koichi Eguchi. Comparative study on ammonia oxidation over ni-based cermet anodes for solid oxide fuel cells. *Journal of Power Sources*, 305:72–79, 2016.

[56] Adam Wojcik, Hugh Middleton, Ioannis Damopoulos, et al. Ammonia as a fuel in solid oxide fuel cells. *Journal of Power Sources*, 118(1-2):342–348, 2003.

[57] Petach Tikvah. Gencell, https://www.gencellenergy.com/news/bird-energy-awards-1-7m-multi-year-rd-grant-to-gencell-energy-and-american-energy-technologies/, (accessed: 17-03-2020).

[58] C Zamfirescu and I Dincer. Ammonia as a green fuel and hydrogen source for vehicular applications. *Fuel processing technology*, 90(5):729–737, 2009.

[59] Guangyao Meng, Cairong Jiang, Jianjun Ma, Qianli Ma, and Xingqin Liu. Comparative study on the performance of a sdc-based sofc fueled by ammonia and hydrogen. *Journal of Power Sources*, 173(1):189–193, 2007.

[60] A Fuerte, RX Valenzuela, MJ Escudero, and L Daza. Ammonia as efficient fuel for sofc. *Journal of Power Sources*, 192(1):170–174, 2009.

[61] Anthony J Martyr and Michael Alexander Plint. *Engine testing: the design, building, modification and use of powertrain test facilities.* Elsevier, 2012.

[62] Crookes R J Rose J W Cooper, J R and A Mozafari. Ammonia as a fuel for the ic engine, Dec 1991.

[63] Peter Van Blarigan. Advanced internal combustion engine research. *DOE Hydrogen Program Review NREL-CP-570-28890*, pages 1–19, 2000.

[64] Ernest S Starkman, HK Newhall, R Sutton, T Maguire, and L Farbar. Ammonia as a spark ignition engine fuel: theory and application. *Sae Transactions*, pages 765–784, 1967.

[65] Christine Scott Gable. What is spark ignition https://www.thoughtco.com/what-is-spark-ignition-85381, (accessed: 20-12-2019).

[66] Pavlos Dimitriou and Rahat Javaid. A review of ammonia as a compression ignition engine fuel. *International Journal of Hydrogen Energy*, 2020.

[67] Emtiaz Brohi. Ammonia as fuel for internal combustion engines? Master's thesis, 2014.

[68] Jeroen Reurings. A modeling study to investigate performance of sofc-ice hybrid systems for marine applications. 2019.

[69] Aaron J Reiter and Song-Charng Kong. Combustion and emissions characteristics of compression-ignition engine using dual ammonia-diesel fuel. *Fuel*, 90(1):87–97, 2011.

[70] Rouhollah Ahmadi and S Mohammad Hosseini. Numerical investigation on adding/substituting hydrogen in the cdc and rcci combustion in a heavy duty engine. *Applied energy*, 213:450–468, 2018.

[71] Sage Lucas Kokjohn. *Reactivity controlled compression ignition (RCCI) combustion.* PhD thesis, The University of Wisconsin-Madison, 2012.

[72] Jun Li, Hongyu Huang, Lisheng Deng, Zhaohong He, Yugo Osaka, and Noriyuki Kobayashi. Effect of hydrogen addition on combustion and heat release characteristics of ammonia flame. *Energy*, 175:604–617, 2019.

[73] JH Lee, SI Lee, and OC Kwon. Effects of ammonia substitution on hydrogen/air flame propagation and emissions. *International journal of hydrogen Energy*, 35(20):11332–11341, 2010.

[74] Jun Li, Hongyu Huang, Noriyuki Kobayashi, Zhaohong He, and Yoshihiro Nagai. Study on using hydrogen and ammonia as fuels: Combustion characteristics and nox formation. *International journal of energy research*, 38(9):1214–1223, 2014.

[75] Praveen Kumar and Terrence R Meyer. Experimental and modeling study of chemical-kinetics mechanisms for h2–nh3–air mixtures in laminar premixed jet flames. *Fuel*, 108:166–176, 2013.

[76] Akihiro Hayakawa. Enhancement of reaction and stability of ammonia flames using hydrogen addition and swirling flows. *Ammonia Fuel Conference*, 2015.

[77] Akinori Ichikawa, Akihiro Hayakawa, Yuichi Kitagawa, KD Kunkuma Amila Somarathne, Taku Kudo, and Hideaki Kobayashi. Laminar burning velocity and markstein length of ammonia/hydrogen/air premixed flames at elevated pressures. *International journal of hydrogen energy*, 40(30):9570–9578, 2015.

[78] X He, B Shu, D Nascimento, K Moshammer, M Costa, and RX Fernandes. Auto-ignition kinetics of ammonia and ammonia/hydrogen mixtures at intermediate temperatures and high pressures. *Combustion and Flame*, 206:189–200, 2019.

[79] Aliasghar Mozafari-Varnusfadrani. *Predictions and measurements of spark-ignition engine characteristics using ammonia and other fuels.* PhD thesis, 1988.

[80] Fredrik R Westlye, Anders Ivarsson, and Jesper Schramm. Experimental investigation of nitrogen based emissions from an ammonia fueled si-engine. *Fuel*, 111:239–247, 2013.

[81] James G. Speight. Chapter 7 - hydrocarbons from biomass. In James G. Speight, editor, *Handbook of Industrial Hydrocarbon Processes*, pages 241 – 279. Gulf Professional Publishing, Boston, 2011.

[82] Andre Lanz, P Eng, James Heffel, and Colin Messer. Hydrogen use in internal combustion engine. *Published by College of the Desert, Palm Desert, CA, USA Energy Technology Training Center Rev. 0*, page 18, 2001.

[83] Chapter 7. Flame quench modeling, https://shodhganga.inflibnet.ac.in /bitstream/10603/17399/12/12_chapter%207.pdf, (accessed: 29-01-2020).

[84] Guoming G Zhu, Chao F Daniels, and James Winkelman. Mbt timing detection and its closed-loop control using in-cylinder pressure signal. Technical report, SAE Technical Paper, 2003.

[85] M Azzopardi. Dynamic model implementation for a multi-purpose 1-d planar sofc: Gaining insight behaviour into an intermediate temperature sofc. 2017.

[86] Randall S Gemmen and Christopher D Johnson. Effect of load transients on sofc operation—current reversal on loss of load. *Journal of power sources*, 144(1):152–164, 2005.

[87] Y Komatsu, G Brus, Shinji Kimijima, and JS Szmyd. The effect of overpotentials on the transient response of the 300 w sofc cell stack voltage. *Applied energy*, 115:352–359, 2014.

[88] Niels de Vries. New research shows benefits of ammonia as marine fuel,https://www.maritime-executive.com/article/new-research-shows-benefits-of-ammonia-as-marine-fuel, (accessed: 07-01-2020).

[89] Song-Charng Kong and Rolf D Reitz. Numerical study of premixed hcci engine combustion and its sensitivity to computational mesh and model uncertainties. *Combustion Theory and Modelling*, 7(2):417–433, 2003.

[90] Shao-Hua Zhong, Bin Kong, Wyszynski Miroslaw, and Hong-Ming Xu. Comparison of single-zone and multi-zone combustion model for hcci engine. *Neiranji Gongcheng(Chinese Internal Combustion Engine Engineering)*, 28(3):6–10, 2007.

[91] Yu Ding. Characterising combustion in diesel engines: using parameterised finite stage cylinder process models. 2011.

[92] Stijn Broekaert, Thomas De Cuyper, Michel De Paepe, and Sebastian Verhelst. Evaluation of empirical heat transfer models for hcci combustion in a cfr engine. *Applied Energy*, 205:1141–1150, 2017.

[93] HS Soyhan, H Yasar, H Walmsley, B Head, GT Kalghatgi, and C Sorusbay. Evaluation of heat transfer correlations for hcci engine modeling. *Applied Thermal Engineering*, 29(2-3):541–549, 2009.

[94] Günter F Hohenberg. Advanced approaches for heat transfer calculations. *SAE Transactions*, pages 2788–2806, 1979.

[95] Junseok Chang, Orgun Güralp, Zoran Filipi, Dennis Assanis, Tang-Wei Kuo, Paul Najt, and Rod Rask. New heat transfer correlation for an hcci engine derived from measurements of instantaneous surface heat flux. *SAE transactions*, pages 1576–1593, 2004.

[96] Maxime Pochet, Véronique Diasa, Bruno Moreaud, Fabrice Foucherd, Hervé Jeanmarta, and Francesco Continob. Investigation of ammonia ignition delay at low temperatures and lean conditions. In *25th Journées d'Etude*, 2018.

[97] E Sher and Ilai Sher. Theoretical limits of scaling-down internal combustion engines. *Chemical Engineering Science*, 66(3):260–267, 2011.

[98] Charles Lhuillier, Pierre Brequigny, Francesco Contino, and Christine Mounaïm-Rousselle. Experimental study on ammonia/hydrogen/air combustion in spark ignition engine conditions. *Fuel*, 269:117448, 2020.

[99] Flavio DF Chuahy, Jamen Olk, Dan DelVescovo, and Sage L Kokjohn. An engine size–scaling method for kinetically controlled combustion strategies. *International Journal of Engine Research*, page 1468087418786130, 2018.

[100] Chang-Wook Lee, Hai-Wen Ge, Rolf D Reitz, Eric Kurtz, and Werner Willems. Computational optimization of a down-scaled diesel engine operating in the conventional diffusion combustion regime using a multi-objective genetic algorithm. *Combustion science and technology*, 184(1):78–96, 2012.

[101] Xinyi Zhou, Tie Li, Zheyuan Lai, and Bin Wang. Theoretical study on similarity of diesel combustion. Technical report, SAE Technical Paper, 2018.

[102] Xinyi Zhou, Tie Li, Zheyuan Lai, and Bin Wang. Scaling fuel sprays for different size diesel engines. *Fuel*, 225:358–369, 2018.

[103] Michael J Tess, Chang-Wook Lee, and Rolf D Reitz. Diesel engine size scaling at medium load without egr. *SAE International Journal of Engines*, 4(1):1993–2009, 2011.

[104] Hans J Klein Woud and Douwe Stapersma. Design of propulsion and electric power generations systems. *Published by IMarEST, The Institute of Marine Engineering, Science and Technology. ISBN: 1-902536-47-9*, 2003.

[105] T Arisawa, T Arai, Y Sakane, Y Kobashi, G Shibata, and H Ogawa. Cfd analysis of engine size dependence of diesel combustion. In *Proceedings of the 27th ICE symposium of JSAE CDROM, Sapporo*, pages 19–21, 2016.

[106] Xinyi Zhou, Tie Li, Yijie Wei, and Sichen Wu. Scaling spray combustion processes in marine low-speed diesel engines. *Fuel*, 258:116133, 2019.

[107] Goldenstein Christopher. Advanced combustion engines, http://large.stanford.edu/courses/2011-/ph240/goldenstein2/, (accessed: 08-07-2020).

[108] S Bernhard Gand. *Invloed van de slag-boorverhouding "a verhouding op het proces van de benzinemotor.* PhD thesis, Rheinisch-Westf "a lische Technische Hochschule Aachen, 1986.

[109] Werner Bick. *Invloed van geometrische basisgegevens op het werkproces van de benzinemotor met verschillende slag-boorverhoudingen.* PhD thesis, Rheinisch-Westf "a lische Technische Hochschule Aachen.

[110] Harry Hamann, Daniel Münning, Philip Gorzalka, Michael Zillmer, and Peter Eilts. Efficiency scaling method of gasoline engines for different geometries and the application in hybrid vehicle simulation. *International Journal of Engine Research*, 18(7):732–751, 2017.

[111] René Wolf and Peter Eilts. Comparison of fuel consumption and emissions of automotive and large-bore diesel engines. *SAE International Journal of Engines*, 7(1):221–233, 2014.

[112] Prasad Shingne, Dennis N Assanis, Aristotelis Babajimopoulos, Philip Keller, David Roth, and Michael Becker. Turbocharger matching for a 4-cylinder gasoline hcci engine using a 1d engine simulation. Technical report, SAE Technical Paper, 2010.

[113] Hanho Yun, Nicole Wermuth, and Paul Najt. Extending the high load operating limit of a naturally-aspirated gasoline hcci combustion engine. *SAE international Journal of Engines*, 3(1):681–699, 2010.

[114] Hua Zhao. *HCCI and CAI engines for the automotive industry*. Elsevier, 2007.

[115] Neofytos P Komninos, Dimitrios T Hountalas, and DA Kouremenos. Description of in-cylinder combustion processes in hcci engines using a multi-zone model. Technical report, SAE Technical paper, 2005.

[116] Mahdi Shahbakhti, Robert Lupul, and Charles Robert Koch. Sensitivity analysis & modeling of hcci auto-ignition timing. *IFAC Proceedings Volumes*, 40(10):303–310, 2007.

[117] Seokwon Cho, Jihwan Park, Chiheon Song, Sechul Oh, Sangyul Lee, Minjae Kim, and Kyoungdoug Min. Prediction modeling and analysis of knocking combustion using an improved 0d rgf model and supervised deep learning. *Energies*, 12(5):844, 2019.

[118] Mahdi Shahbakhti. Modeling and experimental study of an hcci engine for combustion timing control. 2009.

[119] Kevin Swan, Mahdi Shahbakhti, and Charles Robert Koch. Predicting start of combustion using a modified knock integral method for an hcci engine. *SAE Transactions*, pages 611–620, 2006.

[120] Octane Rating. Table, https://www.degruyter.com/view/journals/pac/55/2/article-p199.xml, (accessed: 08-07-2020).

[121] Jerald A Caton. Thermodynamic considerations related to knock: Results from an engine cycle simulation. *Journal of Engineering for Gas Turbines and Power*, 140(9), 2018.

[122] Peter Eilts, Claude-Pascal Stoeber-Schmidt, and René Wolf. Investigation of extreme mean effective and maximum cylinder pressures in a passenger car diesel engine. Technical report, SAE Technical Paper, 2013.

[123] Halit Yasar, Hakan Serhad Soyhan, Harold Walmsley, Bob Head, and Cem Sorusbay. Double-wiebe function: An approach for single-zone hcci engine modeling. *Applied Thermal Engineering*, 28(11-12):1284–1290, 2008.

[124] G Abbaszadehmosayebi and Lionel Ganippa. Characterising wiebe equation for heat release analysis based on combustion burn factor (ci). *Fuel*, 119:301–307, 2014.

[125] A Uludogan, David E Foster, and Rolf D Reitz. Modeling the effect of engine speed on the combustion process and emissions in a di diesel engine. Technical report, SAE Technical Paper, 1996.

[126] Thomas Johansson, Patrick Borgqvist, Bengt Johansson, Per Tunestal, and Hans Aulin. Hcci heat release data for combustion simulation, based on results from a turbocharged multi cylinder engine. Technical report, SAE Technical Paper, 2010.

[127] Miguel Torres García, Francisco José Jiménez-Espadafor Aguilar, Tomás Sánchez Lencero, and José Antonio Becerra Villanueva. A new heat release rate (hrr) law for homogeneous charge compression ignition (hcci) combustion mode. *Applied Thermal Engineering*, 29(17-18):3654–3662, 2009.

[128] Hossein Ghomashi. *Modelling the combustion in a dual fuel HCCI engine. Investigation of knock, compression ratio, equivalence ratio and timing in a Homogeneous Charge Compression Ignition (HCCI) engine with natural gas and diesel fuels using modelling and simulation.* PhD thesis, University of Bradford, 2015.

[129] Ahmet Uyumaz, Bilal Aydoğan, Alper Calam, Fatih Aksoy, and Emre Yılmaz. The effects of diisopropyl ether on combustion, performance, emissions and operating range in a hcci engine. *Fuel*, 265:116919, 2020.

[130] Agustin Valera-Medina, M Gutesa, H Xiao, D Pugh, A Giles, B Goktepe, R Marsh, and P Bowen. Premixed ammonia/hydrogen swirl combustion under rich fuel conditions for gas turbines operation. *International Journal of Hydrogen Energy*, 44(16):8615–8626, 2019.

[131] Hadi Nozari and Arif Karabeyoğlu. Numerical study of combustion characteristics of ammonia as a renewable fuel and establishment of reduced reaction mechanisms. *Fuel*, 159:223–233, 2015.

[132] MF Ezzat and I Dincer. Development and assessment of a new hybrid vehicle with ammonia and hydrogen. *Applied energy*, 219:226–239, 2018.

[133] Frederic Vitse, Matt Cooper, and Gerardine G Botte. On the use of ammonia electrolysis for hydrogen production. *Journal of Power Sources*, 142(1-2):18–26, 2005.

[134] Russ College of Engineering and Technology. Ammonia electrolysis https://www.ohio.edu/engineering/ceer/ammonia-electrolysis.cfm, (accessed: 20-12-2019).

[135] Norlista Saliman. *The Effect of Nitrogen Dilution on the Flammability Limits of Hydrogen Enriched Natural Gas.* PhD thesis, UMP, 2010.

[136] Michael Dolan. Metal membrane for hydrogen separation, https://nh3fuelassociation.org/2017/10/01/delivering-clean-hydrogen-fuel-from-ammonia-using-metal-membranes/, (accessed: 10-02-2020).

[137] Bettergy. Ammonia cracking membrane reactor, https://arpa-e.energy.gov/?q=slick-sheet-project/ammonia-cracking-membrane-reactor, (accessed: 10-02-2020).

[138] CSIRO. Delivering clean hydrogen fuel from ammonia using metal membranes, https://www.csiro.au/en/research/ef/areas/renewable-and-low-emission-tech/hydrogen/hydrogen-membrane, (accessed: 10-02-2020).

[139] Valentina Ruiz. Analysis of existing refrigeration plants onboard fishing vessels and improvement possibilities. *Second International Simposium on Fishing Vessel Energy Efficiency E-Fishing*, 2012.

[140] Cruise Lines International Association et al. *2018 Cruise Industry Outlook.* Cruise Line International Association, 2017.

[141] Eke Eijgelaar, Carla Thaper, and Paul Peeters. Antarctic cruise tourism: the paradoxes of ambassadorship,“last chance tourism” and greenhouse gas emissions. *Journal of Sustainable Tourism*, 18(3):337–354, 2010.

Appendices

Appendix A

Analysis of various ship types

A.1 Chapter overview

The ammonia driven SOFC-ICE concept provides a great overall efficiency, however, limitations in the system design makes the concept not useful for all different ship types. In this chapter the most promising ship types will be analysed based on several criteria.

A.2 Criteria

1. Waste heat recovery

As mentioned in **Chapter 2**, high overall efficiencies of the SOFC-ICE system greatly depend on the maximum utilization of the generated waste heat. Nonetheless, not all ship types can benefit from the latter CHP configuration. For instance, the heat demand for cruise ships is significantly higher in contrast to standard cargo vessels. A huge portion of the heat is needed for passenger and crew accommodation, HVAC pre-heater and for the hot water heater [31]. Engine heat recovery systems and large auxiliary boilers are being used to satisfy the demand. These boilers also have the function to cover the periods of mismatch between the availability of waste heat and the heat demand. In terms of exhaust gas recovery, the recommended exhaust temperature after heat exchange should not go below 180 [$°C$] to minimize the risk of corrosion [139]. Fishing trawlers generally only require low temperature heat for defrosting the evaporation heat exchangers. In this respect, the high temperature waste heat can only flow through a turbine to create additional electricity. This will, however, not fully utilise the available waste heat energy. Factory fishing vessels, specialised in canning on the other hand, do need steam to be used for the cooking process.

2. SOFC-ICE ratio

The operational range of the ammonia hydrogen fueled ICE is limited by the occurrence of ringing and knocking. Therefore the hydrogen flow supplied to the ICE has to stay within the boundaries during full load and part load. As mentioned in the preliminary system configuration, the SOFC will be predominantly used to power the auxiliary systems, while the ICE is mechanically connected to the propeller. As depicted in Figure A.1a, the power requirement for the propulsion system is usually 3-4 times higher than that of the auxiliary systems. However, some ship types, including fishing and offshore vessels require auxiliary propulsion ratios in the order of 0.4-0.5. The preferred vessel type will be selected using the results from the dynamic model.

3. Operational profile

In contrary to IC engines, start up times for SOFCs are considerably longer and are also not designed for transient loading. Because of this, a vessel type which requires a long and steady demand of auxiliary and propulsion power is favored for the SOFC-ICE system. A major disadvantage of the SOFC-ICE layout is the ICE's hydrogen dependency. In other words, the SOFC has to run continuously to provide enough hydrogen for the ICE. Therefore vessel types with low deviations in propulsion and electric power demands are highly favored. Long distance cargo vessels equipped with slow-speed direct driven ICEs could benefit from the SOFC-ICE layout, since they are usually operating at a single cruising speeds. The deviations in the heat and electric power requirement for cruise ships on the other hand are typically much smaller in contrast to the propulsion power as can be seen in Figure A.1b. When no propulsion power is required, the hydrogen storage tank has to be big enough to temporarily store the hydrogen gas from the anode-off gas. Another solution is to temporarily lead the anode-off gas together with the cathode-off gas into a burner to create additional heat.

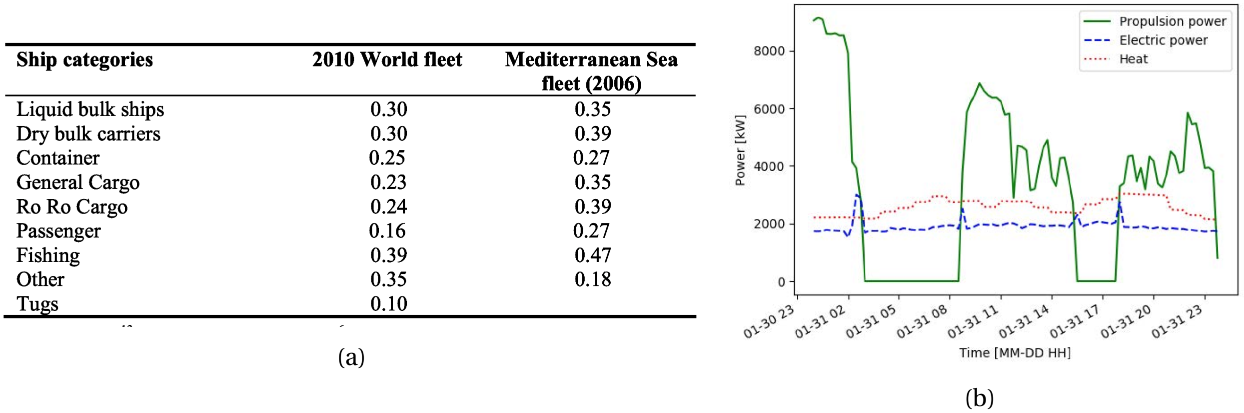

Ship categories	2010 World fleet	Mediterranean Sea fleet (2006)
Liquid bulk ships	0.30	0.35
Dry bulk carriers	0.30	0.39
Container	0.25	0.27
General Cargo	0.23	0.35
Ro Ro Cargo	0.24	0.39
Passenger	0.16	0.27
Fishing	0.39	0.47
Other	0.35	0.18
Tugs	0.10	

(a)

(b)

Figure A.1: (a) Estimated average vessel ratio of auxiliary propulsion for various ship types [30]. (b) Measured propulsion, electric power and heat requirement for a cruise ship during a 24h operation, winter (31 January) [31].

4. Safety

Great precaution measurements have to be taken for the ammonia storage and transport design, because of its toxicity to the environment. The risk and impact of ammonia leakage is more problematic for passenger vessels in contrast to cargo and off-shore vessels. Although proper ventilation and a doubled-walled piping design can significantly mitigate the impact, cargo vessels have the additional benefit of having sufficient gas masks on-board and a trained crew to cope with the situation.

5. Convenience

Yacht owners typically favor comfort, efficiency and total cost over fast traveling. Depending on the size of the vessel, diesel or battery electric propulsion systems provide convenient, less complex and fast responsive system designs. Passengers generally do not care about the type of power plant as long as it does not make noise or leave soot on the decks. In this case an SOFC-ICE combination could be beneficial in reducing noise and vibrations because of the smaller size of the diesel engine.

6. Expenditures

Carbon neutral fuels have shown much lower volumetric densities in comparison to nowadays bunker fuels. In this respect, more expensive and efficient system layouts to save on fuel and storage space or lengthen the travel distance may be more cost-effective to reduce the overall cost. Cruise ships and long distance cargo vessels are therefore interesting options.

A.2.1 Overview

Table A.1: Overview of the criteria analysis, in which the fishing ship has been set to zero for comparison.

	Cruise	Fishing	Cargo	Ferry	Yacht	off-shore
Waste heat	++	0	0	+	+	0
Operational profile	-	0	++	-	-	-
Safety	- -	0	+	-	0	+
Convenience	0	0	++	0	- -	0
Expenditures	++	0	+	++	- -	0

A.3 Ship proposal

From the criteria analysis in **Appendix A**, cruise ships can benefit the most from the SOFC-ICE layout. The recently adopted greenhouse gas reduction strategy by IMO discussed in **Chapter 1** and the fast growing rate of cruise ship passengers, which have increased from 17.8 M in 2009 to 25.8 M in 2017 [140] are great challenges faced by the cruise industry. Cruises are among the most carbon intensive in the whole tourism industry, with an estimated average of 160 $[kg]$ per passenger and per day [141]. Growing attention has been displayed on energy efficiency and the transition from fossil fuel to a more emission free approach, making it for a ship easier to dock at a heavily regulated harbour. Zero carbon fuels have a much lower volumetric energy density, meaning that carbon neutral cruise ships will need much larger fuel storage tanks resulting in less capacity for passengers. Some advantages of an SOFC-ICE layout are, waste heat recovery and the much higher system efficiency because of the SOFC. This will significantly decrease the fuel consumption and therefore also the size of the fuel storage.

Because of the hydrogen dependency of the ICE, large deviations in its operational profile are difficult to manage for the SOFC-ICE layout. Large hydrogen tanks and batteries are needed to maintain the stability of the system. In this respect, long distance direct driven cargo ships can also benefit from the SOFC-ICE layout. Those ships are usually operating at one cruising speed, which will result in a less deviated propulsion and auxiliary power demand throughout the time.

Appendix B

HCCI engine model supplementation

B.1 Chapter overview

B.2 Data acquisition

As mentioned in **Chapter 5**, the pressure crank angle Figures that are required for the HRR model are obtained from the paper by pochet et al. [23]. To get an acceptable accuracy, a plot digitizer has been used for the data extraction. In addition, the step size for the crank angle has been chosen to be 0.1 [CAD] to maintain a decent accuracy for the HRR and temperature block model. Therefore, interpolation of the pressure crank angle data is necessary to determine the missing values for each crank angle step:

$$y = y_1 + (x - x_1)\frac{y_2 - y_1}{x_2 - x_1} \tag{B.1}$$

B.2.1 Pressure crank angle HCCI engine

The pressure crank angle Figures from Pochet only provide data for crank angles between -30 to 30 [CAD], meaning that the remaining part of the 4-stroke combustion cycle process has to be manually extended. The pressure trace from Sapra, which is based on hydrogen natural gas combustion gives us a slight indication on how to fill in the missing data gaps. As can be seen in Figure B.1b, his pressure data fits almost seamlessly with the HCCI data at the ranges -360 to -10 [CAD]. The slope during compression has been slightly modified to comply with the 1.5 [bar] inlet pressure requirement at inlet valve opening (IVO).

B.2.2 Right side (expansion stroke) extension

Finding a reasonable extension for the pressure distribution after reaching 30 [CAD] is much more difficult, since the hydrogen natural gas data does not overlap the HCCI data. As can be seen in Figure B.1b, the experiment performed by Sapra has shown a significantly larger delay of the maximum pressure.

For 55% hydrogen, five different pressure crank angle variations as shown in the Figure B.2 have been investigated. The versions V1 and V5 can be seen as the lower and upper limit, respectively. For V5, we assume that the pressure distribution eventually converges with the NG data from Harsh, resulting in identical $p6$ values. V1 on the other hand, has been based on the already known slope at 30 [CAD], which has been extrapolated. In this case, the $p6$ value is almost 2.5 times lower compared to the V5 version. Variations V2, V3 and V4 are in between the upper and under boundaries.

As shown in Figure B.3a, for all pressure crank angle variations, the heat release rate is approaching zero at 205 [CAD]. This is because the pressure crank angle values between 150-210 [CAD] are known

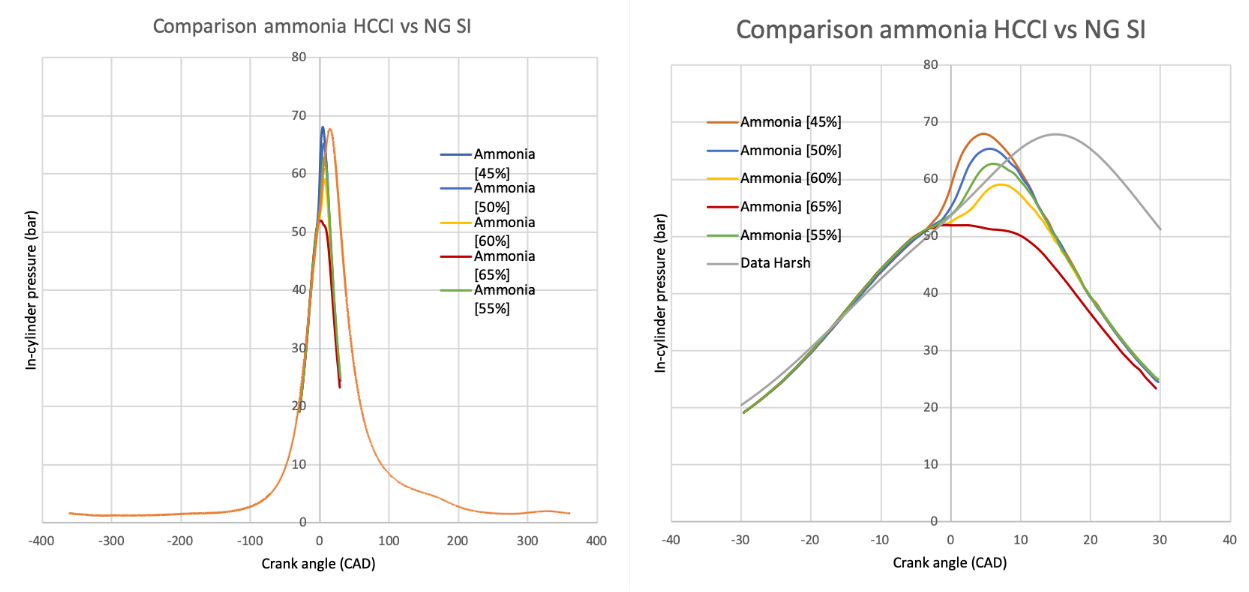

(a)

(b)

Figure B.1: (a) Pressure crank angle HCCI data for various hydrogen concentrations plotted together with the hydrogen NG data from Harsh [32]. (b) Close up pressure crank angle diagram.

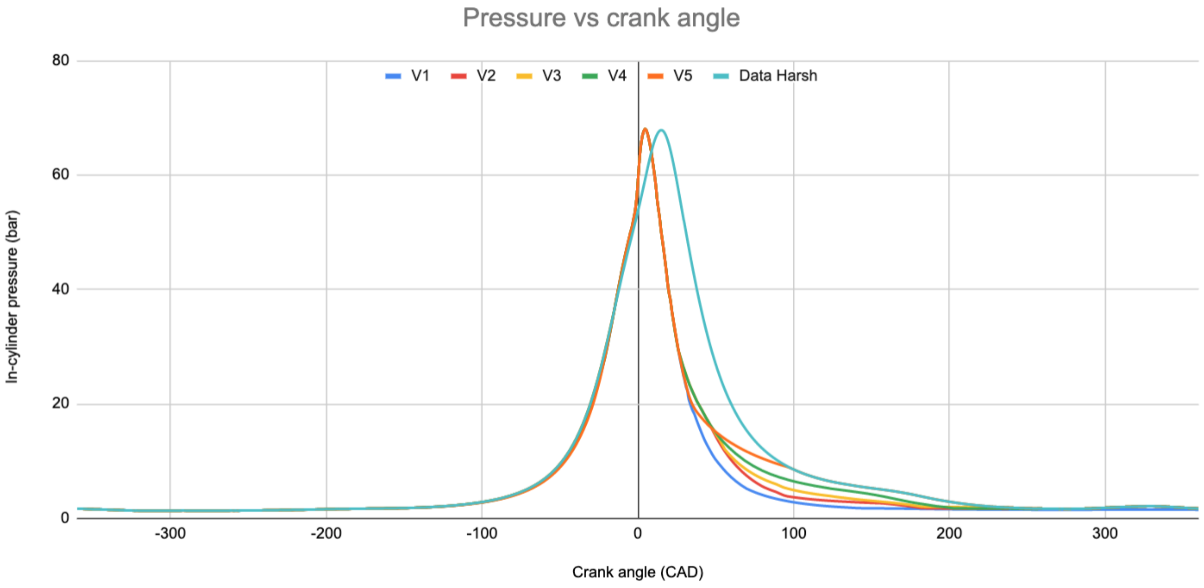

Figure B.2: Pressure crank angle variations for 55% hydrogen

from the HCCI data and this may imply that there is no late combustion after 205 [CAD]. In addition, the RCO slope (Figure B.3a), which is almost zero between 190 and 205 [CAD] can be seen as another indication of no late combustion after 205 [CAD]. Taking this into account, V1 has been modified to get a nearly zero heat release rate after 205 [CAD] and will be used in the in-cylinder model. It must be clarified that this V1 extension only applies for the 55% hydrogen pressure crank angle, meaning that the right side extension has to be re-calibrated, when using different hydrogen-ammonia ratios.

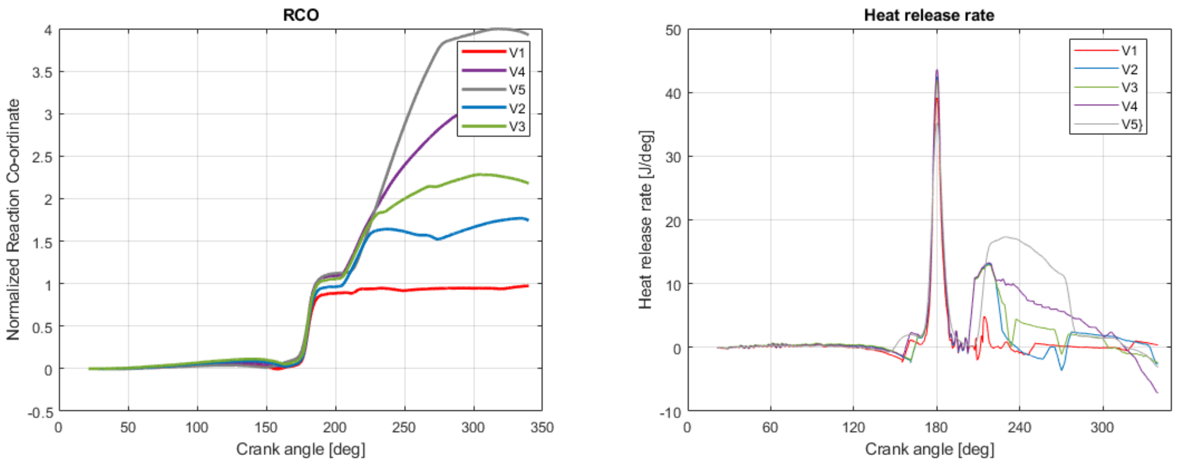

(a)

(b)

Figure B.3: (a) The *RCO* and (b) HRR slope for the five different variations.

B.3 Cylinder process model

This section gives an concise overview of the mass balance and composition model components and the fuel and air property components that are part of the in-cylinder model described in **Chapter 5**.

B.3.1 Initial conditions and input parameters

It is assumed that the gas mixture from the trapped condition (BDC) inside the cylinder obeys the ideal gas equation, in which R is the molar ideal gas constant:

$$P_t \cdot V_{IC} = R \cdot T_t \tag{B.2}$$

Gas constant

The gas constant can be calculated using Equation B.3 in which $\bar{R}$ is the universal gas constant 8.31441 $[KJ/kmol/K]$ and M the molecular weight (M) $[kg/kmol]$. The change in R can normally be neglected for fossil fuels, since there is only a slight increase in molecular weight during combustion. The gas constant value for air is therefore almost similar to that of the exhaust gas. However, this is not the case for hydrogen combustion, meaning that the change in R during each crank angle for hydrogen-ammonia combustion has to be taken into consideration.

$$R = \frac{\bar{R}}{M} \tag{B.3}$$

$$M = \frac{m}{n} \tag{B.4}$$

The overall in-cylinder gas constant can be determined by Equation B.5. To do this, the mass fraction of each component has to be calculated at every crank angle (steps of 0.1 $[CAD]$):

$$R_{mixture} = x_{air} \cdot R_{air} + x_{sg} \cdot R_{sg} + x_{fuel} \cdot R_{fuel} \tag{B.5}$$

Mass balance

To get the mass fractions, first a mass balance inside the control volume has to be established.

$$m_{tot} = m_f + m_{air} + m_{sg} \tag{B.6}$$

The mass of the fuel (m_f) can be obtained by integrating the combustion reaction rate (CRR) from the HRR model.

$$m_f = RCO = \int CRR \tag{B.7}$$

In order to determine the mass of air (m_{air}), first the trapped air fraction ($m_{air,t}$) and the trapped in-cylinder mass (m_t) have to be calculated.

$$m_{air} = x_{air,t} \cdot m_t - m_f \cdot \sigma \tag{B.8}$$

$$m_{sg} = x_{rg,t} \cdot m_t + m_f \cdot (\sigma + 1) \tag{B.9}$$

The trapped mass can be estimated from the ideal gas law, in which the trapped volume and pressure are obtained from the engine measurements. The trapped gas constant (R_t) of the mixture can be easily determined from Equation B.3.

$$m_t = \frac{P_t \cdot V_t}{R_t \cdot T_t} \tag{B.10}$$

At last, the trapped mass temperature can be determined from Equation B.11, in which V_{IC}, V_{EC} and V_{IO} are the in-cylinder volumes at inlet valve closing, outlet valve closing and inlet valve opening, respectively.

$$\frac{1}{T_t} = \frac{V_{IC} - V_{IO}}{V_{IC} \cdot T_{ind}} + \frac{V_{EC} \cdot P_{bld}}{V_{IC} \cdot P_t \cdot T_{bld}} \tag{B.11}$$

Mass fraction

$$x_f = \frac{m_f}{m} \tag{B.12}$$

An in-detail derivation of $x_{air,t}$ can be found in the paper written by Sapra et al. [32].

$$x_{air,t} = \frac{m_{air,t}}{m_t} = \frac{(1 - x_{rg,t}) \cdot \sigma \cdot \lambda}{\sigma \cdot \lambda + 1} \tag{B.13}$$

$$x_{sg} = \frac{m_{sg}}{m} \tag{B.14}$$

The summation of the mass fractions should equal 1:

$$x_{air} + x_{sg} + x_f = 1 \tag{B.15}$$

B.3.2 In-cylinder gas properties

In order to obtain the gas properties, we assume the in-cylinder gas to be defined as two mixtures (air and stoichiometric gas) that are considered to be mixtures of several types of molecules. The composition of the mixture can be regarded as a function of temperature, if we assume the mixture to be ideal but non-perfect. Then the gas properties can be easily determined by combining the species fractions which are obeying the ideal mixture [91]. The specific heats of the stoichiometric gas is always higher than that of air, since the combustion product (H_2O) has a higher specific heat than the oxidizer O_2.

For each of the components in the air and stoichiometric gas mixture, a power series of the temperature is required to obtain the specific heat at constant pressure. The air components j are N_2, O_2, Ar and CO_2, while the stoichiometric gas components j consist of N_2, Ar, CO_2 and H_2O.

$$c_{p,j} = a_{1,j} + a_{2,j} \cdot \theta + a_{3,j} \cdot \theta^2 .....a_{k,j} \cdot \theta^{k-1} .....a_{m,j} \cdot \theta^{m-1} = \sum_{k=1}^{m} a_{k,j} \cdot \theta^{k-1} \tag{B.16}$$

Here the temperature θ that will be used consists of a temperature shift (T_{shift}) and a normalized temperature (T_{norm}).

$$\theta = \frac{T - T_{shift}}{T_{norm}} \tag{B.17}$$

The specific heat based power terms $(k = 1$ to $5)$ do not give accurate results for all temperature ranges. In this respect, different power terms have to be used for temperatures below 1000 $[K]$ and higher than 1000 $[K]$, which can be found in Table B.1.

Table B.1: Coefficients for the polynomial to calculate c_p [35] for the air.

	a_1	a_2	a_3	a_4	a_5	Range $[K]$
N_2	3.5310	-1.2366 e^{-4}	-5.0300 e^{-7}	2.4353 e^{-9}	-1.4088 e^{-12}	< 1000
N_2	2.9526	1.3969 e^{-3}	-4.9263 e^{-7}	7.8601 e^{-11}	-4.6076 e^{-15}	> 1000
O_2	3.7825	-2.9967 e^{-3}	9.8473 e^{-6}	-9.6813 e^{-9}	3.2437 e^{-12}	< 1000
O_2	3.6610	6.5636 e^{-4}	-1.4115 e^{-7}	2.0580 e^{-11}	-1.2991 e^{-15}	> 1000
Ar	2.5000	0	0	0	0	< 1000
Ar	2.5000	0	0	0	0	> 1000
CO_2	2.3568	8.9846 e^{-3}	-7.1236 e^{-6}	2.4592 e^{-9}	-1.4370 e^{-13}	< 1000
CO_2	4.6366	2.7413 e^{-3}	-9.9583 e^{-7}	1.6037 e^{-10}	-9.1610 e^{-15}	> 1000
H_2O	72.5575	-6.62453 e^{-1}	2.5620 e^{-3}	-4.3659 e^{-6}	2.7818e^{-9}	< 1000
H_2O	0	0	0	0	0	> 1000

When the air mass fraction is known, the overall entropy of the air and stoichiometric gas mixture can be determined:

$$dh_j = c_{p,j} \cdot dT \tag{B.18}$$

$$h = x_{air} \cdot h_{air} + (1 - x_{air}) \cdot h_{sg} \tag{B.19}$$

$$du = c_v \cdot dT \tag{B.20}$$

$$u = x \cdot u_{air} + (1 - x) \cdot u_{sg} \tag{B.21}$$

The same procedure has to be followed for the calculation of $c_{p,fuel}$ and h_{fuel}. The polynomial coefficients for nitrogen have to be taken into account if a hydrogen nitrogen mixture is being used instead of pure hydrogen. This could be the case when the hydrogen in the anode-off gas is not extracted from the exhaust gas.

Table B.2: Coefficients for the polynomial to calculate c_p [35] for the fuel.

	a_1	a_2	a_3	a_4	a_5	Range $[K]$
NH_3	4.3018	-4.7713 e^{-3}	2.1934 e^{-5}	-2.2986 e^{-8}	8.2899 e^{-12}	< 1000
NH_3	2.7171	5.5686 e^{-3}	-1.7689 e^{-6}	2.6742 e^{-10}	-1.5273 e^{-14}	> 1000
H_2	2.3443	7.9805 e^{-3}	-1.9478 e^{-5}	2.0157 e^{-8}	-7.3761 e^{-12}	< 1000
H_2	2.9329	8.2661 e^{-4}	-1.4640 e^{-7}	1.5410 e^{-11}	-6.8880 e^{-16}	> 1000
N_2	3.5310	-1.2366 e^{-4}	-5.0300 e^{-7}	2.4353 e^{-9}	-1.4088 e^{-12}	< 1000
N_2	2.9526	1.3969 e^{-3}	-4.9263 e^{-7}	7.8601 e^{-11}	-4.6076 e^{-15}	> 1000

B.4 Seiliger model

The Seiliger model has been developed to obtain insight in the distribution of the heat release during the combustion process. In addition, the results can also serve as a foundation for the development of a complete ICE model, which includes the in-cylinder process and the gas exchange process model that is able to simulate the interaction between the in-cylinder process and the turbocharger system. The Seiliger results can then be used to simulate the engine based on the mean value first principle (MVFP) methodology. This design principle is favored for its simplicity, accuracy and real-time capability and enables the in-cylinder engine to be integrated to larger systems. In this respect, the ammonia fueled SOFC-ICE combination (mentioned in **Chapter 1**) could be dynamically modeled. However, this part of the engine modeling is outside the scope of the thesis, due to the short amount of time.

When T_{max}, p_{max} and total heat release are known, the V3-1 model developed by Ding et al [91] is able to fit the data in order to determine the three most significant Seiliger parameters a, b and c, which can be determined by solving the Equations B.22-B.24. Knowing these parameters, the heat quantities, work, temperature and pressures during each Seiliger stage can be determined from the formulas in Figure B.4.

$$P_{max,Seiliger} = P_1 \cdot r_c^{n_c} \cdot a \tag{B.22}$$

$$T_{max,Seiliger} = T_1 \cdot r_c^{n_c - 1} \cdot a \cdot b \tag{B.23}$$

$$q_{net,Seiliger} = q_{23} + q_{34} + q_{45} \tag{B.24}$$

$$= c_v \cdot T_1 \cdot r_c^{n_c-1} \cdot (a-1) + c_v \cdot T_1 \cdot \gamma \cdot r_c^{n_c-1} \cdot a \cdot (b-1) + c_v \cdot T_1 \cdot (\gamma - 1) \cdot r_c^{n_c-1} \cdot a \cdot b \cdot ln(c) \tag{B.25}$$

Because of the high amount of variables, an exact solution for the Seiliger parameters require lots of processing power. In addition, the step size of the model is 0.1 $[CAD]$, which means that it needs 7200 iterations in total for one combustion cycle (when assuming a 4-stroke engine). Estimating the three variables using the Newton Raphson method, which is based on iterations and a stop criteria could drastically decrease the required amount of processing power. The method offers a fast response time while keeping a decent accuracy and will therefore be implemented in the model.

According to the observations by Ding et al. [91] and Sapra et al. [32], the Seiliger parameters a, b and c represent different physical phenomenon in the combustion process. Parameter a has a great effect on T_{max} and P_{max} and can be directly related to the increase in combustion rate when increasing the hydrogen ratio. Seiliger parameter b mainly influences the maximum temperature and signifies a measure of combustion stability. Both parameters can be accurately determined from the available HCCI data (-30 to 30 $[CAD]$). Parameter c has a major impact on the pressure and temperature at EO of the

Seiliger stage	**Volume V**	**Pressure p**	**Temperature T**	**Specific work w**	**specific Heat q**
Compression 1-2	$\frac{V_1}{V_2}=r_c$	$\frac{p_2}{p_1}=r_c^{\kappa_a}$	$\frac{T_2}{T_1}=r_c^{(\kappa_a-1)}$	$w_{12}=\frac{R_a(T_2-T_1)}{\kappa_a-1}$	–
Isochoric combustion 2-3	$\frac{V_3}{V_2}=1$	$\frac{p_3}{p_2}=a$	$\frac{T_3}{T_2}=a$	–	$q_{23}=c_{v,a}(T_3-T_2)$
Isobaric combustion 3-4	$\frac{V_4}{V_3}=b$	$\frac{p_4}{p_3}=1$	$\frac{T_4}{T_3}=b$	$w_{34}=R_a(T_4-T_3)$	$q_{34}=c_{p,a}(T_4-T_3)$
Isothermal combustion 4-5	$\frac{V_5}{V_4}=c$	$\frac{p_4}{p_5}=c$	$\frac{T_5}{T_4}=1$	$w_{45}=R_aT_4\ \ln\ c$	$q_{45}=R_aT_4\ \ln\ c$
Expansion 5-6	$\frac{V_6}{V_5}=\frac{r_{eo}r_c}{bc}$	$\frac{p_5}{p_6}=\left(\frac{r_{eo}r_c}{bc}\right)^{n_{exp}}$	$\frac{T_5}{T_6}=\left(\frac{r_{eo}r_c}{bc}\right)^{n_{exp}-1}$	$w_{45}=\frac{R_a(T_6-T_5)}{(n_{exp}-1)}$	–

Figure B.4: Basic Seiliger process Equations [33]

Seiliger process and can be physically related to the late combustion. However, the pressure distribution from 30 $[CAD]$ to EO is not known and has been manually extended as described in **Section B.2.2**. This results in an inaccurate c value estimation and therefore also a weird shaped Seiliger diagram.

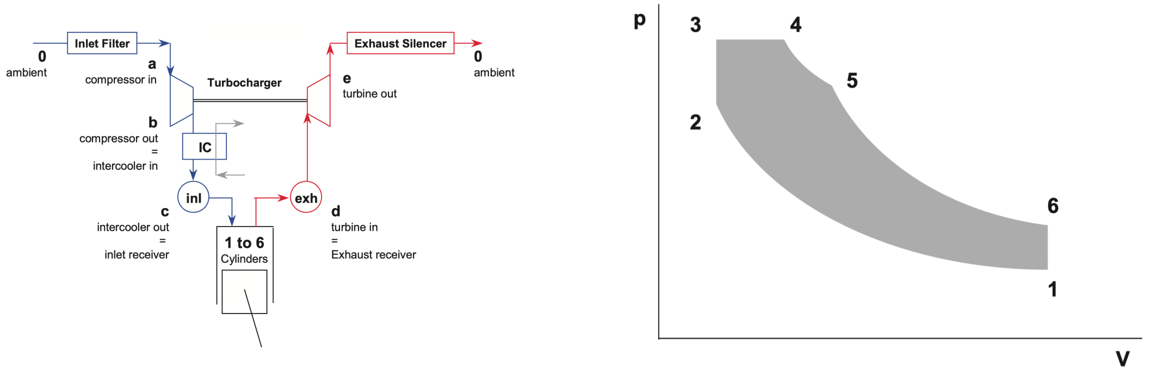

(a)

(b)

Figure B.5: (a) Gas exchange process (labelled a-e) to the cylinder [34] and (b) Seiliger in-cylinder process (labelled 1-6) in P-V diagram [34].

The polytropic exponent of compression parameter (n_c) can be represented as the heat loss during the compression process. n_c is required in the $q_{net,Seiliger}$ formula (equation B.24) and can be deter-

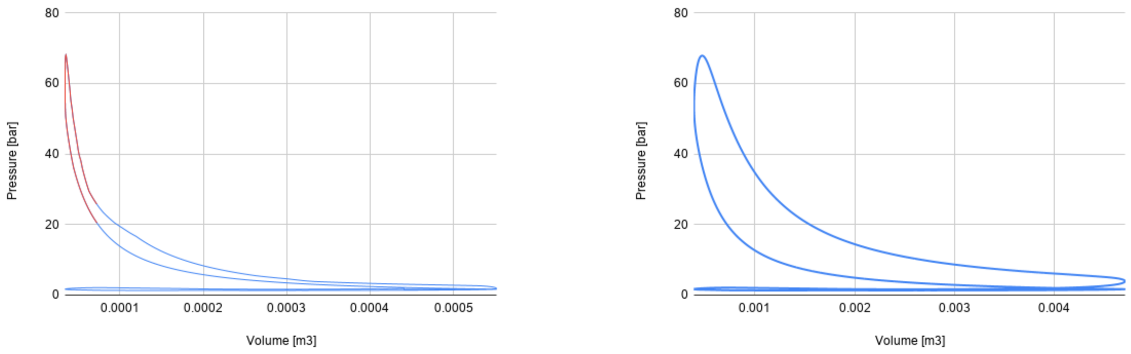

(a)

(b)

Figure B.6: (a) P-V diagram ammonia hydrogen (55%H) HCCI engine in which the available data is shown in red and the extrapolated data in blue and (b) P-V diagram hydrogen NG Harsh data [32]. As can be seen, the shape of the HCCI P-V diagram is much smaller than the one for SI.

mined as follows:

$$n_c = ln(\frac{P_1}{P_2}/\frac{V_2}{V_1}). \tag{B.26}$$

The same way goes for the parameter representing the heat loss during the expansion process, which is known as the polytropic exponent of expansion parameter (n_e):

$$n_e = ln(\frac{P_5}{P_6}/\frac{V_6}{V_5}). \tag{B.27}$$

B.4.1 Seiliger results

The Seiliger parameters a, b and c are the results from the first iteration and are therefore lacking in accuracy. The Newton Raphson method for solving the Equations B.22-B.24 in order to obtain more accurate results has not been performed due to the short amount of time. As can be seen in the Figures B.7a and B.7b, the results from the first iteration are decent, however, the Seiliger shapes are not completely aligning with the pressure distributions from the experiments.

The main reason for the development of the Seiliger model is to obtain insight in the distribution of the heat release. As can be seen in Figure B.8a the heat release at 47H is dominated by the Seiliger stage of iso-volumetric combustion (q_{23}). However, the latter slowly swifts to the isobaric combustion and expansion stage (q_{34}), when decreasing the hydrogen content. At 31H, stage 3-4 (q_{34}) of the Seiliger cycle almost makes up 99% of the total heat release. These results may differ slightly, since the Seiliger parameters have not been fully optimised.

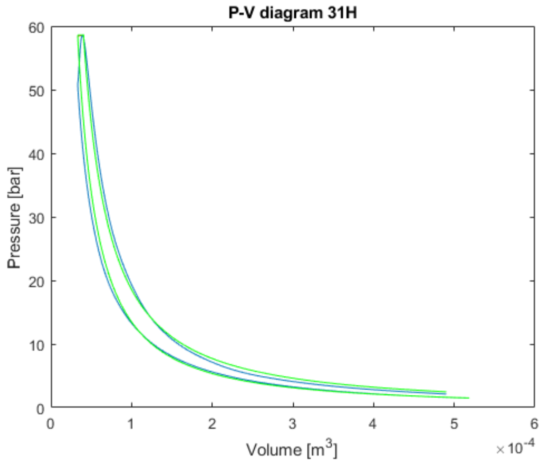

(a) (b)

Figure B.7: (a) Pressure volume diagram for 31 volumetric percent hydrogen and (b) pressure volume diagram for 47 volumetric percent hydrogen. The Seiliger shapes in green are also included in both figures. Note: these results are not completely accurate.

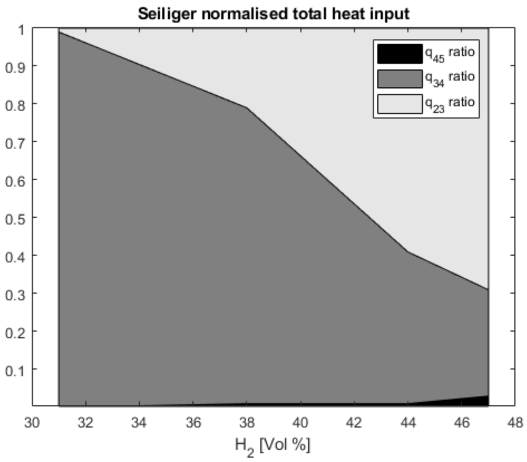

(a)

Figure B.8: (a) a schematic overview of the heat release distribution at the Seiliger stages 2-3 (isovolumetric combustion), 3-4 (isobaric combustion and expansion) and 4-5 (isothermal combustion and expansion) for a range of hydrogen fractions. Note: these results are not completely accurate.

Appendix C

MKIM and Wiebe model supplementation

This appendix includes additional figures and tables from the results in **Chapter 7**.

C.1 MKIM and Wiebe function results for 31H

C.1.1 Wiebe function results for 31H

Table C.1: Comparison in combustion characteristics between the in-cylinder model (heat loss calibrated S Law engine) and the Wiebe function for 31 vol. % hydrogen (31H).

	Unit	**In-cylinder model**	**Wiebe function**	**Error [%]**
IMEP	$[bar]$	2.532	2.581	-1.94
P_i	$[kW]$	11.40	11.61	-1.94
LHV fuel	$[MJ/kg]$	22.738	22.738	0
m_{bf}	$[mg]$	99.178	103.044	-3.90
$m_{f,injected}$	$[mg]$	139.471	144.909	-3.90
$FuelMEP$	$[bar]$	8.810	8.848	-3.90
RCO	$[-]$	0.711	0.711	0
Heat loss	$[kJ/cycle]$	0.914	0.907	0.77
η_{comb}	$[-]$	0.706	0.706	0
η_q	$[-]$	0.592	0.610	-3.04
η_{td}	$[-]$	0.673	0.655	2.57
η_i	$[-]$	0.2810	0.2819	-0.32

C.1.2 MKIM function results for 31H

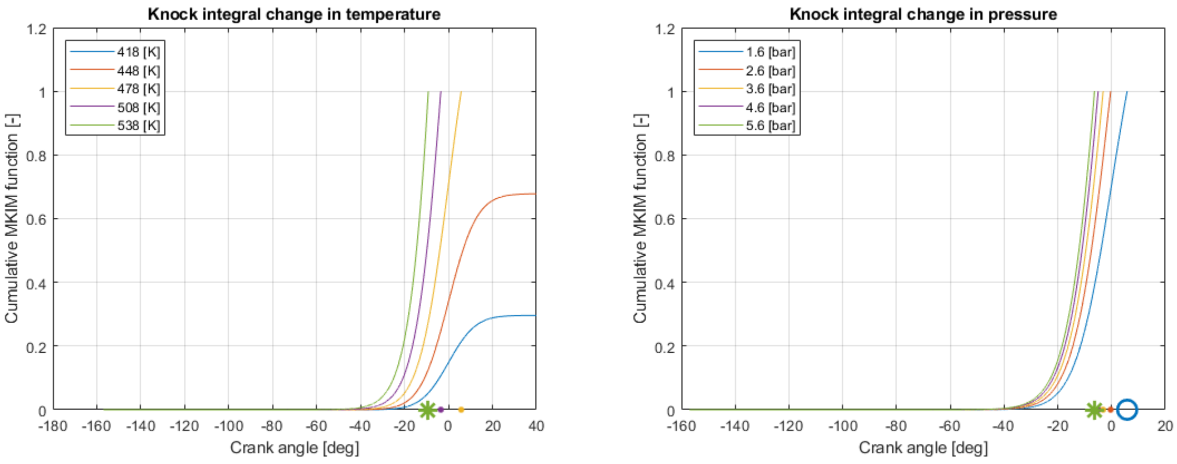

(a)

(b)

Figure C.1: The knock integral function for a range of initial inlet temperatures (a) and pressures (b) at inlet valve closing. The baseline temperature and pressure values that have been used in the in-cylinder model are 478 $[K]$ and 1.6 $[bar]$ (for 31H), respectively.

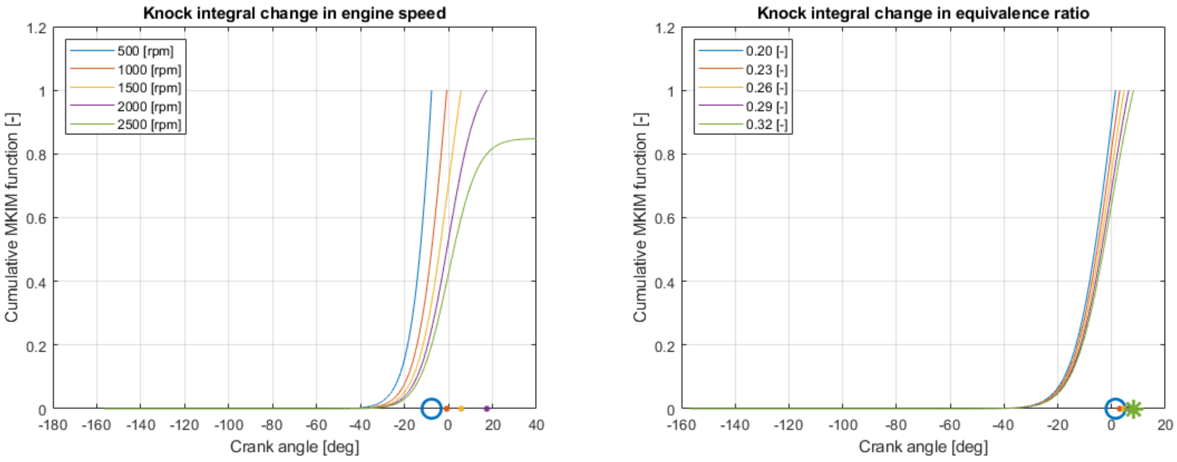

(a)

(b)

Figure C.2: The knock integral function for a range of initial engine speeds (a) and equivalence ratios (b) at inlet valve closing. The baseline engine speed and equivalence ratio that have been used in the in-cylinder model are 1500 $[rpm]$ and 0.26 $[-]$ (for 31H), respectively.

C.2 Parametric study 31H

C.2.1 Change in initial pressure

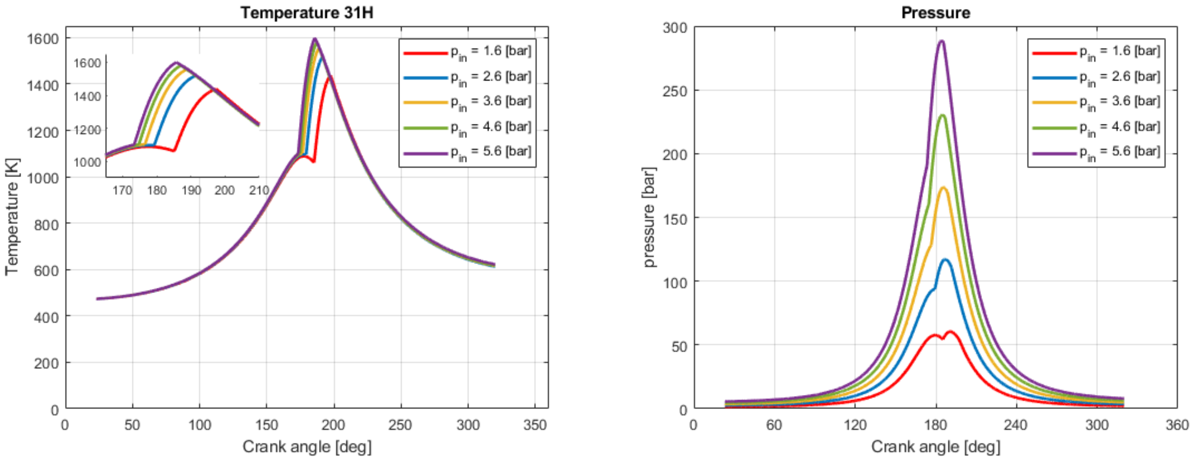

(a)

(b)

Figure C.3: (a) Temperature and (b) pressure distribution for a range of initial inlet pressure conditions. The initial pressure of 1.6 $[bar]$ (coloured in red) is the baseline condition that has been used in **Chapter 6** (Engine scaling).

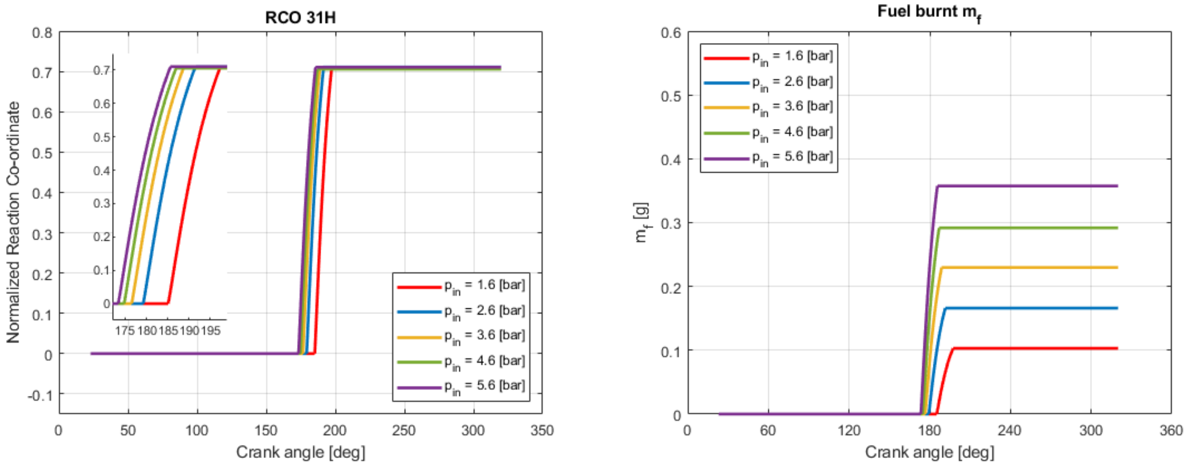

(a)

(b)

Figure C.4: (a) RCO and (b) fuel burnt curve for a range of initial inlet pressure conditions. The initial pressure of 1.6 $[bar]$ (coloured in red) is the baseline condition.

C.2.2 Change in engine speed

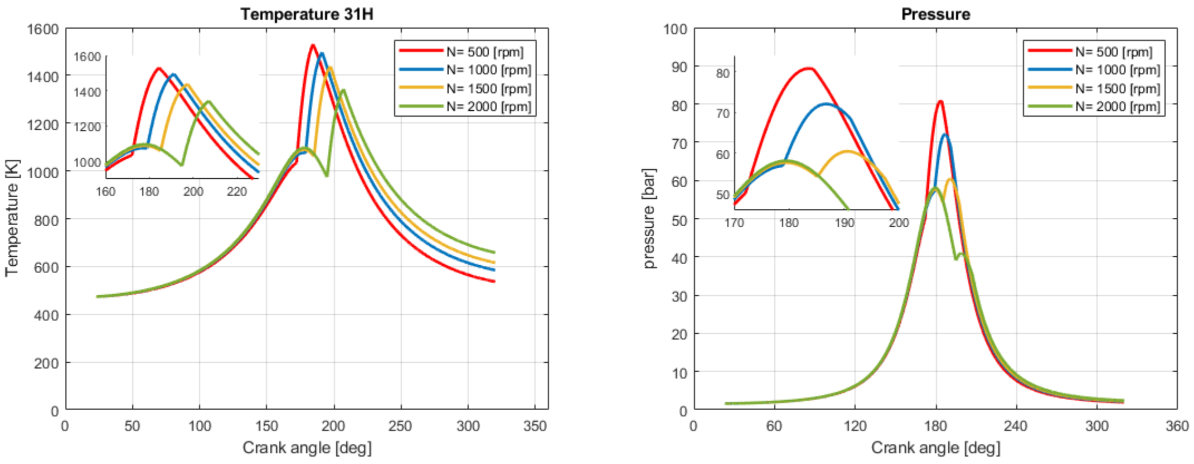

(a)

(b)

Figure C.5: (a) Temperature and (b) pressure distribution for a range of engine speed (N) conditions. The engine speed of 1500 [rpm] (coloured in yellow) is the baseline condition that has been used in **Chapter 6** (Engine scaling).

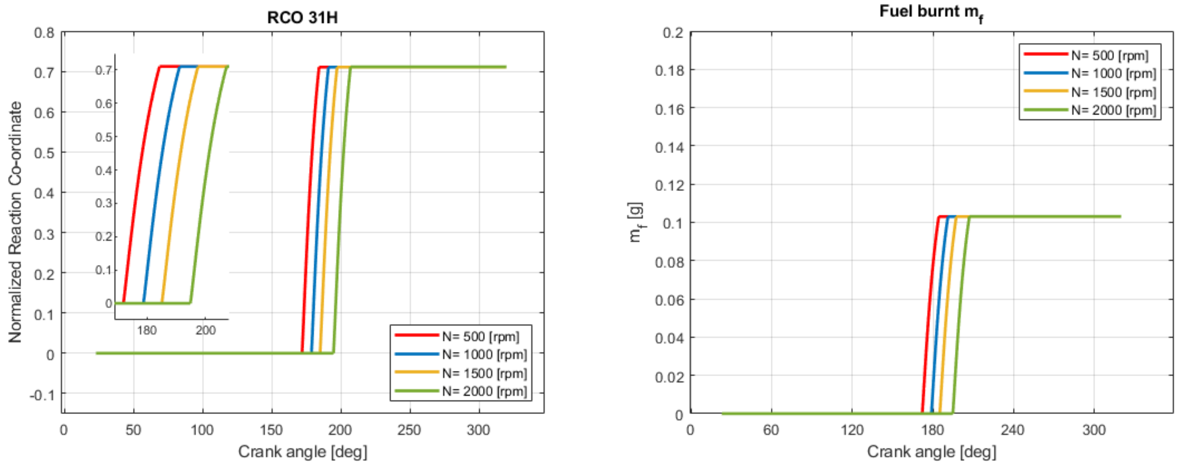

(a)

(b)

Figure C.6: (a) RCO and (b) fuel burnt curve for a range of engine speed (N) conditions. The engine speed of 1500 [rpm] (coloured in yellow) is the baseline condition.

C.2.3 Change in equivalence ratio

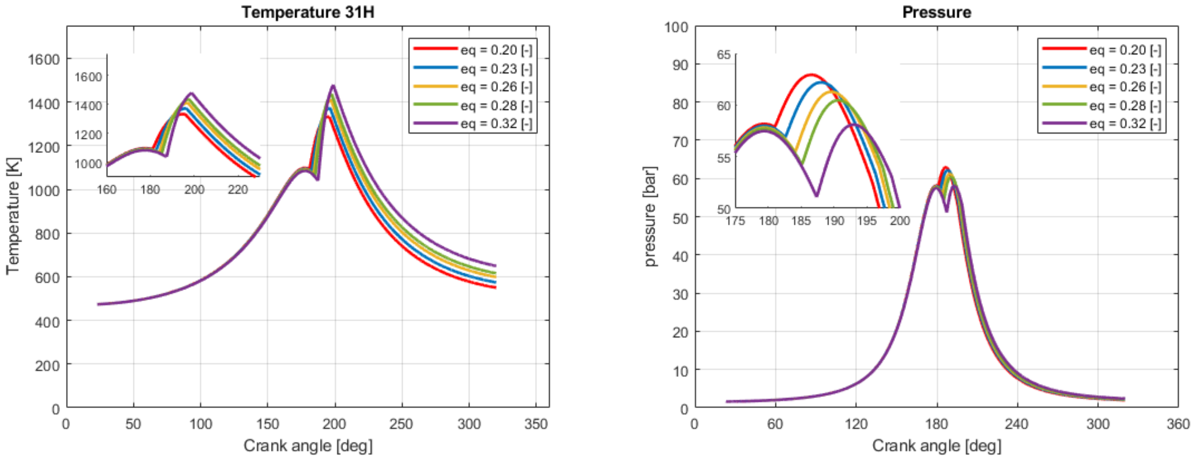

(a)

(b)

Figure C.7: (a) Temperature and (b) pressure distribution for a range of equivalence ratio conditions. The initial equivalence ratio of 0.26 [−] (coloured in yellow) is the baseline condition that has been used in **Chapter 6** (Engine scaling).

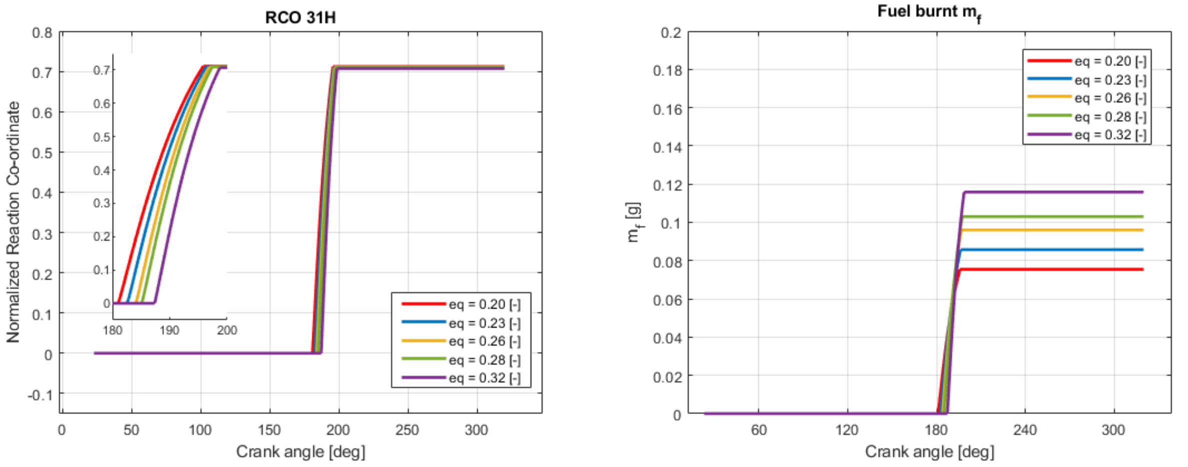

(a)

(b)

Figure C.8: (a) *RCO* and (b) fuel burnt curve for a range of equivalence ratio conditions. The initial equivalence ratio of 0.28 [−] (coloured in green) is the baseline condition.

C.2.4 Change in inlet temperature

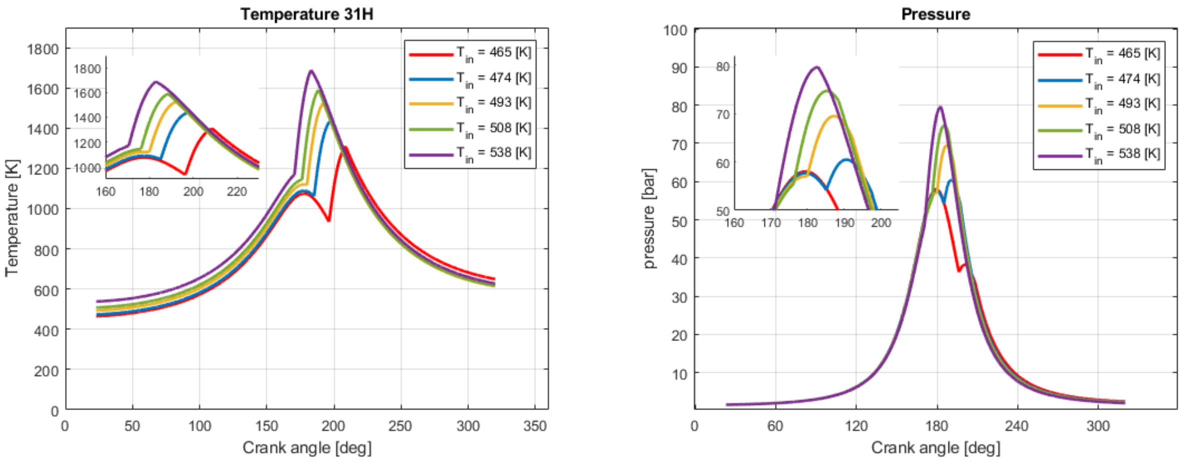

(a)

(b)

Figure C.9: (a) Temperature and (b) pressure distribution for a range of initial temperature conditions. The initial temperature of 474 $[K]$ (coloured in blue) is the baseline condition.

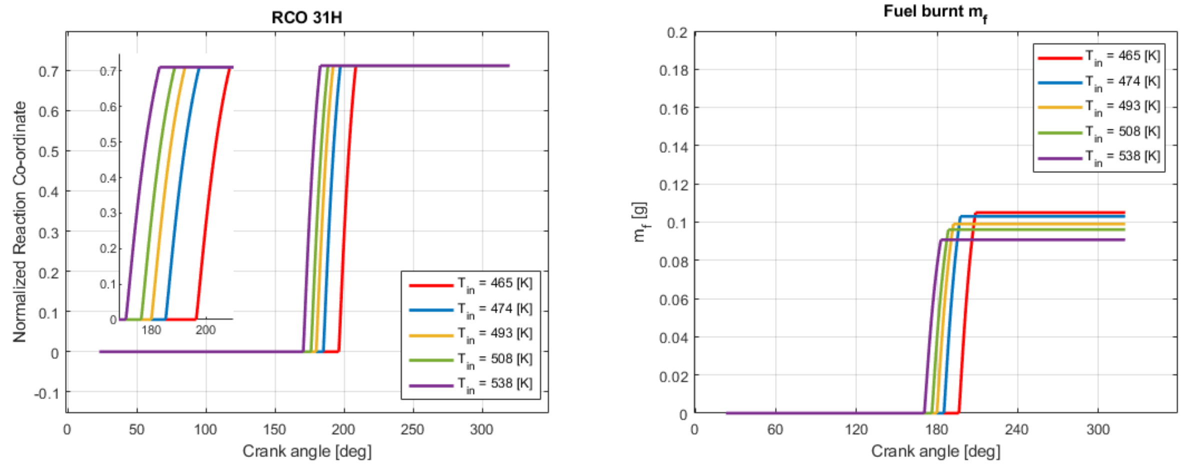

(a)

(b)

Figure C.10: (a) RCO and (b) fuel burnt curve for a range of initial temperature conditions. The initial temperature of 474 $[K]$ (coloured in blue) is the baseline condition.

C.3 Parametric study 47H

C.3.1 Change in initial pressure

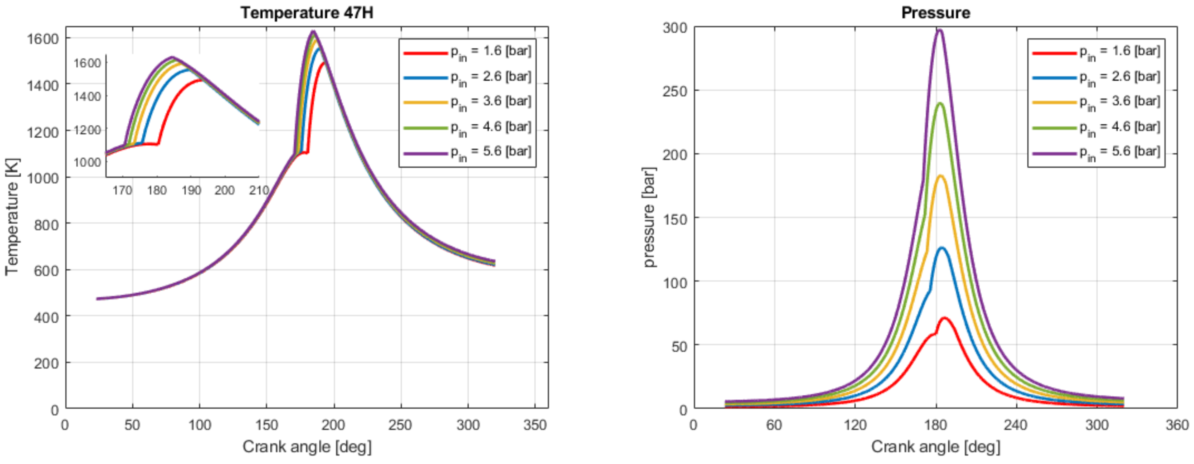

(a) (b)

Figure C.11: (a) Temperature and (b) pressure distribution for a range of initial inlet pressure conditions. The initial pressure of 1.6 $[bar]$ (coloured in red) is the baseline condition that has been used in **Chapter 6** (Engine scaling).

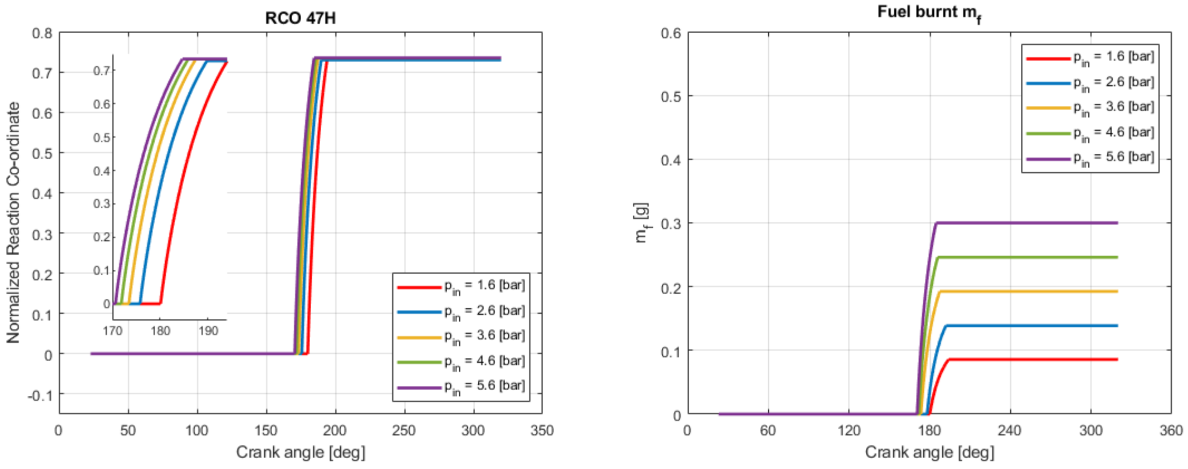

(a) (b)

Figure C.12: (a) RCO and (b) fuel burnt curve for a range of initial inlet pressure conditions. The initial pressure of 1.6 $[bar]$ (coloured in red) is the baseline condition.

C.3.2 Change in engine speed

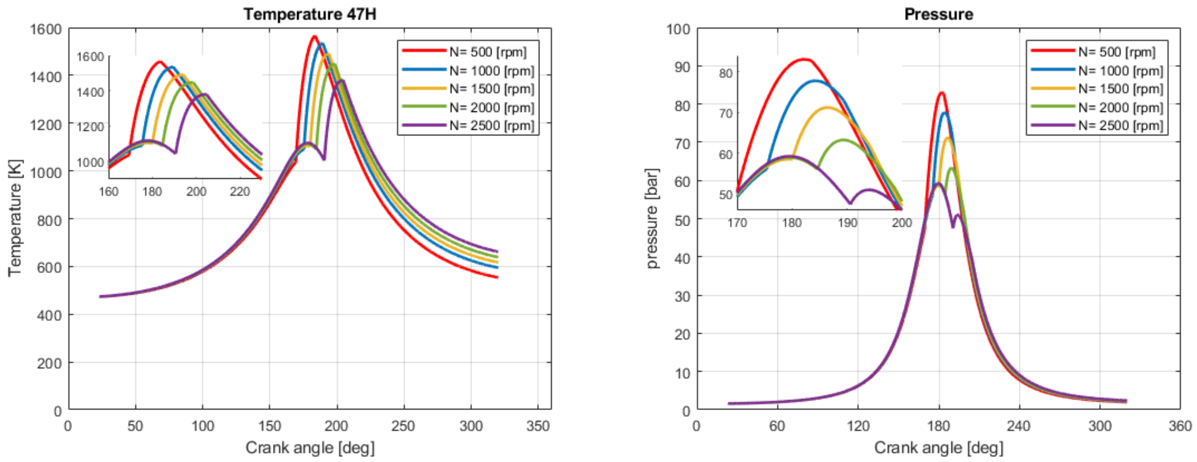

(a) (b)

Figure C.13: (a) Temperature and (b) pressure distribution for a range of engine speed (N) conditions. The engine speed of 1500 $[rpm]$ (coloured in yellow) is the baseline condition that has been used in **Chapter 6** (Engine scaling).

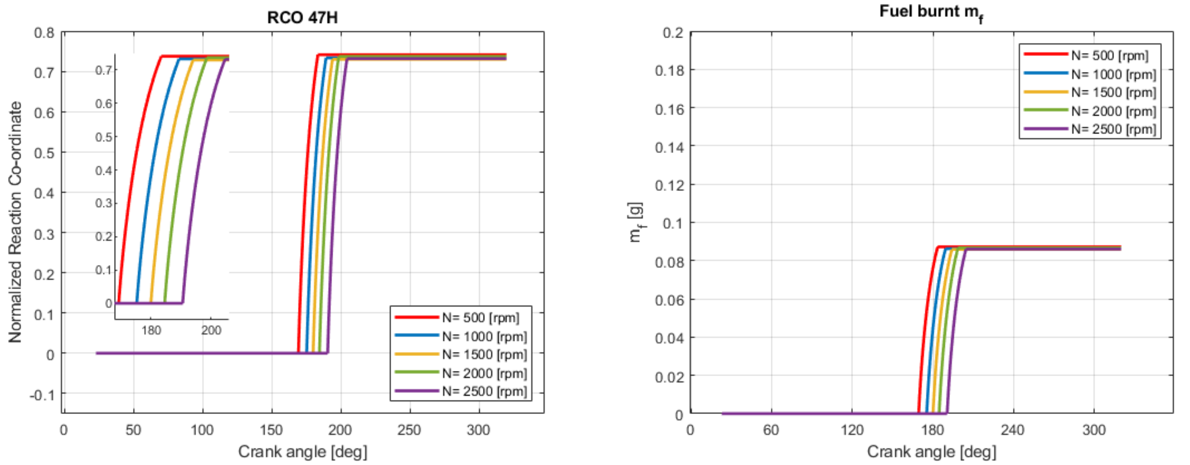

(a) (b)

Figure C.14: (a) RCO and (b) fuel burnt curve for a range of engine speed (N) conditions. The engine speed of 1500 $[rpm]$ (coloured in yellow) is the baseline condition.

C.3.3 Change in equivalence ratio

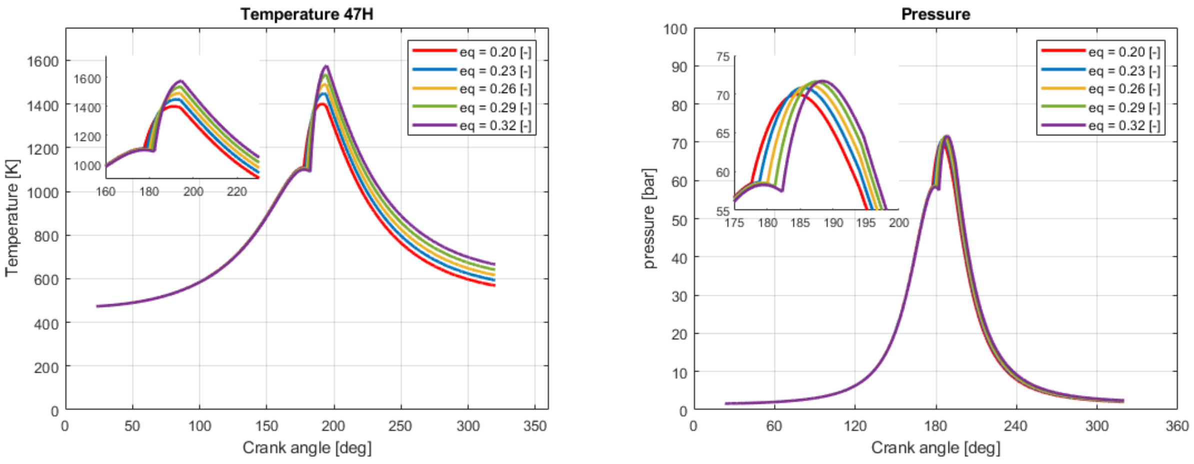

(a)

(b)

Figure C.15: (a) Temperature and (b) pressure distribution for a range of equivalence ratio conditions. The initial equivalence ratio of 0.26 [−] (coloured in yellow) is the baseline condition that has been used in **Chapter 6** (Engine scaling).

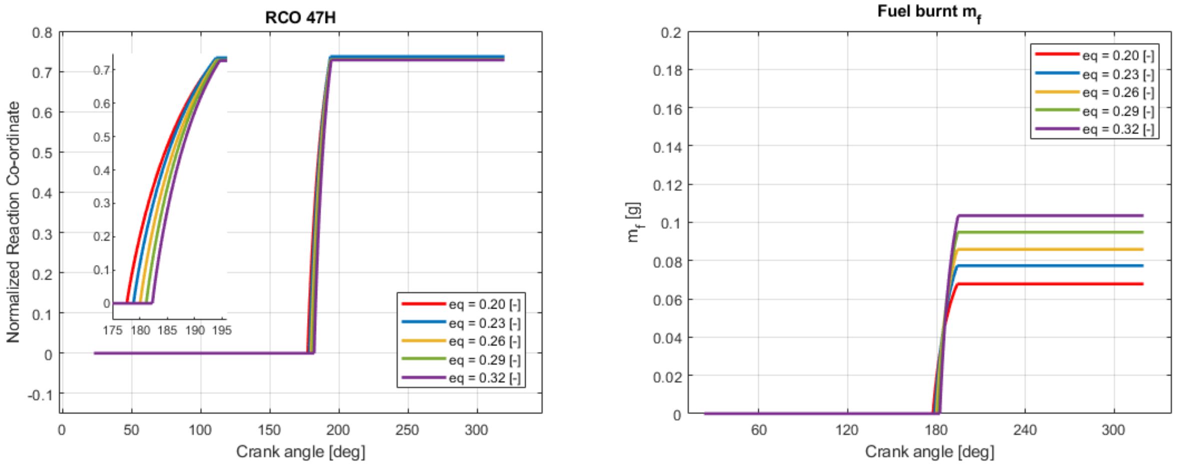

(a)

(b)

Figure C.16: (a) *RCO* and (b) fuel burnt curve for a range of equivalence ratio conditions. The initial equivalence ratio of 0.26 [−] (coloured in yellow) is the baseline condition.

C.3.4 Change in inlet temperature

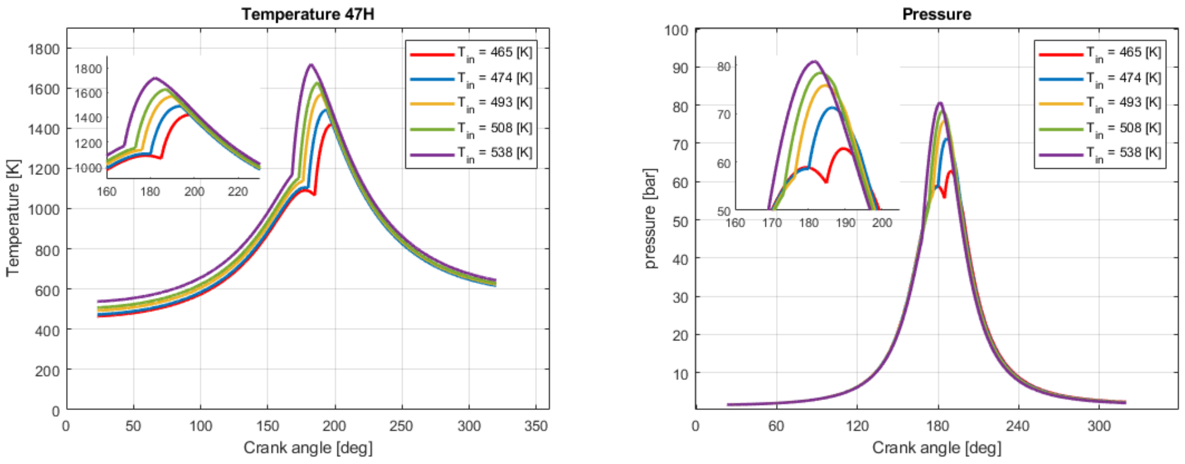

(a) (b)

Figure C.17: (a) Temperature and (b) pressure distribution for a range of initial temperature conditions. The initial temperature of 474 $[K]$ (coloured in blue) is the baseline condition.

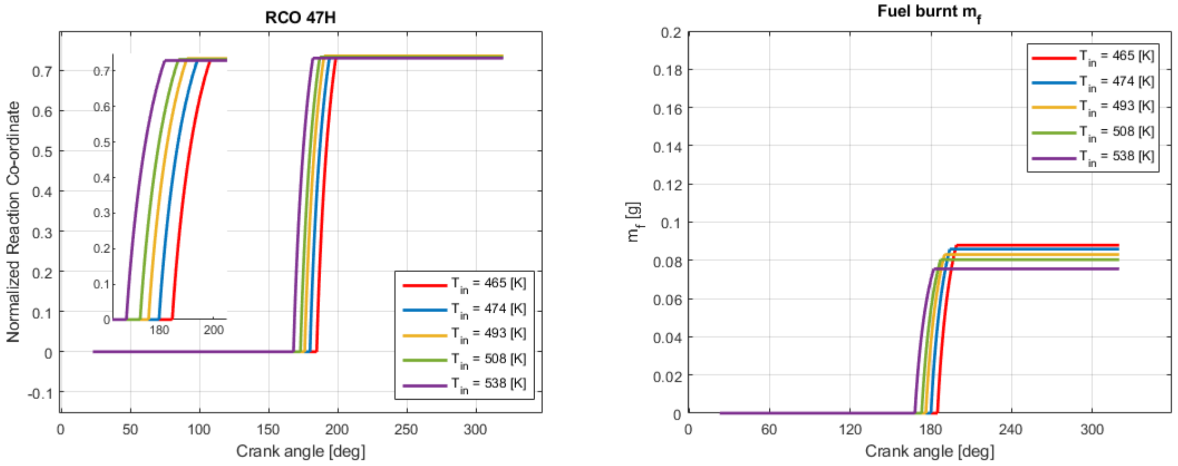

(a) (b)

Figure C.18: (a) *RCO* and (b) fuel burnt curve for a range of initial temperature conditions. The initial temperature of 474 $[K]$ (coloured in blue) is the baseline condition.

C.3.5 Overview results parametric study 31H

Table C.2: Overview of the engine modeling results for a range of initial conditions. The values in green represent the baseline results from **Chapter 6** (Engine scaling).

Inlet pressure	Unit	$P_{in} = 1.6\ [bar]$	$P_{in} = 2.6\ [bar]$	$P_{in} = 3.6 [bar]$	$P_{in} = 4.6\ [bar]$	$P_{in} = 5.6\ [bar]$
SOC	$[CAD]$	**185.09**	179.23	176.49	174.67	173.33
Burn duration	$[CAD]$	**12.31**	12.31	12.31	12.31	12.31
IMEP	$[bar]$	**2.581**	4.343	6.101	7.803	9.624
P_i	$[kW]$	**11.61**	19.54	27.45	35.11	43.31
η_i	$[-]$	**0.2819**	0.2968	0.3015	0.3037	0.3057
P_{max}	$[bar]$	**60.45**	117.00	173.40	230.40	288.40
T_{max}	$[K]$	**1437**	1519	1553	1575	1580
$m_{f,injected}$	$[mg]$	**144.99**	233.58	323.02	410.21	502.60
Engine speed	Unit	$N = 500\ [rpm]$	$N = 1000\ [rpm]$	$N = 1500\ [rpm]$	$N = 2000\ [rpm]$	$N = 2500\ [rpm]$
SOC	$[CAD]$	172.03	178.83	**185.09**	194.81	Misfire
Burn duration	$[CAD]$	12.31	12.31	**12.31**	12.31	-
IMEP	$[bar]$	2.001	2.466	**2.581**	2.448	-
P_i	$[kW]$	3.00	7.398	**11.61**	14.69	-
η_i	$[-]$	0.2204	0.2716	**0.2819**	0.2692	-
P_{max}	$[bar]$	80.75	72.06	**60.45**	58.06	-
T_{max}	$[K]$	1530	1495	**1437**	1334	-
$m_{f,injected}$	$[mg]$	144.99	144.85	**144.99**	144.99	-
Equivalence ratio	Unit	eq = 0.20 [−]	eq = 0.23 [−]	eq = 0.26 [−]	eq = 0.28 [−]	eq = 0.32 [−]
SOC	$[CAD]$	181.00	182.52	184.05	**185.09**	187.29
Burn duration	$[CAD]$	14.80	13.71	12.82	**12.31**	11.44
IMEP	$[bar]$	1.675	2.020	2.356	**2.581**	2.973
P_i	$[kW]$	7.54	9.088	10.60	**11.61**	13.38
η_i	$[-]$	0.2518	0.2672	0.2784	**0.2819**	0.2911
P_{max}	$[bar]$	62.93	62.18	61.25	**60.45**	58.08
T_{max}	$[K]$	1332	1373	1413	**1437**	1479
$m_{f,injected}$	$[mg]$	106.10	120.57	135.03	**144.99**	162.99
Inlet temperature	Unit	$T_{in} = 465\ [K]$	$T_{in} = 474\ [K]$	$T_{in} = 493\ [K]$	$T_{in} = 508\ [K]$	$T_{in} = 538\ [K]$
SOC	$[CAD]$	196.29	**185.09**	179.88	176.16	170.66
Burn duration	$[CAD]$	12.31	**12.31**	12.31	12.31	12.31
IMEP	$[bar]$	2.410	**2.581**	2.434	2.285	1.956
P_i	$[kW]$	10.85	**11.61**	10.95	10.28	8.800
η_i	$[-]$	0.2603	**0.2819**	0.2790	0.2699	0.2448
P_{max}	$[bar]$	57.99	**60.45**	69.42	74.64	79.60
T_{max}	$[K]$	1309	**1437**	1526	1590	1688
$m_{f,injected}$	$[mg]$	147.66	**144.99**	139.26	135.18	127.63

C.4 Iso-octane vs n-heptane on the MKIM and Wiebe function 47H

C.4.1 Excluding temperature calibration

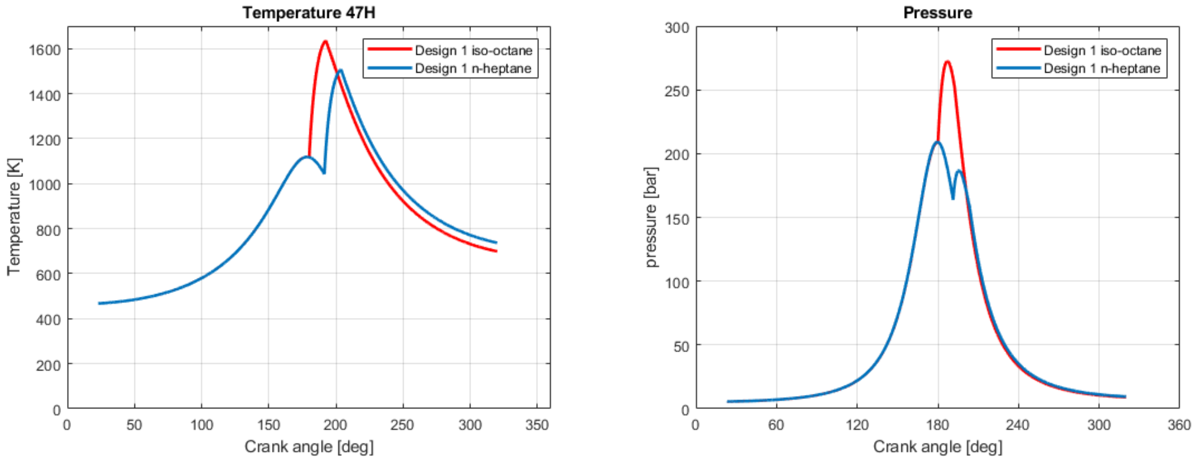

(a) (b)

Figure C.19: (a) Temperature and (b) pressure distribution for the designs 1 and 2. The input parameters can be found in Table 7.4.

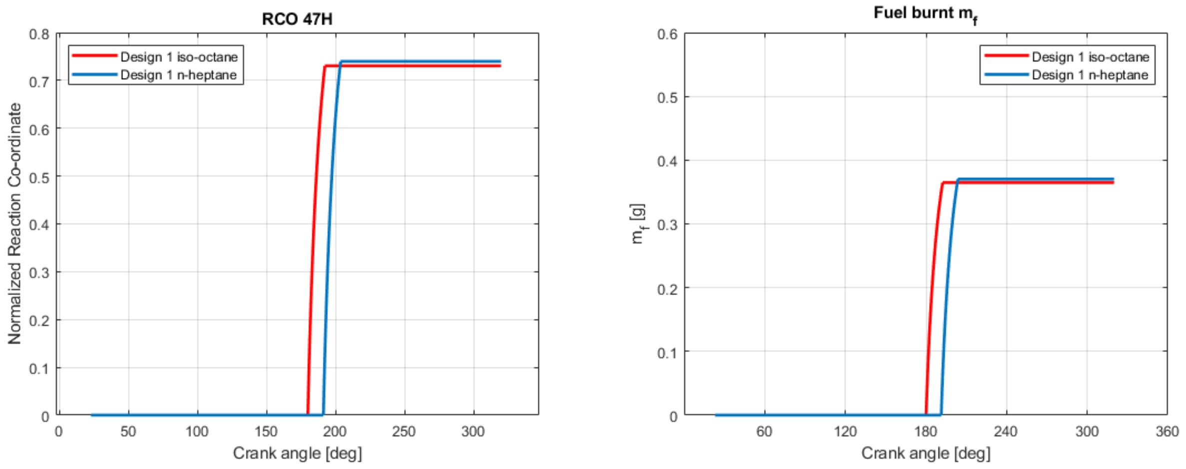

(a) (b)

Figure C.20: (a) *RCO* and (b) fuel burnt curve for the designs 1 and 2. The input parameters can be found in Table 7.4.

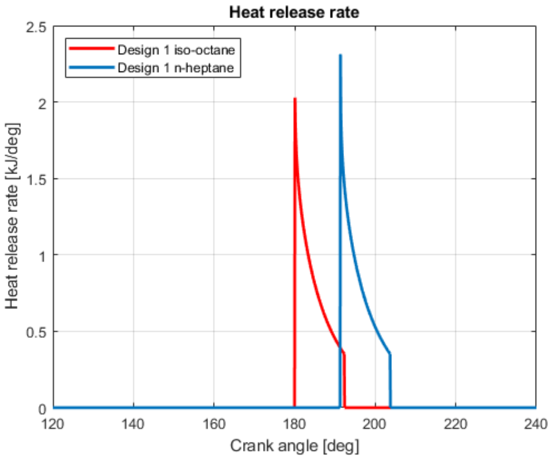

(a)

Figure C.21: (a) The heat release rate curve.

C.4.2 Including temperature calibration

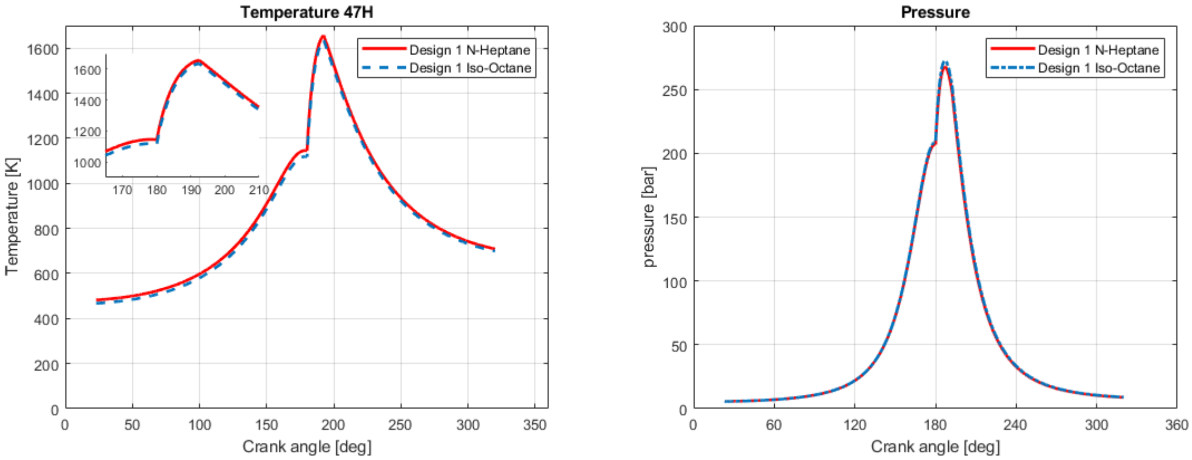

(a) (b)

Figure C.22: (a) Temperature and (b) pressure distribution for the designs 1 and 2. The input parameters can be found in Table 7.4.

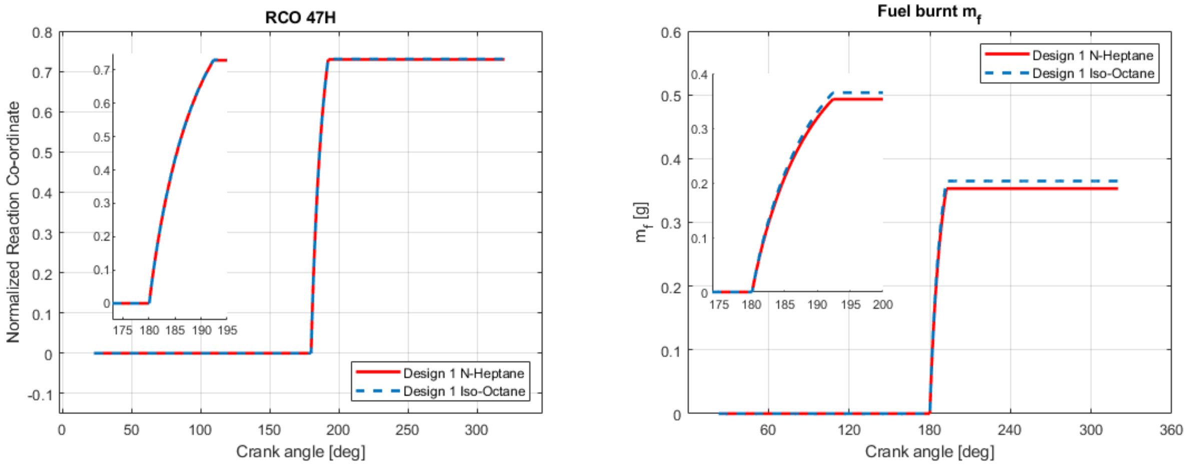

(a)
(b)

Figure C.23: (a) *RCO* and (b) fuel burnt curve for the designs 1 and 2. The input parameters can be found in Table 7.4.

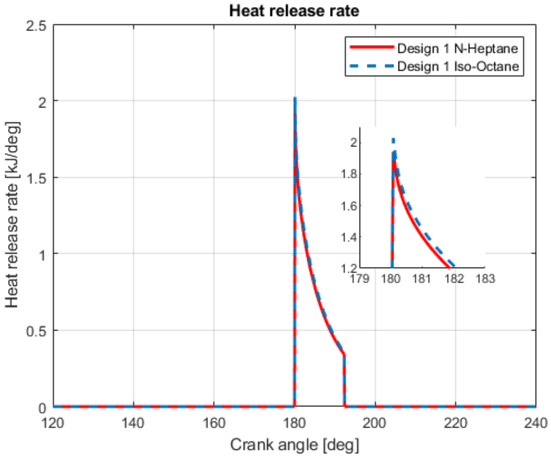

(a)

Figure C.24: (a) The heat release rate curve.

C.4.3 Influences temperature calibration 31H

Table C.3: Overview results in which design 1 + T_{opt} includes an inlet temperature calibration to shift the SOC to TDC, while design 1 (without T_{opt}) uses the same inlet temperature for 47H.

	Unit	Design 1 + T_{opt}	Design 1	Design 2 + T_{opt}	Design 2
SOC	$[CAD]$	180.01	178.89	180.03	177.00
Burn duration	$[CAD]$	11.44	11.44	14.80	14.80
IMEP	$[bar]$	11.55	11.42	5.76	5.54
P_i	$[kW]$	86.61	85.64	34.54	33.21
η_i	$[-]$	0.3291	0.3281	0.2940	0.2892
P_{max}	$[bar]$	262.1	268.1	190.0	201.6
T_{max}	$[K]$	1608	1629	1356	1410
$m_{f,injected}$	$[mg]$	560.40	555.90	312.33	305.16